#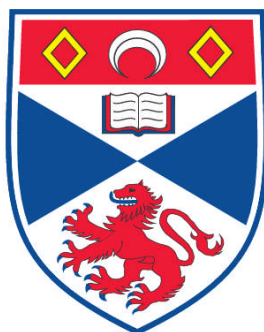 CHARACTERISATION OF THE CERIA AND YTTRIA CO-DOPED SCANDIA ZIRCONIA; PRODUCED BY AN INNOVATIVE SOL-GEL AND COMBUSION PROCESS

Eduarda Maria Soares de Carvalho Tomás

**A Thesis Submitted for the Degree of PhD
at the
University of St. Andrews**

2010

Characterisation of the Ceria and Yttria Co-doped Scandia Zirconia; Produced by an Innovative Sol-Gel and Combustion Process

A thesis submitted for the degree of Doctorate in Philosophy

By

Eduarda Maria Soares de Carvalho Tomás

Supervised by

Professor John T. S. Irvine

University
of
St Andrews

April 2010

Abstract

In the last decade new materials appeared that are candidates to be used as an electrolyte in a Solid Oxide Fuel Cell, SOFC. Some materials show high ionic conductivity but lack in important properties, such as mechanical stability or chemical compatibility with other materials in the fuel cell.

Scandia Stabilised Zirconia, SSZ, became a possibility when the scandia price dropped with the opening of the Chinese and Russian markets. In the starting system $Ce_xY_{0.2-x}Sc_{0.6}Zr_{3.2}O_{8-\delta}$, ($0 \leq x \leq 0.2$), scandia is introduced to improve conductivity and stabilise the cubic phase; yttria is introduced to fully stabilise the cubic phase and ceria to enhance conductivity lost with the introduction of yttria.

The aim of this project is to develop a reliable new method to produce quality ceramics that are not strongly composition dependent, then to prepare a range of compositions and compare intrinsic properties without having to be concerned that poor sintering dominates conduction properties.

This project can be divided in two sections, the first section the powder production method, the characteristics of the powders and its final products are in focus. In the second section the relation between electric characteristics and microstructure of the material is reported.

In the first section, the effect of different compositions of the system $Ce_xY_{0.2-x}Sc_{0.6}Zr_{3.2}O_{8-\delta}$, ($0 \leq x \leq 0.2$) is studied, in terms of structure, phase and microstructure. The nature, size and shape of the powders are discussed, and their effect on the final product. The sol-gel and combustion method gives the formation of hard agglomerates (shells), during the combustion, a wide range of grain sizes, between less than $1\mu m$ and $200\ \mu m$, and the formation of grains with non spherical shape. In this project, the sol-gel and combustion process and solid state method are also compared.

In the second section of this project, AC Impedance measurements, as a function of temperature, oxygen partial pressure and time are discussed. The Arrhenius plot for all compositions shows two regions (high and low temperature) and the change of region occurs at 580 °C. At low temperatures there is a slight difference between compositions but this difference is less at high temperatures. The obtained ionic

conductivity, at 350 °C, varies from 3.84×10^{-6} to 5.53×10^{-5} S/cm; at 700 °C, ionic conductivity from 0.013 to 0.044 S/cm.

At low temperatures, the activation energy associated with bulk process is generally lower than grain boundary process; for example, the composition $Ce_{0.1}Y_{0.1}Sc_{0.6}Zr_{3.2}O_{7.65}$ has an activation energy, for the bulk process, of 1.05 eV and an activation energy, for the grain boundary process, of 1.17 eV. For compositions with higher ceria content, activation energy, for bulk and grain boundary, have similar values.

The AC impedance as function of oxygen partial pressure show that the amount of ceria introduced as an effect on the conductivity at low oxygen partial pressure. For the sample with no ceria in its composition, $Y_{0.2}Sc_{0.6}Zr_{3.2}O_{7.60}$, the conductivity does not vary significantly as the oxygen partial pressure is decreased; for oxygen partial of 0.21 atm, conductivity is 0.018 S/cm and when oxygen partial pressure is approximately 10^{-24} atm conductivity is 0.018 S/cm. For the sample with a higher content of ceria, $Ce_{0.12}Y_{0.08}Sc_{0.6}Zr_{3.2}O_{7.66}$, there is a decrease in conductivity while oxygen partial pressure decreases; and there is also the appearance of a semi-circle for lower oxygen partial pressures. For oxygen partial pressure approximately 0.21 atm, conductivity is 0.019 S/cm, but when oxygen partial pressure is decreased to 10^{-24} atm conductivity decreases to 0.011 S/cm.

AC impedance measurements as a function of annealing time at 600 °C were performed. Total conductivity is fairly stable, for all compositions, until 1800 hours but after this time, conductivity slowly decreases. Some compositions show a second semi-circle in the AC impedance spectra, either from the beginning, time equals 0 hours, or after some working hours. Here, the changes in conduction and conduction processes with time are discussed.

Chapter I - Introduction

Chapter II - Experimental

Chapter III – Powders: Synthesis and characterisation

Chapter IV – Electrical Characterisation

Chapter V - Ageing

Chapter VI – Conclusions

Chapter I

Introduction

1.1 Fuel cells

Fuel cells have emerged as one of the most promising technologies for the power source of the future. They are devices that convert chemical energy directly into electrical energy, using fuels such as hydrogen or hydrocarbons. In theory, fuel cells have high efficiency and produce negligible pollutant emissions, and are environmentally friendly when applied correctly.

1.2 Definition

A single fuel cell is constituted by an ion conducting electrolyte, a cathode and an anode. In a planar design, as shown in Figure 1.1, the electrolyte is placed between the positive and the negative electrode, cathode and anode, respectively. The fuel is provided to the anode electrode, while oxidant is provided in the cathode electrode. The electrolyte is a material that separates the two sides where half reactions occur and allow ions to flow but not electrons [1-4].
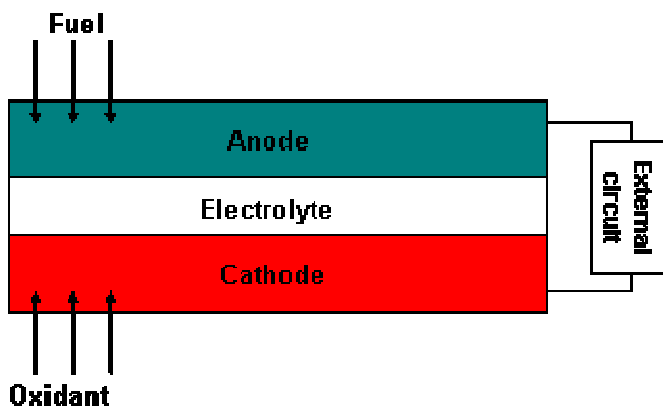
Figure 1.1: Scheme of the basic operation of a fuel cell

1.3 How Fuel Cells Work

A Solid Oxide Fuel Cell (SOFC) is a solid state device that uses an oxide ion-conducting ceramic material as the electrolyte; there are only two phases: gas and solid. For a fuelled SOFC two electrochemical half reactions occur; in the anode there is the ionisation of hydrogen (1.1), releasing the electrons that will travel through the external circuit to enter the cathode where the oxygen reacts with the electrons to form O^{2-} ions (1.2) that pass through the electrolyte, reach the anode and react with H_2 to form water in the form of steam (1.3) [1-3].

$$2H_2 \rightarrow 4H^+ + 4e^- \qquad (1.1)$$

$$O_2 + 4e^- \rightarrow 2O^{2-} \qquad (1.2)$$

$$2H_2 + O_2 \rightarrow 4H^+ + 2O^{2-} \qquad (1.3)$$
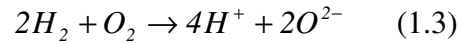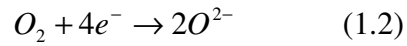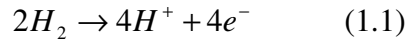
1.3.1 Thermodynamics

Traditionally, when power production is mentioned, we think about hydro-thermal power plant, which uses oil, gas, coal, or nuclear. Figure 1.2 shows a scheme of how electricity is produced from an oil fuelled power plant.
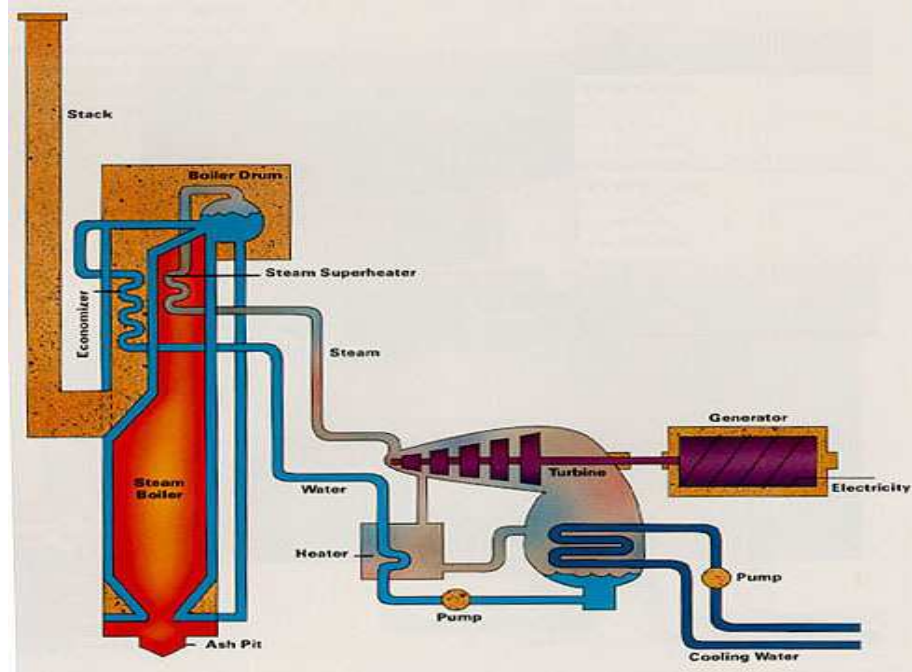
Figure 1.2: Schematic of a thermal, oil burning, plant in the Hydro-Québec system

The combustion of the fuel transforms the water in the boiler into steam. This steam is collected in the boiler drum, after it is superheated, dried, the steam is directed towards the turbines. As it expands, the steam spins the turbine which drives the generator. After leaving the turbines, the steam passes through condensers which return it to a liquid state; the water is pumped back into the boiler - and the cycle is repeated.

This process is subject to Carnot's theorem, which says that no engine operating between two reservoirs can be more efficient than a Carnot engine operating between those same reservoirs.

The efficiency of these systems is given by the equation

$$\eta = \frac{-w}{q} = 1 - \frac{T_C}{T_H} \qquad (1.4)$$

Where

$\eta \rightarrow$ Thermal efficiency

$w \rightarrow$ Work done by the system

$q \rightarrow$ Heat energy entering in the system

$T_C \rightarrow$ Absolute temperature in the cold reservoir

$T_H \rightarrow$ Absolute temperature in the hot reservoir

Carnot's theorem has limitations when applied in cyclic heat engines, such as internal combustion engines and steam engines.

In the electrochemical processes a direct method of energy is provided and the Carnot theorem is not applied. A typical case in the use of the Carnot cycle is a hydro-thermal power plant, where the superheated steam has a temperature of approximately 550 °C and the cooling recipient is approximately 100 °C. The thermodynamic efficiency is only around 55 %, the remaining 45 % of heat is lost throughout the system [5-7].

Thermodynamics of Solid Oxide Fuel Cell

Efficiency of a solid oxide fuel cell

A fuel cell is often compared with a battery but there are some differences. In a fuel cell, the fuel and oxidant are continually fed and not stored, as happens in a battery. The exhaustion of the products of reaction has to be continuously. This continuous- flow system produces a steady electric current.

A fuel cell produces its own electricity by combining electrochemically a fuel with a cell without combustion and discarding the heat waste. The electric power generated by a single fuel cell is usually not enough to be of any practical use, but when fuel cells are stacked they produce enough electricity to be of any use.

The Gibbs free energy, ΔG, is the important term, which has to be defined in order to determine the thermodynamics and efficiency of the fuel cell. The Gibbs free energy changes in a chemical reaction, varying with temperature and with reactants pressure and concentration [8-11].

The simpler configuration of a solid oxide fuel cell, Figure 1.1, is composed of two electrodes, anode and cathode, separated by a dense electrolyte. The operation of a hydrogen-oxygen fuel cell is illustrated in Figure 1.3.
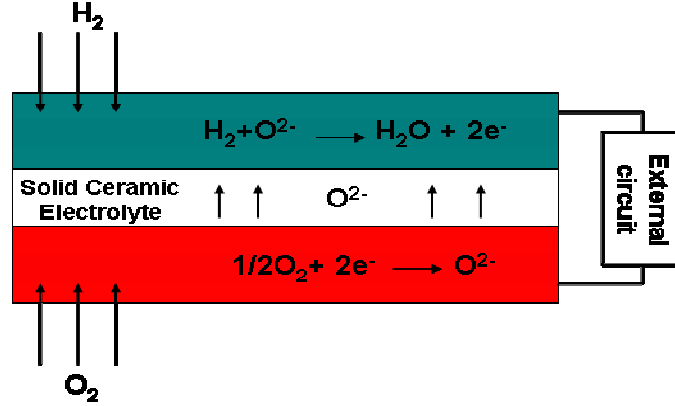
Figure 1.3: Scheme of the basic operation of a fuel cell.

At the anode-electrolyte interface, hydrogen molecules dissociate into hydrogen ions and electrons according to the equation (1.4). There is a difference in the potential between the anode and cathode.

$$2H_2(g) \rightarrow 4H^+ + 4e^- \quad (1.4)$$
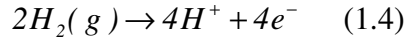
The free electrons flow from the anode to the cathode using an external circuit. Meanwhile the oxygen associate with the arrived free electrons, equation (1.5)

$$O_2 + 4e^- \rightarrow 2O^{2-} \quad (1.5)$$
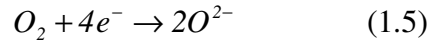
The oxygen anions will pass through the electrolyte and reach the anode and the reverse reaction of the oxygen will occur according to the following reaction, equation 1.6:

$$2O^{2-} \rightarrow O_2 + 4e^- \quad (1.6)$$
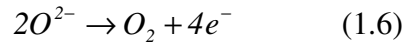
The reversible transformation of the oxygen during this process is the driving force for the SOFC. Molecular oxygen will react with hydrogen to form water in the form of steam:

$$H_2 + \frac{1}{2}O_2 \rightarrow H_2O \quad (1.7)$$
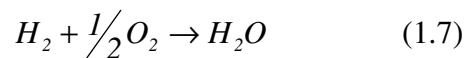
The equilibrium constant, k, is given by the equation (1.8)

$$k = \left(\frac{pH_2O}{pH_2 \times (pO_2)^{1/2}} \right) \qquad (1.8)$$

In order to calculate the fuel cell performance (efficiency), the voltage has to be found.

$$E = E^0 + \frac{RT}{2F} ln\left(\frac{pH_2 \times (pO_2)^{1/2}}{pH_2O} \right) \qquad (1.9)$$

Where,

$E^0 \rightarrow$ Reversible open circuit voltage, at standard pressure. See values in Table 1.1.

$R \rightarrow$ Constant of perfect gases (gas constant, 8.314 $JK^{-1}mol^{-1}$)

$T \rightarrow$ Temperature, K

$pH_2 \rightarrow$ Hydrogen partial pressure

$pO_2 \rightarrow$ Oxygen partial pressure

$pH_2O \rightarrow$ Water partial pressure

E^0 can be calculated with the knowledge of the thermodynamic reactions

Gibbs free energy, ΔG, is calculated for the reaction with the equation (1.10)

$$\Delta G = \Delta G^0 - RT \, ln\left(\frac{pH_2 \times (pO_2)^{1/2}}{pH_2O} \right) \qquad (1.10)$$

Where,

$\Delta G^0 \rightarrow$ Variation of molar Gibbs free energy, at standard pressure; these values are tabulated, Table1.1, or can be calculated from the formation energies of the species involved.

When the system is reversible, or has no losses, the electrical work done will be equal to the Gibbs free energy released, ΔG. So

$$E = -\frac{\Delta G}{nF}$$

$$\Delta G = -nF \times E \qquad (1.11)$$

Where,

$n \rightarrow$ Number of transferred electrons

$F \rightarrow$ Faraday's constant, 96485 J/volt.mol

$E \rightarrow$ Equilibrium voltage

Table 1.1: ΔG^0 and E^0 for water reaction

Form water product	T, °C	ΔG^0, kJ/mol	E^0, V
Gas	600	-199.6	1.04
Gas	800	-188.6	0.98

Combining equations (1.10) and (1.11) and rearranging, the final equation for the voltage is as follow

$$E = -\frac{\Delta Gf^0}{2F} + \frac{RT}{2F} ln\left(\frac{pH_2 \times (pO_2)^{1/2}}{pH_2O} \right)$$

After obtaining the values for the voltage, E, the value for ΔG, can be calculated by equation (1.11), where n equals 4 electrons.

Maximum efficiency

In a SOFC, the free enthalpy variation (ΔH) of the cell reaction, ΔG, may be totally converted to electrical energy. Thus, a fuel cell has an intrinsic (maximum) thermodynamic efficiency given by the equation (1.12)

$$\eta_{max} = \frac{\Delta G}{\Delta H} \times 100\% \qquad (1.12)$$

[2, 3, 8, 12-14]

The hydrogen fuel cell efficiency limit is $\eta_{max} \approx 70\%$, [3], this efficiency is calculated in higher heating value, HHV, basis. This is the conversion from chemical to electrical. The heat can be reclaimed for example recovered to be introduced in the system again.

1.4 Types of Fuel Cells

There are five types of fuel cells, and the main difference is in the electrolyte used. Table 1.2 shows five types of fuel cell, the electrolyte material used for each type of fuel cell, the charge carrier and temperature operation.

Table 1.2: Type of fuel cells

Fuel Cell Type	Electrolyte	Charge carrier	Temperature operation, °C
PEMFC	Polymer membrane	H^+	80
PAFC	Phosphoric acid (immobilised)	H^+	200
AFC	KOH solution (immobilised)	OH^-	60-220
MCFC	Molten Carbonate	CO_3^{2-}	650
SOFC	Ceramic	O^{2-}	600-1000

The material used in the electrolyte gives different characteristics to the fuel cell, such as operation temperature, fuel used and performance characteristics.

1.4.1 Polymer Electrolyte Membrane Fuel Cell (PEMFC)

PEMFC uses a polymer membrane as an electrolyte and is a proton conductor membrane, Figure 1.4 show a scheme of basic construction of a PEMFC. High power density at low operation temperature is a great advantage of this type of fuel cell, although to achieve this high density power, sophisticated catalyst and electrodes have to be used. There are some concerns about durability, and it also requires hydration in order to maintain the high conductivity. The fuels used are typically hydrogen and methanol [3, 8, 15].
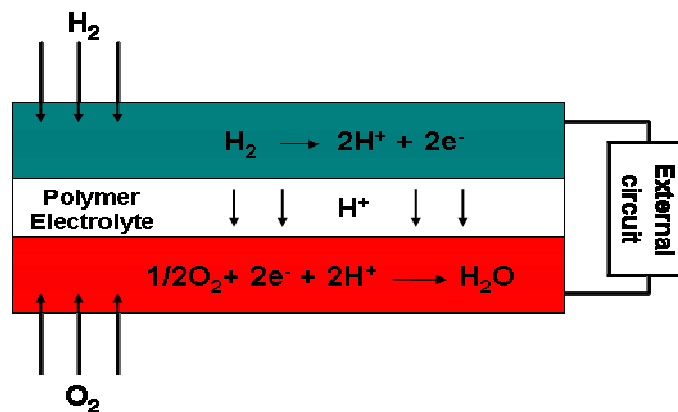
Figure 1.4: Scheme of the basic construction of a Polymer Electrolyte Membrane Fuel Cell (PEMFC)

The catalyst used is platinum but it is expensive and also subjected to carbon monoxide, CO, poisoning from hydrocarbon fuels. There is some research to substitute platinum by non-precious metal catalysts. The acceptable CO concentration is below 10 ppm at Pt anode and below 100 ppm at CO-tolerant alloy anodes [16, 17].

Recent Advances

The most widely implemented electrolyte in PEMFC is Nafion manufactured by Dupont. Portable applications, transportation and power distribution are the three main areas where PEMFC are being applied [18, 19].

For portable applications, these fuel cells can be used in consumer electronics, such as laptops and mobile phones, in roadway and traffic signage, and in power backup.

Figure 1.5: Prototype Casio laptop [20]

This prototype Casio laptop can run for more than 20 hours on one refuelling of its fuel cell power supply, shown here removed from the computer [20], see Figure 1.5.

PEMFC are applied in the transportation industry and are applied in several areas, such as automotive industry, marine and military applications.

Canadian Department of National Defence (DND) has been developing PEMFC technology since the mid-1980s. Ballard was awarded a contract to design, build and test a 40 kW PEMFC power plant for an air-independent fuel cell propulsion system for use in submarines.

The German submarine industry and the German Defence Ministry decided that a fuel cell offered the most effective solution for providing air-independent propulsion (AIP) system for diesel-electric submarines, to allow longer underwater endurance.

The German consortium Shipbuilder, Howaldtswerke-Deutsche Werft (HDW), started to develop the first generation of fuel cell plants for submarines. PEMFCs are still being developed (German Defence Ministry has commissioned Siemens to develop special PEMFCs for submarine applications), and the early systems used alkaline fuel cells. In

1998, HDW began producing Class 212A submarines (now called the U31) incorporating an AIP system, with a fuel cell system comprising nine Siemens PEM fuel cell modules, each with a capacity of 30-50 kW [21].

Power distribution, such as distribution for homes, commercial and industrial sites is used in places where it is difficult to provide energy [15, 18].

1.4.2 Alkaline Fuel Cells (AFC)

AFC are the most developed type of fuel cell technology, Figure 1.6 show a scheme of the basic construction of an AFC. They were also used to fly man, as an electricity generator to power electrical systems, to the Moon and were used by NASA in mid-1960s in Apollo-series missions and on the space shuttle. There are several types of alkaline electrolyte fuel cells; sodium hydroxide and potassium hydroxide solutions are the electrolytes used, and the working temperature is between 50 and 200 °C.

The advantages are the low cost of the materials, electrodes are made from non-precious metals, and the overvoltage at the cathode is generally less than the acid electrolyte, as AFC can operate at voltages as high as 0.875 V per cell [3, 8, 15].
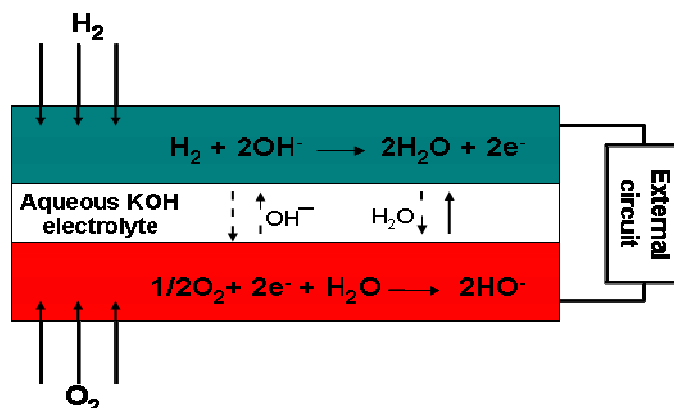
Figure 1.6: Scheme of the basic construction of an Alkaline Fuel Cell (AFC)

Recent advances

Transportation is the main area where this type of fuel cell is being applied.

AFCs are used to supply electricity in HYDRA, the first Fuel Cell Boat. It has an AFC system with 6.5 kW net output. The electrolyte used is 30 % potassium hydroxide (KOH).

HYDRA uses a propulsion system called "Europ 21" developed by Etaing GmbH, which developed a fuel cell system, with maritime requirements influencing the decision to use AFC as fuel cells, Figure 1.7 show the Hydra boat and how much of the AFC fuel cells space occupy [22, 23].

Figure 1.7: (a) Hydra, boat with fuel cell propulsion. It's a cruise boat 12 m long, with 6.5 kW AFC fuel cell, which has a capacity of twenty two passengers plus one skipper. (b) Alkaline Fuel Cell [22, 23]

At the University of Surrey, UK, a solid-state alkaline fuel cell has been developed, using anion-exchange membrane rather than a liquid [22-24].

1.4.3 Phosphoric Acid Fuel Cell (PAFC)

Phosphoric Acid Fuel Cell was the first fuel cell to be commercialised. Liquid phosphoric acid (H_3PO_4) electrolyte (pure or highly concentrated) is contained in a thin SiC matrix between two porous graphite electrodes with a platinum catalyst, see Figure 1.8 a scheme of the basic construction of a Phosphoric Acid Fuel Cell. The solidification point of pure phosphoric acid is 42°C; this type of fuel cell must work above this

temperature and below 210 °C, as phosphoric acid has an undesirable phase transition which makes it unsuitable to be used as an electrolyte. The temperature operation is 180 to 210 °C.

The advantages of PAFC are excellent reliability, long term performance, low maintenance power system, and low cost of the electrolyte. On the other hand, the platinum catalyst is expensive; these fuel cells are susceptible to CO, carbon monoxide, in concentrations above 1.5%, cobalt, Co, and sulphur, S, poisoning. The electrolyte is a corrosive liquid that must be refilled during operation. There is a need to use a reformer to transform natural gas, e.g. methane, to hydrogen and carbon dioxide which will increase the cost and the size of the fuel cell system [3, 8, 15].
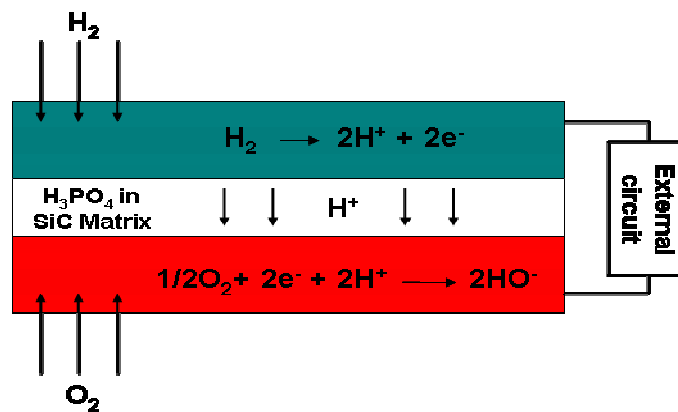
Figure 1.8: Scheme of the basic construction of a Phosphoric Acid Fuel Cell

Recent Advances

PAFC are used in transport, and plant power generators. H-Power, University of Georgetown and the U.S. Department of Energy adapted a 50 kW Figi Electric PAFC for transit buses, which are at the moment powered by a 100 kW PAFC from International Fuel Cells Corporation.

A model PC25 power plant from ONSI Corporation recently began supplying supplemental power in the Conde Nast Building at 4 Times Square in New York City.

Also in New York, the Yonker Waste Treatment Plant has been powered by a 200 kW ONSI unit since 1997.

1.4.4 Molten Carbonate Fuel Cell (MCFC)

MCFC uses, for an electrolyte, a mixture of alkali carbonates, Li_2CO_3 and K_2CO_3 immobilised in a $LiAlO_2$ ceramic matrix, Li^+ and K^+ are used as ionic conductors in the electrolyte. At high operating temperature, the alkali carbonates form a highly conductive molten salt, with carbonate ions, CO_3^{2-}, providing ionic conduction. Carbon dioxide, CO_2 and oxygen, O_2, must be supplied to the cathode to be converted to carbonate ions, which provide the means of ion transfer between the cathode and the anode, as it can be observed on Figure 1.9.

The anode and the cathode reactions are therefore as follows:

$$\text{Anode:} \quad H_2 + CO_3^{2-} \rightarrow CO_2 + H_2O + 2e^-$$

$$\text{Cathode:} \quad \tfrac{1}{2}O_2 + CO_2 + 2e^- \rightarrow CO_3^{2-}$$
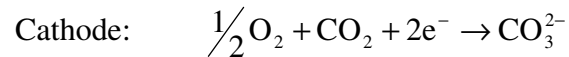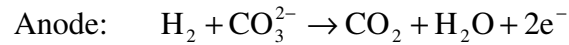
In the MCFC, CO_2 is produced at the anode and consumed at the cathode. Therefore, MCFC systems must extract the CO_2 from the anode and redirect it to the cathode.

The electrodes are nickel based: the anode usually consists of a nickel/chromium alloy while the cathode is made of a lithiated nickel oxide. At both electrodes, the nickel provides catalytic activity and conductivity. At the anode, the chromium additions maintain high porosity and surfaces are of the electrode structure. At the cathode, the lithiated nickel oxide minimises nickel dissolution that can have adverse effects on the fuel cell performance [3, 8, 15].
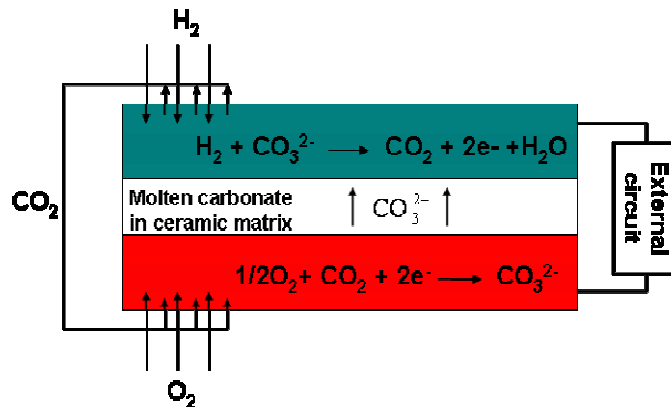
Figure 1.9: Scheme of the basic construction of a Molten Carbonate Fuel Cell (MCFC)

Because they operate at high temperatures, MCFC have flexibility in the chosen fuel, there is no need to use precious metals as catalyst, and they have high quality waste heat for cogeneration applications. There are also some disadvantages: a CO_2 recycling system must be implemented, the molten electrolyte is corrosive which gives degradation issues, and the materials are relatively expensive.

Recent Advances

Power distribution is the main area where this type of fuel cell is being applied.

Europe and Japan have several developers working in MCFC: MTR Friedrishshafen (Germany), a partner of Fuel Cell Technology, Ansaldo (Italy), Hitachi Ishikawajima-Harima Heavy Industries, Mitsubishi Electric Corporation, and Toshiba Corporation, 2-MW demonstrations by Fuel Cell Energy, the MTU "hot module" and 1-MW pilot plant that has been operated by the Central Research Institute for Electrical Power Industries (CRIEPI), in Japan.

Mercedes Benz US International has a 250 kW MCFC plant at the new Mercedes museum and visitor centre in Tulcalousa, Alabama, USA.

In 1997, the Office of Naval Research (ONR) and the Naval Sea System Command (NAVSEA) initiated an advanced technology development programme to develop a Ship Service Fuel Cell (SSFC) system for future Navy ships. Fuel Cell Energy (formerly

Energy Research Corporation) developed a molten carbonate fuel cell of 2.5 MW SSFC Power Plant.

1.4.5 Solid Oxide Fuel Cells (SOFC)

Oxygen conducting electrolytes were discovered by Nernst [25], in 1899, when he found a solid oxide electrolyte. However, it was only in 1937 that the first ceramic fuel cell was operated by Bauer and Preis [25, 26]. SOFC can offer an alternative process to generate electricity in a clean, low-pollution technology. These fuel cells use a solid ceramic electrolyte and Yttrium Stabilised Zirconia (YSZ) is the most common material, which is an oxygen ion (oxygen vacancy) conductor. Since O^{2-} is the mobile conductor in this case, the anode and cathode reactions are, these reactions can be observed on Figure 1.10:

$$\text{Anode:} \quad H_2 + O^{2-} \rightarrow H_2O + 2e^-$$

$$\text{Cathode:} \quad \tfrac{1}{2}O_2 + 2e^- \rightarrow O^{2-}$$
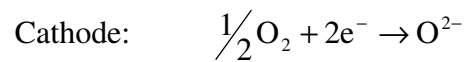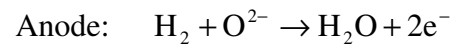
The electrodes are made of different materials. The fuel must be highly reducing at high temperatures at the anode side, while air must be highly oxidising at high temperatures at the cathode side.

Anode electrode is a nickel-YSZ cermet, with the nickel providing conductivity and catalytic agent, while the YSZ adds ion conductivity, compatible thermal expansion, mechanical stability, and maintains the high porosity and surface area of the anode structure.
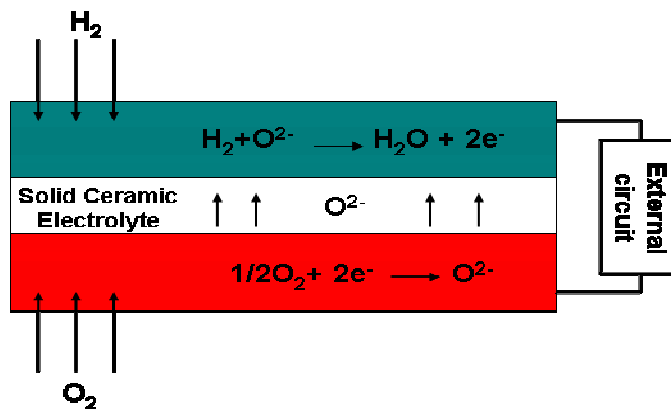
Figure 1.10: Scheme of the basic operation of a Solid Oxide Fuel Cell (SOFC)

SOFCs have the advantages of high operation temperature, ability to use a wide range of fuels, and the ability to employ cogeneration schemes using the high quality waste heat that is generated. They also have high efficiency and can use a non-precious metal catalyst; on the other hand, there are some issues of using high temperature operation, problems with the chosen materials, issues with sealing, and relatively expensive components/ fabrication.

When a fuel cell system is assembled, internal reforming has to be introduced, and there are also some difficulties in achieving a quick start-up [3, 8, 15].

Recent advances

The new tendency is towards a drop in size of fuel cells in order to be able to use SOFC directly in the automotive industry or home/office/store co-generation. On Figure 1.11 (a), show an example of SOFC/gas turbine hybrid system, and Figure 1.11 is a schematic of this system and the place of the components.

(a)   (b)
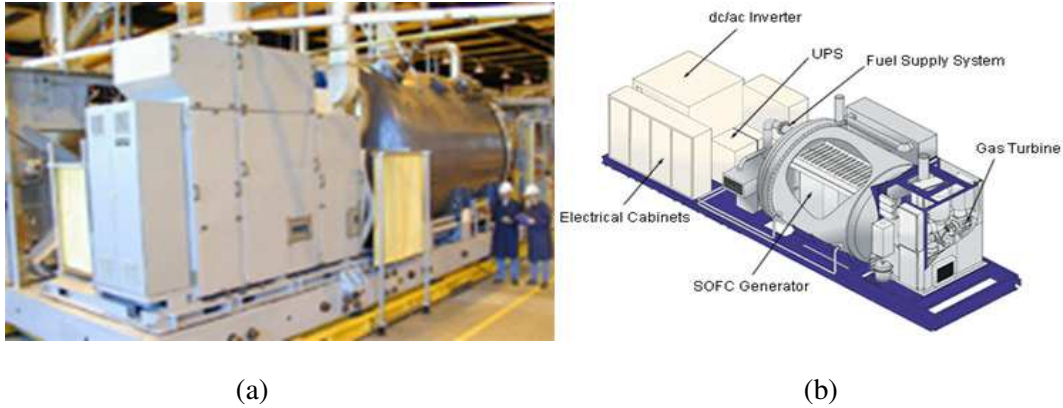
Figure 1.11: (a) A 300 kW SOFC/gas turbine hybrid system demonstrated in Pittsburgh, Pennsylvania, USA, (b) Scheme of the SOFC/gas turbine [27]

Siemens-Westinghouse has successfully used a 100 kW system for more than 20000 hours without significant measurable degradation during performance. The most recent advance for Siemens-Westinghouse was the incorporation of microturbines in 200 kW units to improve the electrical efficiency up to 70 % [14, 27].

1.5 Solid Oxide Fuel Cell Design

1.5.1 Planar Design

The planar design has the simplest configuration of the components. All components are stacked one on the top of the other (Figure 1.12). The shape of the plates is usually rectangular or circular. In circular shape, the fuel is fed from the middle of the cell and exhausted in the outside of the cell [28].
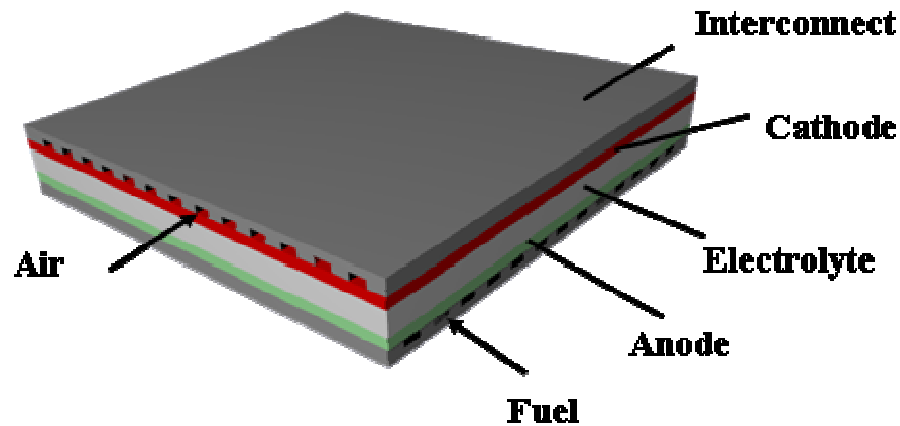
Figure1.12: Scheme of Planar Fuel Cell Design, with rectangular plate shape. Image ceded by Dr. Paul Connor from University of St. Andrews.

Because of the simple design there are more options of techniques for the processing; for different layers, a different technique can be used. Therefore the electrodes can use slurry casting, screen-printing and plasma spraying. For electrolyte, tape casting is the technique widely used because of the density requirements of the electrolyte [28-30].

The interconnect material used usually is bipolar which has ribs on each side to allow the passage of gases. Different geometries can be obtained by controlling the direction of these interconnects, either co-flow or cross-flow [29, 31].

For the planar design there can exist some combination, Figure 1. 13 and 1.14 illustrate a concept of different configurations, self-supporting and external- supporting. Self-supporting is when one of the main components is thick enough to support the whole fuel cell and external-supporting is when the fuel cell is built on top of an external material to the main components, which will support the fuel cell.

Self-supporting

<div align="center">

(1)   (2)   (3)

</div>
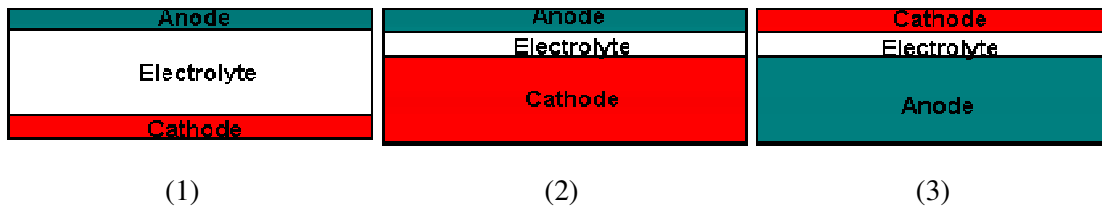
Figure 1.13: Schematic of self supporting configuration for planar fuel cells. (1) Electrolyte supported, (2) Cathode supported, (3) Anode supported

Figure 1.13 show self supporting configuration for planar fuel cells, Figure 1.13 (a) uses an electrolyte to support the fuel cell, the electrolyte thickness approximately of 150 µm. This configuration has a high mechanical strength and less possibility of reduction of the cathode and the reoxidation of the anode. On the other hand, with such thick electrolyte it might increase the fuel cell resistance.

The cathode supported fuel cell configuration, Figure 1.13 (2), has the cathode component supporting the fuel cell. This configuration can be used at lower temperatures due to the thinner electrolyte and has no oxidation problems although presents lower conductivity and has a mass transport limitation.

The anode supported fuel cell, Figure 1.13 (3), is one of the configurations most commonly used at the moment due to the high conductivity of the anode and the thinner electrolyte gives the possibility to be used at intermediate temperatures. On the other hand, it has a mass transport limitation and such large electrode can be reoxidised [29].

External-supporting

<div align="center">

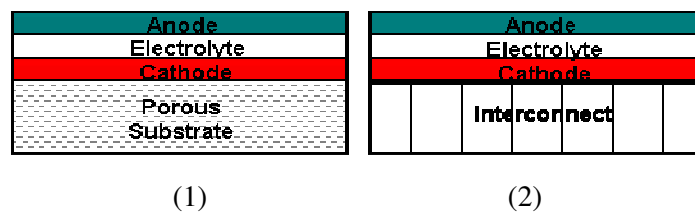(1)   (2)

</div>

Figure 1.14: Schematic of self supporting configuration for planar fuel cells. (1) Electrolyte supported, (2) Cathode supported, (3) Anode supported

External supporting is the new trend configuration for planar fuel cell. Using a porous substrate, as in Figure1.14 (1), makes it possible to use thinner components, therefore making possible to be used at lower temperature. The introduction of a new material, a porous substrate, can raise new problems of compatibility.

A fuel cell supported by the interconnect material has a high mechanical strength due to the metallic interconnect and can be used at intermediate temperatures due to the thinner components. The oxidation of the interconnect material can be a disadvantage [31].

1.5.2 Monolithic

Monolithic designs consist of a compact corrugated structure and the direction of the gas flow can be done in two ways: co-flow and crossflow. In the case of the co-flow, the oxidant and the fuel have the same direction but for crossflow the oxidant and fuel flow in perpendicular directions. Crossflow has a lower power density than co-flow due to the less efficient means of the circulation of gases [29].

The monolithic designs are produced by tape casting and tape calendaring (the process in which two or more green films are sandwiched together), and it is co-fired; this process has advantages, due to time and energy reductions.

Advantages of this design:

- High power density per mass or volume

- Easier and cheaper fabrication process than tubular design

- Lighter fuel cells than the other designs because do not need a structural support

Disadvantages of this design:

- Difficulty of fabrication of the corrugated structure

- Need for sealing

- Fragility.

[29, 31]

1.5.3 Tubular Design

US Westinghouse Corporation (now Siemens - Westinghouse) was the first company to use this type of cell, in the late 1970s [3]. The cathode supports (cathode-supported) the structure of the fuel cell, as shown in Figure 1.15, this is a porous supported fuel cell. The cathode is extruded and sintered and the electrolyte is then deposited over the cathode by electrochemical vapour deposition (EVD) process to form a dense layer. The electrolyte is deposited over almost the entire area of the cathode, except a narrow strip along the cell length, which is covered by the interconnect layer also fabricated by EVD technique. To deposit the anode, a process with two stages is needed. At the first stage, the cell is plunged in nickel slurry, and the second stage is to add YSZ by the process of EVD. An alternative process for depositing the anode material is to use Ni\YSZ slurry depositing the cermet. Comparing these two processes, the alternative one has proved to produce anodes of a similar standard and due to the cost of the EVD process, reduces the cost of fabrication [3, 28, 31].
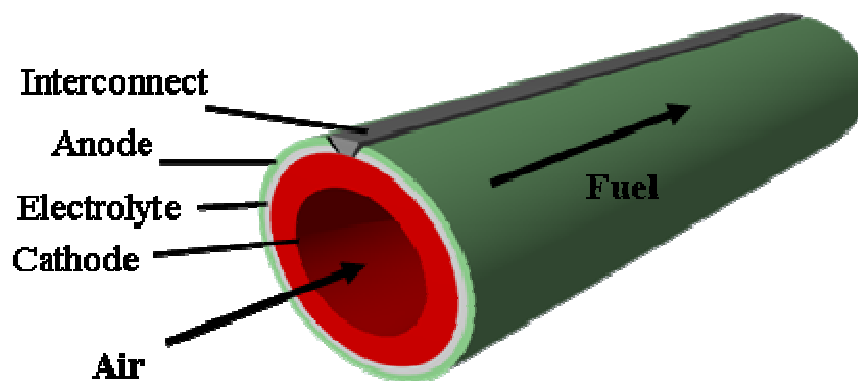
Figure 1.15: Scheme of Tubular Fuel Cell Design. Image ceded by Dr. Paul Connor from University of St. Andrews.

Air flows into the centre of the cathode tube and the fuel flows along the outside of the cell.

Advantages of this design:

- The gases are kept separate from each other

- The oxidant gas is introduced through a tube, sealing is not required because the tube is introduced at low temperatures and it will expand at high temperatures

- The long cell length is good for in-situ reforming

Disadvantages of this design:

- High production cost due to the fabrication processes and all layers are sintered separately

1.5.4 SOFCRoll Design

SOFCRoll is a new Solid State Fuel Cell design, as shown in Figure 1.16 [32]. This design allows production by tape casting and laminating. All components are assembled before they are given the geometrical shape and before co-firing [33].
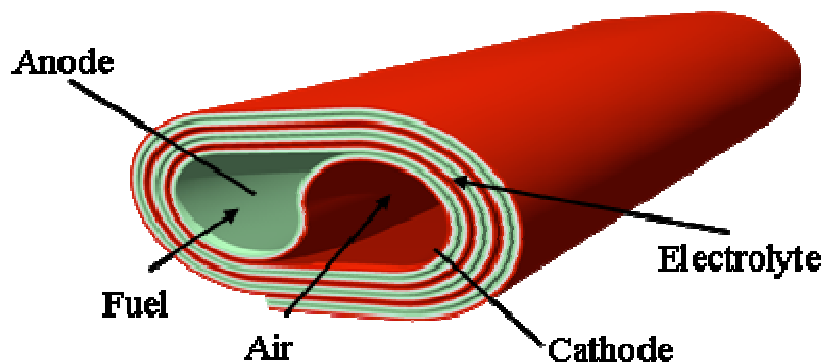
Figure 1.16: Scheme of SOFCRoll fuel cell design. Image ceded by Dr. Paul Connor from University of St. Andrews.

This cell consists of five different layers, one central layer of electrolyte (dense layer), in one of the sides of the electrolyte is the anode and on the other side the cathode.
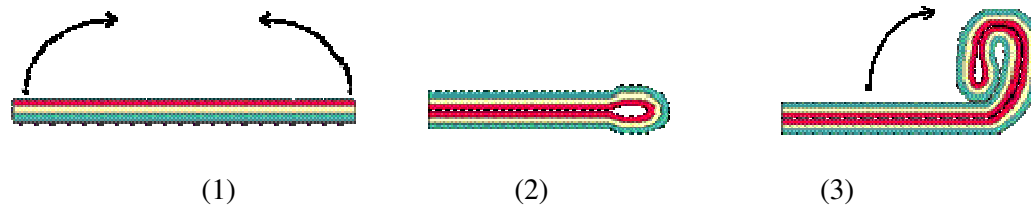
Figure 1.17: Schematic of assemblage of e SOFCRoll.

Figure 1.17 shows the scheme of three steps to assemble and give shape to a SOFCRoll. Figure1.17 (1) shows all layers already overlapped, after this the fuel cell must allow bending, as is shown in the Figure 1.17 (2). When the fuel cell is bent in the middle, it has to be rolled to give it shape, Figure 1.17 (3).

Advantages:

- Do not need interconnect
- Do not need expensive seals
- Lower production cost; the fuel cell is made by tape casting technique and all components are co-fired.

Disadvantages:
- Long current path.

1.6 Solid Oxide Fuel Cell Materials

1.6.1 Electrolytes

An electrolyte should have high ionic conductivity, be a dense material to prevent gas diffusion, which must also be thin enough to reduce ohmic resistance. This material has to have very low levels of impurities, which can decrease the oxide ion conductivity and enable the electrons to pass through the electrolyte. When the electrolyte is porous, it will allow gas diffusion and will decrease ionic conductivity [3, 29, 34-36].

The material most commonly used as an electrolyte is Yttria Stabilised Zirconia (YSZ) but recently there have been some other candidates to replace it. Scandia Stabilised Zirconia (SSZ), rare earth doped ceria (CRO) and Lanthanum Strontium Gallate Magnesite perovskite (LSGM) are some of the alternatives to replace YSZ [35, 37, 38].

Zirconia

Pure zirconia (zirconium dioxide) exhibits polymorphism and has a large variation in volume, which makes it difficult for use in many industrial applications. Pure zirconia has low ionic conductivity that makes it difficult to be used as a fuel cell electrolyte material, and it has a high melting point (2700 °C) and low thermal conductivity [39, 40].

Table 1.3 shows the crystal structure changes with temperature. When the material is heated and reaches around 1170 °C, the crystal structure changes from monoclinic to tetragonal. This transformation occurs with a decrease of volume of 3 to 5 %, which reverses on cooling at 900 °C; this is a known example of a martensitic transition. The increase in the volume is sufficient to exceed elastic and fracture limits, which can create cracks within its structure. The transition of crystal structure occurs above fuel cell operating temperatures but below the sintering temperature required to create a dense electrolyte [29, 40-43].

Further heating until above 2370 °C, melting point 2680±50 °C, will cause the transition from tetragonal to cubic fluorite [29, 43-45]. This fluorite-type crystal structure has a zirconium coordinated by eight equidistant oxygen and each oxygen is tetrahedrally coordinated by four zirconiums [46].

Table 1.3: Zirconia crystal structure, when temperature varies [29, 40-42].

Temperature, °C	Crystal Structure	Thermal expansion coefficient, K^{-1}
25 – 1170	Monoclinic	7×10^{-6}
1170 – 2370	Tetragonal	12×10^{-6}
>2370	Cubic fluorite	-

Zirconia stabilised in a cubic fluorite structure has the potential to be used in solid oxide fuel cell, chemical sensors and electrochemical oxygen membranes [47].
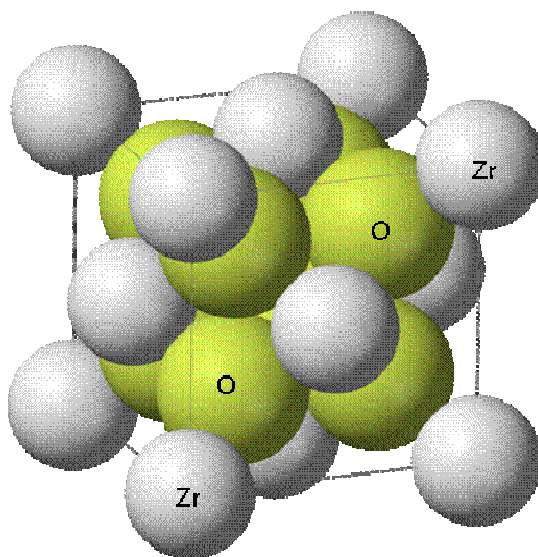
Figure 1.18: Fluorite crystal structure, ZrO_2. The white spheres represent the Zr cation site and yellow spheres represent the oxygen sites.

Figure 1.18 represents the cubic fluorite structure. On the representation the white spheres represent the Zr cation site and yellow spheres represent the oxygen sites. A cubic fluorite is a type of ionic crystal structure in which has an expanded face-centred cubic arrangement with the anions occupying both type of tetrahedral hole. The cations have a coordination number of 8 and the anions have a coordination number 4 [46].

Fluorite structure is very tolerant to dissolve lower valent metal oxide, in some cases can dissolve up to 40% of the metal oxide in the fluorite matrix. The purpose for the dissolution of these metal oxides is to introduce oxygen vacancies.

An undistorted lattice provides higher concentration of oxygen vacancies (charge carriers) and the charge carriers are also more mobile in the structure, therefore higher conductivity.

A fluorite structure with an initial higher concentration of oxygen vacancies should be a better conductor. In conclusion a doped fluorite is a better conductor when the cubic lattice is kept as free of strains and distortions as possible [29, 44, 48].

Before the introduction of any dopant in the zirconia, in order to stabilise it, some factors deserve some attention:

- The minimum number of vacancies

- The size, charge and concentration of the dopant ions

- The crystal structure of the dopant oxide

- The role of electronic energy levels [43, 46, 48, 49].

The addition of a certain amount of CaO, MgO, Y_2O_3 and Sc_2O_3 is known to stabilise the cubic zirconia solid solution, which is of the fluorite type structure that increases the oxygen ion conductivity [39, 43, 49].

Some Zr^{4+} ions are replaced by Mg^{2+}, Ca^{2+}, Y^{3+} and Sc^{3+} creating oxygen vacancies, which occur to restore the electrical charge balance of the system, these oxygen vacancies enable the O^{2-} ions to migrate through the electrolyte. In order to fully stabilise the fluorite structure the additions must be more than 12 mol% of CaO, 16 mol% MgO, 8 mol% of Y_2O_3 or 9 mol% of Sc_2O_3 into the zirconia lattice [3, 29, 40, 44].

2-2.5 mol% Y_2O_3 and several rare-earth oxides is the amount of dopants required to stabilise the tetragonal phase. This phase is metastable and when subjected to stress it will transform to monoclinic. The tetragonal phase is known to have high strength and toughness [50].

Compositions between stabilised tetragonal and stabilised cubic phase are a mixture of tetragonal, cubic and sometimes monoclinic precipitates. They are classified as partially stabilised zirconias [40].

From 3 to 7 mol % M_2O_3 there is another metastable phase, dopant-rich tetragonal, known as t'-phase. When this phase is rapidly cooled down from sintering temperature

to room temperature, the final phase will be in the cubic phase field. For compositions between 4.5 and 8 mol% Sc_2O_3, this rapid cooling is not required [40, 50].

Zirconia doped with a trivalent oxide is well known to exhibit a higher conductivity than when it is doped with a divalent oxide. Although divalent oxide substitution creates more vacancies, it will have lower ionic conductivity due to its higher tendency to defect association and it also lowers the thermodynamic stability of the cubic fluorite-type solid solutions in ZrO_2-AO system [51].

Usually zirconia-based systems have low conductivity and it does not vary significantly from one composition to another. The Arrhenius plot has a change in the slope; for lower temperatures the activation energy has a higher value than the activation energy for higher temperatures and the conductivity increases with the temperature. This behaviour indicates a change in conductivity that has been discussed and some explanations were suggested, such as ordering of vacancies, different defect configurations and defect pair association [50, 51]. The ionic conductivity typically has Arrhenius behaviour with thermal activation energy about 1 eV [37, 52].

Yttria Stabilised Zirconia, YSZ

YSZ was discovered by Nernst [25] and was the first material to be used in a SOFC built by Bauer and Preis, in 1937. YSZ has been well studied for several decades, the material itself as well as the process of obtaining powders. High ionic conductivity, low electronic conductivity, good mechanical properties, stability in long-term experiments and stability under reducing and oxidising atmospheres are characteristics that made YSZ a good option for an electrolyte and oxygen sensor [37, 40, 53-55]. Over a wide range of oxygen partial pressure, 1 to 10^{-23} atm, YSZ shows that is a pure oxygen conductor, therefore without electronic conduction.

When zirconia is doped, the ionic conductivity depends on the size of dopants; and this dependence is more visible for dopants with ionic radii similar to the Zr^{4+} host cation [56]. The minimum amount of yttria necessary to stabilise zirconia corresponds to the maximum of ionic conductivity of YSZ [36, 49, 57].
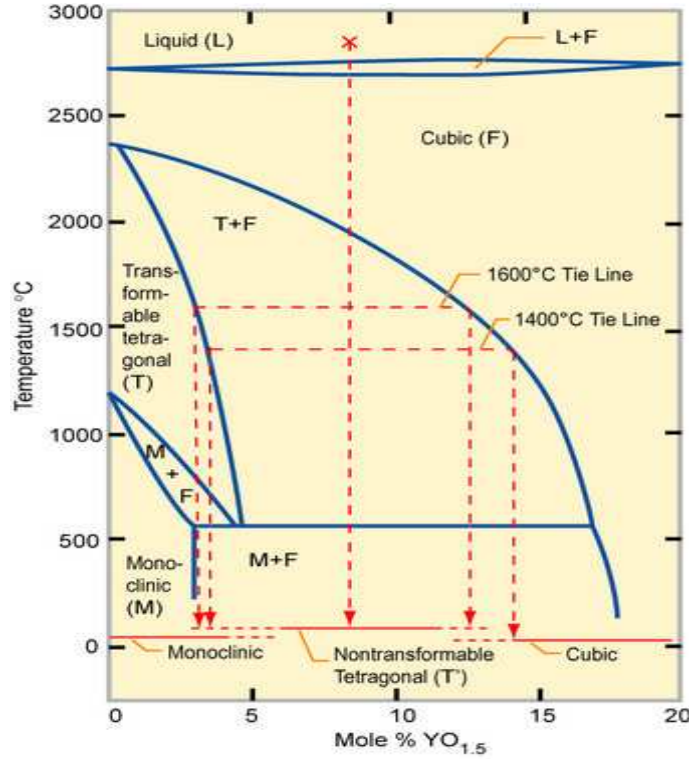
Figure 1.19: Phase diagram of the Zirconia-rich region of the ZrO_2-Y_2O_3 system [58].

The introduction of Y_2O_3 in ZrO_2 will create one mobile oxygen vacancy into the compound. The incorporation reaction can be written as shown in equation (1.12)

$$Y_2O_3 \xrightarrow{\quad ZrO_2 \quad} 2Y_{Zr}^{'} + 3O_O^{\times} + V_O^{\cdot\cdot} \qquad (1.12)$$
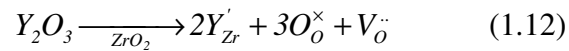
One vacancy is created for each two yttrium atoms incorporated. For zirconia conductivity increases when the increasing dopant concentration is up to a maximum values and the conductivity decreases sharply [15, 59, 60].

By considering the phase diagram, Figure 1.19, observation of some information can be obtained. 3-4 mol % Y_2O_3 partially stabilises zirconia, and is called tetragonal zirconia polycrystal. 3 mol % Y_2O_3, commonly called 3YSZ, has a higher mechanical strength but lower ionic conductivity at 1000 °C than the 8 mol % Y_2O_3, commonly called 8YSZ.

5-7 mol % Y_2O_3, is not 100 % cubic phase and has some degradation issues of ionic conductivity, caused by the tetragonal zirconia phase precipitation from the cubic zirconia matrix and there is also the formation of yttria or oxygen vacancy clusters [40, 52, 61-63].

8-9 mol % Y_2O_3 fully stabilises zirconia and yields the highest ionic conductivity in the system, when operated at 1000 °C, although for fully stabilised zirconia ionic conductivity degradation at less than 1000 hours at a high temperature is an important issue as 8YSZ has a drop of 50 % in ionic conductivity. There are some explanations for the cause of this degradation, a phase transition from the cubic phase into another phase with lower symmetry and lower ionic conductivity. Yttria segregation, at the grain boundaries, leads to a decrease of the grain boundary conductivity. A complex formation between oxygen vacancies and Y^{3+} ions, due to Coulombic interaction and formation of long-range ordered phases, increases the grain boundary resistance by a formation of a glassy phase and also the increase of short-range order (SRO) of oxygen vacancies around Zr^{4+} ions occurs, which reduces the concentration of mobile oxygen vacancies [40, 61-63].

The total conductivity of a ceramic is influenced by the presence of impurity phases. To improve the material characteristics, the control of the phase is very important, as the accumulation of impurity phase at the grain boundaries will effectively block ion conduction. This grain boundary effect leads to a reduction of several orders of magnitude in the total direct current (DC) conductivity. At high temperature, this influence of the grain boundaries is small when compared to intermediate and low temperatures [52, 64].

Scandia Stabilised Zirconia, SSZ

SSZ is probably the most promising material to be used as an electrolyte for intermediate temperatures due to its high ionic conductivity, stability under reducing and oxidising atmospheres and low electronic conductivity. The ionic conductivity of SSZ is three time higher than 8YSZ, at 800 °C, and enables SSZ to work at lower temperatures. According to Lee *et al.* [65], the ionic conductivity of 8 SSZ, at 800 °C, is 0.159 S/cm

but for 8YSZ the ionic conductivity, at 800 °C, is 0.039 S/cm. Over the last decades, scandia has become more available in the market due to political and economic changes. The increase of availability from Russia and China opens new possibility to use scandia for commercial applications.

SSZ electrolytes can be operated at intermediate temperature, 600-800 °C. Working at intermediate temperatures can increase the range of materials to be used, such as stainless steel for interconnects. In addition, the material degradation is reduced [29, 42, 53, 64, 66].

Due to its high ionic conductivity, SSZ can be applied in electrochemical devices, such as SOFCs and catalytic membrane reactors [67].

In this case ZrO_2, there are some distrotions in the structure which occur between coordination number of 6 and 8. It has a borderline radius ratio (0.68 for coordination number of 6 and 0.78 for coordination number of 8), at high temperature, 2000 °C, it may have the cubic fluorite structure with the coordination number of 8 but at room temperature it form as the mineral baddeleyite with coordination number of 7 [59]. Irvine *et al.* , say that it was found that yttrium tends to have a coordination number of 8 and zirconium tends to approach 6 as scandium. This behaviour could be explained by the ionic radii sizes, Table 1.4.

Table 1.4: Element, coordination and distance between atoms

Element, coordination	Length, pm
Y^{3+} (8 coordinate)	115.9
Zr^{4+} (6 coordinate)	86
Sc^{3+} (6 coordinate)	88.5

Badwall, *et al.* [36], states that Sc^{3+} and Zr^{4+} have the same coordination, the driving force for the distribution of these cations is smaller.

There is no clear agreement on an equilibium phase diagram of Sc_2O_3- ZrO_2, Spiridonov *et al.*, [68], reported an equilibrium phase diagram of the scandia stabilised zirconia system, Figure 1.20.
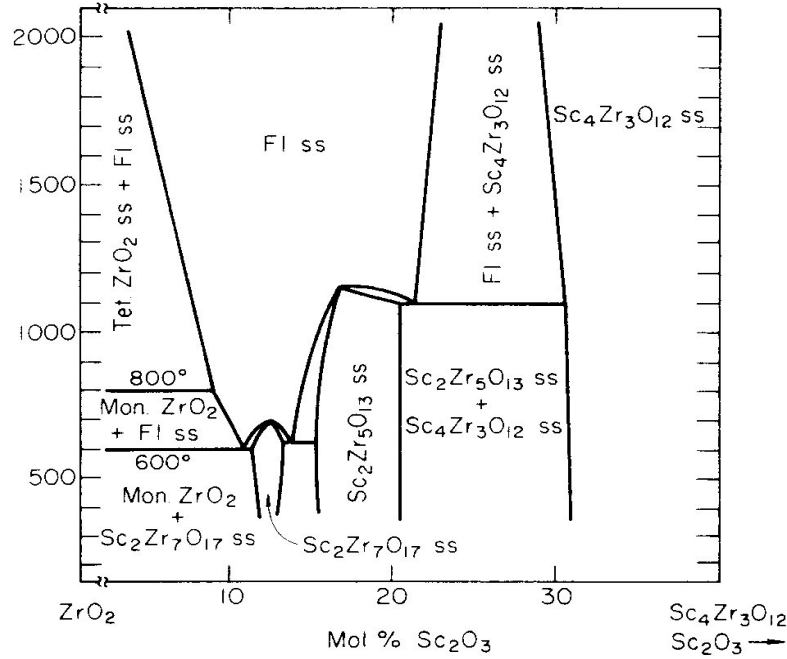
Figure 1.20: Phase diagram of the Scandia Stabilised Zirconia system, according to Spiridonov *et al.* [68]

The introduction of Sc_2O_3 in ZrO_2 will create one mobile oxygen vacancy into the compound. The incorporation reaction can be written as shown in equation (1.13)

$$Sc_2O_3 \xrightarrow{ZrO_2} 2Sc'_{Zr} + 3O^x_O + V^{\cdot\cdot}_O \qquad (1.13)$$
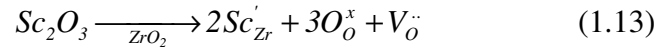
One vacancy is created for each two scandium atoms incorporated [30].

At equilibrium, the cubic phase is never stable below 650 °C and on thermal cycling phase transitions will be expected to occur. The main concern for SSZ is about its phase transition. The maximum ionic conductivity in ZrO_2-based systems is observed when the concentration of acceptor-type dopant(s) is close to the minimum necessary to completely stabilise the cubic-type phase. The pure cubic phase has a higher ionic conductivity than mixed phases [51, 53].

According to the phase analyses of ceramics synthesised by standard methods in the SSZ system, by Badwal *et al.* [66], there is not a well defined limit of the phase boundaries. Three main phases are reported: cubic, tetragonal and rhombohedral [51, 66, 69].

For 5-7 mol% Sc_2O_3 content there are two phases, cubic and tetragonal, for 8 and 9 mol% of Sc_2O_3 there is a single cubic phase and for 10-15 mol% of Sc_2O_3 the phase is rhombohedral . This is more or less consistent with the equilibrium phase diagram allowing for likely thermal history. Higher additions of scandia decrease the ionic conductivity due to increasing association of the oxygen vacancies and dopant concentration range providing maximum ionic transport are well established [53, 66].

At 800, °C for the compositions 8 to 10 mol % scandia stabilised zirconia, the ionic conductivity is between 0.11-0.12 S/cm [36, 62] and Mizutani et. al [70] state that the composition 11 mol % scandia stabilised zirconia the conductivity is 0.11 S/cm. When Sc_2O_3-ZrO_2 is doped with 1 mol % Y_2O_3 the ionic conductivity at 800 °C drops to 0.059 S/cm [53].

At high temperatures, bulk resistance has the main contribution while grain boundary becomes more important when temperature decreases. Bulk and grain boundary contributions have similar contributions at temperatures around 600 °C [56]. Composition and concentration of dopant affect directly the electrical conductivity of SSZ.

There are some problems with SSZ materials, the difficulty to obtain a pure and stable cubic phase after sintering, the cations are not distributed homogenously in a SSZ material and poor sintering property [71]. When this material is subjected to annealing, the precipitation of a low conductive t'-phase will occur [72-74].

Table 1.5: Annealing time and conductivity for 8ScSZ and 11ScSZ, at 1000 °C [73]

Annealing time, hours	Conductivity, S/cm	
	8ScSZ	**11ScSZ**
0	0.32	0.27
1000	0.16	0.28
5000	0.12	0.27

(Y$_2$O$_3$) (Sc$_2$O$_3$) (ZrO$_2$) system

The introduction of Sc$_2$O$_3$ in ZrO$_2$ will create one mobile oxygen vacancy into the compound. The incorporation reaction can be written as:

$$Sc_2O_3 \xrightarrow[ZrO_2]{} 2Sc_{Zr}^{'} + 3O_O^x + V_O^{\cdot\cdot} \qquad (1.13)$$
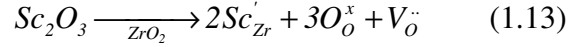
And the same will happen when the introduction is of Y$_2$O$_3$ in ZrO$_2$

$$Y_2O_3 \xrightarrow[ZrO_2]{} 2Y_{Zr}^{'} + 3O_O^x + V_O^{\cdot\cdot} \qquad (1.12)$$
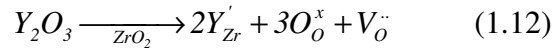
One vacancy is created for each two scandium or yttrium atoms are incorporated. In either case there is the substitution of an ion 3+ by a 4+ ion [15, 30, 59].

When Sc$_2$O$_3$-ZrO$_2$ is doped by Y$_2$O$_3$ there is an apparent elimination of the phase transition, from the low conductivity β-phase to the high conductivity cubic-phase, with stabilisation of the cubic fluorite phase, but the ionic conductivity decreases [75, 76]. The minimum amount of dopant to stabilise zirconia, in a (Y$_2$O$_3$)-(Sc$_2$O$_3$)-(ZrO$_2$) system, is around 8 mol% of dopant, and only 1 mol% of Y$_2$O$_3$ needs to be added to stabilise the (Sc$_2$O$_3$)-(ZrO$_2$) system [76, 77].

The (Y$_2$O$_3$)$_x$(Sc$_2$O$_3$)$_{(11-x)}$(ZrO$_2$)$_{89}$ system has been studied by Politova et. al. [53]. All compositions of the system showed the presence of a single phase cubic fluorite. When the yttria content increases, the ionic conductivity will decrease and the activation energy will increase [72].
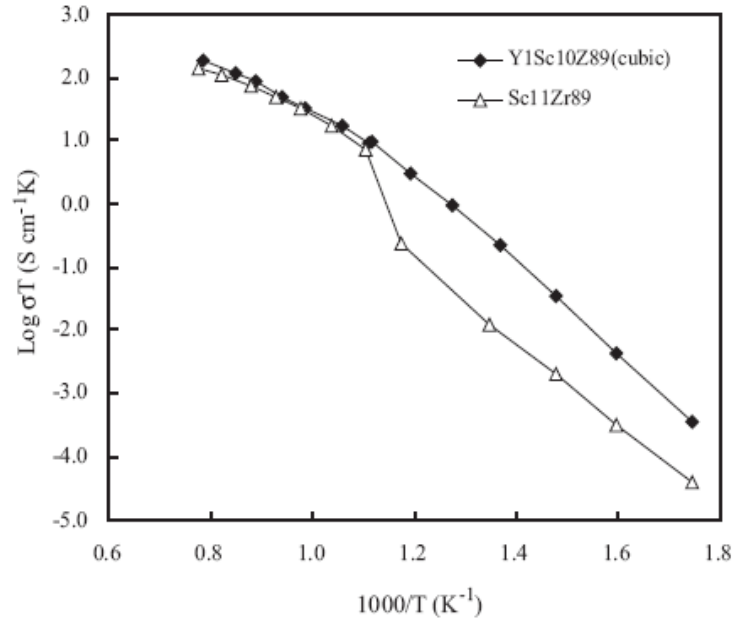
Figure 1.21: Temperature dependences of conductivity of the Sc11Zr89, Y1Sc9Zr89 compositions [53]

In Figure 1.21, the composition $(Sc_2O_3)_{11}(ZrO_2)_{89}$ sample contains both cubic and rhombohedral structures and $(Y_2O_3)_1(Sc_2O_3)_{10}(ZrO_2)_{89}$ contains a single phase cubic fluorite. The sample with the single phase has the highest value of ionic conductivity for any temperature. There is a visible phase transition that occurs at 580 °C from rhombohedral to the high conductivity pure cubic-phase.
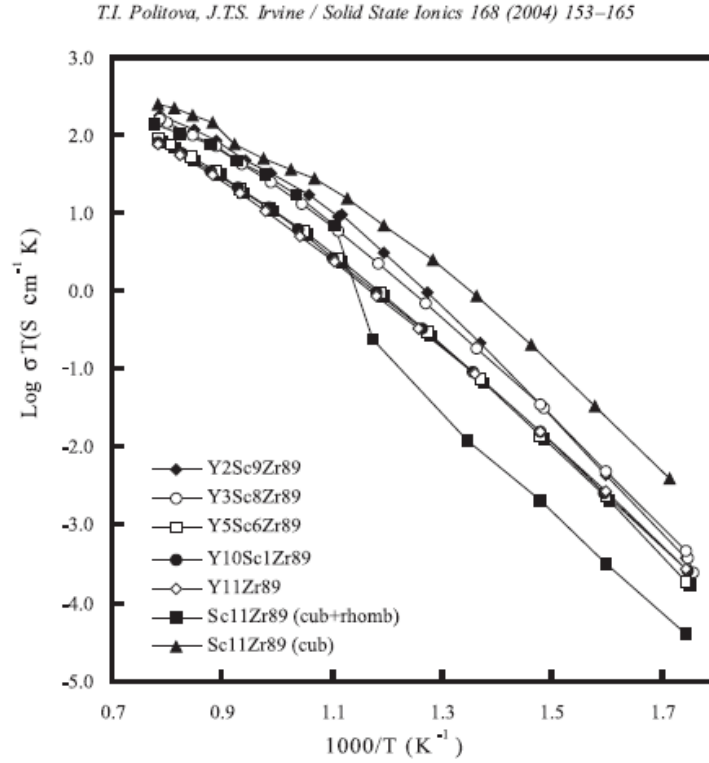
Figure 1.22: Arrhenius plot for several compositions of $(Y_2O_3)_x(Sc_2O_3)_{(11-x)}(ZrO_2)_{89}$ system [53].

By the analyses of Figure 1.22, the highest ionic conductivity belongs to the pure scandia zirconia composition with the single phase of a cubic fluorite structure, although the single phase, for this composition, is very difficult to achieve. For the same pure scandia zirconia composition, but with a cubic and rhombohedral phase mixture, a lower conductivity is observed. At approximately 600 °C, it shows a phase transition from cubic and rhombohedral to a pure cubic with higher ionic conductivity. The sample with 2 mol% of Y_2O_3 is slightly better than the other compositions doped with Y_2O_3 and when the Y_2O_3 content increases there is a decrease in ionic conductivity. This behaviour could be explained by the difference of the ionic radius of scandium and yttrium, the Y cation is larger than the Sc cation, which can create a barrier to free migrating vacancies [53].

At high temperatures the major contribution for the total resistivity appears to be from the bulk [72].

Table 1.6: Activation energy of the $(Y_2O_3)_x(Sc_2O_3)_{(11-x)}(ZrO_2)_{89}$ system for low and high temperature regions

Specimen	Activation energy, eV		Ordering or "association" enthalpy, eV
	Low temperature section 300 - 500 °C	High temperature section 800 – 1000 °C	
Y2Sc9Zr89	1.42	0.68	0.74
Y3Sc8Zr89	1.33	0.75	0.58
Y4Sc7Zr89	1.31	0.85	0.56
Y10Sc1Zr89	1.27	0.87	0.41
Y11Zr89	1.25	0.91	0.32
Sc11Zr89 (cub. + rhomb.)	1.30	0.61	0.69
Sc11Zr89 (cub.)	1.21	0.65	0.55

Table 1.6 shows the activation energy for low and high temperature and the association enthalpy, in eV. At low temperature the activation energy decreases with the decrease of scandia content, on the other hand at high temperature the activation energy increases with the decrease of scandia content. Ordering or association gives rise to the big difference in the activation energy.

In a Sc-rich phase, oxygen vacancies tend to form association defects, such as formation of ordered clusters or the appearance of a second phase. An explanation for the big difference of activation energy, between low and high temperature regions is due to the ordering of vacancies [53, 78]. As Politova et al. [53] say, at low temperature the total activation energy is the sum of "*oxygen vacancy migration (E_m) and association energy (E_{ass}). The association is the sum of the coulombic attraction caused by effective charges in the lattice together with the cation polarisability and strain energy caused by the different sizes of the host and dopant cation. The association energy would be the energy required to dissociate the vacancy-dopant cluster. According to this model, at high temperature isolated vacancies migrate freely and activation energy is equal to only the migration enthalpy. At low temperature, the activation energy has a significant contribution from association. Therefore, the existence of the complexes ($Y'_{Zr} V_O^{\cdot\cdot}$) in yttria stabilised zirconia and ($Sc'_{Zr} V_O^{\cdot\cdot}$) in scandia stabilised zirconia and their concentration should control the ionic properties of scandia and yttria stabilised at low temperature.*"

The substitution of the scandia by yttria leads to a decrease in ionic conductivity and the increase of the activation energy; this indicates that there is a dependence on ionic conductivity and yttria content.

The ionic conductivity decreases when Y_2O_3 content increases and the activation energy increases. This could be explained by the introduction of a large size cation, the steric blocking effect of the large cation (the migration of vacancies is more effectively blocked by a larger dopant) [55].

(Y_2O_3)-(ZrO_2) system doped with CeO_2

Ceria based electrolytes are known to have higher electrical conductivity than most zirconia-based systems, however it shows high levels of electronic conductivity at low oxygen partial pressures.

The introduction of ceria in (Y_2O_3)-(ZrO_2) system is expected to open the lattice, as cerium is a large cation. Therefore make possible the improvement of oxygen-ion mobility. Ananthapadmanabaham *et al.* [79], states the opposite and explained that this behaviour occurs due to the excessive distortion of the conduction path as a consequence of the presence of large cation when compared to the host cation.

(Sc_2O_3)-(ZrO_2) system doped with CeO_2

Kimpton *et al.* [80], studied compositions from $Zr0._{75}Ce_{0.08}M_{0.17}O_{1.92}$, where M= Nd, Sm, Gd, Dy, Ho, Y, Er, Yb, Sc. The highest ionic conductivity is from the composition $Zr_{0.75}Ce_{0.08}Sc_{0.17}O_{1.92}$. They also observed that the substitution of larger cations, in this case Ce^{4+} and/or M^{3+}, when compared to the host cation (Zr^{4+}) increases the steric blocking in the conduction path and consequently it will decrease the oxygen-ion conductivity.

Wang *et al.* [71], states that for all compositions of the system $(ZrO_2)_{(100-x)}(CeO_2)_x(Sc_2O_3)_{10}$ have a cubic phase structure, although there is always the existence of a minor metastable tetragonal phase (t'-phase), even when CeO_2 content is as high as 10 mol%. This tetragonal phase predominates at the grain boundary.

(Y$_2$O$_3$)-(Sc$_2$O$_3$)-(ZrO$_2$) system doped with CeO$_2$

The system (Y$_2$O$_3$)-(Sc$_2$O$_3$)-(ZrO$_2$) system was previously referred in this Chapter. Here I am going to provide the reasons why ceria can be used as a dopant to the ternary system of yttria, scandia and zirconia.

As shown by Politova *et. al.*, the introduction of even 1mol% of yttria in the scandia zirconia will stabilise the cubic phase, but the conductivity decreases drastically. The introduction of ceria on the system is expected to open the crystal lattice and therefore enhance the conductivity.

Observing Table 1.7, cerium has a large ion and ceria has a fluorite-type structure. Table 1.7, show some properties of cerium, such as atomic number, atomic weight and the ionic radius for a 6-coordinate for the oxidation state of Ce^{4+} and Ce^{3+}.

Table1.7: Cerium properties [81].

Properties	Cerium
Atomic number	58
Atomic weight, g/mol	140.12
Ionic radius (6-coordinate), pm	
IV	87
III	102

A low concentration of ceria is introduced, in order to maintain the electronic conductivity in a small amount relatively to the ionic conductivity.

There are three possibilities when the CeO$_2$ is introduced in the (Y$_2$O$_3$)-(Sc$_2$O$_3$)-(ZrO$_2$) system.

The introduction of CeO$_2$ will not produce defects of the structure. If the cerium will substitute the zirconium, it will occur as equation (1.14)

$$CeO_2 \xrightarrow{ZrO_2} Ce_{Zr}^x + 2O_O^x \qquad (1.14)$$
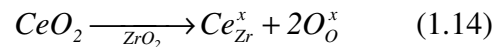
In this case there are no defects created just the substitution for one metal ion to another. In the case of ceria substitute yttria, it will create an interstitial oxygen ion for each two ions of ceria incorporated.

$$2CeO_2 \xrightarrow{Y_2O_3} 2Ce_Y^{\cdot} + 3O_O^x + O_i^{''} \qquad (1.15)$$
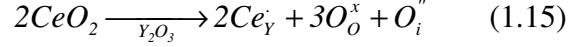
The same will occur for the substitution of ceria by scandia, an interstitial oxygen ion will be created for each two ions of ceria introduced

$$2CeO_2 \xrightarrow{Sc_2O_3} 2Ce_{Sc}^{\cdot} + 3O_O^x + O_i^{''} \qquad (1.16)$$
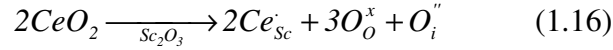
It is favoured the inclusion of interstitial ions than ions with superior valance and the concentration of interstitial species has the tendency to increase to make a easier maintenance of the electronic neutrality.

The amount of ceria, maximum 5 %, is smaller when compared with the amount of yttria plus the amount of scandia (15%< yttria+scandia <20%). The predominant defect is the oxygen vacancies, $V_O^{\cdot\cdot}$; therefore it can be affirmed that the initial amount of $V_O^{\cdot\cdot}$ is high.

Rare Earth Doped Ceria

Ceria-based electrolytes have higher conductivities than most zirconia-based electrolytes (with the exception of scandia doped zirconia).

A ceria-based electrolyte develops electronic conductivity under reducing environments and has to be coated with a protective layer as doped zirconia of a stable electrolyte such as the one on the fuel side. Ceria and zirconia in contact with each other form solid solutions at low temperatures than 1200 °C. This solid solution phase has a much lower ionic conductivity than either zirconia or doped electrolytes [8, 62].

For samaria-doped ceria, the conductivity increases with increasing samaria doping and reaches a maximum for $(CeO_2)_{0.8}(SmO_{1.5})_{0.2}$, which has a conductivity of 5.6×10^{-1} S/cm at 800 °C. Sintering conditions have significant effects on the resistivity of the $Sm_{0.2}Ce_{0.8}O_{1.9}$ material, the overall resistivity decreases with lower sintering temperature

and has its minimum at the sintering temperature of 1100-1200 °C. This makes $Sm_{0.2}Ce_{0.8}O_{1.9}$ material capable of working as a SOFC electrolyte at temperatures below 700 °C to avoid possible reduction of cerium (4+) to cerium (3+) [82].

Perovskites, ABO₃

Ceramics with perovskite crystal structure have many applications due to their wide range of properties. They can be applied as ferroelectrics, piezoelectric, pyroelectrics and materials with high permittivity [83].

The cubic structure is the ideal structure of perovskites with the space group Pm3m and the cubic unit cell size is about 0.39nm, see Figure 1.23.
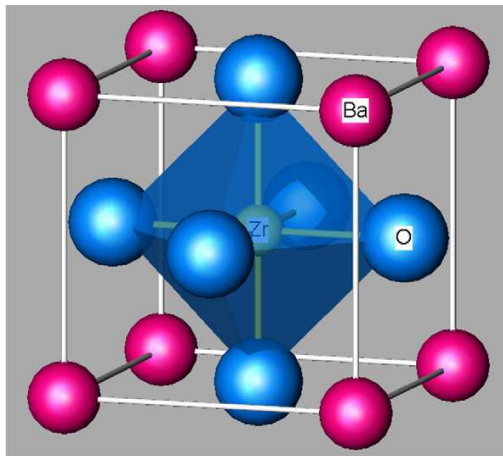
Figure 1.23: Perovskite crystal structure, $BaZrO_3$. The yellow spheres represent the Zr cation site, pink spheres represent the Ba cation site and blue spheres represent the oxygen sites.

The majority of the materials characterised as perovskites are not cubic due to distortions or tilt of the oxygen octahedra surrounding the B-site ions. In some other cases, they have other crystal forms, such as tetragonal, orthorhombic or rhombohedral [83, 84]. A-site cation is the larger and will be a 12-coordinated by the anions in the lattice; the A-site cations usually are rare earth elements. On the other hand, the B-site cation is typically smaller 6-coordinate cation, forming a BO_6 octahedra, and frequently

is a transition metal. It is usually through distortions of the BO_6 octahedron that a deviation from perfect cubic symmetry occurs [84-86].

The structure is strongly correlated with the amount of the dopants, the stoichiometry and temperature but again there is no agreement [84, 85]. The higher the symmetry of the structure, the better the oxide ion conductivity. In order to achieve a stable cubic structure, A and B site ions must have a definite radios with O^{2-} to form 12- and 6-fold coordination, hence $r_A > 0.09$ nm and $r_B > 0.051$ nm. For the perfect perovskite structure to be formed, it must fulfil the relation in equation (1.17)

$$r_A + r_0 = \sqrt{2}\left(r_B + r_0\right) \qquad (1.17)$$

The dependence on the level of interaction between A- and B- site ions with O^{2-} is given by the tolerance factor t, where

$$t = \frac{\left(r_A + r_0\right)}{\sqrt{2}\left(r_B + r_0\right)} \qquad (1.18)$$

The perovskite type structure is usually obtained when t is in the interval $0.75 < t < 1.0$, although to obtain the cubic structure t must equals 1 [48, 84]. The Goldschmidt tolerance factor has been used to predict conductivity but obtain t equals 1 is not sufficient enough to ensure high oxide ion conductivity [48].

As it happens with the fluorite structure, perovskites have the maximum oxide ion conduction when the lattice is stress-free. Ideally a perovskite has a cubic closest packing, the A-site ions should be equal in size of the oxide ion [87]. The size and charge of B-site is an important parameter, since B-O octahedra constitutes the framework of the perovskites structure, the bonding of the oxide to the small B-ion is longer than to the larger A-ion. The perfect matching radii for the B-site is r=0.58 Å, the radii should be the octahedral hole [48].

Perovskite LaGaO$_3$ family

A new family of perovskites based on LaGaO$_3$ doped at both A- and B- sites have been widely investigated as an alternative SOFC electrolyte. There is a large variety and concentration of dopants that can be accommodated in a wide range of host compounds. Table 1.8, shows possible cations for A- and B- sites to dope LaGaO$_3$ [62, 85, 88].

Table 1.8: Possible doped cations for A- and B-sites

Site	Cation
A-	Strontium Calcium Barium Neodymium Samarium
B-	Magnesium Indium Aluminium Zinc Scandium

Although there is a disagreement about the best elements to dope LaGaO$_3$ to give the highest conductivity, it is known that lanthanum is the element among the rare earth elements that exhibit the highest conductivity as an A-site ion [86].

Table 1.9 present three different elements on a B-site of this perovskite. The different crystal structure, phase transition and type conduction when B-site has the elements Ga, Al or Sc.

LaGaO$_3$ at room temperature has the orthorhombic crystal structure, at around 145 °C the orthorhombic changes to a cubic crystal structure. This material is an ion conductor. LaAlO$_3$ has the rhombohedral crystal structure at room temperature; at 450 °C a phase transition occur to cubic crystal structure. This material is a mix conductor, electronic and ionic conduction. LaScO$_3$ has the orthorhombic crystal structure, from room temperature to 1000 °C. This material has a n-type and ionic conduction.

Table 1.9: Material, crystal structure, phase transition and type of conduction [86].

Material	Crystal structure	Phase transition	Type of conduction
$LaGaO_3$	orthorhombic	145 °C to cubic	Ionic
$LaAlO_3$	rhombohedral	450 °C to cubic	mixed electronic and ionic
$LaScO_3$	orthorhombic	No transition on interval, 25-1000°C	p-type and ionic

These materials have relatively high ionic conductivities in both oxidising and reducing atmospheres and thermal expansion coefficients comparable with those fuel cell components.

$La_{1-x}Sr_xGa_{1-y}Mg_yO_{3-\delta}$

The system $La_{1-x}Sr_xGa_{1-y}Mg_yO_{3-\delta}$ (LSGM) has been recently investigated to be used as an electrolyte for SOFCs, at intermediate temperatures (600-800 °C). The ionic conductivity for the composition $La_{0.8}Sr_{0.2}Ga_{0.83}Mg_{0.17-\delta}$,.is 0.17 S/cm at 800 °C when compared to 8YSZ is 0.034 S/cm at 800 °C [62, 89, 90].

LSGM structure is strongly dependent on the concentration of dopants and temperature, in Table 1.10, there are concentration and correspondant structures for the system $La_{1-x}Sr_xGa_{1-y}Mg_yO_{3-\delta}$, [91].

When the concentration of x+y is less than 25 %, in the system $La_{1-x}Sr_xGa_{1-y}Mg_yO_{3-\delta}$, the material has the orthorhombic crystal structure. When x+y is between 25 and 30 %, it has a mixture of orthorhombic and rhombohedral crystal structure. For x+y concentration more than 35 % and x and y has a higher concentration than 20 %, it show the presence of a cubic structure.

Table 1.10: Concentration and correspondent structures

Concentration	Structure
x+y ≤ 25%	Orthorhombic
25% ≤x+y ≤ 30%	Mix Orthorhombic and Rhombohedral
x+y ≥ 35% and x or y ≥ 20%	Cubic

Ionic conductivity depends on the type of structure but compositions with less lattice distortion are expected to have higher oxygen conduction. Secondary phases, from

perovskites based on lanthanum gallate, are reported, as they are strongly dependent, even for small variations in the stoichiometry. There are several secondary phases, such as $SrGaO_3$, La_4SrO_7, $LaSrGaO_4$ and $LaSrGa_3O_7$, and in secondary phases Sr/Mg ratios need to be controlled in order to obtain single-phase materials [15, 62, 85].

There are some disadvantages of this material:

- High cost of gallium oxide

- Relatively weak mechanical strength

- Chemical stability problems under highly reducing conditions, at high temperatures.

The reactivity of the nickel and lanthanum gallate makes difficult the use of the latter in a typical SOFC, as nickel is the anode electrocatalyst.

These materials show higher oxygen ion conductivity than YSZ but they are less stable at low oxygen partial pressures such as those found at the anode. This increases the defect oxide formation and electronic conductivity, which lowers the cell potential.

Bismuth Oxide

Bismuth oxide has a phase transition around 700 °C which leads to an increase in conductivity by almost three orders of magnitude. The high temperature, δ phase compound has a cubic fluorite structure, with an extremely high (25%) oxygen vacancy content. Below the transition, the vacancies are ordered and hence the low conductivity.

Stabilisation at high temperature has led to $(Bi_2O_3)_x(Ln_2O_3)_{1-x}$ phase materials (Ln= lanthanum), which shows much less pronounced transition behaviour but retains overall high conductivity [8].

Limitation:

- High electronic conductivity

Tendency of bismuth, to become reduced, in hydrogen or fuel containing atmospheres [15].

1.6.2 Anode

The anode is usually a cermet, which consists of a metallic element in a ceramic skeleton. At first some precious metals, such as platinum, palladium and gold, and some transition metals, iron, cobalt, and nickel were tried such as were the candidates to be used as anode materials. Platinum peels off after a few hours under SOFC operating conditions [92].

It is on the anode side where the gas fuel reacts with the oxide ions, which passed through the electrolyte; the anode material has to have kinetic properties fast enough to make the reaction of the fuel oxidation and the oxide ions. There is also the product of the electrode reaction that has to be conducted to the external circuit.

The catalytic activity in the anode is variable with the design chosen, especially when used at intermediate temperatures [82].

A good candidate for anode materials should have the following characteristics:

- Have high porosity, 20 to 40 % of porosity, in order to allow the mass transport of the reactants and the gases to circulate

- Have similar thermal expansion coefficient to the interconnect and electrolyte materials

- Be an electronic conductor to allow the electrons, product of the electrode reaction, to pass the external circuit

- Be ionic conductive to allow the oxide ions that arrive from the cathode to be spread abroad the region anode/electrolyte interface

- Be chemically and physically stable as it can occur corrosion by the fuel oxidation products

- Be stable at low oxygen partial pressures as the equilibrium between fuel gas and oxidation products create a low oxygen partial pressure

- Be refractory due to the high working temperatures [30].

Ni/YSZ Cermets

The most commonly used materials are nickel metal in a YSZ ceramic matrix. Nickel is used due to its low cost and good catalytic properties and YSZ usually is the same material used for electrolyte. They are prepared in a ~50:50 wt ratio NiO:YSZ mixture, the nickel particles are dispersed in a porous YSZ matrix.

In this cermet, the function of the zirconia when added to the nickel is:

- To prevent sintering of the metal particles

If the nickel particles sinter, there will be a reduction of the active surface area available for oxidation to occur.

- To provide a thermal expansion co-efficient comparable to the electrolyte

The thermal expansion of the nickel is 13.3 $\mu mcm^{-1}k^{-1}$ and the YSZ is 10.5 $\mu mcm^{-1}k^{-1}$. Mixing these two materials, with this different thermal expansion co-efficient, would cause warping and cracking of components during processing and during heating to operating temperature.

- To increase the triple-phase boundary, (TPB)

The anode must be porous; it must have approximately 20% to 40 % of porosity, because the gas, fuel and the product of the reaction have to pass and reach the electrolyte or be exhausted [8, 29, 60].

- To provide ionic conductivity

The function of the nickel is to provide:

- Electronic conductivity

- Catalytic activity [29, 60].

TPB is the reaction site, where the fuel cell charge takes place. Here the gas, catalytic electrode and the electrolyte are all in physical contact. It is in TPB that the

electrochemical reactions happen, where gaseous species, ions and electrons get together. This area of contact between the three phases consists on Ni grains (conducting electrons), YSZ (conduction ions), and pores (diffusion of gases). The properties of TPB have an enormous variation influencing properties, such as average particle size and the particle size distribution; therefore have an enormous impact on the electrochemical performance of the anode [1, 93, 94]. The TPB reaction zone is important for both electrodes, the cathode and the anode. In a composite electrode, the TPBs extend from the interface, as shown in Figure 1.24.
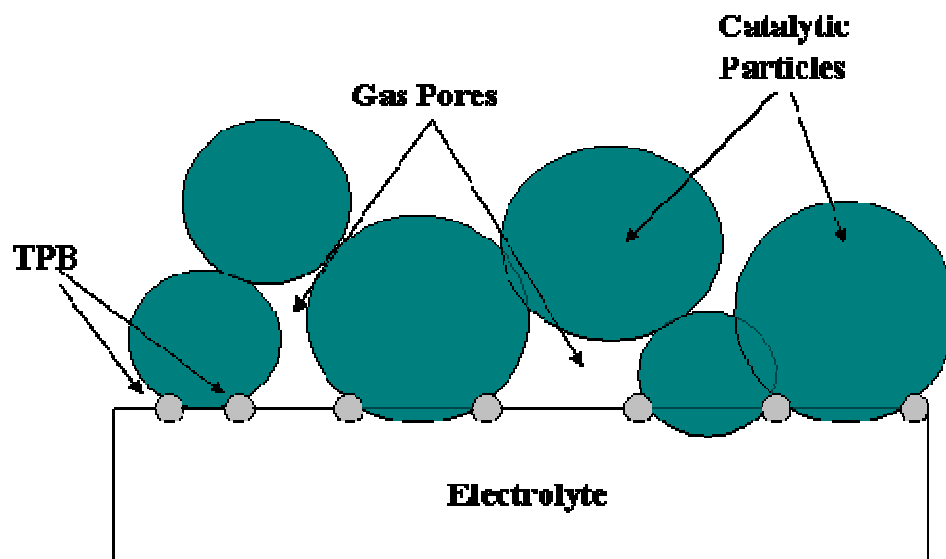
Figure 1.24: Schematic of the interface of the anode/electrolyte in a fuel cell, illustrating the triple phase boundary reaction zones where the catalytically active electrode particles, electrolyte phase and gas pores intersect.

The connection between the electrolyte and the anode sometimes gives some loss due to ohmic polarisation; therefore, several developers put two layers of anode in an attempt to reduce this effect.

In the last decade there was shift on the configuration of the SOFC, it came from an electrolyte supported cell to an anode and cathode supported cell. There are some advantages using this configuration, decreases the working temperature of SOFC, and with a thin electrolyte it will decrease also the sintering temperature of the electrolyte (1400 °C). It will lower the polarisation of the anode with hydrogen as fuel and it can be

processed by traditional ceramic techniques. There are also some problems with this configuration as the compatibility of thermal expansion coefficient of nickel and YSZ is poor.

Other Anode Materials

There are some alternatives to nickel/YSZ cermets; some of them can be the cermet of ruthenium/stabilised ZrO_2, cobalt/stabilised ZrO_2 or cooper/stabilised ZrO_2. The case of ruthenium/stabilised ZrO_2 studies show that it has a higher resistance to sintering, for the cobalt/stabilised ZrO_2 it has a higher tolerance of sulphur than nickel/YSZ cermets, although the cost can be a disadvantage.

Nickel/SCD (nickel/samaria doped ceria) has higher open-circuit voltages, and a lower degree of polarisation than for Ni/YSZ with either methanol or methane as fuel [76].

1.6.3 Cathode

In the cathode side the reduction of the oxygen to oxygen ions occur, those oxygen ions will pass through the electrolyte and reach the anode. There are five steps for cathode reactions:

1. Oxygen molecule must be adsorbed and dissociate into the oxygen atoms at the cathode surface

2. Surface diffusion of adsorbed oxygen

3. Incorporation and subsequent bulk diffusion of oxygen inside the oxide lattice

4. Incorporation of adsorbed oxygen in the O_2/cathode/electrolyte three phase boundary

5. Transport of oxide ions in the solid electrolyte

A good candidate for cathode material, should have the following characteristics, it should:

- Have high electrical conductivity

- Have high catalyst characteristics

- Have high porosity, between 25 to 40 % porosity

- Compatible but not reactive with the electrolyte and interconnect

- Thermal expansion should match other components

The first catalytic material to be used as cathode was platinum because other materials were not available, but platinum is very expensive. In 1960, Tedmon *et al.* [95], tested $LaCoO_3$ and it showed good performance, had higher diffusion and surface exchange coefficient, but it degraded rapidly with time due to the reaction with YSZ.

Lanthanum manganite ($LaMnO_3$) is a p-type perovskite oxide mixed conductor. Electronic conduction occurs by the hopping of electron holes between the Mn^{3+} and Mn^{4+} states. It shows reversible oxidation-reduction behaviour, as it can have oxygen excess or deficiency depending upon the ambient oxygen partial pressure.

Although the degradation of $LaMnO_3$ is not as severe as $LaCoO_3$, there are some issues with the reaction between the $LaMnO_3$ and the zirconia from the YSZ electrolyte; in this reaction it will form lanthanum zirconate, $La_2Zr_2O_7$. The $La_2Zr_2O_7$ is a pyrochlore phase with a much lower conductivity than YSZ; and it is formed for temperatures above 1200 °C, during sintering.

This material also reacts with the material of the oxide interconnects. Doped $LaCrO_3$ at high temperature will form $(Sr,La)_3Mn_2O_7$ and $(Ca,La)_3Mn_2O_7$, which occurs due to chromium and strontium ions migrating to the interface. This is one of the reasons why oxide interconnects are not generally used.

To attempt to eliminate the secondary phase, doping $LaMnO_3$ with some transition metals was tried, such as cobalt, iron and manganese, and also strontium has been studied to be used as cathode materials for SOFCs. Doping $LaMnO_3$, with strontium will change some of the La^{3+} and replaced by Sr^{2+}, which increases the Mn^{4+} content, decreases the activation energy (E_a) and greatly increases the electronic conductivity.

Strontium doped lanthanum manganite ($LaSrMnO_3$) is the material usually used in SOFC, these materials are p-type semiconductors and have high electronic conductivity in oxidation atmospheres.

1.6.4 Interconnects

Interconnects have two main functions in a SOFC system, electrical connection between the cells and separation between gases in a cell stack, the interconnect will be in contact with the anode of one cell and the cathode of another. The fact that interconnects are in contact with both sides of the cell it makes material choice more difficult, as the two sides are exposed to different atmospheres and different oxygen partial pressures. At the oxidising side $p(O_2)=2.13\times10^4$ Pa and at the reducing side $p(O_2)=1\times10^{-13}$ Pa, at 1000 °C. These severe conditions will have an impact on the properties that a perfect interconnect should hold [96, 97].

Typically interconnect requires the following properties:

- High electronic conduction but low ionic conduction

- Chemically stable in environments, reducing and oxidising

- Thermal expansion and chemical stability should be compatible with all other components

- High mechanical strength

The first three are essential for a good interconnect performance, although the choice for an interconnect material has to have the design, the material and fabrication cost in consideration [30].

The materials elected to be used as interconnects for SOFCs are perovskite-type oxide ceramics based on rare earth chromites, for working temperature between 900-1000 °C and metallic alloys for intermediate temperatures (600-800 °C).

Ceramic based interconnects

A widely used material is doped lanthanum chromite based oxide ($LaCrO_3$), which is a p-type perovskite oxide conductor. Alkaline earths are the dopants that can be used, and they can substitute on either the La or Cr sites, and they are introduced to increase the electronic conductivity. The perovskite, ABO_3 in this case is doped in the form:

$A_{1-y}A'_yBO_3$, where

A can be lanthanum or yttrium

A' can be calcium or strontium

B can be chromium, iron, cobalt and manganese [96, 97]

In order to maintain the charge balance, when an alkaline earth ion (M^{2+}) is introduced, the trivalent chromium ion (Cr^{3+}) is oxidised to tetravalent ion (Cr^{4+}), this will act as an electronic hole carrier. If the tetravalent chromium ions are subjected to reducing atmospheres, it will reduce again to trivalent chromium. This problem is more serious due to the formation of oxygen vacancies which leads to oxide ion conduction or to lattice expansion [98].

Alkaline earths are selected to dope $LaCrO_3$ but in oxidising atmospheres will react from chromates. Although $LaCrO_3$ is more stable than $CaCrO_4$ and $SrCrO_4$, it is not more stable than $BaCrO_4$. Doped $LaCrO_3$ is similar to the cathode material, and this can be a problem because when these two materials are being processed they can form a new phase, such as $(Sr,La)_3Mn_2O_7$ and $(Ca,La)_3Mn_2O_7$.

Metallic alloys

Metallic alloys can be used as interconnect materials, some examples are chromium-based alloys, iron-based alloys, and nickel-based alloys. These materials have some advantages when compared to ceramic interconnects, such as:

- Lower cost

- Easier to fabricate

- Better mechanical strength

- Higher electronic conductivity (ohmic losses in metals can be neglected)

- Similar thermal conductivity to ceramic interconnects (uniform heat distribution)

At oxidising environment and at high temperature, the formation of oxide layer on the surface of metal will occur. This oxide layer rapidly decreases the electronic conductivity (increases the contact resistance), and will also decrease the life time of a stack; this problem can be solved by coating the metals with some perovskite oxides. Poisoning of the cathode side is also an issue but Seo *et. al* [99] tried to solve these two issues by replacing chromium by manganese, alloys such as Crofer22APU and ZM9232. Manganese not only increases the electronic conductivity of the oxide layer but also stabilises the chromia forming alloys [99, 100].

Chromium-based Alloys

Ducrolloy ($Cr-5Fe-1Y_2O_3$) is the best alloy from this type of material; its purpose is to match the thermal expansion with all other components of the SOFC, chromia forming alloys have a relatively high electronic conductivity and a slow growth rate at operating temperatures of SOFCs. Ducrolloy was developed to work at temperatures above 900 °C. There is a deposition of chromia on the surface of the alloy, at oxidising atmospheres and at high temperatures; this will produce a protective layer that will slow down further chromium dissipation from the substrate [101, 102].

Iron-based Alloys

Iron-based alloys are known as stainless steels. They are used at operating temperatures approximately 800 °C, and their main advantage is they match thermal expansion coefficient with the other SOFC components.

Fe-26Cr-1Mo alloy has the formation of a surface layer of Cr_2O_3, with higher contact resistance when compared to chromium-based alloys.

FeCrAl-alloys are not adequate to be used as interconnects due to the development of an insulating alumina scale; this will give a higher contact resistance [103, 104].

Nickel-based Superalloys

Absorption of the thermal stress from several components of the SOFC is the great advantage which nickel-based alloys have. Haynes 230 alloy (57Ni-22Cr-14W-5Co) is suitable for use in long term continuous exposure at high temperatures, as high as 1150 °C, has high resistance to oxidation damage and high strength [105].

Haynes 230 has the slowest oxidation kinetics; it forms an oxide scale of Cr_2O_3 phase, and a minor spinel phase ($Mn_{1-\delta}Cr_{2-\delta}O_{4-\lambda}$). These alloys not only have oxidation on the cathode side but also on the anode side. The fuel atmosphere has an oxygen partial pressure between 10^{-22} and 10^{-17} atm, depending on the temperature and the fuel used. At these oxygen partial pressures, Cr_2O_3 is thermodynamically more stable than chromium; therefore the formation of Cr_2O_3 is favoured [106].

Ni-based alloys containing chromium and all other chromia-forming alloys can encounter several problems, such as:

- High oxidation rate

- Formation of an oxide scale when subjected to high temperature

- Volatisation of high valence chromium species and will form Cr_2O_3 or $Cr(OH)_2O_2$

The first two issues increase the surface layer and so they will increase the contact resistance and the last issue will poison the atmosphere of the electrode caused by the reduction of Cr(VI) species to a solid Cr(III) oxide at the cathode and electrolyte interface. The three problems will lead to a rapid degradation of the cell performance [107].

Coating the metal with a ceramic can be one solution for these issues. Perovskites oxides can be one solution, but there must be a careful selection of the possible materials for the coating layer, and it has to take into account:

- The diffusion coefficient of the chromium and the coating material, chromium should have a smaller diffusion coefficient than the coating material

- The chemical compatibility and stability between the substrate, the coating material and the electrode

- The stability in oxidising and reducing atmospheres, at working temperatures

- The low ohmic resistance in order to have a high electrical conductivity

- The thermal expansion coefficient has to be compatible with all components of SOFC but especially with the substrate so that the contact resistance does not increase during thermal cycling

There are two selected materials, strontium-doped $LaCrO_3$ (LSC) and strontium-doped $LaMnO_3$ (LSM). Coating chromium-based alloys with LSM gives low level of contact resistance at high temperatures, over an extended period of time. Introducing the coating process will increase the production cost [98, 108, 109].

There are several options to solve this problem:

- Decrease or even eliminate the amount of chromium in materials used

- Reduce working temperature, to 700 °C or below

1.7 Defects and non-stoichiometry

1.7.1 Defects

In a perfect crystal all atoms have a defined lattice position in the structure, as the definition of a crystal is the repetition of atoms, or ions, according to a specific lattice. Above 0 K there are always defects in the structure, these defects can be extended defects such as dislocations or they can occur at isolated atomic positions, known as point defects [110, 111].

Point defects can occur due to the presence of foreign atom at a particular site or to a vacancy where one atom would be expected. These defects can occur by external perturbation, for example, sufficient energetic radiation to excite an atom or at high temperature. Theses defects can lead to a distortion in the crystalline structure, which difficult ionic conduction. Although, the increase of entropy energy results of the presence of defects, it can be enough to provoke an increase in the Gibbs free energy, making the incorporation of more defects easier [112].

Point defects can have significant effect on the chemical and physical properties of the solid, such as the diffusion, electric conductivity and in the reactivity in crystalline solids. Note that atom or ion movement is facilitated when there are free atomic positions. For this study, point defect is significant for the material properties; therefore extended defects are not included [110, 111].

The Kroger-Vink notation for crystal defects:

The notation used for ionic defects, in general, indicates the species in cause, location in the lattice (in subscript) and the effective charge (in upscript).

Vacancies

Atoms and ions occupy regular positions to define the respective crystalline system. Some of these positions may be free known as vacancies. In the proximity of a vacancy, in a crystal, charges are not compensated. The notation used for vacancy is the letter V, where the index indicates the lattice position and the symbol (˙) is used for positive

effective chargers and (´) for negative effective chargers. The species vacancy charge has the opposite charge of the missing ion charge. See notation on Table 1.11.

Table 1.11: Notation of vacancy.

Notation	Definition
$V_M^\times$ or simply V_M	Neutral vacancy of element M
$V_A^{'}, V_B^{''}$	Vacancy of cations A^+, B^{2+}
$V_\times^{\cdot}, V_Y^{\cdot\cdot}$	Vacancy of anions X^-, Y^{2-}

Example:

A +1charge vacancy of silver in the crystal lattice of AgBr, is noted as $V_{Ag}^{'}$ and +2 charge vacancy of oxygen in the crystal lattice of ZrO_2, is noted as $V_O^{\cdot\cdot}$ [111, 113].

Interstitial ions or atoms

In this case, the atoms or ions introduced will occupy interstitial positions, positions which are peripheral to the crystal lattice, see notation on Table 1.12.

Table 1.12.: Notation of vacancy.

Notation	Definition
$M_i^\times$	Neutral vacancy of element M
$A_i^{\cdot}, B_i^{\cdot\cdot}$	Vacancy of cations A^+, B^{2+}
$X_i^{'}, Y_i^{''}$	Vacancy of anions X^-, Y^{2-}

Example:

Fluorine ion in CaF is noted as $F_i^{'}$ and oxygen ion in UO_2, is noted as $O_i^{''}$.

Replacement ions or atoms

All crystal lattices always accept a small amount of impurities, which will occupy interstitial positions or regular positions in lattice replacing regular constituents, see notation on Table 1.13.

Table 1.13.: Notation of vacancy.

| Notation	Definition
$A_B^\times$	A atoms in crystal lattice B
$X_Y^{\cdot}$	Cations X2+ replacing Y+
A_B'	Cations A+ replacing on B2+

Example:

It is possible to dissolve 15 % of CaO in the crystal lattice of ZrO_2 with the Ca^{2+} ions occupying the normal positions of Zr^{4+} [111, 113].

Electronic defects

There are some perturbations in the periodic distribution of the crystal electronic orbitals. Formation of electronic defects, electron and electron holes, can be analysed by thermodynamics Fermi statistics, taking into account the principle of the Pauli exclusion, by predicting the typical variation of the electron energy levels. At 0 K only the lower energy levels valence band is occupied; up to the level called Fermi energy level. Electrons in higher levels of energy are located in the so called conduction band; here they are free to participate on the conduction process. At temperatures above 0 K, some of the electrons jump to a higher level, conduction band, if thermal excitation occurs, that enables to participate in the conduction process [111, 112].

In the case of metal, the separation between valence band and conduction band is minimal or do not exist. On the other hand, there are materials where a band gap exists and has the width of E_g, this band. When a transition of an electron from the valence band to the conduction band occurs, it will create an electron plus electron hole pair $(e'+h^{\cdot})$ according to the following equation

$$0 \Leftrightarrow e' + h^{\cdot}$$
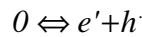
The equilibrium constant of this reaction relates with the band gap according to

$$n.p = N_v N_c \, exp\left[-\frac{E_g}{kT}\right]$$

Where

n=[e′] → concentration of electrons in the conduction band

p=[h˙] → concentration of electrons holes

N_v, N_c → density states

k → Boltzmann constante

T → absolute temperature, K

When the concentration of electronic defects is controlled by the transference from the valence band to the conduction band, the equation is described by:

$$n \approx p \approx (N_v N_c)^{1/2} exp\left[-\frac{E_g}{2kT}\right]$$

The band gap is generally expressed in eV.

The band gap of metal is much reduced or does not exist at all. The values for the band gap, Eg, is lower than 0.1 eV.

Electron mobility, μ_e, is enhanced by the increased conductivity as consequence of the increase of temperature.

$$\sigma_e = e \times n \times \mu_e$$

Conductivity is the product of electron charge, concentration and mobility.

In the case of metals, mobility of electrons can be affected by the lattice distribution, originated by thermal vibration and/or introduction of impurities. See figure 1.25.

For isolators, electrons of the external layers are on the valence band. If any electron reaches the conduction band it must have enough energy to be free from the atom and pass through the band gap, from the valence band to the conduction band. The band gap of the crystal diamond is about 6 eV [111, 114]. See Figure 1.25.
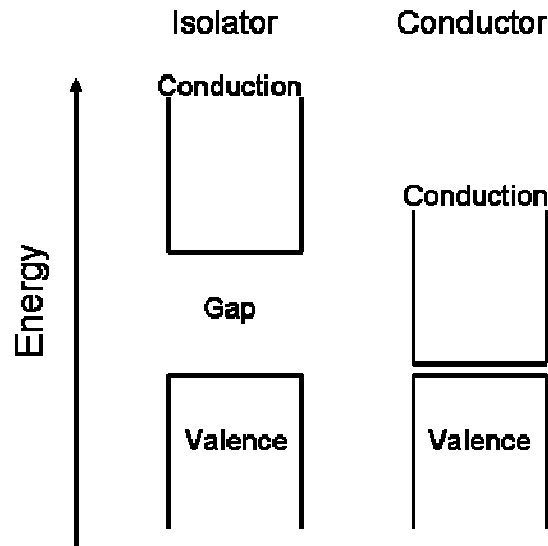
Figure 1.25: Schematic of bands in a conductor and isolator.

Semiconductors

Intrinsic semiconductors

The band gap is relatively small, around 1 eV, for example, the Silicon and Germanium band gap is 1.1 eV and 0.7 eV, respectively.

Semiconductors are materials, which electrical conductivity increases with the increase of temperature. For temperature equals to 0 K, semiconductor materials have similar behaviour as isolators. It is not possible to enhance the flow from the valence band to the conduction band when an external electric field is applied. When temperature is above 0 K the transition of electrons is possible from the valence band to the conduction band. The electrons that abandon the valence band leave a vacancy, which correspond to a positive charge. When another electron occupies this level, it corresponds to a positive charge dislocation [114].

Extrinsic semiconductors

The conductivity of semiconductor materials can be enhanced by several orders of magnitude when dopants are added (impurities). Depending on the type of dopants it can generate either n-type or p-type semiconductor.
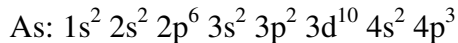
The atom of silicon has the following electronic configuration:

Si: $1s^2\ 2s^2\ 2p^6\ 3s^2\ 3p^2$
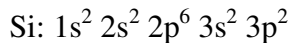
It has four valence electrons, where each atom is connected to another four atoms of Si with a covalent bond.

The atom of arsenic has the following electronic configuration:

As: $1s^2\ 2s^2\ 2p^6\ 3s^2\ 3p^2\ 3d^{10}\ 4s^2\ 4p^3$

Arsenic has five valence electrons. If one sample of Silicon is doped with a small amount of arsenic, in a way where some atoms of arsenic replace some atoms of silicon, in the crystal lattice; four valence electrons of each arsenic atom take part in the covalent bond with four neighbour atoms of silicon while the fifth valence electron stays slightly connected with its original atom. This way the atom of arsenic occupies the energy level right below the conduction band. See Figure. These levels of energy are called donor levels; the electrons that occupy these levels can be easily excited and jump to the conduction band.

The atom of gallium has the following electronic configuration:

Ga: $1s^2\ 2s^2\ 2p^6\ 3s^2\ 3p^2\ 3d^{10}\ 4s^2\ 4p^1$
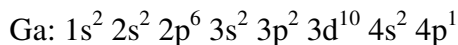
Galium has three valence electrons. If one sample of silicon is doped with a small amount of gallium, in a way where some atoms of gallium replace some atoms of silicon, in the crystal lattice; three valence electrons of each gallium atom take part in the covalent bond with three neighbour atoms of silicon, while the fourth valence electron, of silicon, stays slightly connected with its original atom and this way occupies the energy level right above the conduction band [112, 114]. See Figure 1.26.
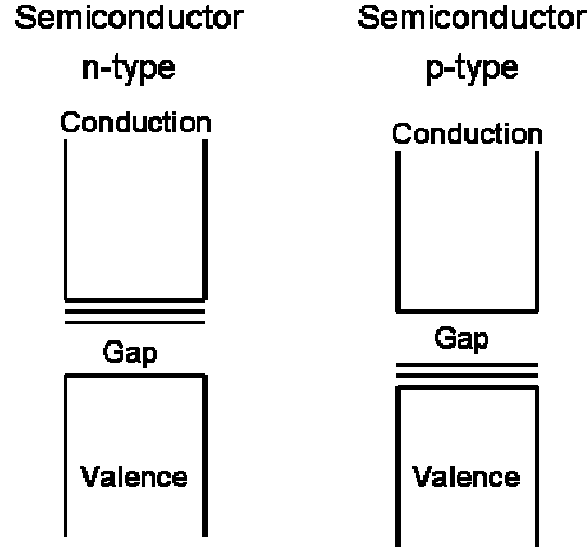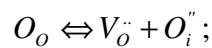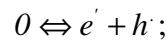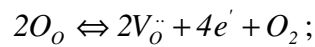
Figure 1.26: Schematic of bands in semiconductors n-type and p-type.

1.7.2 Brouwer Diagrams

Brouwer diagrams are representations of the changes in defects concentration as a function of oxygen partial pressure. Usually, several regions can be distinguished as a function of atmosphere conditions. Brouwer diagrams are made based on the formulation of the representative non-stoichiometry reactions and the formation of defects, ionic and electronic, which persist even when the material recovers to a normal stoichiometry. The analyses of Brouwer diagrams can be used as a guide to study materials and their potential applications, and also dopants effect [111, 115].

Metal oxides is analysed by the combined effects of non-stchoichiometry, formation of native ionic defects and the formation of electronic defects, following the equations:

$$2O_O \Leftrightarrow 2V_O^{\cdot\cdot} + 4e^{'} + O_2 \; ; \qquad\qquad K_{red} = \left[V_O^{\cdot\cdot}\right]^2 n^4 \times pO_2$$

$$0 \Leftrightarrow e^{'} + h^{\cdot} \; ; \qquad\qquad k_e = np$$

$$O_O \Leftrightarrow V_O^{\cdot\cdot} + O_i^{''} \; ; \qquad\qquad k_F = \left[V_O^{\cdot\cdot}\right]\left[O_i^{''}\right]$$

After finding the set of reaction that describes the chemistry of defects and the correspondent equilibrium constant, the possible regions and the correspondent electric neutrality conditions have to be identified.

1) Reduction conditions

When the conditions are reductive enough, the species $n \approx 2[V_O^{\cdot\cdot}]$ controls the reaction. Therefore, $n \approx 2[V_O^{\cdot\cdot}]$ is introduced in the equation $K_{red} = [V_O^{\cdot\cdot}]^2 n^4 \times pO_2$, originating the following equation

$$[V_O^{\cdot\cdot}] = \frac{n}{2} = 2^{-\frac{2}{3}} (K_{red})^{\frac{1}{3}} (pO_2)^{-\frac{1}{6}}.$$

The concentration of the other defects is very low when compared to the oxygen vacancies defect; this way they are not taking into consideration.

2) Intermediate conditions

In these conditions, the predominant species are $[V_O^{\cdot\cdot}] = [O_i'']$. Introducing this in the equation $k_F = [V_O^{\cdot\cdot}][O_i'']$, $[V_O^{\cdot\cdot}] \approx 2[O_i'']$ is obtained, which is introduced in the equations $K_{red} = [V_O^{\cdot\cdot}]^2 n^4 \times pO_2$ and $k_e = np$, originating the following equations:

$$n = K_{aF}^{-\frac{1}{4}} (K_{red})^{\frac{1}{2}} (pO_2)^{-\frac{1}{4}}$$

$$n = K_e K_{aF}^{\frac{1}{4}} (K_{red})^{-\frac{1}{2}} (pO_2)^{\frac{1}{4}}$$

3) Oxidant conditions

In these conditions, the predominant species are $p \approx 2[O_i'']$. When these species are predominant, it is recommended to combine the equilibrium constants in order to obtain a unique relation between their concentrations. In this case:

$$[O_i''] = 2^{-\frac{2}{3}} K_{red}^{-\frac{1}{3}} K_e^{\frac{2}{3}} K_{aF}^{\frac{1}{3}} (pO_2)^{\frac{1}{6}}$$

$$p = 2^{1/3} K_{red}{}^{-1/3} K_e{}^{2/3} K_{aF}{}^{1/3} (pO_2)^{1/6}$$

As oxygen partial pressure and concentrations can change several orders of magnitude, therefore it is convenient to use the logarithm scale. The slope in this type of representation is used to identify the dependence of each species from oxygen partial pressure [111, 112, 115].

Table 1.14 is a recap of all defect concentration for oxide with Frenkel disorder in the anionic crystal lattice.

Table 1.14: Variation of defect concentration for oxides with Frenkel disorder in the anionic crystal lattice, for example ceria [111].

Conduction	Neutrality conditions	Effects on defects concentrations
Reduction	$n \approx 2[V_O^{\cdot\cdot}]$	$log(n) = Const. - (1/6)log(pO_2)$ $log[V_O^{\cdot\cdot}] = Const. - (1/6)log(pO_2)$ $log[O_i''] = Const. + (1/6)log(pO_2)$ $log(p) = Const. + (1/6)log(pO_2)$
Intermediate	$[V_O^{\cdot\cdot}] = [O_i'']$	$log(n) = Const. - (1/4)log(pO_2)$ $log[V_O^{\cdot\cdot}] = Const.$ $log[O_i''] = Const.$ $log(p) = Const. + (1/4)log(pO_2)$
Oxidant	$p \approx 2[O_i'']$	$log(n) = Const. - (1/6)log(pO_2)$ $log[V_O^{\cdot\cdot}] = Const. - (1/6)log(pO_2)$ $log[O_i''] = Const. + (1/6)log(pO_2)$ $log(p) = Const. + (1/6)log(pO_2)$

The representation is not difficult when the equilibrium constants are reasonably estimated. Although rarely all equilibrium constant are estimated, for all regions, therefore Brouwer diagram is generally a representation of a tendency.

The tendency set for each region can be summarised graphically as shown in Figure 1.27, it gives the idea how defects change in (ions, electrons and electron holes) concentration as a function of oxygen partial pressure.
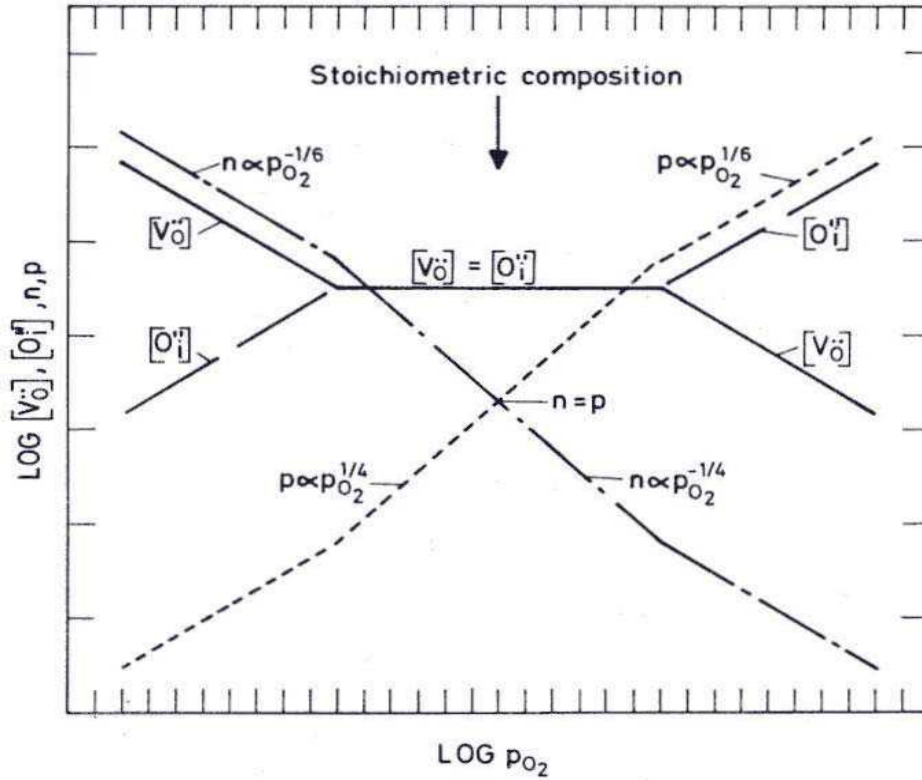
Figure 1.27: Defect equilibrium diagram of pure MO_2 with Frenkel disorder.

In region I, low oxygen partial pressure, shows a $pO_2^{-1/6}$ proportionality and the material is a n-type semiconductor, because the mobility of the electrons is always much higher than the oxygen vacancies.

In region II, intermediate oxygen partial pressure, the majority of charge carrier is the oxide ion, the concentration of which remains constant with changing oxygen partial pressure.

In region III, high oxygen partial pressure, shows a $pO_2^{1/6}$ proportionality and the material is a p-type semiconductor, as it will have oxygen excess [111, 112].

1.8 Aim of the project

Scandia stabilized zirconia (SSZ) is a promising material to be used as an electrolyte, in Solid Oxide Fuel Cells (SOFC) at intermediate temperatures (600-800 °C) due to its high ionic conductivity, stability and low electronic conductivity. Decreasing working temperature will reduce material degradation and will increase the range of materials that can be used for interconnect.

Phase analysis of the scandia zirconia system indicates that the system is complex with many component phases. Spiridonov *et al.* reported that there is no stable cubic phase below 600°C for SSZ and phase transitions occur on cooling from cubic to rhombohedral and/or monoclinic phases at 600 °C or above.

The aim of this project is to prepare a dense material, which can be used as an electrolyte for a SOFC. To achieve this three main topics have to be explored:

- An innovative sol-gel and combustion method was used in an attempt to obtain a compositionally homogeneous dense material. It is study the properties of the powders and the materials produced by the powders (chapter III)

- The introduction of dopants, yttria and ceria in scandia stabilised zirconia, it is expected to stabilize the cubic phase and increase the high ionic conductivity. Electrical measurements were performed to study the effect of the dopants on the grain boundary and bulk contributions (chapter IV).

- The effect of different oxygen partial pressures on the material is studied in chapter IV. The effect of time is studied in chapter V

References

1. EG&G technical service, I., Science Applications International Corporation, *Fuel Cell Handbook*. Sixth ed. 2002, West Virginia: US Department of Energy.
2. O'Hayre, R., Cha, S.-W., Colella, W. and Prinz, F.B., *Fuel Cell Fundamentals*. first ed. 2006, New York: John Wiley & Sons.
3. Larminie, J. and Dicks, A., *Fuel Cell System Explain*. 2nd ed. 2005, London.
4. Council, U.F.C. 2000 [cited 2006 April].
5. Atkins, P.A., *Physical Chemistry*. 5th ed. 1994, Oxford: Oxford University Press.
6. Alberty, R.A., Silbey, R. J., *Physical Chemistry*. 2nd ed. 1996, Chichester: Wiley & Sons, Inc.
7. Kuhn, H., Foersterling, H.-D., *Principles of Physical Chemistry*. 1st ed. 2000, Chichester: Wiley & Sons, Inc.
8. Haile, S.M., Acta Materialia, **51** (2003) p. 5981-6000.
9. Cengel, Y.A., Boles, M.A., *Thermodynamics, An Engineering Approach*. 6th ed. 2007, New York: McGraw-Hill.
10. Hsieh, J.S., *Principles of thermodynamics*. 1975, Washington D. C.: McGraw-Hill.
11. Smith, J.M., Van Ness, H. C., Abbott, M.M., *Introduction to chemical Engineering Thermodynamics*. 7th ed. 2005, New York: McGraw-Hill.
12. Hart, A.B., Womack, G.J., *Fuel cells: Theory and application*. 1967, London: Chapman and Hall, Ltd.
13. McDougall, A., *Fuel Cells*. 1st ed, ed. McAuliffe, C.A. 1976, London: The Macmillian Press, Ltd.
14. Steele, B.C.H. and Heinzel, A., Nature, **414** (2001) p. 345-352.
15. Haile, S.M., Materials Today, (2003) p. 24-29.
16. Park, E.D., Lee, D.,Lee, H. C., Catalysis Today, **139** (2009) p. 280-290.
17. www.fuelcells.org. 1993 [cited 2009 March].
18. www.DuPont.com. 2000 [cited 2009 July].
19. Inc., D.G., *Fuel Cells for Portable Power: Markets, Manufacture and Cost*, ed. Council, B.T.U.S.F.C. 2003, Corona, California: Breakthrough Technologies & U.S. Fuel Cell Council.
20. http://science.nasa.gov/headlines/y2003/18mar_fuelcell.htm. 2003 [cited 2008 August].
21. Graham, W. and Barrett, S., Fuel Cell Bulletin, **2003**(1) (2003) p. 11-12.
22. www.etaing.com. 2006 [cited 2008 August].
23. http://hydrogencommerce.com. 2006 [cited 2008 August].
24. http://en.wikipedia.org/wiki/alkaline_fuel_cell. 2006 [cited 2008 August].
25. Nernst, W., Z Elektrochem, **6** (1899) p. 41-43.
26. Bauer, E. and Preis, H., Z Elektrochem, **43** (1937) p. 727-732.
27. www.powergeneration.siemens.com. 2007 [cited 2009 July].
28. Singhal, S.C., Solid State Ionics, **152-153** (2002) p. 405-410.
29. Minh, N.Q., Journal American Ceramic Society, **76**(3) (1993) p. 563-588.
30. Singhal, S.C. and Kendall, K., *High Temperature Solid Oxide Fuel Cells: Fundamentals, Design and Applications*. Elsevier Advanced Technology. 2003, Oxford.

31.   Minh, N.Q., Solid State Ionics, **174** (2004) p. 271-277.
32.   Irvine, J., Jones, F. G. E., Connor, P. A., *Fuel Cell*, Andrews, U.C.U.S., Editor. 2001: UK.
33.   Jones, F.G.E. and Irvine, J. in *Fifth European Solid Oxide Fuel Cell Forum*. 2002. Lucerne, Switzerland.
34.   Feighery, A., *Zirconia-Based Electroceramic Materials for SOFC Applications*, Ph. D., 1998s, University of St. Andrews, St. Andrews.
35.   Dokida, M., Solid State Ionics, **152-153** (2002) p. 383-392.
36.   Badwal, S.P.S., Ciacchi, F. T., Rajendram, S. and Drennan, J., Solid State Ionics, **109** (1998) p. 167-186.
37.   Karton, V., Marques, F.M.B. and Atkinson, A., Solid State Ionics, **174** (2004) p. 135-149.
38.   Singhal, S.C., Solid State Ionics, **153** (2000) p. 304-313.
39.   Smith, W.F., *Principles of Materials Science and Engineering*. 3rd ed. 1998, Lisboa: McGraw-Hill.
40.   http://www.americanelements.com/zr.html. 2005 [cited 2008 November].
41.   Scott, H.G., Journal Material Science, **10**(9) (1975) p. 1527-1535.
42.   Yashima, M., Kakihana, M. and Yoshimura, M., **86-88** (1996) p. 1131-1149.
43.   Schneider, S.J., *Ceramics and glasses*. 1st ed. Engineered Materials Handbook, ed. International, A. Vol. 4. 1991, USA: ASM International.
44.   Florio, D.Z., *Estudos de sinterizacao e de envelhicemento termico de ceramicas de zirconia-itria por espectroscipia de impedancia*, Ph. D., 1998s, Universidade de Sao Paulo, Sao Paulo.
45.   Taylor, M.A., Kilo, M., Borchrdt, G., Weber, S. and Sherrer, H., Journal of the European Ceramic Society, **25** (2005) p. 1591-1595.
46.   The American Ceramic Society, I., *Science and Technology of Zirconia*, ed. Heuer, A.H., Hobbs, L. W. Vol. 3. 1981, Columbus: The American Ceramic Society, Inc.
47.   Xu, G., Zhang, Y., Liao, C. and Yan, C., Solid State Communication, **121** (2002) p. 45-49.
48.   Mogensen, M., Lybye, D., Bonanos, N., Hendriksen, P.V. and F.W. Poulsen, Solid State Ionics, **174** (2004) p. 279-286.
49.   Subbarao, E.C., *Solid electrolytes and their applications*. 1980, New York: Plenum Publishing Corporation.
50.   Badwal, S.P.S., Solid State Ionics, **52** (1992) p. 23-32.
51.   Arachi, Y., Sakai, H., Yamamoto, O., Takeda, Y. and Imanishai, N., Solid State Ionics, **121** (1999) p. 133-139.
52.   Li, Y., Liu, M., Gong, J., Chen, Y., Tang, Z. and Zhang, Z., Material Science and Engineering B, **103** (2003) p. 108-114.
53.   Politova, T. and Irvine, J.T.S., Solid State Ionics, **168** (2004) p. 153-165.
54.   Mori, T., Drennam, J., Lee, J.-H., Li, J.-G. and Ikegami, T., Solid State Ionics, **154-155** (2002) p. 529-533.
55.   Rey, J.F.Q. and Muccillo, E.N.S., Ceramica, **48**(307) (2002) p. 157-162.
56.   Kosaki, I., Andreson, H., Mizutani, Y. and Ukai, K., Solid State Ionics, **152-152** (2002) p. 431-438.

57.	Gibson, I.R., Dransfield, G.P. and Irvine, J., Journal European Ceramic Society, **18** (1998) p. 661-667.

58.	Miller, R.A., Smialek, J.L. and Garlik, R.G. in *Science and Technology of Zirconia, Advances in Ceramics*. 1981. Columbus, OH: American Ceramic Society.

59.	West, A.R., *Basic Solid State Chemistry*. 2nd ed. 1999, Chichester: John Wiley & Sons, Ltd.

60.	Singhal, S.C., MRS Bull, **25**(3) (2000) p. 16-21.

61.	Butz, B., Kruse, P., Stoermer, P., Gerthsen, D., Mueller, A., Weber, A. and Ivers-Tiffee, E., Solid State Ionics, **177** (2006) p. 3275-3284.

62.	Badwal, S.P.S., Solid State Ionics, **143** (2001) p. 39-46.

63.	Haering, C., Roosen, A. and H. Schichl, Solid State Ionics, **176** (2005) p. 253-259.

64.	Badwal, S.P.S., Solid State Ionics, **76** (1995) p. 67-80.

65.	Lee, D., Lee, I., Jeon, Y., Song, R., Solid State Ionics, **176** (2005) p. 1021-1025.

66.	Badwal, S.P.S., Ciacchi, F. T. and D. Milosevic, Solid State Ionics, **136-137** (2000) p. 91-99.

67.	Lei, Z. and Zhu, Q., Solid State Ionics, **176** (2005) p. 2791-2797.

68.	Spiridonov, M., Popova, L.N. and Popil'skii, R.Y., Journal Solid State Chemistry, **2** (1970) p. 432.

69.	Irvine, J., Politova, T., Zakowsky, N., Kruth, A., Tao, S., Travis, R. and Attia, O. in *Fuel Cell Technologies: State and Perspectives*. 2005: NATO Science series II : Mathematics, physics & chemistry.

70.	Mizutani, Y., Kawai, M., Nomura, K., Nakamura, Y. in *SOFC VI*. 1999.

71.	Wang, Z., Cheng, M., Bi, Z., Dong, Y., Zhang, H., Zhang, J., Zhaochi, F. and Li, C., Materials Letters, **59** (2005) p. 2579-2582.

72.	Ciacchi, F.T. and Badwal, S.P.S., Journal European Ceramic Society, **7** (1991) p. 197-206.

73.	Nomura, K., Mizutari, Y., Kawai, H., Nakamura, Y., Yamamoto, O., Solid State Ionics, **132** (2000) p. 235-239.

74.	Haering, C., Roosen, A., Schichl, H. and M. Schnoeller, Solid State Ionics, **176** (2005) p. 261-268.

75.	Leoni, M., Jones, R.L. and Scardi, P., Surface & Coatings Technology, **108-109** (1998) p. 107-133.

76.	Ciacchi, F.T., Badwal, S.P.S. and Drennan, J., Journal European Ceramic Society, **7**(3) (1991) p. 185-195.

77.	Jones, R.L. and Derek, M., Surface & Coatings Technology, **86-87** (1996) p. 94-101.

78.	Stafford, R.J., Rothman, S.J. and Routbort, J.L., Solid State Ionics, **37** (1990) p. 67-72.

79.	Ananthapadmanabham, P.V., Venkatramani, N. and Rohatgi, V.K., Journal Ceramic Society, **6** (1990) p. 111-117.

80.	Kimpton, J., Randle, T.H. and Drennan, J., Solid State Ionics, **149** (2002) p. 89-98.

81.	Greenwood, N.N.a.E., A., *Chemistry of the Elements*. 1st ed. 1984, Oxford: Pergamon Press, Ltd.

82. Huang, T., *Materials and catalysis studies for solid oxide fuel cell*, National Tsing Hua University, Taiwan.

83. Richerson, D.W., *Modern Ceramic Engineering: Properties, Processing, and use in Design*. 3rd ed. 2006, Boca Raton: Taylor & Francis Group.

84. McColm, I.J., *Ceramic Science for Materials Technologists*. 1st ed. 1983, Glasgow: Blackie & Son, Ltd.

85. Skinner, S.J. and Kilner, J.A., Materials Today, (2003) p. 30-37.

86. Lybye, D., Poulsen, F.W. and Mogensen, M., Solid State Ionics, **128** (2000) p. 91-103.

87. Kilner, J.A., Brooks, R.J., Solid State Ionics, **6**(3) (1982) p. 253-259.

88. Slater, P.R., Irvine, J., Ishihara, T. and Takita, Y., Solid State Chemistry, **139** (1998) p. 135.

89. Jang, J.H.a.C., G. M., *Partial Electronic Conductivity Of Sr and Mg Doped LaGaO₃*, Department of Materials Science and Engineering, Pohang University of Science and Technology. p. 1.

90. Cho, P.-S., Park, S.-Y.,Cho, Y. H., Kim,S.-J., Kang, Y. C.,Mori, T., Lee, J.-H., Solid State Ionics, **180**(11-13) (2009) p. 788-791.

91. Datta, P., Majewski, P., Aldinger, F., Journal of Alloys and Compounds, **438**(1-2) (2007) p. 232-237.

92. Spacil, H.S., US Patent 3, 360, Editor. 1970: USA.

93. Gorte, R.J., Vohs, J.M. and McIntosch, S., Solid State Ionics, **175** (2004) p. 1-6.

94. http://www-rpl.stanford.edu/research/energy/micro-fuel-cell/sofc/electrode/tpb/. 2007 [cited 2008 August].

95. Tedmon jr., C.S., Spacil, H.S. and Mittoff, S.P., Journal Electrochem Society, **116** (1969) p. 1170.

96. Hassel, B.A., Kawada, T., Sakai, N., Yokokawa, H. and Dokiya, M., Solid State Ionics, **66**(3-4) (1993) p. 295-305.

97. Hassel, B.A., kawada, T., Sakai, N., Yokokawa, H., Dokiya, M., Solid State Ionics, **66**(1-2) (1993) p. 41-48.

98. Yokokawa, H., Horita, T., Sakai, N., Yamaji, K., Brito, M.E., Xiong, Y.-P., Kishimoto, H., Solid State Ionics, **177** (2006) p. 3193-3198.

99. Seo, H.S., Jin, G., Jun, J.H. and Kim, K.Y., Journal of Power Sources, **178** (2008) p. 1-8.

100. Geng, S., Zhu, J., Journal of Power Sources, **160** (2006) p. 1009-1016.

101. Quadakkersa, W.J., Greinerb, H., Htinse M., Pattanaik, A., Khannac, A.S., Mallher, W., Solid State lonics, **91** (1996) p. 55-67.

102. Quadakkersa, W.J., Piron-Abellan, J., Shemet, V., Singheiser, L., Materials at high temperature, **20**(2) (2003) p. 115-127.

103. Quadakkers, W.J., Piron-Abellan, J., Shemet, V., Singheiser, L., Materials at high temperature, **20**(2) (2003) p. 115-127.

104. Sakai, N., Horita, T., Yamaji, K.,Xiong, Y. P., Kishimoto, H., Brito, M.E., Yokokawa, H., Surface & Coatings Technology, **201** (2006) p. 4476-4483.

105. www.Haynesintl.com. 2008 [cited 2008 August].

106. Yang, Z., Xia, G.-G., Maupin, G.D. and W., S.J., Surface & Coatings Technology, **201** (2004) p. 4476-4483.

107. Tiez, F. and Sebold, D., Material Science and Engineering B, **150** (2008) p. 135-140.

108. Zhu, W.Z. and Deevi, S.C., Materials Research Bulletin, **38** (2003) p. 957-972.

109. Batawi, E., Glatz, W., Kraussler, W. and Janousek, M. in *Sixth International Symposium on Solid Oxide Fuel Cells, (SOFC VII)*. 2001. Tsukuba, Ibaraki, Japan.

110. Agullo-Lopez, F., Catlow, C.R.A., Townsend, P.D., *Point defects in materials*. 1988, San Diego: Academic Press Limited.

111. Frade, J.M.R., *Transformacoes e reacoes no estado solido*. 2001: Aveiro.

112. Smart, L.a.M., E., *Solid State Chemistry: An introduction*. 2nd ed, ed. Hall, C.a. 1995, Corwall.

113. Kroger, F.A., *The chemistry of imperfect crystals*. 1974, Amesterdam: North-Holland Publishing company.

114. www.ebah.com.br. 2009 [cited 2009 October].

115. Gao, W., Sammes, N., *An introduction to electronic and ionic materials*. 1999, Singapore: World Scientific.

Chapter II

Experimental

2.1 Powder Production

Research in solid state chemistry focuses upon understanding properties in terms of composition and structure. The final properties strongly depend upon the method chosen. Some methods can start at the level of particles or at the atomic level, for example, if the composition homogeneity has relevance in the final properties, a method that starts at the atomic level should be chosen. The method for the materials preparation should be carefully chosen as well as the quality of the starting materials [1].

2.1.1 Solid State Synthesis Method

Solid State Synthesis (SSS) is the oldest and the simplest method to produce materials; it has been widely used, but recently is being replaced by more sophisticated methods, particularly by wet chemistry routes, which need less time and heating, and can yield better results. Using SSS, the final product may not have high enough homogeneity and/or density; the method is slow due to the powder being mixed at the particles level and not at the atomic level [2, 3].

To produce a compact body by solid state reaction, there must be local matter transport in the crystalline structure; although it does not mean that gaseous or liquid phase may not be involved. This transport of matter depends on the reactivity of the solid and the mobility of the individual particles in the lattice. Ideally, the crystal has an ordered crystalline structure, but in practice the structure has defects.

There are several options to increase the diffusion rate and the reactivity of the individual particles:

- Increase temperature – two thirds of the components melting point is typically suggested

- Decrease the particle size - in order to increase the surface area of the components

- Compact the powders in a pellet body - the pressure used to compact the powders will force the particles to make contact between them, as shown in Figure 2.1 [1-3].
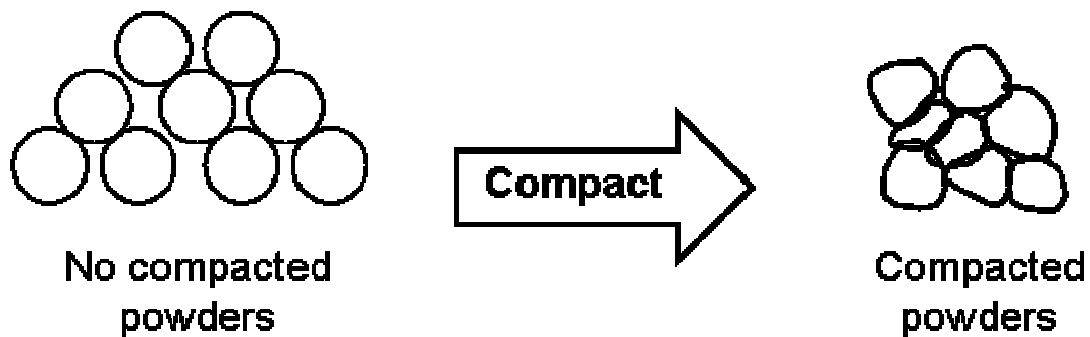

Figure 2.1: Powders forced to have contact with each other

In order to promote contact between powders, a force must be applied. This force will deform powders to increase the superficial area, and therefore has better conditions for sintering.

For the SSS method, the initial powders should be the purest and the simplest oxides and as less impurities as possible should be introduced. Compacting the powders into a pellet shape will not modify on the nature of the powders; it will only join them together.

Figure 2.2 shows the scheme for the solid state synthesis performed for this project.
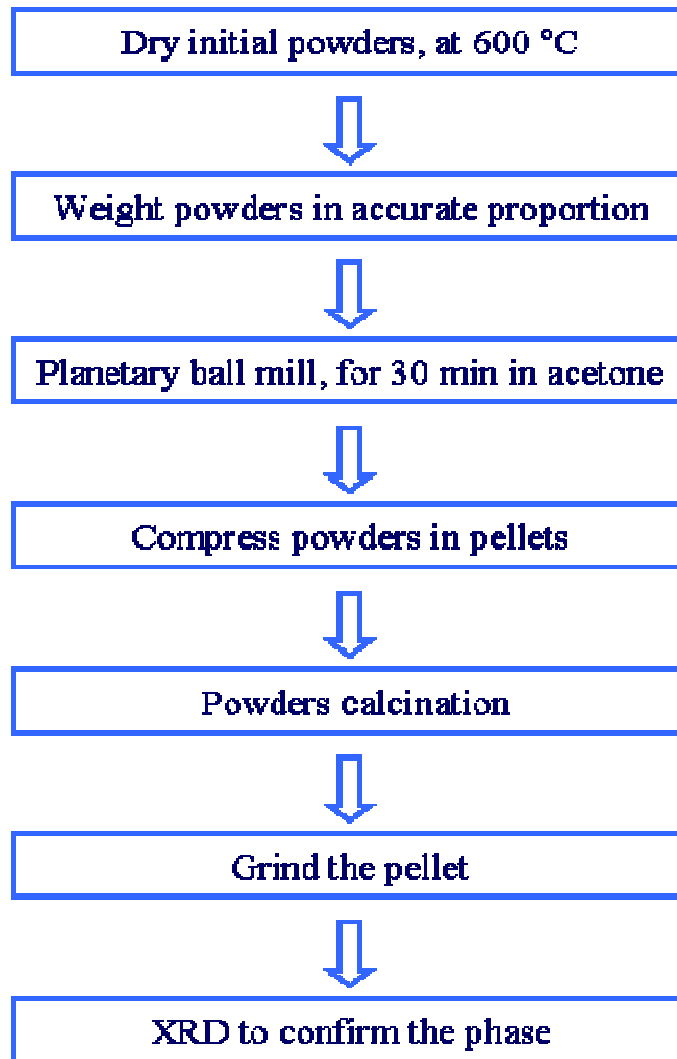
Figure 2.2: Scheme of Solid State Syntheses Method.

The first step is used to remove all the water content that can be trapped in the initial powders. For this the powders are put through a thermal treatment at 600 °C, during 6 hours.

The ball mill stage is introduced to give an intimate mixture of the initial powders, to eliminate aggregates and/or to reduce the particle size. Acetone is used as a solvent in the wet-ball milling. The powders are introduced in a cylindrical container, 12 ml volume, with six balls of alumina, for 30 minutes. The Fritsh planetary micro mill "Pulverisette 7" is the equipment used for this stage.

To promote a better contact between particles, the powder must be compressed in a pellet shape. After that, the pellets are calcined to obtain the desired phase. The pressure and the heat provided will force particles to interact by ion interdiffusion.

After the calcination, the pellets have to be crushed back into powders using a mortar, in order to perform an X-ray diffraction to confirm the phase, as the X-ray machine used is the transmission method.

2.1.2 Sol-Gel Method

Sol-gel method is gaining interest over the last decades due to the final properties of its product. The final product is pure, homogeneous and the process temperature is lower when compared to other processes, such as solid state synthesis or co-precipitation [2].

The sol-gel process is a versatile process to produce ceramic and glass materials. In general, this process involves the transition of a system from a liquid "sol" (mostly colloidal) into a "gel" phase. The oxide net can be obtained by inorganic polymerisation reactions, which occur in solution.

An important characteristic of the sol-gel process is the possibility to control all stages, which occur during the passage through molecular precursor to the final product. A better control of the process can produce materials with specific characteristics and proprieties [4, 5]. The aim is to prepare a homogeneous solution containing all the cationic ingredients. In the first stage the heat will transform the homogeneous solution into a viscous sol, which contains particles of colloidal dimensions. Maintaining the solution heated, it will be finally transformed into a transparent, homogeneous, and amorphous solid called gel. This gel has no precipitation of any crystalline phase. After the formation of the gel, it will be fired at higher temperatures (<1200 °C) to remove the volatile compounds that might be trapped in the gel pores or chemically-bound with organic groups and to crystallise the final product [1, 2, 4].

The chemistry of the sol-gel process is based on hydrolysis and condensation of the molecular precursor. The versatile precursors used in this kind of synthesis are alkoxide metals (metal-organic compounds), $M(OR)_n$ (metal, ethyl, propyl, isopropyl, butyl, tert-

butyl, etc.), e.g. tetraethylorthosilicate (TEOS), $Si(OCH_2CH_3)_4$, as source of SiO_2. These precursors usually are covalent liquids that are mixed in appropriated ratios, often with an alcohol to promote miscibility between the alkoxide and water. Water is the key reagent for the hydrolyses of alkoxides, which usually occurs in the presence of acid or base conditions as a catalyst to accelerate the reaction [6, 7].

The high electronegativity of the group alkoxide (OR) means that the metallic atom is attacked by the nucleophiles. Hydrolysis occurs by the reaction of the alkoxide with the water, producing a hydroxide group M-OH and an alcohol. The second stage of the sol-gel process is the condensation polymerization of M-OH species, making the formation of -M-O-M-, and the elimination of water. After several stages of condensation, the final result is $(M-O)_n$. There have been other studies of producing oxides by sol-gel process, for example, producing SiO_2, TiO_2, SnO_2, V_2O_5, WO_3 [2, 7, 8].

2.1.3 Combustion Method

Combustion synthesis is also known as self propagating high temperature synthesis (SHS) and solid state methathesis (SSM). This method is so fast that the reaction occurs in minutes or even seconds. Once the reaction is initiated, the heat provided is enough to generate high temperature to complete the reaction.

Starting materials for this method are known as "fuel" and "oxidants"; there is a wide range of materials that can be prepared by SHS and SSM methods, such as oxides, nitrides, borides and carbides [2].

2.1.4 Glycine Nitrate Process

The glycine nitrate process is based on the exothermic nature of the redox reaction between the fuel (glycine) and the oxidiser (nitrate).

This process is divided into three stages:

- Dissolution of metal nitrates and glycine in water

- Auto ignition of the solution at temperatures around 180 °C

- Calcination of the end product, after combustion, to burn out the organic material left after combustion

The final product is a clean homogeneous powder of the required stoichiometry [9].

2.1.5 Sol-Gel and Combustion Method

The sol-gel and combustion method is a combination of the traditional sol-gel method and combustion method. In the first part of this method, the solution prepared, called sol, is heated up to form the gel and more heat is supplied in order to induce the combustion. The fuel used in this process is glycine [2, 10-12].

Figure 2.3 is a schematic of all steps of the process used to produce powders. The powders were prepared by a sol-gel and combustion method. Scandia powders (Stanford Materials Corporation, 99.99 % purity) were dissolved in nitric acid (Fisher Scientific, d=1.42, 70 %) and hydrogen peroxide (Fisher Scientific, >30 % wv). The ratio between nitric acid and hydrogen peroxide amount is 4:1. Separately, cerium (IV) nitrate hexahidrate (Aldrich, 99 % purity), yttrium (III) nitrate hexahidrate (Aldrich, 99.9%) and zirconia acetylacetonate (IV) (Aldrich, 98% purity) were dissolved in distilled water. The first solution, scandia in nitric acid, is added to the second solution; after the two solutions were mixed glycine is introduced. The amount of glycine added was twice of the initial molar fraction of the metals. Ammonia is introduced until the pH is approximately 6. When the solution is ready, the temperature was increased until 150 °C and left until the gel is formed. After the gel is formed the temperatures is increased until 270 °C, and wait until the gel burned off.
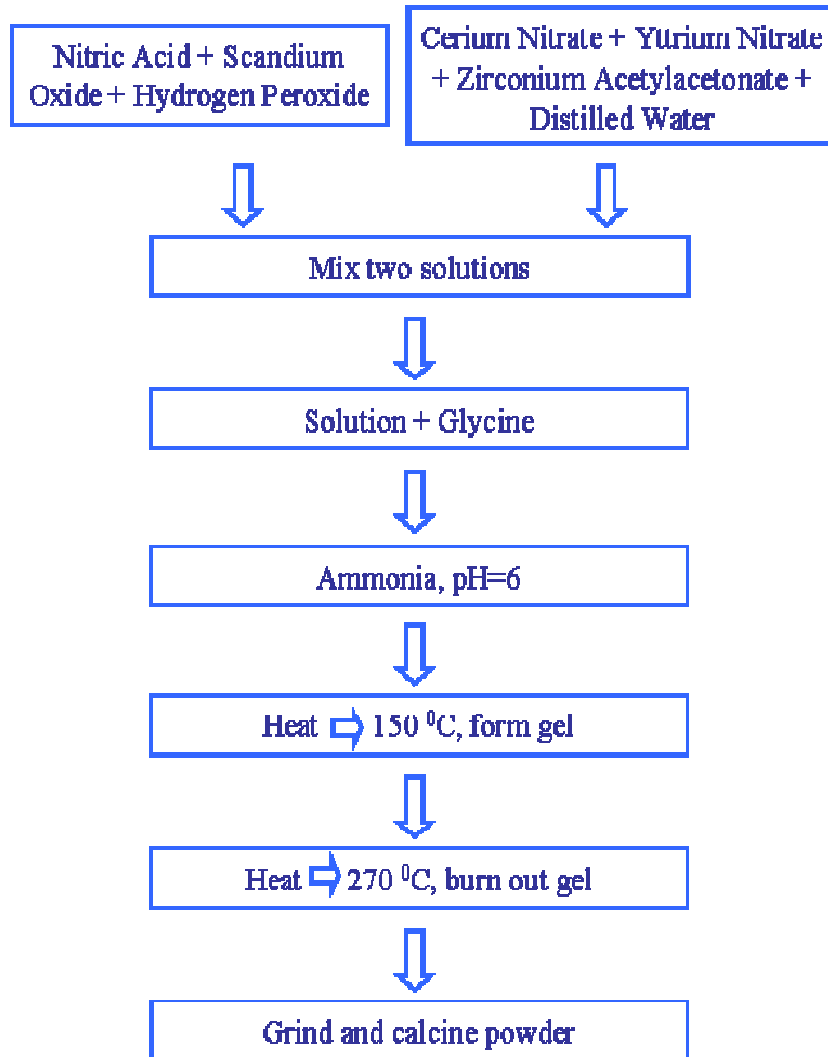
Figure 2.3: Process for producing powders by Sol-Gel and Combustion Method [12]

2.2 Calcination

Calcination uses temperature and time to purify and homogenise powders or pellets. Materials are exposed to high temperature to remove water, to give physical and chemical stability and absorbent properties of the materials [13].

Figure 2.4 shows the scheme of the thermal cycle used by my initial method and on Figure 2.5 shows the scheme of a thermal cycle that replaces the thermal cycle on Figure 2.4. To calcine, the powders are introduced in the furnace at room temperature. Then the temperature is increased by 2 °C/min, until reaching 1000 °C, where a dwell of 20 hours

is performed. After cooling, the powders are ground and introduced again in the furnace. Starting at room temperature, the furnace is heated by 5 °C/min until reaching 1000 °C, at this temperature a dwell of 3 hour is performed. After the dwell, the powders are removed from the furnace and left in air to cool down and are grinded again, as shown on Figure 2.4.
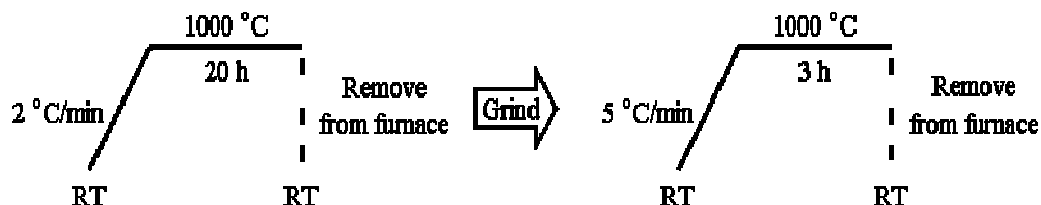
Figure 2.4: Thermal cycle for calcination of my initial method

After the observation of powders at several temperatures calcination, it was decided to calcine the powders with the thermal cycle as shown on Figure 2.5. The powders are introduced in the furnace at room temperature, the temperature is increased until 400 °C with a ramp rate of 0.5 °C/ min, and a dwell of 3 hours is performed. Powders are removed from the furnace at 400 °C, left on air to cool down at room temperature and ground.
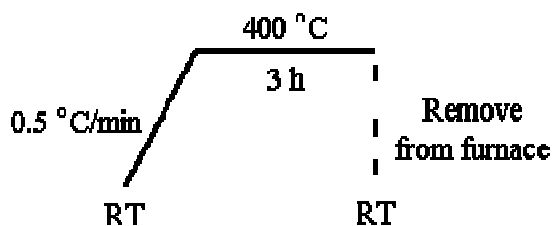
Figure 2.5: Thermal cycle for new calcination

For any of the procedures described above, an X-ray diffraction is performed to confirm that the process produces the material with the desired phase.

2.3 Powder Characterisation

2.3.1 X-ray Diffraction, XRD

The X-ray diffraction technique is versatile, rapid, and sensitive; it has reproducible results and does not destroy the sample. For these reasons X-ray diffraction is considered one of the most important characterisation tools used in solid-state chemistry and materials science. It is used in the characterisation of solid crystalline materials and/or for the determination of their structure [13, 14].

In the middle of the nineteenth century, the discharge of electricity through a gas at low pressures was an interesting area of working for the physicists. In 1859, Plücker showed that the fluorescence gases inside an ampoule, with vacuum, was due to some sort of discharge or radiation; he thought it was coming from the cathode but after more experiments he realised that this discharge was coming from the anode [13, 14].

In 1897, J.J. Thomson deduced that this fluorescence was caused by negative particles travelling at high speed. These negative particles are now called electrons. In 1895, W. Röntgen discovered a type of radiation that he could not fully understand the nature of so he called X-rays [15]. This discovery enabled scientists to investigate crystalline structures at the atomic level as X-ray is an electromagnetic radiation of wavelength between 0.5 and 2.5 Å ($1\text{Å}=1\times10^{-10}$m), which is about the same size as an atom and distance between atoms, and the x-ray photon has a high energy. This radiation occurs in the portion of the electromagnetic spectrum between gamma rays,γ and the ultraviolet, UV, as shown in the spectrum of electromagnetic radiation, Figure 2.6 [16].

Laser Rays	Cosmic Rays	γ-Rays	X-Rays	UV	Visible	IR

0.1 Å   100 Å   4000 Å   7500 Å

λ
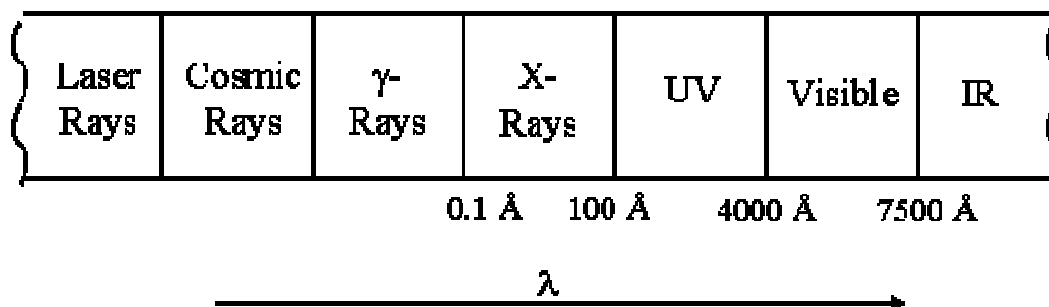
Figure 2.6: Spectrum of electromagnetic radiations and wavelength

The X-ray diffraction technique is used to investigate the structure of matter at the atomic level. Every crystalline material has its unique diffraction pattern and the result is a "fingerprint" of its atomic and molecular structure. The position and intensity of each peak is unique for each material and is the basic information required in a crystal structure analysis [2, 13, 16-19].

Applications:

- To investigate how atoms and molecules are arranged in a sub-microscopic structure. Giving some examples of areas where this can be useful and their immediate application. For physicists, they study the structure of liquids; for Material Scientists, they study the orientation of polymer molecules, in fibres and films and; in biology it can be applied to determine the arrangement of molecules in such complicated and diverse systems such as muscles, viruses and cell membranes.

- Can be used in a simple and rapid method of identification of unknown compounds and their lattice parameters. To identify new compounds, this is done by comparison. After the acquisition of the X-ray diffraction pattern of the new compound, it will be compared with X-ray diffraction patterns in database.

- It can be used to measure size distribution, crystal grain size, internal elastic strains and extended defects [13, 18-21].

Production of X-rays

The production of X-rays must be performed in vacuum, it is necessary to apply a difference of potential, of tens to hundreds kV, between cathode and a metallic target that works as an anode. Copper and molybdenum are the materials used for the target. When the cathode filament of tungsten is hot, it frees electrons by thermo ionic effect; they are accelerated through vacuum due to the difference of potential between cathode and anode. Before colliding with the metallic target, the electron has high kinetic energy; during this collision it will displace one electron in the internal layers of the atom close

to the nuclei, ionising the atom. When an atom of the internal layer is ionised, an electron of the external layer will be dislocated to the internal layer, causing the emission of X-ray radiation characteristic of this atom [13, 14, 16].

In X-ray diffraction, two collecting data methods can be used, either by reflection or transmission diffraction. The main differences between these methods are the beam collector position, in relation to the sample position and the thickness of the sample. In the reflection method, the incident beam will penetrate the top layers of the sample, being reflected towards the collector. The incident angle varies in order to sweep all possible angles to obtain constructive interference. For the transmission method, the beam passes through the sample. Samples of different thickness have to be used in the two different methods: in the reflection cases the sample has to be thick enough so the incident beam can only penetrate the top sample layer without reaching the sample support; in the transmission method, the sample has to be thin enough the incident beam can pass trough the sample [2, 16].

Law of Bragg

The law of Bragg refers to the simple equation derived by the English physicists Sir W.H. Bragg and his son Sir W.L. Bragg, in 1913, to explain why the cleavage faces of crystals appear to reflect x-ray beams at certain angles of incidence (theta, θ). Although Bragg's law was used to explain the interference pattern of X-rays scattered by crystals, diffraction has been developed to study the structure of all states of matter with any beam, e.g., ions, electrons, neutrons, and protons, with a wavelength similar to the distance between the atomic or molecular structures of interest [22].

The beam propagation occurs in different directions due to the symmetry of the crystal lattice and by diffraction, leading to an intensity pattern, which can be interpreted according to the atom distribution in the crystal, applying the law of Bragg, as shown in Figure 2.7.
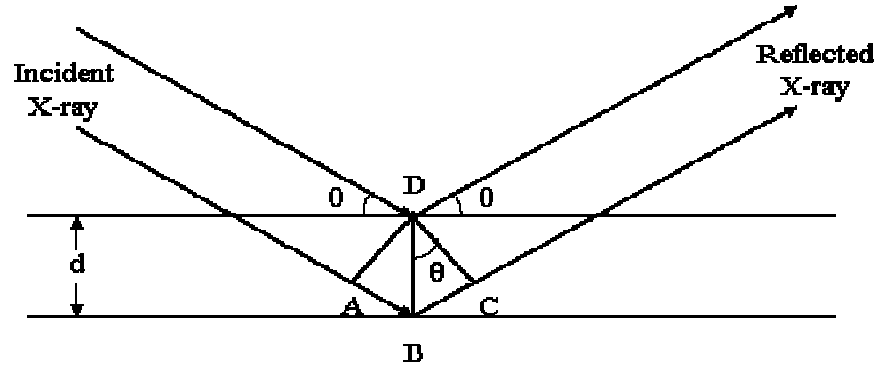
Figure 2.7: Reflection of X-rays from two lattice planes belonging to the family H=(h, k, l) is interplanar spacing

The variable d is the distance between atomic layers in a crystal, and the variable lambda λ is the wavelength of the incident x-ray beam; n is an integer.

The wavelength, λ, of the X-ray is approximately the distance between atomic planes of a crystal. When an X-ray beam collides with an array of planes, two possible results can occur, as described below:

- If the wave reflected by the plans is in phase, meaning the distance, d, is equal to the wavelength. A reinforcement of the beam will happen and will produce radiation peaks of different intensities - constructive interference. As shown in Figure 2.8.
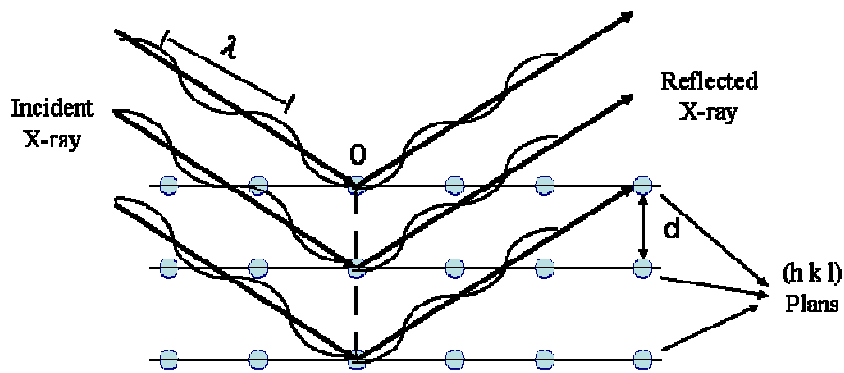
Figure 2.8: Schematic of incident and reflected X-ray beam – constructive interference

- If the wave reflected by the planes is in opposite phase, it will cancel and gives zero intensity peaks - destructive interference. As shown in Figure 2.9.
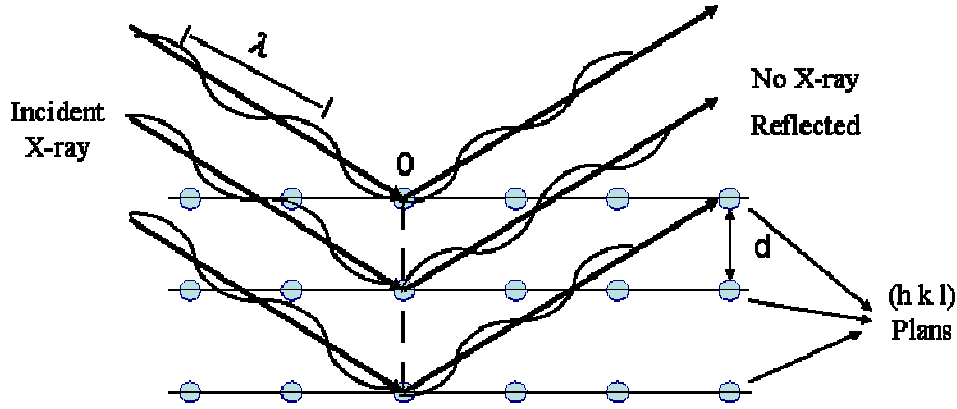
Figure 2.9: Schematic of incident and reflected X-ray beam – destructive interference

Bragg Equation

The Bragg's Law is derived using the reflection geometry and applying trigonometry. The lower beam must travel the extra distance (AB + BC) to continue traveling parallel and adjacent to the top beam. Consider Figure 2.9, beam 1 and 2. For these beams to be in phase, the additional distance that beam 2 has to travel, which is equal to AB+BC, has to be equal to a integer number of the wavelength, $n\lambda$,

$$n\lambda = AB + BC \qquad (2.1)$$

Where,

$n = 1, 2, 3, ... \rightarrow$ Order of diffraction.

Since

$$AB = BC = d_{hkl} \times \sin\theta \qquad (2.2)$$

$$AB = BC = 2AB$$

Where,

$d_{hkl} \rightarrow$ Distance between planes, of the planes (h k l)

$$n\lambda = 2d_{hkl} \times sin\,\theta \qquad\qquad (2.3)$$

Equation (2.3) is called Bragg equation, which relates diffraction in terms of reflection of crystal lattice planes [16, 20, 21].

Miller indices of crystallographic planes in cubic cells, d_{hkl}

Crystal and crystal faces can have variable size and shape, but the angles between faces are constant for a given element. The size and face location is less important when compared to the relative face orientation, which can be used to calculate the crystalline system and symmetry.

The procedure to assign the Miller indices is a straightforward one. For this project a cubic crystal system will be considered; where a cubic unit cell has the dimensions $a \times a \times a$, as shown in Figure 2.10, with a equals to the lattice parameter [16, 20, 23].
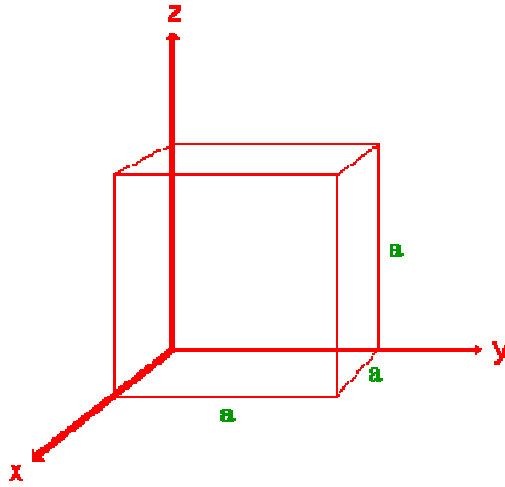
Figure 2.10: Identification of the lattice parameter [23, 24]

The best way to explain this procedure is by illustrating an example, as follow. A surface/plane will be first considered as shown in Figure 2.11.
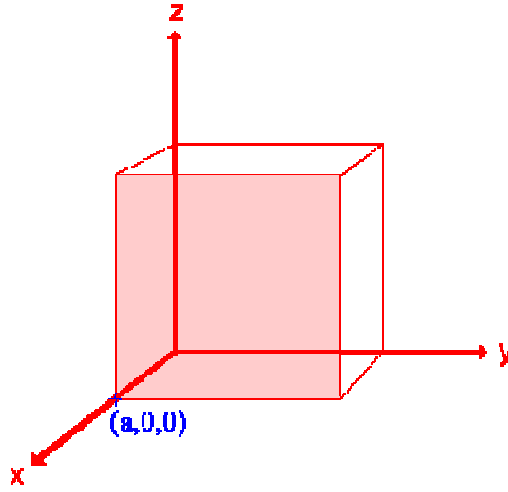
Figure 2.11: Identification of intercepts on the x-, y- and z-axes [23, 24]

In this case the x-axis is intercepted in x equals a, at the point (a,0,0), but the plane is parallel to the y- and z-axes. As the last two axes do not intercept, it will be consider that the interception to be at the infinity (∞). The intercepts on the x-, y- and x-axes are thus intercepts: a, ∞, ∞.

The coordinates have to be converted to a fractional coordinates to obtain the inverse of the interception, in this case , the point (a,0,0) in a unit cell of dimentions a×a×a, the fractional coordinates are $\left(\frac{a}{a},\frac{\infty}{a},\frac{\infty}{a}\right)=(1,0,0)$.

To obtain the Miller indices, the reciprocals of the fractional intercepts should be taken. By convention, the Miller indices should be presented without being separated by any commas, enclosed in standard brackets. In this case, the reciprocal of 1 and ∞ are 1 and 0, respectively; therefore the Miller indices (100) plane of the cubic crystal.

Next, two examples for the Miller indices will be shown in Figure 2.12 and 2.13., plane (110) and (111), respectively [16, 20, 25].
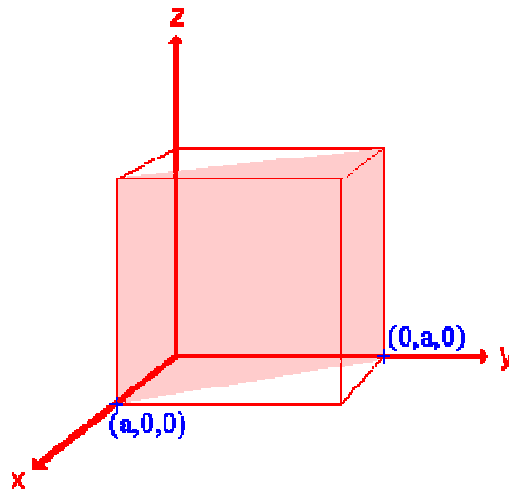
Figure 2.12: Plane (110) [23, 24]

In Figure 2.12, the plane intercepts are a,a,∞; the fractional intercepts are 1,1,∞, therefore the Miller indices are (110).
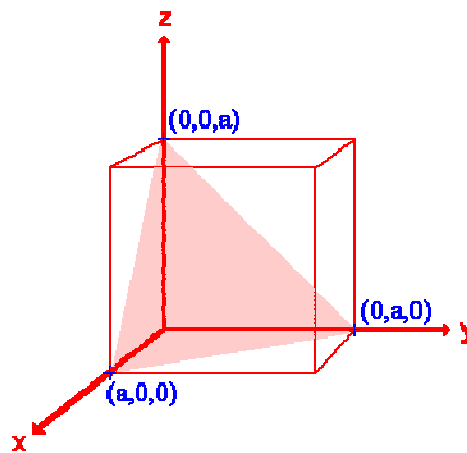
Figure 2.13: Plane (111) [23, 24]

In Figure 2.13, the plane intercepts are a,a,a, the fractional intercepts are 1,1,1, therefore the Miller indices:(111).

The (100), (110) and (111) planes are considered low index planes of a cubic crystal system, as the numbers used being 0 or 1. These planes have a particular relevance, but there are a large number of other planes which can be defined by the Miller indices notation [2, 16, 20, 23-25].

Debye Equation

The polycrystalline or "powder" X-ray diffraction technique was developed by Debye and Scherrer, and independently by Hull in the period of 1914-1919. Their technique is classified as "fixed λ, varying θ" in which the oriented crystals in the specimen such that some of the hkl planes in some of them will be orientated, by chance, at the appropriate Bragg angles for reflection. All the planes at given d_{hkl}-spacing reflect at the same 2θ angle to the direct beam and all these reflected beams lie on a cone of semi-angle 2θ about the direct beam [20, 21].

The Debye scattering equation is applied to different types of powder diffraction data, with or without three-dimensional ordering, such as liquids, amorphous or crystalline solids, and any intermediate stage.

$$f(s) = \sum_m \sum_n \frac{f_m f_n (\sin(\theta) 2\pi s r_{mn}}{2\pi s r_{mn}} \qquad (2.4)$$

Where,

$s = \dfrac{2\sin(\theta)}{\lambda}$, and r_{mn} is the magnitude of the distances of each atom from other atom with f_m and f_n scattering factor.

In 1918, Scherrer stabilised his famous relation giving mean crystallite size from the X-ray line profile width. In that sense "crystallite" is equivalent to "homogeneous domain giving rise to coherent diffraction", so that it is supposed that there is no complete break in the three-dimensional order inside of it, though there could be some limited distortion.

Bertaut demonstrated in 1949, the important result that the size distribution can be estimated by Fourier analysis of the diffraction line profile. The Bragg law ($\lambda = 2d_{hkl}\sin(\theta)$) expresses the ideal geometrical conditions of diffraction, it implies that the crystal dimensions can be considered as infinite compared to the distance between two diffraction centres, otherwise a size effect broadens the Bragg peaks. To characterise the peak broadening, several parameters are useful:

- The half width, ω, introduced by Scherrer corresponding to the angular range in which the intensity is larger or equal to half maximum intensity (now designed as the FWHM, full width at half maximum) A size parameter, ε_ω,

$$\varepsilon_\omega = \frac{K_\omega \lambda}{\omega \cos(\theta)} \qquad (2.5)$$

Where,

$\varepsilon_\omega \rightarrow$ Size parameter

$K_\omega \rightarrow$ Scherrer constant, $0.89 \leq K_\omega \leq 1$

$\lambda \rightarrow$ X-ray wavelength, Å

$\omega \rightarrow$ Peak width, in radians [19, 20]

In this project powder was characterized in two different types of X-ray diffractometer, by reflection and transmission method. When powder was analysed by reflection, the Philips X-ray difractometer is a Philips PW1710 reflector with fixed omega (20-90° 2θ, step size 0.02° 2θ, Cu Kα radiation) was used, and in case of transmission method, the STOE Transmission Powder Difractometer System Stadi P (20-90° 2θ, step size 0.02° 2θ, Cu Kα radiation and germanium monochrometer) was used.

In both cases, a Stoe software program was used to determine crystalline structure and unit cell parameters.

2.3.2 Particle Size Analyser, PSA

A particle size analysis is a quantitative measurement of the distribution of size of the powder. This is a simple, fast, flexible technique, and produces high quality data [26].

Particle size distribution has an important role to the compaction and sintering processes. The way particles are arranged during compaction can create irregularities in the final sintered product. Ideally, particles should be monosized and spherical, packed in a perfectly ordered structure, although this is difficult to create in reality. Usually particles have a range of sizes and can have different shapes. When packing a wide range of particle sizes, the large particles will control the packing process while smaller particles will fill the voids. These smaller particles will give a well sintered region surrounded by large pores [27, 28].

Particle sizes are measured in suspension by laser diffraction. The technique uses the scattering of light, delivered by a laser, which is passed through a chamber containing the particles in suspension. The scattered light is detected by a photo detector array. The intensity of light on each detector is then converted into particle size distribution plots calculated by a mathematical algorithm. In some cases, the algorithm can introduce some errors due to the assumption that the particle shape is regular when in reality this is not true [29].

Describing a three-dimensional (3-D) particle is a complex process; the analyser captures a 2-dimensional (2-D) image of a particle (3-D particle), from the image captured it is estimated the principle diameter and calculates is Circle Equivalent diameter (CE Diameter). This CE diameter is the diameter of a circle with the same area as the 2-D image of the particle, Figure 2.14. In this method, the analyser assumes that particles are a circle. This will introduce an error particularly when particles have an irregular shape [29, 30].
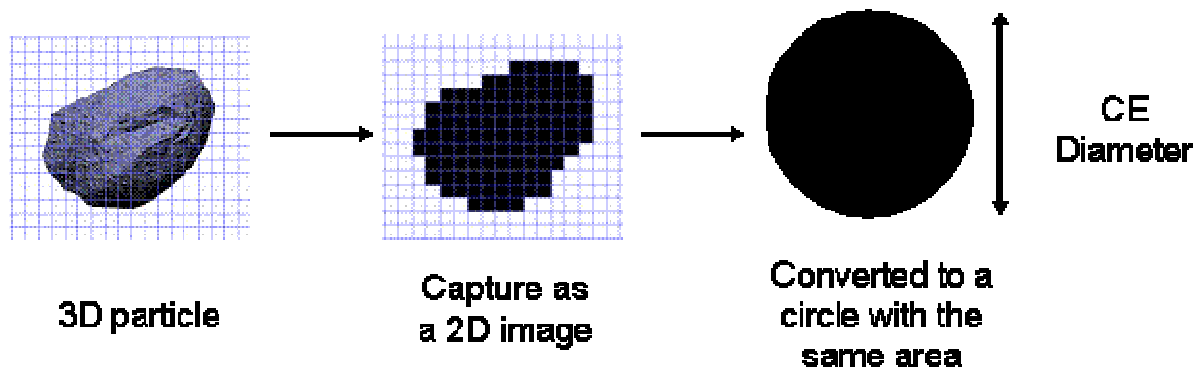
Figure 2.14: How to calculate the CD Diameter [29]

For characterisation of the powder a particle size distribution was made at the EEA, Earth and Environmental Analysis in the Geosciences section at the Department of Geography, University of St. Andrews. The EEA facilities have a Coulter LS230 instrument, which measures particle size distributions in granular natural and synthetic samples by diffraction. Laser particle size analysis is based on the principle that particles scatter and diffract light at certain angles based on their size, shape, and optical properties. A 750 nm diode laser is used for analysis in the size range from 0.375 μm to 2000 μm. The beam passes through filters as well as the projection and Fourier lenses and is spatially recorded onto 126 photodiode detectors [30].

To measure the particle size three cycles are performed inside of the equipment. For the first measurement, particles just pass in front of the laser light; while in the second measurement the equipment applies a weak ultrasonic, in order to separate soft particle agglomerates, before the powder passes a second time in front of the laser light, and finally, in the last measurement, particles pass in front of the laser light, as shown in Figure 2.15.
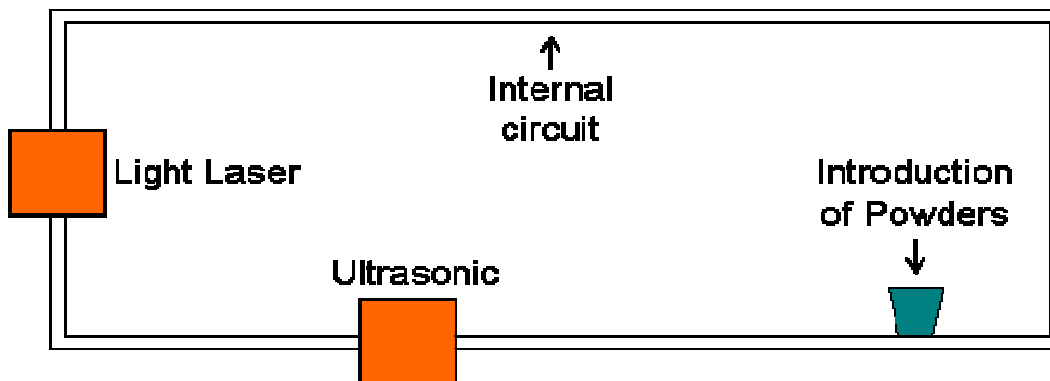
Figure 2.15: Scheme of the internal circuit of the particle size analyser

2.3.3 Electron Microscopy

Electron microscopy is a powerful and versatile tool to give information of materials microstructure. This technique is widely used to supply information on particle size, and shape of powders and also can observe fully or partially dense bodies to study porosity, and microstructure [2, 28].

Scanning Electron Microscopy (SEM)

A SEM picture shows the surface of materials; morphology and topography. In topography, some aspects can be observed, such as micro-texture, fracture and wearing of materials. The information obtained on powder morphology can be size and shape of the powders and confirmation of the existence of agglomerates and their nature (hard and soft). The main advantage of a SEM picture is the high quality 3-D image that can be obtained [26, 31].

The SEM working principle is based on the emission of an electron beam by a tungsten filament when a difference in potential, which can vary from 5 and 30 kV, is applied. This voltage allows the acceleration of the electrons and induces the filament to heat up.
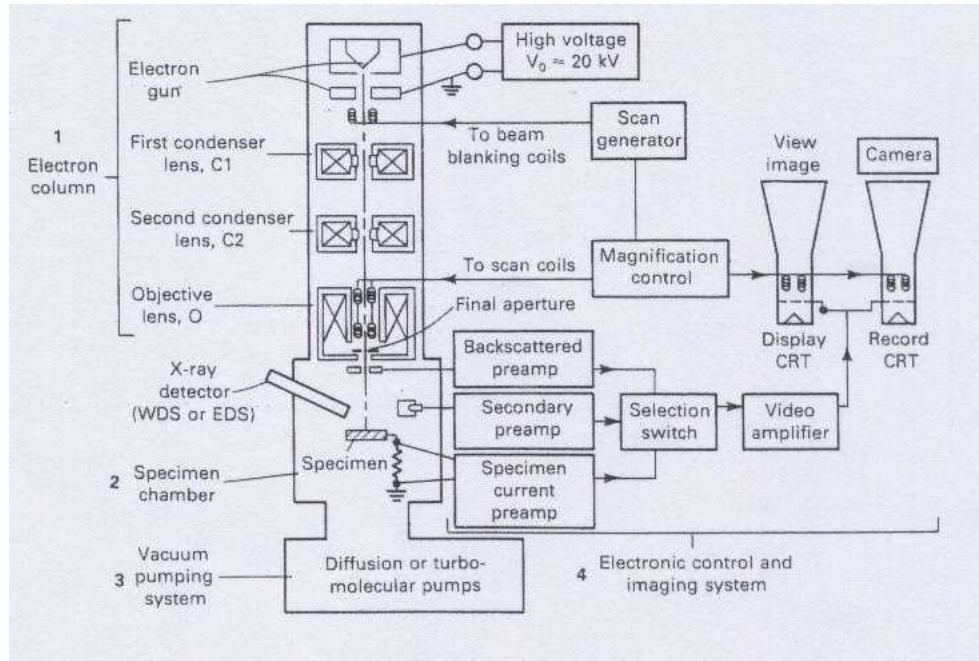
Figure 2.16: Schematic of basic components of the scanning electron microscope [17].

Figure 2.16 shows the basic components of scanning electron microscope. Different components of the microscope are divided in four different areas.

- Electron column

- The specimen chamber

- The vacuum pumping system

- The electronic control and imaging system

Vacuum Pumping System

The column and the specimen chamber must always operate under vacuum conditions, otherwise the electron beam would be scattered by the gas atoms. A system of valves must be introduced in order to allow the continuation of an active electron beam even when the specimen is changed or introduced in the specimen chamber[17, 26].

Electron gun

It is in the electron gun where a beam of electrons is produced and is directed down to the column centreline. Figure 2.17 show a conventional tungsten gun. The tungsten filament is heated up to approximately 2500 ℃ and the electron source is a 0.25 nm, in diameter. The heat results in an incandescent filament with a bent tip, thermionic emission, where the electrons are expelled towards the anode. This anode is kept at a voltage ranging from 5 kV to 30 kV, defined by the operator.

The Wehnelt cylinder bent negatively relative to the filament, it functions as a grid that repels the emitted electrons and focuses them into a spot of diameter, d_0 and divergence half angle, α_0 [17, 26].
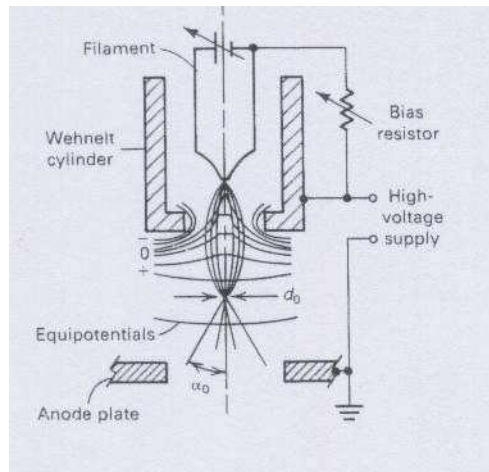
Figure 2.17: Schematic of a conventional tungsten hairpin filament electron gun [17].

Lenses

The function of a lens in the SEM is to converge the electron beam diameter to concentrate it on the sample surface. Electron microscopes have magnetic lenses, consisting in a simple solenoid coils. In Figure 2.16, the X represents a cooper coil wire shaped by the iron fixture giving the geometry which produces the lens effect.

Scan coils and raster formation

The SEM electron beam scans the sample surface. The two sets of scan coils, located in the bore of the objective lens cage, as shown in Figure 2.16, perform the scanning function. These coils lead the beam to scan over a square area on the sample surface.

Detector and image formation

On a conventional SEM there are four detectors which use specimen current, secondary electrons, backscattered electrons and X-ray signals. The secondary electron detectors usually are used for image formation in the SEM [17, 26, 32].
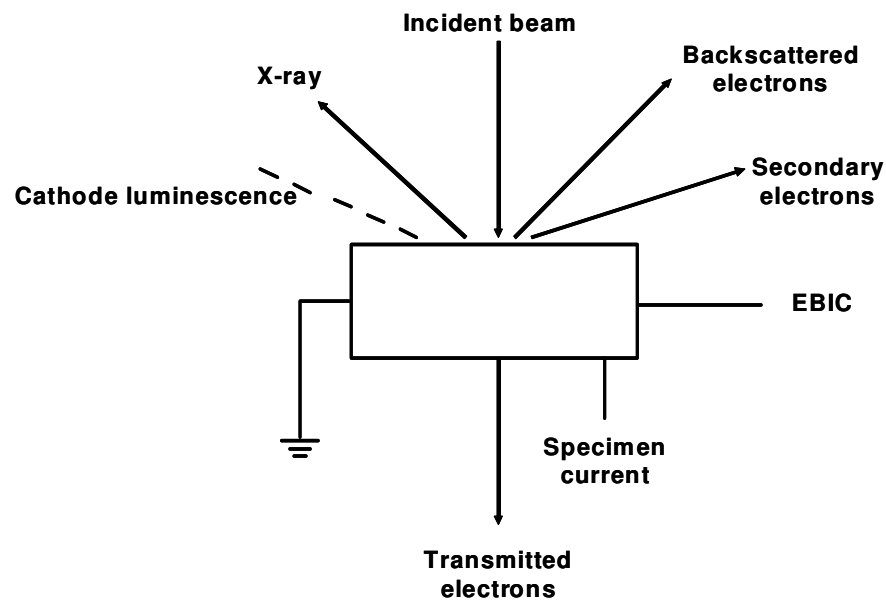
Figure 2.18: Signals which may be used to build a SEM picture

A SEM image is built from an electronic signal returned to its detectors by the sample. The signal returned by the sample includes, as shown in Figure 2.18:

- Backscattered reflected electrons; primary electrons that still have high incident energy.

- Secondary ejected electrons, electrons that are ejected by the specimen in inelastic collisions.

- X-ray [26, 31, 32].

Sample preparation

To prepare pellets to be observed in SEM, they have to be cut following the diameter, to verify microstructure, densification, porosity and grain boundaries. The two halves of pellets are sandpapered and polished, as shown in Table 2.1 and Table 2.2.

Table 2.1: Time and SiC size used on pellets to be observed in the SEM

SiC size	Time, min
600	10
1200	12

Table 2.2: Time and diamond size used on pellets to be observe in the SEM

Diamond size, μm	Time, min
6	10
3	6
1	3

An etching cycle is required to reveal the grain boundaries of the material. Pellets are introduced in the furnace at 1000 °C, the temperature is increased at 10 °C/min until 1250 °C, held for of 3 hours, decrease the temperature until 1000 °C. Remove the pellets and leave cooling in air. Sputtering gold is the last stage of the procedure, when a layer of gold is laid on the surface of the ceramic materials, to provide the electric conductivity.

Powders and sintered samples are analysed in JEOL JSM-5600 scanning electron microscope. The voltage used is from 5 to 20 kV.

Transmission Electron Microscopy (TEM)

A TEM picture provides information about the internal structure of thin specimens, it is used not only because it gives more details than the SEM, but it shows structure itself:

The size, shape and arrangement of the particles, as well as the interaction between them on the scale of atomic diameters [2, 32, 33].

A chemical analysis of the sample composition is a technique that can be performed in SEM and TEM instruments. This technique has become an important tool for characterisation of materials due to the possibility of analysing the chemical composition of a material at the atomic level. There are three instruments able to perform this technique: a SEM with X-ray detector (AEM), the electron probe micro analyser (EPMA) and transmission electron microscope (TEM and STEM, scanning transmission electron microscope) fitted with an X-ray detector.

This technique is performed locally; this means that only in a small region of the sample is going to be characterised. When a sample is bombarded with high energy electrons, it will generate different types of emissions and among them also X-ray. X-ray emits in wavelength dependent on the nature of the atoms of the specimens. There are two types of information that can be collected:

- Qualitative analysis, all wavelengths (or energies) have a characteristic amount of energy that is associated to each element

- Quantitative analysis or how many X-rays are emitted per second, which provides information of how much of the element is present in that region of the material [2, 32]

2.3.4 Milling

Milling is a process used in several industries, such as ceramic, mining, chemical and food industry. The main purpose of milling is to reduce the particle size using mechanical forces, however there are other purposes, such as mixing and to homogenise the different components, to control the kinetics of reactions and to help the densification.

There are different types of mechanical fragmentation processes:

- Crushing

- Impact (collision between particles and milling media)

- Attrition

- Cut (shear forces)

To choose the right type of milling the nature of the material should be considered, e.g. if it is a hard or soft material and, also the type of the reduction, mill to fine powders or coarse milling.

For fine milling the machines in use are:

- Roller Mill

- Planetary ball mill

- Hammer

In this project, two different types of ball mill are used. The planetary ball mill and the roller ball mill. The planetary ball mill is more violent than the roller ball mill. If these particles or agglomerates are a soft material, then it is necessary to use the roller ball mill, but if, the agglomerates are a brittle/hard material, it is necessary to use the planetary ball mill.

In this project, the planetary ball mill is a Fritsh planetary micro mill "Pulverisette 7". The container used has a capacity of 12 ml each, and used six zirconia balls. The Roller ball mill is a home made machine, as shown in Figure 2.19.

Figure 2.19: The Roller Ball Mill, with two containers of material

2.4 Powder Compaction

This stage is very important as it is the first stage to give a final density. Powders do not fill effectively the space in a compact body. For example, monosized and spherical particles will give approximately 60 % of initial density. Compacting powders in rigid dies may lead to anisotropic green densities, with gradients in both axial and radial directions.

For the compaction of the powders, a cylindrical steel die of 13 mm diameter is used. The powders are pressed uniaxially into pellets under 75.3×10^6 Pa and pressed isostatically at 2×10^8 Pa.

Isostatic pressure works on a simple principle: compressing a liquid or a gas, in order to obtain equal pressure from all directions. There are two possibilities to increase the pressure: decrease the volume of the chamber or increase the amount of liquid or gas

inside the chamber. The pressurisation medium used is N-Hexane 95 %, GR, density 0.658.

2.5 Thermal Analysis

Thermal analysis is a group of techniques that record data when a sample is subjected to heating or cooling at a controlled rate, the results can present qualitative and quantitative analytical information. For better results, some techniques can be combined, e.g. Thermo-gravimetric, TG with Differential Scanning Calorimeter, DSC or Differential Thermal Analysis, DTA [2, 28, 34, 35].

Enthalpy, heat capacity, mass variation and coefficient of thermal expansion are some of the parameters obtained in these techniques. When these techniques are applied to solid state science, it will provide information on:

- Thermal composition

- Phase transition

- Determination of phase diagram [2]

Thermo-Gravimetric Analysis (TGA)

This method uses the change in the sample mass as a function of temperature, and can provide qualitative and quantitative analysis. A curve provides information concerning the thermal stability and composition of the initial sample, as well as the thermal stability and composition of any intermediate compounds that can be formed during the process.

A sensitive balance is used to accurately weight the variation of the sample mass. A controlled atmosphere can be used.

In this project, powders were used, to perform TGA measurements, powder is used, the temperature is increased from 25 to 1000 °C by 2 °C/min ramp rate, left for 1 hour at 1000 °C, and finally the temperature was decreased to 25 °C by 2 °C/ min.

Differential Scanning Calorimeter (DSC)

DSC is a method that uses the difference in energy provided to the sample and to the reference. In DSC experiment, the sample and the reference, usually alumina, are heated in separate chambers, the temperature difference between the sample and the reference must be zero, and the power supplied to maintain both at the same temperature is measured. The difference in power supplied to the two heaters is monitored as the analytical signal (ΔE). This experiment can be performed in different atmospheres [35].

The experiment is performed in a NETZSCH DSC 404C Pegasus and measurement are performed in powders, the temperature is increased from 25 to 1000 °C by 2 °C/min ramp rate, left for 1 hour at 1000 °C, finally the temperature is decreased until 25 °C by 2 °C/ min.

Dilatometry

Dilatometry uses the change in volume of the sample as it is heated or cooled at a fixed ramp rate under negligible mechanical load. These measurements can be performed under several atmospheres. Data generated from this method provides a trace in the form of dimensions vs. time vs. temperature.

Samples must have the shape of a pellet, which is placed between alumina pellets. Pressure is provided by a piston, which has a pressure sensor to measure the variation of the length, a thermocouple is placed close to the sample to measure the temperature.

For the dilatometry, pellets are prepared and the dimensions used were 9 mm of diameter and a thickness between 3mm and 5 mm. The dilatometry has the following parameters: a ramp rate of 5 °C/min, from 25 °C to 1450 °C, a dwell of 3 hours and a ramp rate of 5 °C/min, from 1000 °C to 25 °C. The gas used for all experiments was air. All experiments were performed in a NETZSCH, DIL 402C.

2.6 Sintering

Sintering is a thermal treatment that transforms a compact agglomerate of particles into a more or less dense material. It takes place at high temperatures, involves mass transport events at atomic level, and gradual porosity elimination that initially was occupied by inter-particle spaces. The process leads to an increase in strength but reduces the surface energy of the system.

Compact body
⇓
Heat at high temperatures
⇓
Time to consolidate into a sole mass
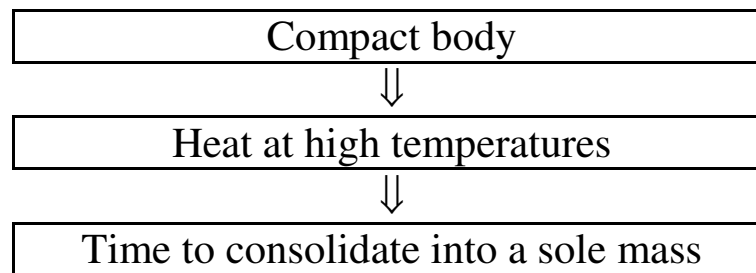
To achieve a compact body, there are several possibilities, such as dry pressing, isostactic pressing, extrusion, tape-casting and screen printing.

To achieve a full dense body, usually it must pass through four stages:

- Adhesion

- Initial

- Intermediate

- Final

In the adhesion stage, the compact is produced. Here either, there is no loss of surface area, or there is a minimal loss of surface area in case of using high pressures.

In the initial stage, the neck growth starts, and is here that the surface area has a great loss, up to 50 %. The microstructure has a change mainly resulting from the surface diffusion of ions from the convex surfaces, where the energy is higher, to the concavities where the particles are in contact, where the energy is lower. Densification is not significant at the beginning but becomes more significant in end of this stage. For

densification to occur, it is necessary to have mass transport from the pore. This process usually happens by vacancy diffusion from regions close to the pore surface, where the vacancy concentration is higher compared to the concentration of the bulk, to the grain boundaries which act as vacancy sink. At the intermediate stage, the pore starts to become round and elongates, and the total loss of the difference in the surface area will occur. Here the pores are open; it is only in the final stage where the pores close and they are no longer connected to the compact surface. Here the close pores have the final shape and if there is any gas inside these closed pores, it will be very difficult to remove. In the final stage there is a rapid growth of the grain boundary as the open pores are the only effective barrier to the grain boundary growth.

Sintering is a process of microstructure change which involves contributions from two sub processes:

- Densification: replacement of free surface energy by grain boundary energy

- Coarsening: reduction of extent of free surface or grain boundary energy

The relative contributions of the two sub-processes depend on the processing variables, i.e. temperature of sintering, time of sintering, composition, and shape and particle size [28].

Several trial experiments were performed to assess the best temperature and time of sintering, as shown in Table 2.3.

Table 2.3: Temperature and times of sintering

Temperature, °C	Time, hours
1400	2, 5, 12, 24
1500	2, 5, 10

The highest density, from this group, is obtained at 1500 °C, for 12 hours. The sintering cycle chosen to be used during this project is at 1500 °C, for 12 hours.

2.7 Density Measurements

Geometrical

The density is calculated by comparison with the theoretical density, which is calculated by XRD data (cell volume).

The theoretical density for each composition is obtained with equation (2.6)

$$D_T = \frac{Mr}{V_{cell} \times N_A} \qquad (2.6)$$

Where:

$D_T \rightarrow$ Theoretical density, g/molÅ^3

$Mr \rightarrow$ Molecular number of the composition, g

$N_A \rightarrow$ Avogadro number $= 6.023 \times 10^{23}$, mol

$V_{Cell} \rightarrow$ Volume of a unit cell, Å^3

The relative density can be calculated with equation (2.7), if the pellet dimensions, diameter and thickness, are known.

$$V_{Pellet} = \pi \times \left(\frac{\emptyset}{2} \right)^2 * h \qquad (2.7)$$

Where:

$V_{Pellet} \rightarrow$ Volume of the pellet, cm^3

$\emptyset \rightarrow$ Diameter of the pellet, cm

$h \rightarrow$ Thickness of the pellet, cm

The density of the pellet can be obtained with equation (2.8)

$$D_{Pellet} = \frac{m_{Pellet}}{V_{Pellet}} \qquad (2.8)$$

Where:

D_{Pellet} $\rightarrow$ Geometric density of the pellet, g/cm

m_{Pellet} $\rightarrow$ Mass of the pellet, g

The final density, D_{Final}, is obtained by the ratio between the geometry of the pellet and the theoretical density, as shown in the equation (2.9)

$$D_{Final} = \frac{D_{Pellet}}{D_T} \times 100 \qquad (2.9)$$

Where:

D_{Final} $\rightarrow$ Density compared with theoretical density, %

2.8 AC Impedance Measurements

2.8.1 Introduction

Electrochemical Impedance Spectroscopy (EIS) is a valuable and powerful technique to study different electrical processes that take place in materials. This technique can be applied to study the properties of:

- Corrosion on materials

- Electrode kinetics

- Membranes (electrolytes)

- Conducting polymers

- Semiconductors

- Surface treatments

- Batteries

- Fuel cells [36, 37]

Interfaces are extremely important in the study of materials, as it is here where physical properties, such as crystallography, mechanical, compositional and electrical, reveal changes when a perturbation is applied. Polarization will change or rearrange the total conductivity of the system.

All interfaces have a particular way to polarise, when a perturbation is applied to the system. For different processes, electrochemical and electric, it will have different responses to the polarisation.

In a simple and general approach of this technique, an electrical stimulus is applied (a known voltage or current) to the sample to be analysed and a response will be observed (the resulting voltage or current measured as function of the frequency). Different atmospheres, such as argon, hydrogen or an oxidising atmosphere are very often used.

2.8.2 Fundamentals

The only information that can be taken by an AC impedance plot is the resistance (impedance). AC impedance data can be presented in a complex plane plot, Figure 2.20.
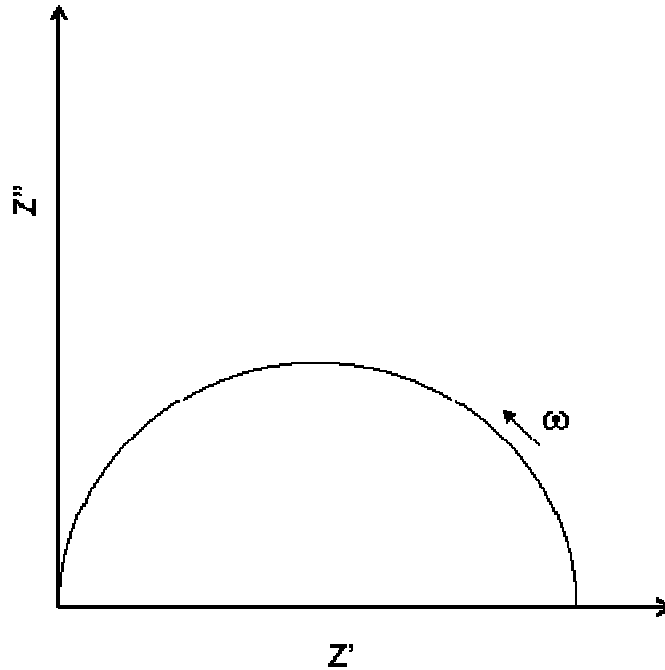
Figure 2.20: Scheme of the Impedance complex plane plot

From AC Impedance experiment data measured, it is possible to obtain the impedance and from it calculate three other quantities:

- Electric modulus or complex permittivity, M

- Admittance, A

- Permittivity, ε.

Impedance

Impedance can be defined as the ability of a circuit element to resist the flow of electrical current,

$$Z = \frac{V}{I} \qquad (2.10)$$
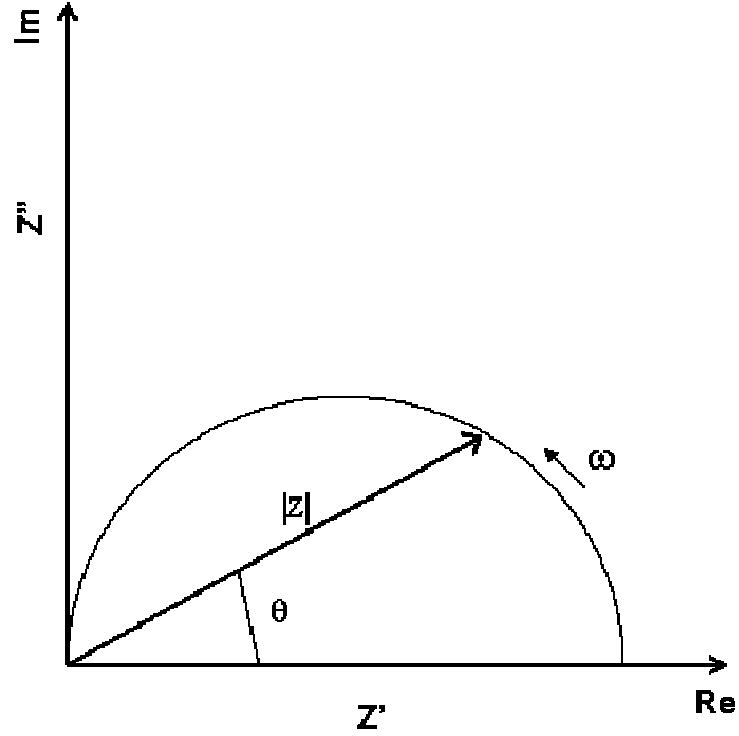
Figure 2.21: Scheme of the Impedance complex plane plot, D'Argand diagram

Complex impedance can be described by cartesian or polar coordinates, at any frequency, as shown in Figure 2.21. Complex impedance can be expressed as

$$Z^* = Z' - jZ'' \qquad (2.11)$$

In Cartesian coordinates

$$Z' = |Z|\cos\theta$$

$$Z'' = |Z|\sin\theta$$

Where

$$\text{Angle} \rightarrow \theta = \tan^{-1}\left(\frac{Z''}{Z'}\right)$$

$$\text{Modulus of impedance} \rightarrow |Z| = \sqrt{(Z')^2 + (Z'')^2}$$

And in polar coordinates

$$Z^* = |Z|\exp(j\theta) \qquad (2.12)$$

Complex Admittance

Complex admittance is the inverse of the complex impedance

$$Y^* = (Z^*)^{-1} = Y' + jY'' \qquad (2.13)$$

Electric modulus and complex permittivity

Complex permittivity, is derived from the complex impedance

$$M^* = j\omega C_0 Z'' \qquad (2.14)$$

$$M^* = M' + jM'' \qquad (2.15)$$

Where

$\omega \rightarrow$ Angular frequency, $\omega = 2\pi f$

$C_0 \rightarrow$ Vacuum capacitance of the measuring cell, $C_0 = \varepsilon_0 \dfrac{A}{I}$

$\varepsilon_0 = 8.854 \times 10^{-14}$ F/cm

$A \rightarrow$ Area of the sample, cm^2

$I \rightarrow$ Thickness of the sample, cm

Complex Permittivity

Complex permittivity is the inverse of the complex electric modulus.

$$\varepsilon^* = (Y^*) = \varepsilon' - j\varepsilon'' \qquad (2.16)$$

$$\varepsilon^* = \frac{Y^*}{j\omega C_0} \qquad (2.17)$$

Where

$\varepsilon' \rightarrow$ Permittivity of a material, real part

$\varepsilon'' \rightarrow$ Dielectric loss, associated with the dissipation of energy heat [38]

2.8.3 Equivalent Circuit

An equivalent circuit is the association of resistive, capacitive and inductive elements, in series and in parallel, in order to represent the phenomena of a sample.
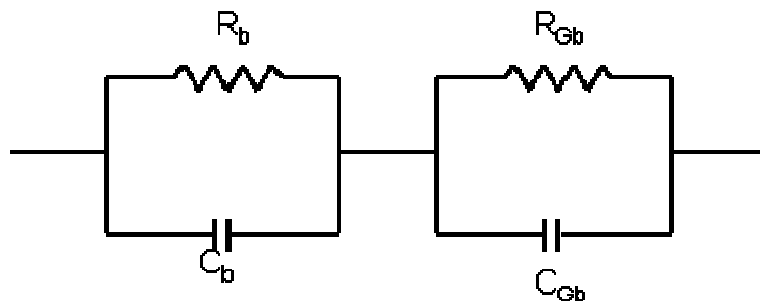
Figure 2.22: Parallel RC Element in series with another Parallel RC Element

Figure 2.22 describes an equivalent circuit with a resistor and capacitor in parallel, Parallel RC Element, in series with another Parallel RC Element.

Figure 2.23 is a typical case for the $Ce_{0.04}Y_{0.02}Sc_{0.67}Zr_{3.27}O_{7.66}$, at 303 °C. There are two semi-circles, where the second one is not a perfect semi-circle as it is connected to a third semi-circle. Each semi-circle is represented by one parallel RC Element.
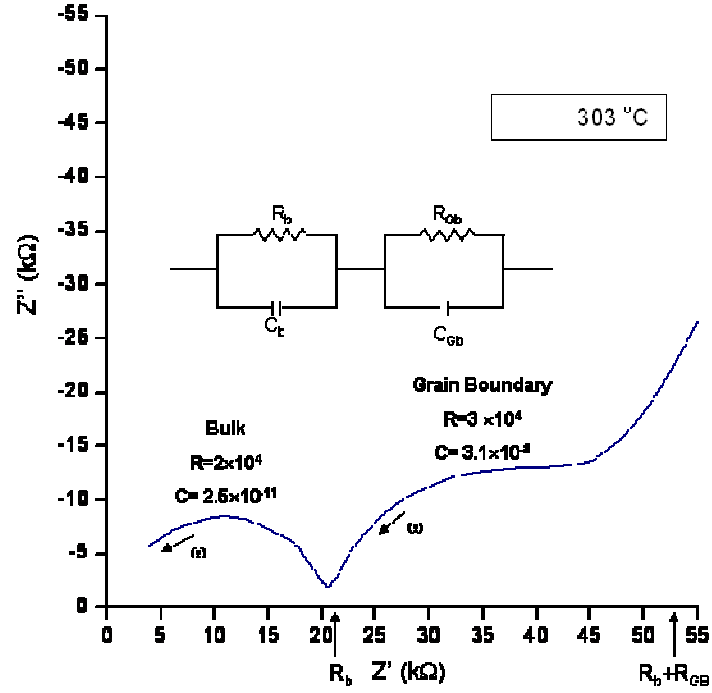
Figure 2.23: The complex impedance plot for a scandia zirconia doped with ceria and yttria, $Ce_{0.04}Y_{0.02}Sc_{0.67}Zr_{3.27}O_{7.66}$

In order to estimate the response of the equivalent circuit, the response of the bulk semi-circle will be calculated first.

Total admittance is given by

$$Y^* = \frac{1}{R} + j\omega C \qquad (2.18)$$

Complex impedance is given by

$$Z^*_{bulk} = (Y^*)^{-1} = \left(\frac{1}{R} + j\omega C_b \right)^{-1}$$

$$Z^*_{bulk} = Z' - jZ''$$

$$Z^*_{bulk} = R_b \left[\frac{1}{1 + (\omega R_b C_b)^2} \right] - jR_b \left[\frac{\omega R_b C_b}{1 + (\omega R_b C_b)^2} \right]$$

$$Z^*_{bulk} = R_b \left[\frac{1}{1 + (\omega \tau_b)^2} \right] - jR_b \left[\frac{\omega \tau_b}{1 + (\omega \tau_b)^2} \right] \qquad (2.19)$$

Where,

$\tau_b = R_b C_b \rightarrow$ Maxwell time constant, also known as conductivity relaxation time

Real Z' has the following behaviour at the limits of ω,

$$\omega = 0, \qquad Z' = R$$

$$\omega = \infty, \qquad Z' = 0$$

The imaginary Z'' component defines a Debye peak with height $Z'' = \dfrac{R}{2}$, when $\omega RC = 1$.

To combine bulk and grain boundary, the total impedance of the system Z^* is given by the sum of the impedance of the parallel RC element of the bulk and grain boundary.

$$Z^*_{Total} = Z^*_{bulk} + Z^*_{GB} \qquad (2.20)$$

$$Z^*_{bulk} = R_b \left[\frac{1}{1 + (\omega \tau_b)^2} \right] + R_{GB} \left[\frac{1}{1 + (\omega \tau_{GB})^2} \right] \qquad (2.21)$$

The equation on top describes two semi-circles, when the first semi-circle intercepts the real Z' axis, resistance of the bulk R_b can be calculated. The sum of bulk and grain boundary resistances, $R_b + R_{GB}$, is calculated when the second semi-circle intercepts the real Z'. From Figure 2.22, the bulk semi-circle has a resistance of 19826 Ω and

capacitance of 2.5×10^{-11} F and for the grain boundary semi-circle, the resistance of 33226 Ω and capacitance of 3.1×10^{-8} F.

The only information that can be extracted from the complex impedance plot is the resistance (impedance). The capacitance can be used as guidance to give some information of the phenomenon involved, see Table 2.4.

Table 2.4: Typical capacitance values [39]

Capacitance, F	Interpretation of phenomenon
10^{-12}	Bulk
10^{-11}	Minor, secondary phase
10^{-11} - 10^{-8}	Grain boundary
10^{-10} - 10^{-9}	Bulk ferroelectric
10^{-9} - 10^{-7}	Surface layer
10^{-7} - 10^{-5}	Sample-electrode interface
10^{-4}	Electrochemical reactions

The values on Table 2.4 can be used as a guide when fitting the raw data.

Sample Preparation

Samples are polished to obtain a smooth surface; this surface is painted platinum paste with a brush. To sinter the platinum the pellets had a thermal treatment at 900 °C for 20 min.

All pellets are analysed in a range of temperatures from 300 to 900 °C.

The impedance measurements are performed by three different analysers:

- Solatron 1260 the frequency range swept from 100 MHz to 1Hz, the effective AC voltage amounted to 50 mV.

- HP Hewlett-Packard (HP), 4192A LF impedance analyzer, range frequency swept from 13 MHz-5 Hz and the effective AC voltage amounted to 20 mV.

- Alpha-A, Novocontrol the frequency range swept from 3 MHz to100 mHz and the effective AC voltage amounted to 20 mV.

2.9 Oxygen Partial Pressure

The total pressure of a gas in a mixture of gases is the sum of the partial pressures of each individual gas in the mixture.

In order to achieve the oxygen partial pressure wanted for these experiments, it was used a mixture of gases, hydrogen, argon and oxygen.

Sample Preparation

Samples were polished to obtain a smooth surface, on that surface was painted with a brush platinum paste, to sinter the platinum the pellets had a thermal treatment at 900 °C for 20 min.

The frequency range swept from 3 MHz-100 mHz and the effective AC voltage amounted to 20 mV. The oxygen partial pressure was varied by application of appropriate gas mixtures in the range from 1 to 10^{-24} bars at 700 °C. The composition of the gas mixture was adjusted and maintained constant by using mass flow controllers (Hastings 302). The oxygen partial pressure was measured by a zirconia-based potentiometric sensor and the temperature was monitored close to the sample by a type-S thermocouples.

References

1. Wold, A. and Dwight, K., *Solid State Chemistry, Synthesis, Structure and Properties of Selected Oxides and Sulphides*. 1993, New York: Chapman & Hall, Inc.
2. West, A.R., *Basic Solid State Chemistry*. 2nd ed. 1999, Chichester: John Wiley & Sons, Ltd.
3. Shmalzried, H., *Solid State Reactions*. Vol. 12. 1981, Deerfiel, Florida: Monographs in Modern Chemistry.
4. Petrova, N. and Todorovsky, D., Materials Research Bulletin, (2005) p. 1-14.
5. http://www.astro.iag.usp.br/~vpagina/Solgel.htm. 2005 [cited 2006 July].
6. Menchi, A., Scian, A., Materials letters, **59** (2005) p. 2664-2667.
7. Spiridonov, M., Popova, L.N. and Popil'skii, R.Y., Journal Solid State Chemistry, **2** (1970) p. 432.
8. Politova, T. and Irvine, J.T.S., Solid State Ionics, **168** (2004) p. 153-165.
9. Boskovic, S.B., Djurovic, D. R., Zec, S. P., Matovic, B. Z., Zinkevich, M., Aldinger, F., Ceramics International, **34** (2007) p. 2001-2006.
10. Lee, D., Lee, I., Jeon, Y., Song, R., Solid State Ionics, **176** (2005) p. 1021-1025.
11. Michael, M.S., Fauzi, A., Prabaharan, S.R.S., International Journal of Inorganic Materials, (2) (2000) p. 261-267.
12. de Carvalho, E.M.S., Irvine, J.T.S. in *X SOFC*. 2007. Nara, Japan: ECS Trans.
13. Willard, H.H., Merritt, J., L. and Dean, J., *Instrumental Methods of Analysis*. Fourth ed. 1965, Princeton, New Jersey: D. Van Nostrand Company, INC.
14. Gomes, C.d.F., *Raios X no Estudo de Materiais*. 1st ed. 1980, Aveiro: Textos Didaticos.
15. Lipson, H.S., *Crystals and X-Rays*. 1st ed, ed. Mott and Noakes. 1970, London & Winchester: Wykeham Publications, LTD.
16. Smith, W.F., *Principles of Materials Science and Engineering*. 3rd ed. 1998, Lisboa: McGraw-Hill.
17. ASM, *Materials Characterization*. 1st ed. ASM Handbook. Vol. 10. 1992, USA: American Society for Metals.
18. Hukins, D.W.L., *X-ray Diffraction by Disordered and Ordered System*. 1st ed. 1981, Oxfrd: Pergamon Press.
19. C. Giacovazzo, H.L.M., D. Viterbo, F. Scordari. G. Gilli, G Zanotti, M. Catti, *Fundamentals of Crystallography*. First ed, ed. Giacovazzo, C. 1992, Oxford: Oxford University Press.
20. Hammond, C., *The Basic of Crystallography and diffraction*. 2nd ed. 2001, Oxford: Oxford Science Publications.
21. Dinnebier, R.E. and Billinge, S.J.L., *Powder diffraction: Theory and Practice*, ed. Publishing, H. 2008, Cambridge: The Royal Society of Chemistry.
22. Crystallography, D.o. 2007 [cited 2009 2009].
23. www.chem.qmul.ac.uk/surfaces. 2008 [cited 2009 November].
24. www.ige.unicamp.br. 2009 [cited 2009 November].
25. Klug, H.P., Alexander, L., *X-ray diffraction procedures for polycrystalline and amorphous materials*. 2nd ed. 1974, New York: Wiley & sons.

26.   Chinn, R.E., *Ceramography, Preparation and Analysis of Ceramic Microstructures*. ASM International. 2002: Materials Park.

27.   German, R.M., *Sintering Theory and Practice*. 1996, New York: John Wiley & Son.

28.   Vieira, J., Monteiro, R. and Senos, A., *Introducao aos modelos de sinterizacao*. 1992, Aveiro: University of Aveiro.

29.   www.Malvern.co.uk. 2002 [cited 2006 July].

30.   http://www.st-andrews.ac.uk/gg/Research/Geoscience/index.shtml. 2004 [cited 2006 Mach].

31.   Valadares, E.d.C., Revista Brasileira de Ensino de Fisica, **14**(2) (1992) p. 63-71.

32.   Goodhew, P.J. and Humphreys, F.J., *Electron Microscopy and Analysis*. 1998, London: Taylor & Francis.

33.   http://www.unl.edu/CMRAcfem/temoptic.htm. 2006 [cited 2007 December].

34.   Slade, P. and Lloyds, J., *Thermal characterization techniques*. 1970, New York: M. Dekker.

35.   Fifield, F.W. and Kealey, D., *Principles and Practice of Analytical chemistry*. 3rd ed, London: Blackie Academic and Professional.

36.   V., E.C.B. 2004 [cited 2005 December 2008].

37.   Christensen, P.A., Hamnett, A., *Techinques and mechanics in electrochemistry*. 1st edition ed. 1994, Glasgow: blackie Academic and professional.

38.   MacDonald, J.R., *Impedance Spectroscopy, emphasizing solid materials and systems*. 1987, New York: John Wiley & Son.

39.   Irvine, J.T.S., Sinclair, D.C., West, Anthony R., Advanced Materials, **2**(3) (1990) p. 132-138.

Chapter III

Powders: Synthesis and Characterisation

3.1. Introduction

In recent years methods to produce powders have shifted from solid state to wet-chemistry. This change is connected to the development and discovery of new organic materials that can facilitate the reaction at lower temperatures and make a faster reaction, such as fuel and catalysts. The solid state synthesis method is the oldest, simplest and most widely known method to produce ceramic, but it has been replaced by other methods such as sol-gel method, combustion method, Pechini-type gel route, and co-precipitation synthesis [1-3].

Scandia stabilised zirconia, SSZ, has been studied using several types of powder production; Nomura [4] used solid state synthesis, Lee [5] produced powders by the glycine nitrate process and Xu [6] produced powders by homogeneous precipitation synthesis.

In this project, a sol-gel and combustion method was used, where it was expected to produce nano-particles. In the first part of the process, the nitrates and oxidants are mixed, then the temperature is increased to transform the solution in a viscous sol that contains particles of colloidal dimensions and finally there is a transformation into a transparent, homogeneous and amorphous solid called gel without precipitation of any crystalline phase; at the end this solution is burned [7, 8].

SSZ show many phases, but the single cubic phase is not stable under 650 °C, and to stabilise zirconia it is necessary to introduce 9 mol% of scandia. When Sc_2O_3-ZrO_2 is doped with Y_2O_3, it eliminates the phase transition and stabilises the cubic fluorite phase. As cerium is a large ion, it is expected to stabilise the cubic fluorite phase and to increase the conductivity of the scandia zirconia system.

Ceria and ceria based materials have been widely studied in recent years, as it has been applied in different areas, such as catalysis, microelectronics, optoelectronics,

electrochemical devices and ultraviolet blockers. The two oxidation states, trivalent (Ce^{3+}) and tetravalent (Ce^{4+}), and the Ce^{4+}-O^{2-} charge transfer, gives ceria based materials the possibility to be used in different areas [9].

Cerium oxides exist in three phases:

- CeO_2, with the CaF_2 fluorite structure

- Hexagonal (h-), Ce_2O_3, categorised as A-type structure, in rear-earth oxides

- Cubic (c-), Ce_2O_3, categorised as C-type structures, in rare-earth oxides

At room temperature, the hexagonal Ce_2O_3 crystal is not stable in air but is stable under anaerobic conditions. The cubic Ce_2O_3 crystal, which can be considered as the CeO_2 crystal with ordered oxygen vacancies, is known to exist at a nonstoichiometric state in the temperature range of 1000-1200 °C in hydrogen atmosphere [10]. Pure CeO_2 is easily susceptible to sintering at temperature higher than 800 °C.

Eight compositions from the system of ceria and yttria co-doped scandia zirconia were prepared by Sol-gel and combustion process aiming at the stabilisation of phase stability at working temperature and improvement of ionic conductivity. Seven compositions belong to the system $Ce_xY_{0.2-x}Sc_{0.6}Zr_{3.2}O_{8-\delta}$ ($0 \le x \le 0.2$) and one composition has the formula $Ce_{0.04}Y_{0.02}Sc_{0.67}Zr_{3.27}O_{7.66}$.

The Gibbs diagram, as shown in Figure 3.1, has three elements, scandia, yttria and ceria.
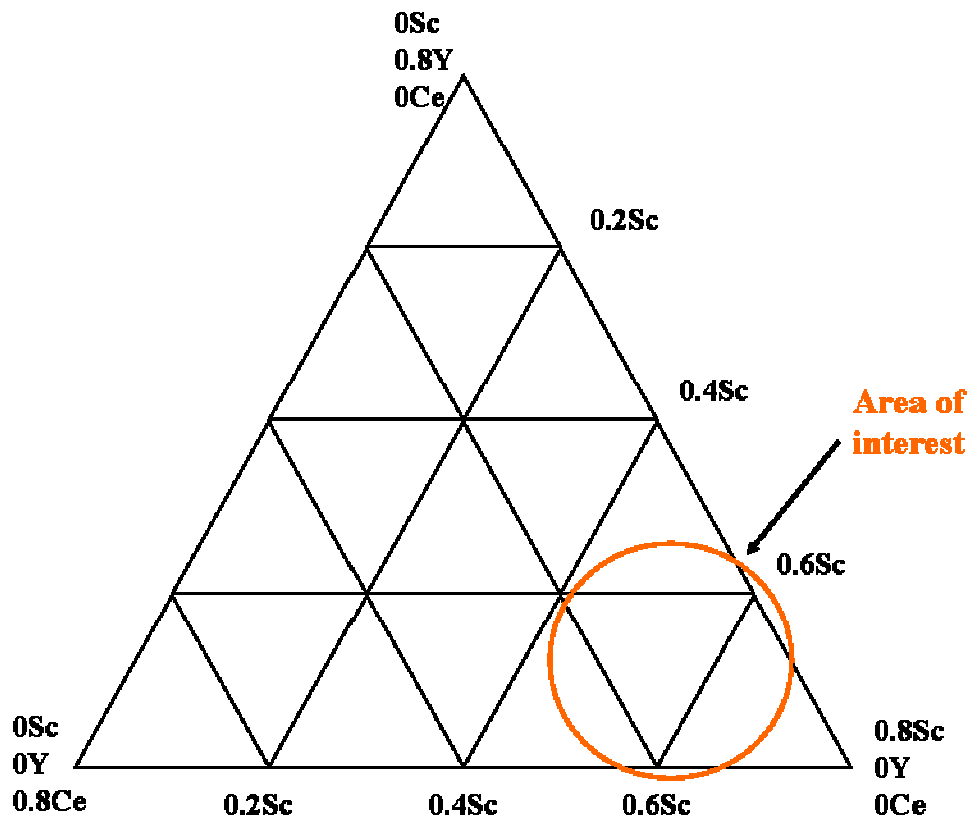
Figure 3.1: Phase diagram of the system $Ce_xY_{0.2-x}Sc_{0.6}Zr_{3.2}O_{8-\delta}$ ($0 \leq x \leq 0.2$).

This system is composed by four elements, with two of a fixed proportion, zirconia and scandia, while the other two, ceria and yttria, the weight varies. For this system, 3.2 atoms of zirconia and 0.6 atoms of scandia are introduced. As scandia has a fixed proportion, the interest compositions were chosen in the line of 0.6 atoms of Sc. In this line cerium and yttrium proportions vary from 0 to 0.2 of atoms, where one element increases the other decreases in the same amount. Figure 3.2 shows a magnification of the circled area from Figure 3.1.

There is another composition that was produced and characterised. This composition was the first one to be tried and it is from it that the protocol for the powders production and characterisation was made. This composition has 0.037 atoms of cerium, 0.015 atoms of yttrium, 0.67 atoms of scandium and 3.28 atoms of zirconium.

Figure 3.2 shows the magnification of the area of interest, i.e. how the compositions are related in the system.
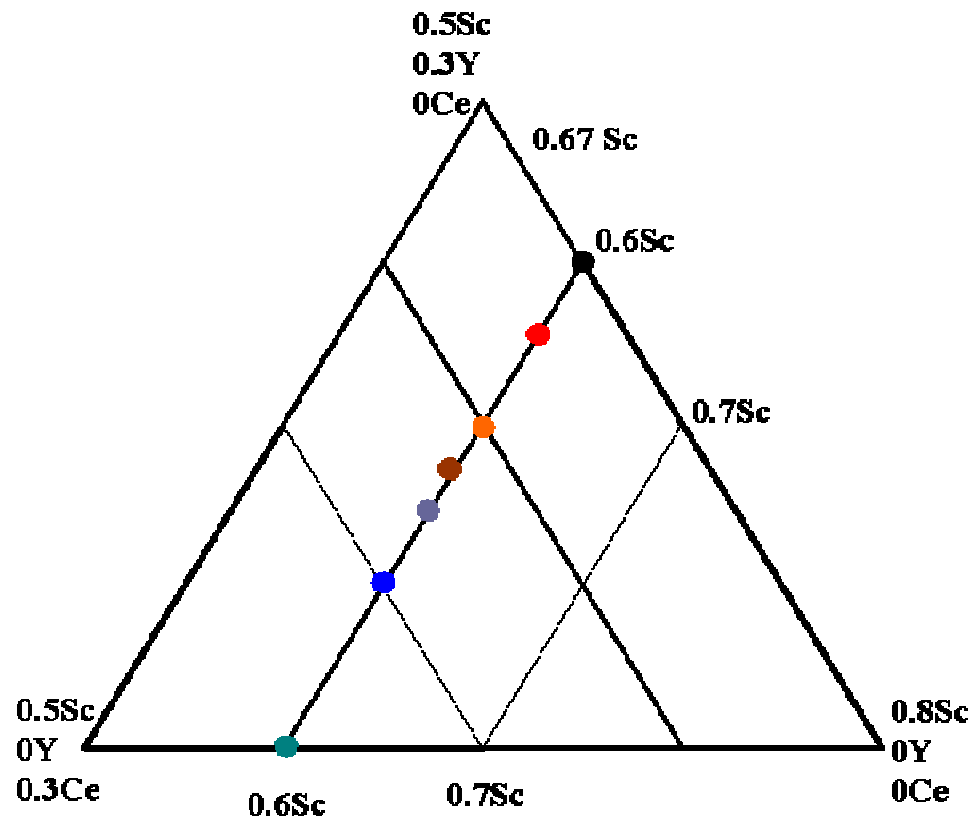
Figure 3.2: Part of the phase diagram of the system $Ce_xY_{0.2-x}Sc_{0.6}Zr_{3.2}O_{8-\delta}$ (0≤x≤0.2).

Legend:

● $Y_{0.2}Sc_{0.6}Zr_{3.2}O_{7.60}$

● $Ce_{0.04}Y_{0.16}Sc_{0.6}Zr_{3.2}O_{7.62}$

● $Ce_{0.08}Y_{0.12}Sc_{0.6}Zr_{3.2}O_{7.64}$

● $Ce_{0.1}Y_{0.1}Sc_{0.6}Zr_{3.2}O_{7.65}$

● $Ce_{0.12}Y_{0.08}Sc_{0.6}Zr_{3.2}O_{7.66}$

● $Ce_{0.16}Y_{0.04}Sc_{0.6}Zr_{3.2}O_{7.68}$

● $Y_{0.2}Sc_{0.6}Zr_{3.2}O_{7.70}$

There is one composition without ceria, $Y_{0.2}Sc_{0.6}Zr_{3.2}O_{7.60}$, and another one without yttria, $Ce_{0.2}Sc_{0.6}Zr_{3.2}O_{7.70}$; the other five compositions are between these two extremes. Table 3.1 shows the elements and the respective amount used for each composition, in atoms based. In the first row, a composition outside the system is shown as it was the initial composition.

Table 3.1: Elements and their amount for each composition

Cerium	Yttrium	Scandium	Zirconium	Oxygen	Nomenclature
0.04	0.02	0.67	3.27	7.66	Initial
0.00	0.20	0.60	3.20	7.60	x=0.00
0.04	0.16	0.60	3.20	7.62	x=0.04
0.08	0.12	0.60	3.20	7.64	x=0.08
0.10	0.10	0.60	3.20	7.65	x=0.10
0.12	0.08	0.60	3.20	7.66	x=0.12
0.16	0.04	0.60	3.20	7.68	x=0.16
0.20	0.00	0.60	3.20	7.70	x=0.20

3.2 Experimental

The powders are prepared by a sol-gel and combustion method [5, 11, 12]. Scandia powders (TTE Metals, 99.9 % purity) are dissolved in nitric acid (Fisher Scientific, d=1.42, 70 %) and hydrogen peroxide (Fisher Scientific, >30 % wv). Separately, cerium (III) nitrate hexahydrate (Aldrich, 99 % purity), yttrium nitrate hexahydrate (Aldrich, 99.9%) and zirconia acetylacetonate (IV) (Aldrich, 98% purity) were dissolved in distilled water. The first solution is added to the second, and after the two solutions are mixed, glycine is introduced. Ammonia is introduced until the pH is approximately 6. When the solution is ready, the temperature is increased to 150 °C and left until the gel is formed. After the gel is formed, the temperature is increased to 270 °C, so that the gel burns off. The powders are calcined for 3 hours at 400 °C; the ramp rate used is 0.5°C/min. A rapid cool down is made from 400 °C to room temperature. The powders are removed from the furnace and ground. After the powders are calcined, a XRD is made; using a Philips X-ray diffractometer, the Philips PW1710 reflector with fixed omega, (20-90 2θ, step size 0.02 ° 2θ, CuKα radiation). A Fritsch Planetary Ball Mill "Pulverisette 7" with zirconia balls is also used with the same suspension in acetone,

triton QS-44 (phosphate ester, Acid form, Sigma Chemical) 4% of powder weight and the zirconia powders. Dried powders are pressed uniaxially into pellets of 13 mm in diameter and 0.6-1.0 mm in thickness at 75 MPa and isostatically at 200 MPa. The pellets are sintered at 1500 °C and removed from the furnace at 1000 °C to cool down to room temperature.

3.3 Results and Discussion

3.3.1 Solid State Synthesis, SSS

Using the SSS, the final product does not have high homogeneity and/or density; the method is slow due to the powder being mixed at the particles level and not at the atomic level [1, 2]. Therefore it is very difficult to produce a dense pellet by this process. To perform the calcination at lower temperatures, the powders must be compressed into pellets. The pressure applied will promote a larger contact area between particles, enhancing the mass transport between particles.

Two pellets were pressed and then calcined at 1500°C, for 24 and 36 hours. Figure 3.3 shows the X–ray diffraction pattern of $Ce_{0.08}Y_{0.12}Sc_{0.6}Zr_{3.2}O_{7.64}$ and the material, after calcination, does not show a single phase. In the X-ray diffraction pattern, there are several peaks, which need a careful analysis; they have a pattern of two crystal structures, monoclinic and cubic. In Figure 3.3, monoclinic is marked by the letter m and cubic by the letter c.
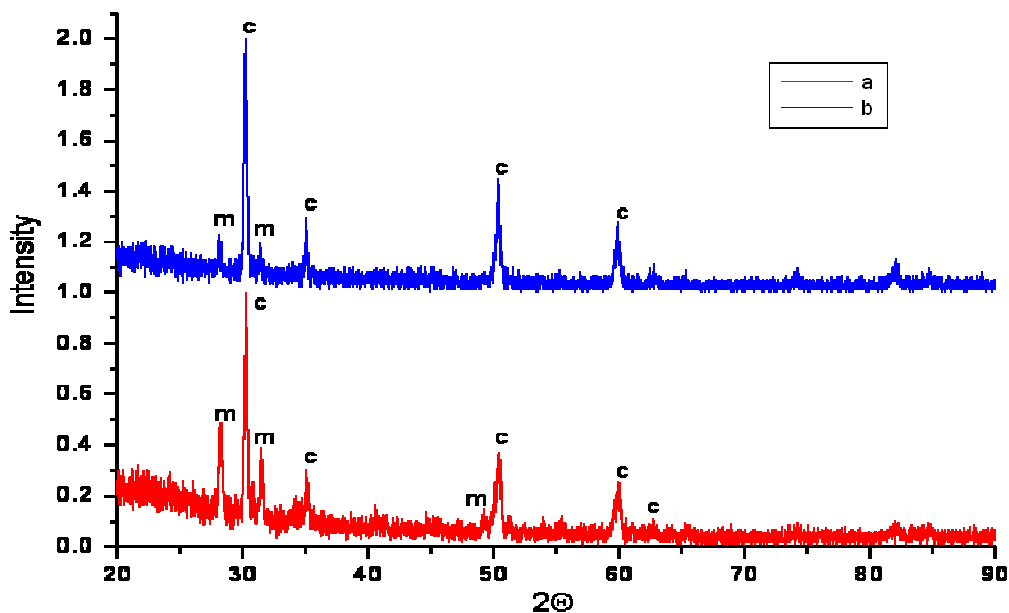
Figure 3.3: X-ray diffraction pattern of $Ce_{0.08}Y_{0.12}Sc_{0.6}Zr_{3.2}O_{7.64}$, calcined at 1500 °C (a) 24 hours, (b) 36 hours.

For a temperature of 1500 °C, even when the sample has been in the furnace for 36 hours, there is the existence of extra peaks than from the desired cubic fluorite structure. The sample from 24-hours calcination has a considerable amount of monoclinic phase, approximately 20 %, but this value decreases to 10 % for sample with 36-hours of calcination. The peaks from the monoclinic phase decrease in intensity, from 24-hours to 36-hours of calcination. This can indicate that if the samples were left in the furnace for longer periods of time, it could eliminate the extra peaks, leaving only a single cubic phase.

Subjecting the pellets to temperatures of 1500 °C was not enough for the powder to react in order to produce the desired crystal structure. Increasing temperature by 100 °C was expected to accelerate the reaction in the particles.

X-ray diffraction

Figure 3.4 shows X-ray diffraction pattern of $Ce_{0.12}Y_{0.08}Sc_{0.6}Zr_{3.2}O_{7.66}$, calcined at 1600 °C (a) 24 hours, (b) 36 hours.
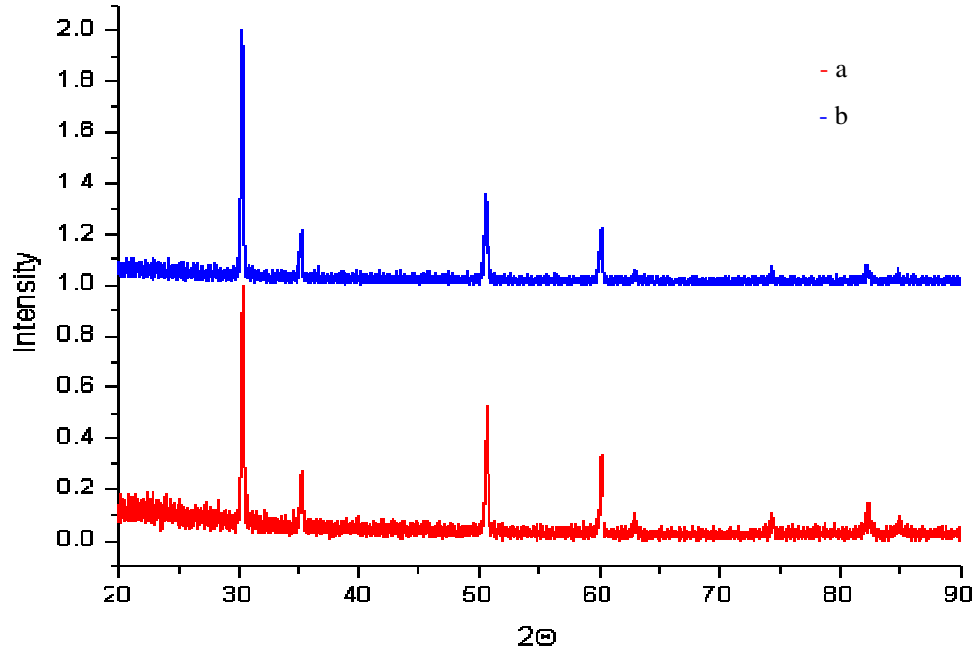
Figure 3.4: X-ray diffraction pattern of $Ce_{0.12}Y_{0.08}Sc_{0.6}Zr_{3.2}O_{7.66}$, calcined at 1600 °C (a) 24 hours, (b) 36 hours.

A calcination of pellets, with the composition $Ce_{0.12}Y_{0.08}Sc_{0.6}Zr_{3.2}O_{7.66}$, was performed at 1600 °C; one pellet was inside the furnace for 24 hours and another for 36 hours. The X-ray diffraction pattern for the two pellets is presented in Figure 3.4; which shows the presence of a single phase with a cubic fluorite-type structure, which belongs to the $Fm\overline{3}m$ space group. Table 3.2 shows the x-ray diffraction for the composition $Ce_{0.12}Y_{0.08}Sc_{0.6}Zr_{3.2}O_{7.66}$, peaks are indentified by the 2θ and by the Miller index, h k l.

Table 3.2: X-ray diffraction data for the composition $Ce_{0.12}Y_{0.08}Sc_{0.6}Zr_{3.2}O_{7.66}$, with the cubic fluorite-type structure, calcined at 1600 °C for 24 hours.

2θ	d, Å	Intensity	h k l
30.329	2.9446	100	1 1 1
35.191	2.5818	27.56	2 0 0
50.578	1.8032	49.88	2 2 0
60.117	1.5378	33.04	3 1 1
63.080	1.4726	5.62	2 2 2
74.327	1.2746	5.62	4 0 0
82.327	1.1703	11.81	3 3 1
84.922	1.1410	6.75	4 2 0

Refined cell parameters:

- Lattice parameter: $a = 5.103 \pm 1.70 \times 10^{-4}$ Å

- Cell volume: $v = 132.89 \pm 8.00 \times 10^{-2}$ Å^3

Density

The sintering period used for the solid state method, was at 1500 °C for 24 hours. The pellets of the solid state method showed low mechanical stability, as they fragment during handling. Table 3.3 shows the density for the composition $Ce_{0.12}Y_{0.08}Sc_{0.6}Zr_{3.2}O_{7.66}$, sintered at 1500 °C for 36 hours. There is also the theoretical density and the density in percentage.

Table 3.3: Density for the composition $Ce_{0.12}Y_{0.08}Sc_{0.6}Zr_{3.2}O_{7.66}$, sintered at 1500 °C for 36 hours.

Composition	Theoretical density, g/cm^3	Sample density, g/cm^3	Density, %
$Ce_{0.12}Y_{0.08}Sc_{0.6}Zr_{3.2}O_{7.66}$	5.814	3.657	63

The final density for this pellet is 63 %, this is a low values when compared to values obtained by the sol-gel and combustion method, higher than 90 %.

SEM

Figure 3.5 is a micrograph of composition $Ce_{0.12}Y_{0.08}Sc_{0.6}Zr_{3.2}O_{7.66}$, sintered at 1500 °C for 36 h.
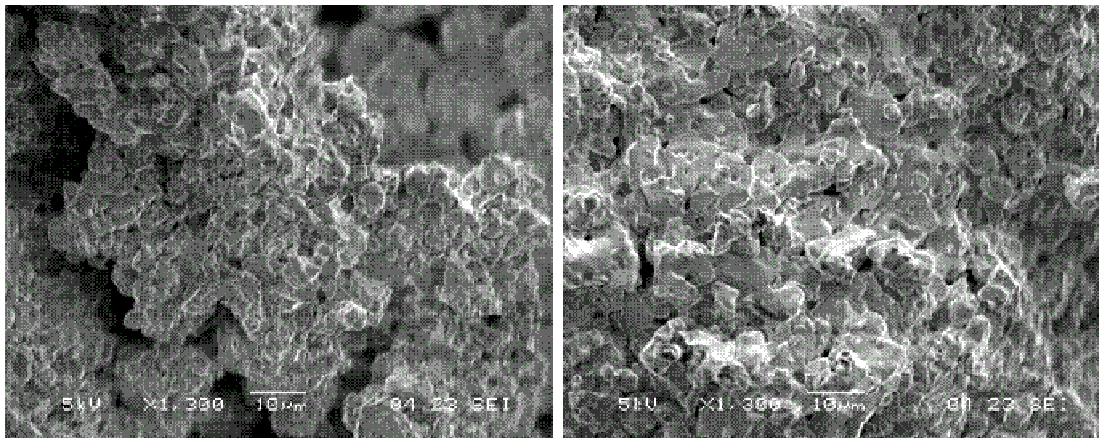
Figure 3.5: SEM pictures of composition $Ce_{0.12}Y_{0.08}Sc_{0.6}Zr_{3.2}O_{7.66}$, sintered at 1500 °C for 36 h.

Figures 3.5 shows that some grains start to sinter as agglomerates but do not sinter as a compact body and they will therefore produce a body with low mechanical strength or low mechanical stability. Those agglomerates always have open porosity. It is very difficult to produce a dense pellet by this process, as calcination is done at 1600 °C, in a pellet. After the calcination, the powder is ground, but the particle size never drops to a size small enough to promote densification. This way, when a new pellet is produced, some parts will have already become sintered material.

3.3.2 Sol-Gel and Combustion method

X-ray diffraction

After calcination of the powders, X-ray diffraction is performed in order to confirm the phase. Figure 3.6 shows the X-ray pattern for seven composition of the system $Ce_xY_{0.2-x}Sc_{0.6}Zr_{3.2}O_{8-\delta}$ (0≤x≤0.2), and the composition $Ce_{0.04}Y_{0.02}Sc_{0.67}Zr_{3.27}O_{7.66}$, calcined at 400 °C for 3 hours.
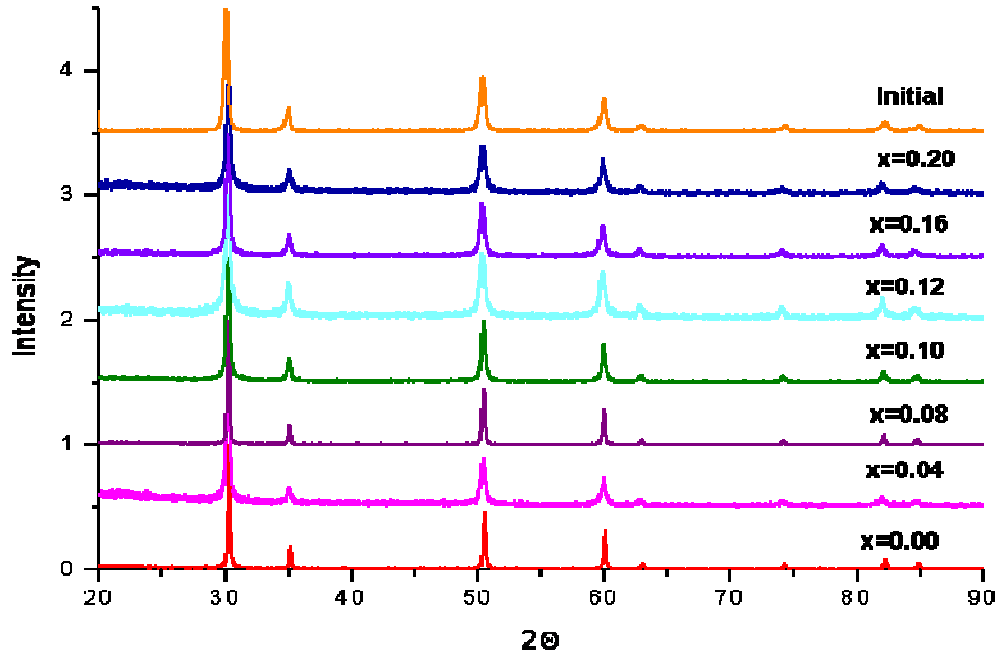
Figure 3.6: X-ray diffraction of the six compositions that belong to the system $Ce_xY_{0.2-x}Sc_{0.6}Zr_{3.2}O_{8-\delta}$ ($0 \leq x \leq 0.2$), and the composition $Ce_{0.04}Y_{0.02}Sc_{0.67}Zr_{3.27}O_{7.66}$, calcine at 400 °C for 3 hours.

The X-ray diffraction for all compositions, in Figure 3.6, shows the presence of a single phase, with a cubic fluorite-type structure, $Fm\bar{3}m$ space group.

Table 3.4: X-ray diffraction data for the composition $Ce_{0.08}Y_{0.12}Sc_{0.6}Zr_{3.2}O_{7.64}$, with cubic fluorite-type structure, calcine at 400 °C for 3 hours

2θ	d, Å	Intensity	h k l
30.258	2.9514	100	1 1 1
35.073	2.5568	16.55	2 0 0
50.469	1.8068	43.74	2 2 0
59.991	1.5408	27.24	3 1 1
62.961	1.4751	4.31	2 2 2
74.180	1.2773	4.10	4 0 0
82.177	1.1720	8.79	3 3 1
84.815	1.1422	4.21	4 2 0

Refined cell parameters for composition $Ce_{0.08}Y_{0.12}Sc_{0.6}Zr_{3.2}O_{7.64}$:

- Lattice parameter: a= $5.107 \pm 1.20 \times 10^{-4}$ Å

- Cell volume: $v = 133.159 \pm 2.18 \times 10^{-3}$ Å^3

Table 3.5 presents the cubic lattice parameter values for the system $Ce_xY_{0.2-x}Sc_{0.6}Zr_{3.2}O_{8-\delta}$ ($0 \leq x \leq 0.2$) and the estimated errors.

Table 3.5: Cubic lattice parameter values and estimated errors

Composition	Lattice parameter, Å	Estimated error
$Y_{0.2}Sc_{0.6}Zr_{3.2}O_{7.60}$	5.104	7.20×10^{-5}
$Ce_{0.04}Y_{0.16}Sc_{0.6}Zr_{3.2}O_{7.62}$	5.104	7.20×10^{-5}
$Ce_{0.08}Y_{0.12}Sc_{0.6}Zr_{3.2}O_{7.64}$	5.110	1.20×10^{-4}
$Ce_{0.1}Y_{0.1}Sc_{0.6}Zr_{3.2}O_{7.65}$	5.106	8.81×10^{-5}
$Ce_{0.12}Y_{0.08}Sc_{0.6}Zr_{3.2}O_{7.66}$	5.111	1.61×10^{-4}
$Ce_{0.16}Y_{0.04}Sc_{0.6}Zr_{3.2}O_{7.68}$	5.115	2.10×10^{-4}
$Ce_{0.20}Sc_{0.6}Zr_{3.2}O_{7.70}$	5.115	1.20×10^{-4}

The lattice parameter values vary from 5.104 and 5.115 Å, showing an increase of 0.2 % in the lattice parameter. According to Vegard's law there is a linear relation between the crystal lattice parameter and the concentrations of the constituent elements [13, 14]. Analysing Table 3.5, a stagnation of the lattice parameter increase can be observed after introducing 0.16 atoms of ceria in the lattice; this can be the result of the saturation of ceria in the lattice. This behaviour can also be observed in Figure 3.7. The introduction of ceria in the matrix will force the lattice parameter to increase, but when it reaches a certain value, the matrix will accommodate the ceria without increasing its lattice parameter.
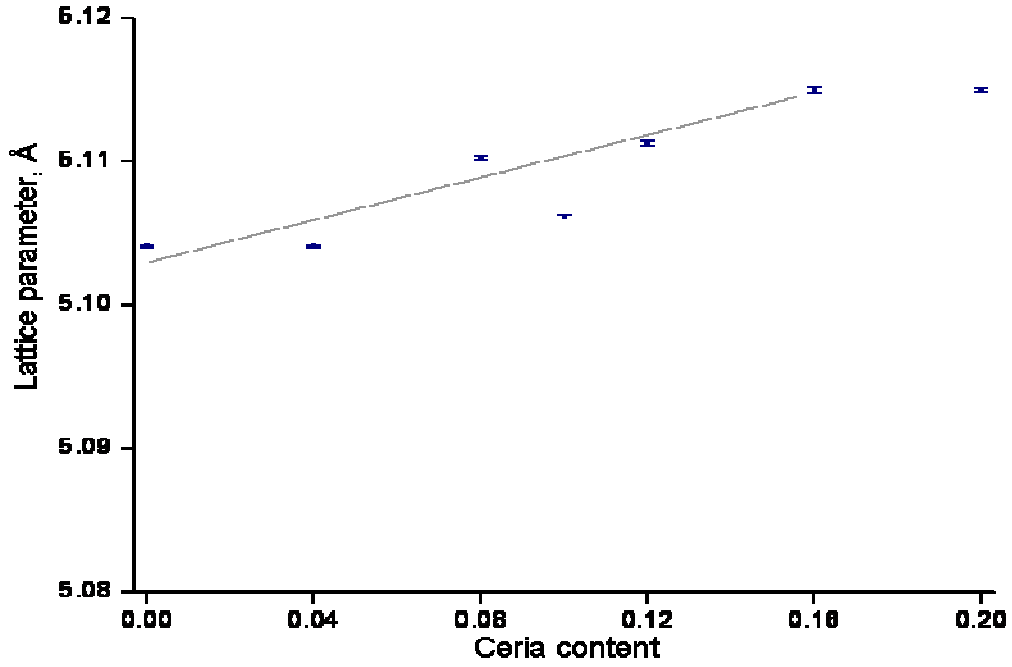
Figure 3.7: Cubic lattice parameter, a, against ceria content in the system.

Particle size from Debye Scherrer equation

The half width, ω, introduced by Scherrer corresponds to the angular range in which the intensity is greater or equal to half maximum intensity (now designed as the FWHM, full width at half maximum). A size parameter,

$$\varepsilon_\omega = \frac{K_\omega \lambda}{\omega \cos(\theta)} \qquad (3.1)$$

Where,

$K_\omega \rightarrow$ Scherrer constant, $0.89 \leq K_\omega \leq 1$

$\lambda \rightarrow$ X-ray wavelength

$\omega \rightarrow$ Peak width, in radians

Table 3.6 presents the particle size for each composition of the system $Ce_xY_{0.2-x}Sc_{0.6}Zr_{3.2}O_{8-\delta}$ and the initial composition, $Ce_{0.04}Y_{0.02}Sc_{0.67}Zr_{3.27}O_{7.66}$ and their estimated errors.

Table 3.6: Particle size of each composition

Composition	Particle size, nm	Estimated error, nm
$Ce_{0.04}Y_{0.02}Sc_{0.67}Zr_{3.27}O_{7.66}$	7.8	0.037
$Y_{0.2}Sc_{0.6}Zr_{3.2}O_{7.60}$	9.1	0.046
$Ce_{0.04}Y_{0.16}Sc_{0.6}Zr_{3.2}O_{7.62}$	7.9	0.038
$Ce_{0.08}Y_{0.12}Sc_{0.6}Zr_{3.2}O_{7.64}$	7.8	0.037
$Ce_{0.1}Y_{0.1}Sc_{0.6}Zr_{3.2}O_{7.65}$	6.8	0.032
$Ce_{0.12}Y_{0.08}Sc_{0.6}Zr_{3.2}O_{7.66}$	5.8	0.028
$Ce_{0.16}Y_{0.04}Sc_{0.6}Zr_{3.2}O_{7.68}$	5.4	0.026
$Ce_{0.20}Sc_{0.6}Zr_{3.2}O_{7.70}$	5.0	0.024

The composition outside the system, $Ce_{0.04}Y_{0.02}Sc_{0.67}Zr_{3.27}O_{7.66}$, has the same particle size as the composition, $Ce_{0.08}Y_{0.12}Sc_{0.6}Zr_{3.2}O_{7.64}$. Inside the system, the increase in ceria content and a decrease in yttria content lead to a decrease in the particle size.

Inductive Coupled Plasma, ICP

The pellet was analysed by ICP to determine the level of impurity species and also to study the homogeneity of the composition $Ce_{0.08}Y_{0.12}Sc_{0.6}Zr_{3.2}O_{7.64}$, as shown in Table 3.7 and Figure 3.8. ICP was performed after the sintering cycle and an etching process; this etching process was performed at 1250 °C and in an alumina crucible.

The theoretical values for the scandium and yttrium are lower than the ICP values. In the case of zirconium, the error is approximately 3 %, this can be explained because there is 4 % of hafnium in each 100% of zirconium. For the cerium values, the difference is larger. This can be explained because the values were measured on the surface of the sample and there is also the possibility of equipment error. The data in Figure 3.8 supports the possibility of an equipment error, as the values of cerium do not vary when compared to the others elements, with time.

Table 3.7: ICP values in ppm by weight, for the composition $Ce_{0.08}Y_{0.12}Sc_{0.6}Zr_{3.2}O_{7.64}$.

$Ce_{0.12}Y_{0.08}Sc_{0.6}Zr_{3.2}O_{7.66}$	Theoretical	Element	Error, %
Zirconium	856629	834890	Negligible
Scandium	79164	77882	Negligible
Yttrium	31310	33645	0.02
Cerium	32896	25670	Negligible
Hafnium	-	12087	Negligible
Titanium	-	4361	1.38
Aluminium	-	11464	1.37
Silicon	-	1	191
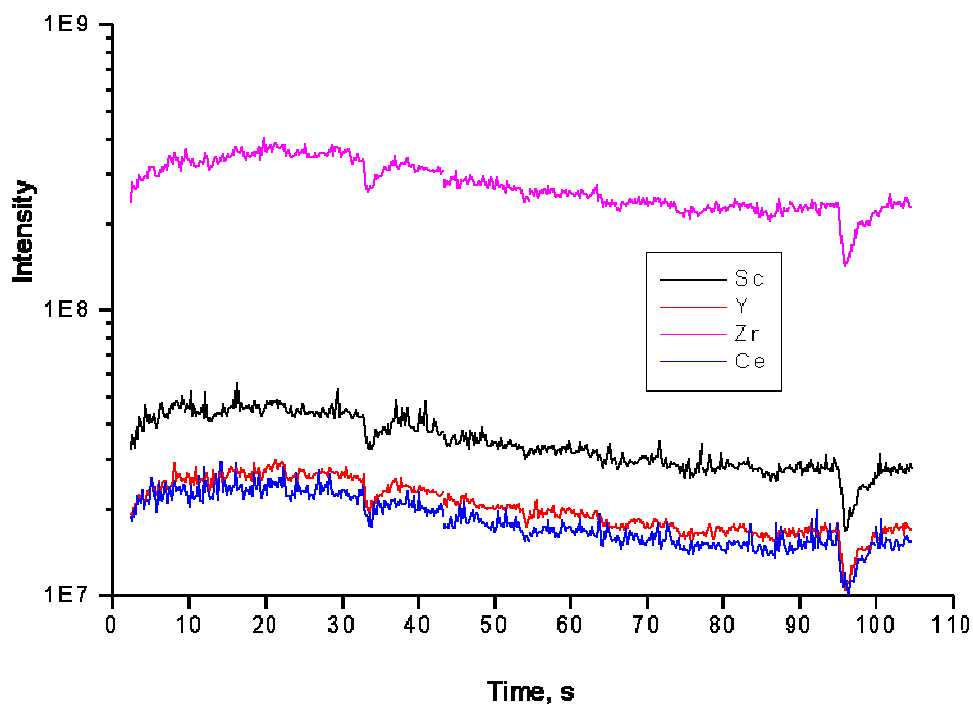
Figure 3.8: ICP relative amount of the elements, in a pellet, against time of drilling the sample

The ICP performed to study the homogeneity of the pellet, Figure 3.8, shows that the different lines, for each element, have the same behaviour. This can indicate that the sample is homogeneous and the sol-gel and combustion process produces homogeneous materials.

There is a high aluminium content, which can have more than one source. Aluminium can be introduced at several stages during the powders processing. This can happen during powder production as alumina is an impurity of scandia, or/and during etching, as the boat is made of alumina. In addition, aluminium can be introduced during the combustion stage as the beaker, where the solution is prepared, is covered by aluminium foil to protect the solution.

To investigate if alumina is not introduced as an impurity of scandia, an ICP of non reacted Sc_2O_3 was performed, as shown in Table 3.8. The error value for aluminium is high as the background counts are higher than the counts of the CPS.

Table 3.8: ICP values in ppm by weight, for $Sc_2O_3.$

Element	ppm by weight	Error, %
Zirconium	16	0.52
Scandium	999934	Negligible
Yttrium	34	0.71
Cerium	3	3.4
Titanium	4	1.2
Hafnium	3	30.6
Aluminium	42	201

Density - Sintering Cycles

These sintering cycles were investigated for the composition, $Ce_{0.04}Y_{0.02}Sc_{0.67}Zr_{3.27}O_{7.66}$, which is not part of the system studied. This was a preliminary composition, as it was investigated in the initial part of the project where the main objective was to develop a consistent process to produce the powders. The samples were in the shape of a pellet, 13 mm in diameter, with variable thickness.

Two different sintering temperatures, 1400 °C and 1500 °C, and different times of dwell were investigated, as shown in Table 3.9 and Table 3.10. The pellets used for this experiment did not have any mechanical treatment of the powder.

Figure 3.9 and Figure 3.10 show a schematic of sintering cycle for 1400 °C and 1500 °C, respectively.
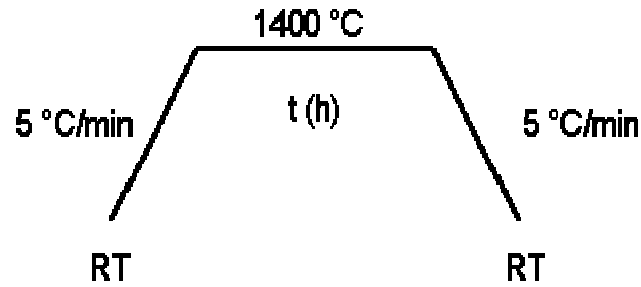
Figure 3.9: Scheme of sintering cycle for 1400 °C with different times of dwell.
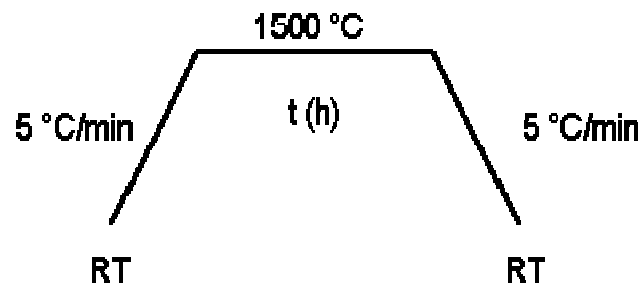
Figure 3.10: Scheme of sintering cycle for 1500 °C with different times of dwell.

In these conditions, the highest density obtained was 82%, for the pellets sintered at 1400 °C for 12 hours.

Table 3.9: Density of pellets sintered at 1400 °C.

Time of dwell, hours	Density, %
2	71
5	76
12	82
24	79

Table 3.10: Density of pellets sintered at 1500 °C.

Time of dwell, hours	Density, %
2	77
5	79
12	79

The next step is to identify the powder characteristics to assess the reasons for insufficient density. To characterise the powders, particle size analyses, SEM and TEM were performed.

SEM
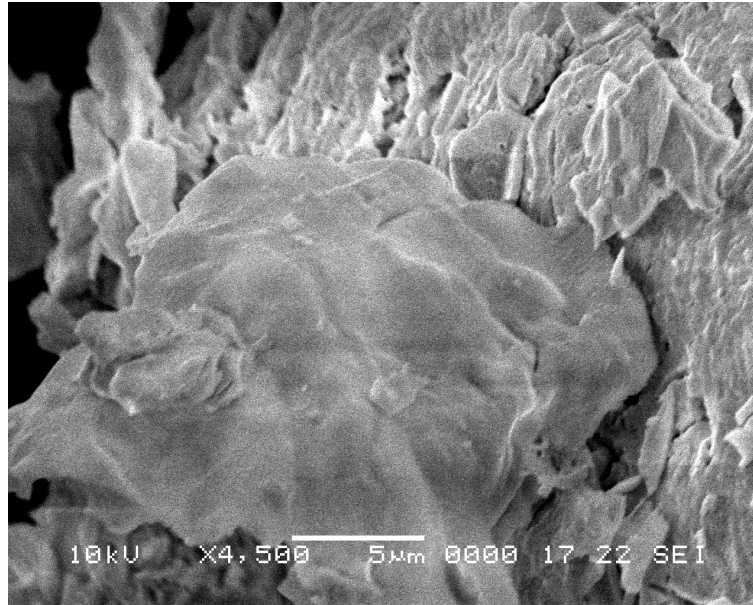
Figure 3.11: SEM picture of powders without mechanical treatment.

Figure 3.11 shows a large hard grain, and on close inspection this large grain results from the densification of smaller grains. Around this large grain, some platelet shape grains can be observed.
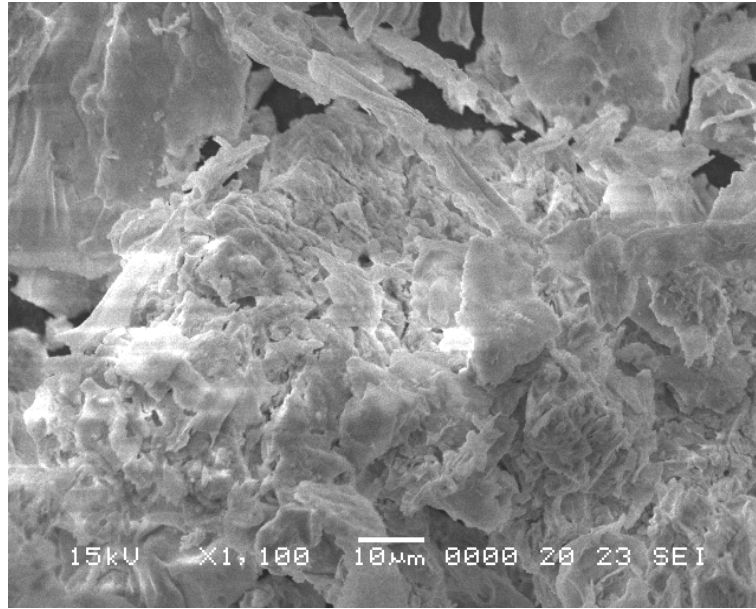
Figure 3.12: SEM picture of powders without mechanical treatment.

Figure 3.12 shows a wide range of grain sizes, some are large as the one on the top left side of the picture, and some smaller grains are agglomerated. These grains are also of different shape; some are of platelet shape, while others are of elongated shape. These images are consistent with an eggshell microstructure.
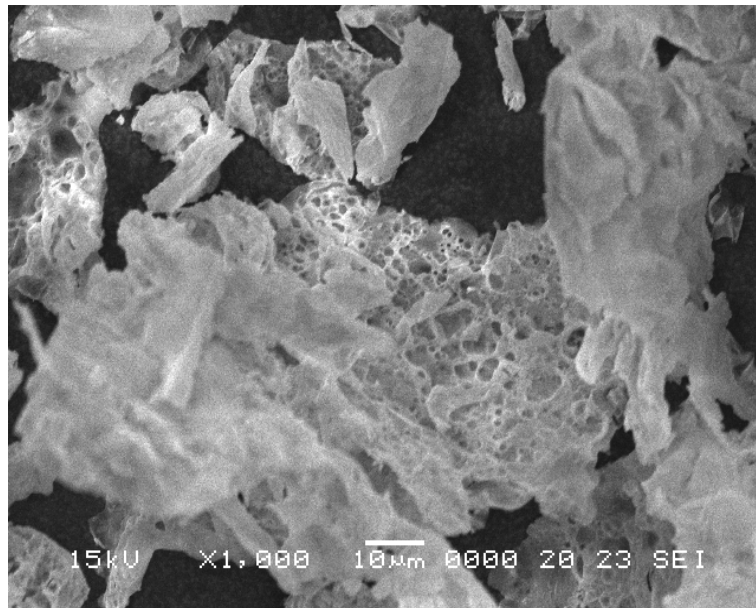
Figure 3.13: SEM picture of powders without mechanical treatment.

Figure 3.13 shows different shapes of particles: there are smaller ones of platelet or elongated shape; but it can also be observed that there is a foam structure that could be formed during the combustion, as the flame is very intense and could originate this type of a hard structure, hard shells, which is difficult to break down.

Particle Size Analysis, PSA

Particle size analyses are a quantitative measurement of the distribution of size of the powder. This is a simple, fast, flexible technique, and produces high quality data [15]. Particle sizes are measured in suspension by laser diffraction. The technique uses the scattering of light, delivered from a laser, which is passed through a chamber containing the particles in suspension [16].
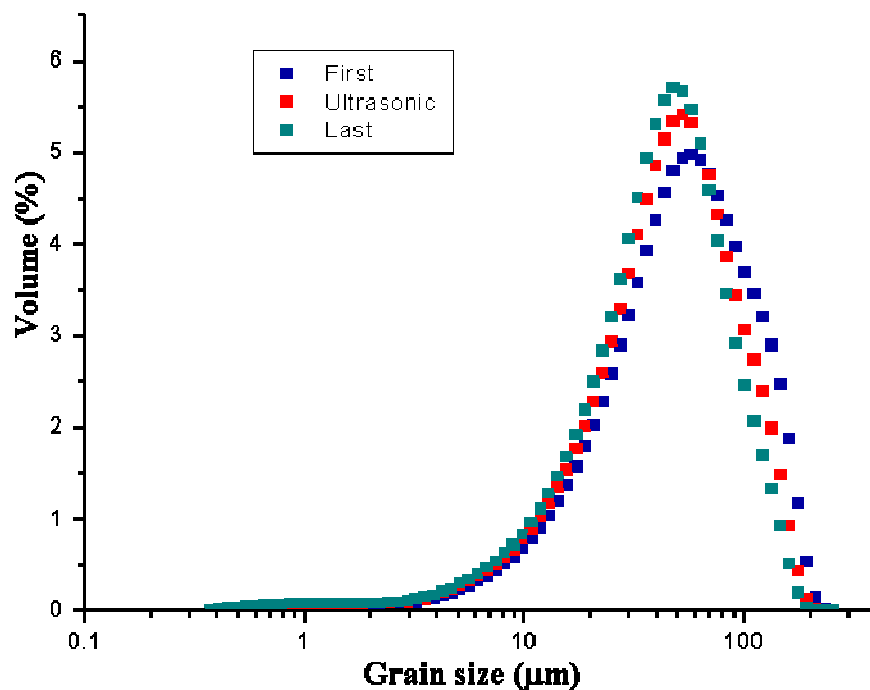
Figure 3.14: Particle size distribution with no mechanical separation treatment.

Figure 3.14 confirms the SEM pictures. It shows a wide range of sizes, from less than 1 to 200 μm. After ultrasonic treatment, there is a slight drop in the particle size, which

could indicate the existence of soft agglomerates which can be easily separated. The majority are hard agglomerates, therefore needing a stronger mechanical separation treatment.

Figure 3.15 shows comparison of particle size distribution curves before and after roll milling.
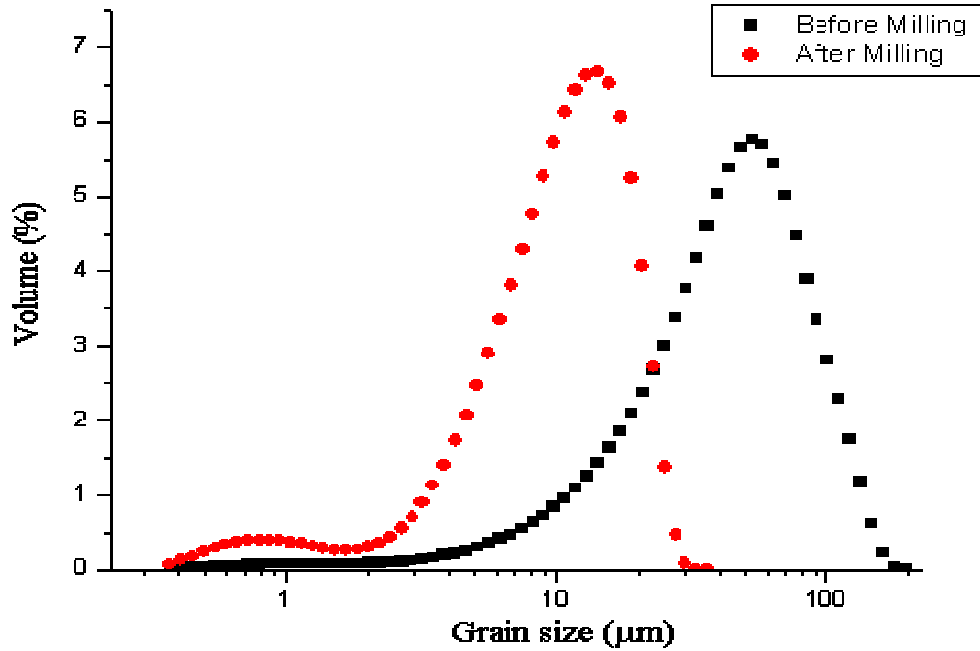
Figure 3.15: Comparison of particle size distribution before and after roll milling.

Before the stage of milling, the average particle size is 51.88 ± 32.74 μm, the larger size of the particle is 194.2 μm and there are particles with the size smaller than 0.375 μm (the smaller size that the equipment can measure accurately), 0.0098 % of the volume. After milling, the average particle size drops to 11.67 ± 6.19 μm, the larger size of particle measured is 33 μm. An increase in the amount of particles smaller than 0.375 μm, is observed. As explained in chapter II, section 2.3.2, the particle size is estimated by the method of the Circle Equivalent Diameter (CE Diameter). If particles have an irregular shape (non-spherical), an error will be introduced, therefore the obtained values are an average.

Sintering is made difficult by the presence of a wide range of sizes and different shapes of the grains; this could be the explanation for the low density obtained in Table 3.8 and Table 3.9. In order to reduce and homogenise the particle size and shape, a milling step is introduced. Several milling techniques are tested to ascertain which is the most appropriate for these particles characteristics.
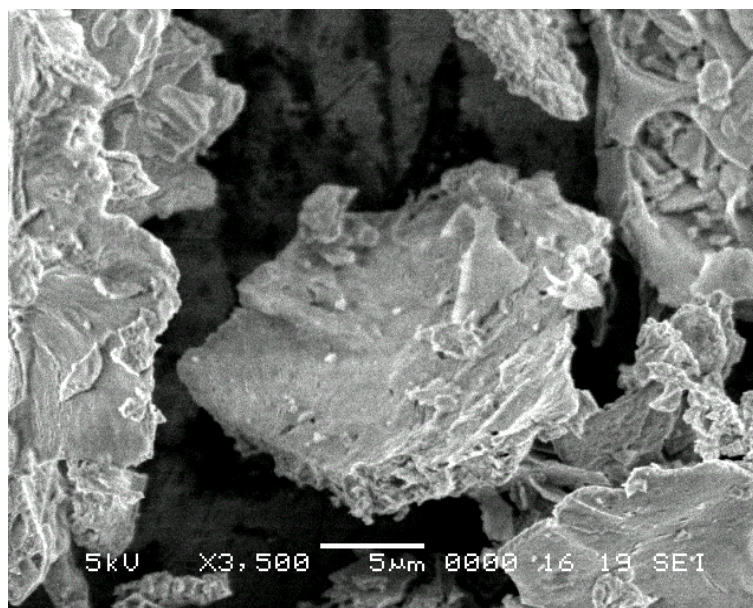
Figure 3.16: SEM picture of powders after 2 and a half hour in the planetary ball mill.

Figure 3.16 confirms Figure 3.16, as there is reduction in the particle size, but not enough to break down all agglomerates and the powders still have the platelet shape, even after 2hours and 30 minutes in the planetary ball mill.

TEM

Figure 3.17 and Figure 3.18 show TEM pictures of powder after 2h30min in the planetary ball mill.
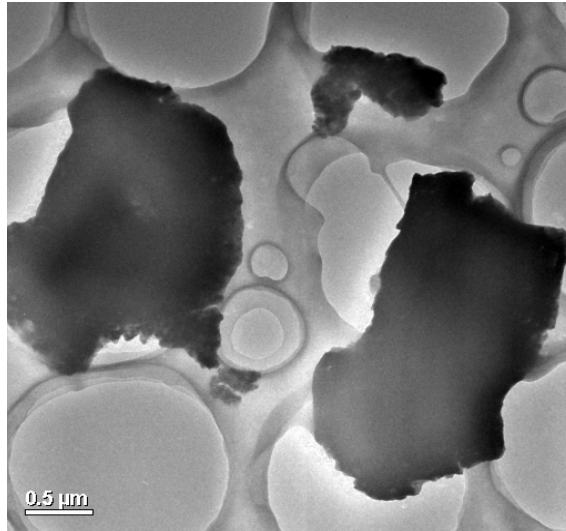
Figure 3.17: TEM picture of the powder milled in the planetary ball mill. TEM operator Dr. David Miller, University of St. Andrews

After the milling stage, Figure 3.17 shows that there is still significant difference between grain sizes. The grains are the dark spots in the picture and the grey circles are the carbon grid, on careful observation of the edges of larger grains reveals that these grains are composed by small particles.
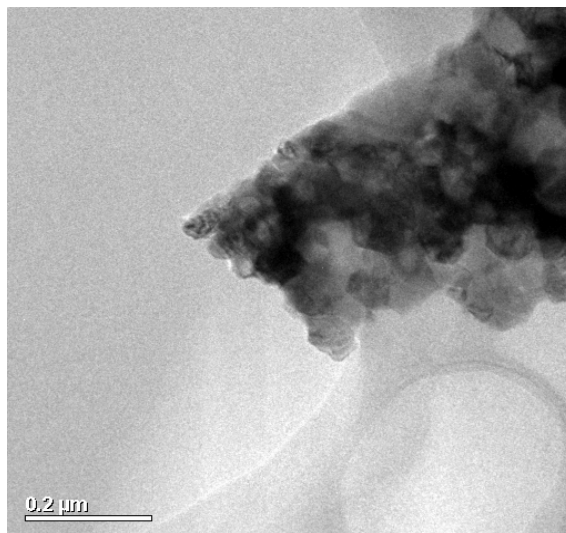
Figure 3.18: TEM picture of the powder milled in the planetary ball mill. TEM operator Dr. David Miller, University of St. Andrews

Figure 3.18 is a magnification of the grains in Figure 3.17; it can be observed that the particle is composed of smaller particles.

Table 3.11 show density values for different mechanical processes of powder separation investigated during this project. The density of pellets without any mechanical treatment is approximately 82 %. Since the results are so poor, mechanical processes and dispersants are introduced in order to separate the agglomerates and reduce the particle size.

Table 3.11: Density values for different mechanical processes of powders separation.

Treatment used	Time, hours	Density, %
Without any treatment	-	82
Roller ball mill + Triton	18	92
Hammer + Triton	18	90
Planetary ball mill + Triton	$2\frac{1}{2}$	98

Note: The solvent used in all mixtures was acetone.

Using the roller ball mill, with triton and acetone for 18 hours, increases the density from 82 % to 92 %; the hammer, using the same mixture of triton and acetone, gives a higher density than when no treatment is used but lower than the density values obtained using the roller ball mill. The planetary ball mill is the mechanical process with higher density values, obtaining up to 98 %; and in addition the planetary ball mill uses less time than the other mechanical processes.

Dilatometry

The experiment is conducted from room temperature to 1500 °C, at a rate of 3 °C/min, in air.
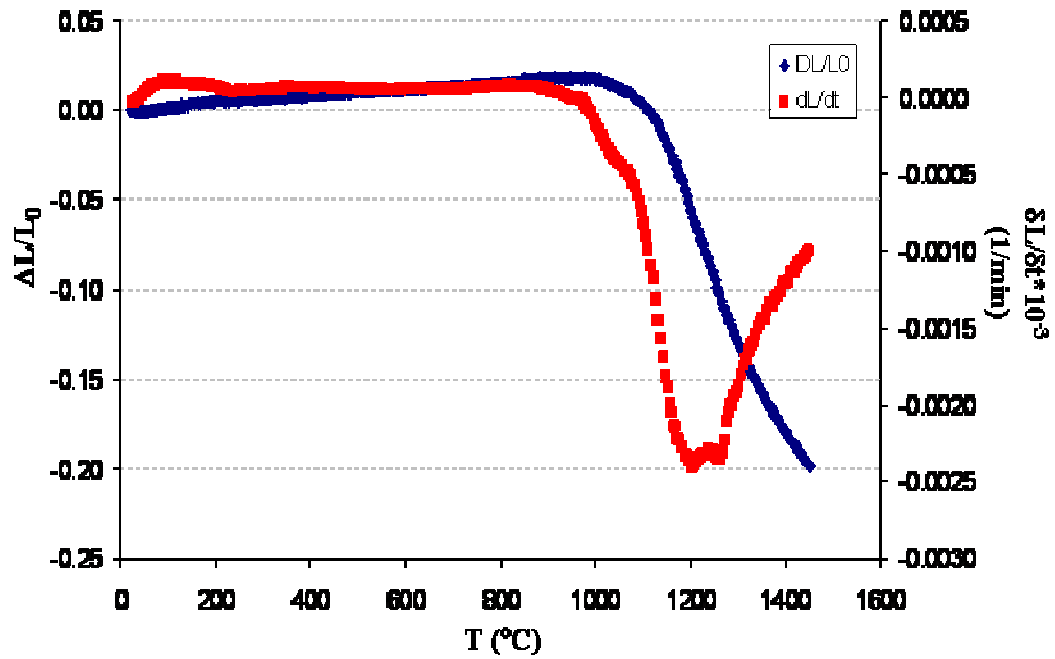
Figure 3.19: Dilatometry of the composition $Ce_{0.04}Y_{0.02}Sc_{0.67}Zr_{3.27}O_{7.66}$

Figure 3.19 shows shrinkage of the pellet when subjected to temperature increase. Sintering initiates at 1089 °C and finishes at 1369 °C. There is a volume reduction of approximately 20 %, from 1089 °C to 1450 °C.
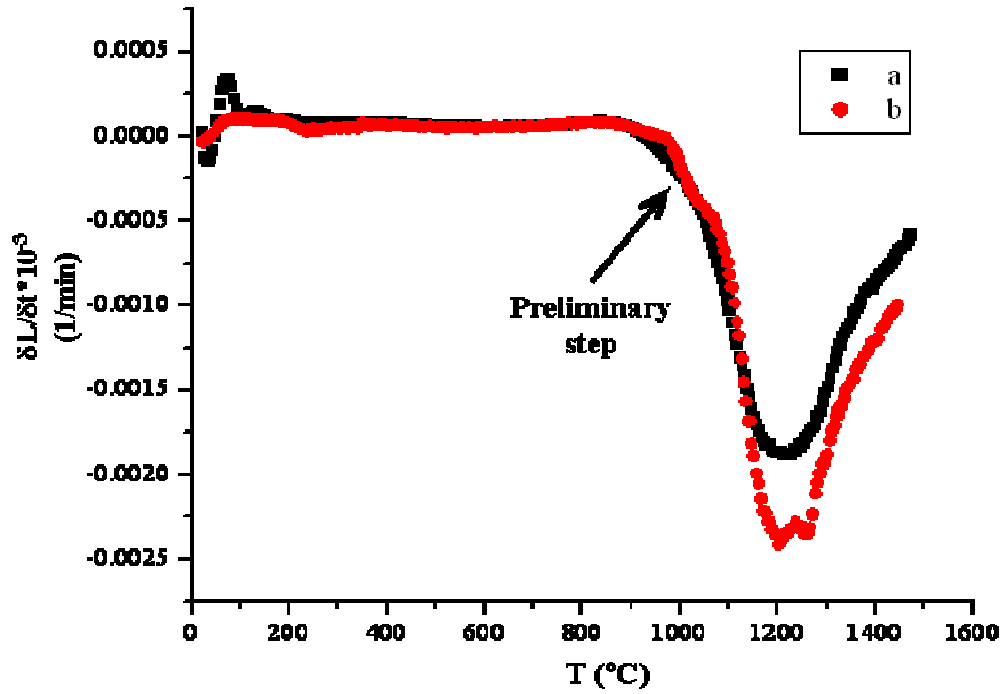
Figure 3.20: Shrinkage vs. temperature for the composition $Ce_{0.04}Y_{0.02}Sc_{0.67}Zr_{3.27}O_{7.66}$; (a) Sample without any mechanical treatment, (b) Sample used the planetary ball mill for 2h30.

Figure 3.20, curve (b), shows the existence of a preliminary step that does not exist on curve (a); this difference on the curves could exist as the smaller grains start to sinter earlier than larger grains.

For the sample studied, green densities are in the range of 36 to 44 %, after sintering the final densities range of 89 to 94 %. The increase in density is almost double; which can be explained by good sinterability of this material and powder production process.

Sintering

All compositions presented in this section are sintered at 1500 °C for 12 hours, as shown in Figure 3.21. Pellets are introduced in the furnace, at 1000 °C, and then temperature is increased by 10 °C/min, until reaching 1500 °C, where it is held for 12 hours. After this, the furnace temperature is decreased by 10 °C/min until reaching 1000 °C. At this stage, pellets are removed from the furnace and left to cool down to room temperature. Figure

3.21 show a schematic of the thermal cycle used to sinter pellets, this cycle was used to sinter all pellets characterised.
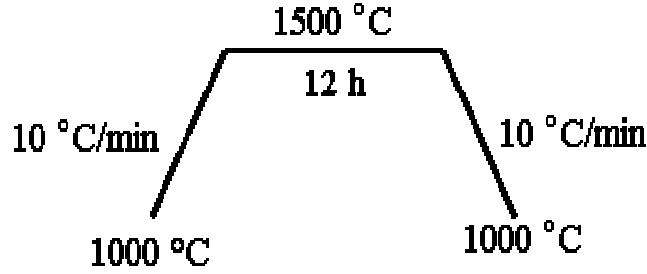
Figure 3.21: Thermal cycle to sinter pellets.

Table 3.12, shows the density of pellets from the system $Ce_xY_{0.2-x}Sc_{0.6}Zr_{3.2}O_{8-\delta}$ ($0 \leq x \leq 0.2$) and from the composition $Ce_{0.04}Y_{0.02}Sc_{0.67}Zr_{3.27}O_{7.66}$, sintered at 1500 C for 12 hours.

Table 3.12: Density of pellets for the system $Ce_xY_{0.2-x}Sc_{0.6}Zr_{3.2}O_{8-\delta}$ ($0 \leq x \leq 0.2$) and the composition $Ce_{0.04}Y_{0.02}Sc_{0.67}Zr_{3.27}O_{7.66}$, sintered at 1500 °C for 12 hours.

Composition	Theoretical density, g/cm^3	Sample density, g/cm^3	Density, %
$Ce_{0.04}Y_{0.02}Sc_{0.67}Zr_{3.27}O_{7.66}$	5.675	5.564	98
$Y_{0.2}Sc_{0.6}Zr_{3.2}O_{7.60}$	5.699	5.228	92
$Ce_{0.04}Y_{0.16}Sc_{0.6}Zr_{3.2}O_{7.62}$	5.691	5.334	94
$Ce_{0.08}Y_{0.12}Sc_{0.6}Zr_{3.2}O_{7.64}$	5.757	5.359	93
$Ce_{0.1}Y_{0.1}Sc_{0.6}Zr_{3.2}O_{7.65}$	5.732	5.551	97
$Ce_{0.12}Y_{0.08}Sc_{0.6}Zr_{3.2}O_{7.66}$	5.771	5.372	93
$Ce_{0.16}Y_{0.04}Sc_{0.6}Zr_{3.2}O_{7.68}$	5.779	5.518	95
$Ce_{0.20}Sc_{0.6}Zr_{3.2}O_{7.70}$	5.798	5.502	95

Density should be compared, first inside the system $Ce_{0.2-x}Y_xSc_{0.6}Zr_{3.2}O_{8-\delta}$ and after that, with the composition $Ce_{0.04}Y_{0.02}Sc_{0.67}Zr_{3.27}O_{7.66}$, which does not belong to the system. The final density of the pellets varies from 92 %, for composition $Y_{0.2}Sc_{0.6}Zr_{3.2}O_{7.60}$, which has no ceria content, to 97 %, for the composition $Ce_{0.1}Y_{0.1}Sc_{0.6}Zr_{3.2}O_{7.65}$, which has equal content of ceria and yttria. The composition with lower density is the one which has no ceria content, but when a small amount of ceria is introduced, density increases reaching the highest value for the composition with the same amount of ceria

and yttria. Compositions with less than 0.1 atoms of ceria per formula unit have lower density values when compared to compositions with more than 0.1 atoms of ceria.

The composition with higher density is $Ce_{0.04}Y_{0.02}Sc_{0.67}Zr_{3.27}O_{7.66}$, which reached 98 %, but this composition does not belong to the system. This composition has a higher content of scandia and zirconia, but for ceria and yttria the content is lower when compared to compositions from the system $Ce_xY_{0.2-x}Sc_{0.6}Zr_{3.2}O_{8-\delta}$.

Observing the density values for compositions with lower yttria content, compositions $Ce_{0.16}Y_{0.04}Sc_{0.6}Zr_{3.2}O_{7.68}$ and $Ce_{0.20}Sc_{0.6}Zr_{3.2}O_{7.70}$, they show higher density than compositions with higher content of yttria. This can indicate that when yttria content is reduced, an increase in density is observed.

3.3.3 Method comparison

Both, sol-gel and combustion method and solid state synthesis method, can produce powders with a single cubic phase, with the fluorite-type structure. The main differences are the time and the temperature that are necessary to be used for the solid state synthesis method. Solid state synthesis method needs more time for preparation of powder before calcination, for the calcination itself and for sintering, as explained in chapter II. It also needs higher temperature in order to achieve the single cubic fluorite-type structure.

Pellets produced by sol-gel and combustion method are sintered at 1500 °C for 12 hours and while pellets produced by solid state synthesis method are sintered at 1500 °C for 36 hours. Density values obtained are significantly higher for the sol-gel and combustion method than solid state method.
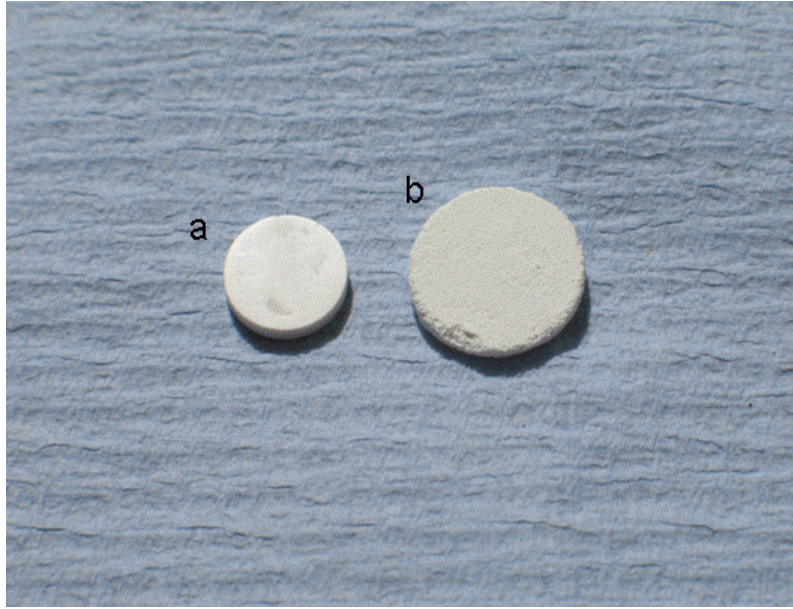
Figure 3.22: Pellets by sol-gel and combustion process (a), sintered at 1500 °C for 12 hours and solid state synthesis method (b), sintered at 1500 °C for 36 hours.

Figure 3.22, shows two pellets, the pellet on the left (a) obtained from powders produced by sol-gel and combustion method and the pellet on the right (b) obtained from powders produced by solid state synthesis method. Both pellets on Figure 3.23 had the same initial diameter, as they were compacted in the same die, but pellet from sol-gel and combustion shrank after sintering. By the observation of both pellets, the one produced by sol-gel and combustion method appears to be more dense and has higher mechanical stability, while pellet produced by solid state synthesis method appears to be porous and with low mechanical stability.

3.4 Summary

- All compositions studied in the system $Ce_xY_{0.2-x}Sc_{0.6}Zr_{3.2}O_{8-\delta}$ and initial composition, $Ce_{0.04}Y_{0.02}Sc_{0.67}Zr_{3.27}O_{7.66}$, show the presence of a single phase, with a cubic fluorite-type structure.

- Lattice parameter increases from 5.1040(7) Å to 5.115(1) Å, in the system $Ce_xY_{0.2-x}Sc_{0.6}Zr_{3.2}O_{8-\delta}$ ($0 \leq x \leq 0.2$), with the introduction of ceria. This variation is in agreement with the Vegard's law.

- ICP results show that the amount of silicon is negligible; on the other hand, the amount of aluminium is significant, as aluminium can be introduced at several stages during the powders production..

- The Debye Scherrer equation shows that the particle size decreases, when the ceria content increases and yttria content decreases.

- Sol-gel and combustion process can be used as an alternative method to solid state synthesis, as it uses less time and heat to produce powders and also the materials obtained from the powders. The sol-gel and combustion method produces nano-particles although some agglomerates can also be formed; there is also the formation of hard agglomerates (shells) during the combustion. This leads to a wide range of grain sizes and the formation of grains with non spherical shape (platelet and some look like sticks).

- Two possible ways to solve or attenuate the agglomerate problem are: (1) to control the combustion; and (2) to introduce chemical dispersants and strong mechanical separation treatments, in order to breakdown these agglomerates.

- Sol-gel and combustion process should be done in a controlled environment, because the combustion stage is too violent and there is a gradient of temperature inside the beaker. If the process would be performed in a controlled environment, the amount of fuel (glycine) and oxidizing element (oxygen) would be reduced. Reducing the quantity of the ignition fuel and/or the oxygen, the combustion could be more progressive and less violent.

- Mechanical processes combined with chemical dispersants are effective to reduce particle size. These processes can breakdown some agglomerates, this way improving the final density, as shown in Table 3.11. The density increased from 82 %, without any treatment, to 98 % using the planetary ball mill.

- In the solid state method, some grains start to sinter as agglomerates but do not sinter as a compact body; this can explain the high porosity, low density and low mechanical stability. The final product, in the sol-gel and combustion method, has higher density and therefore better electrical properties (see chapter IV) and mechanical properties.

References

1. Shmalzried, H., *Solid State Reactions*. Vol. 12. 1981, Deerfiel, Florida: Monographs in Modern Chemistry.
2. West, A.R., *Basic Solid State Chemistry*. 2nd ed. 1999, Chichester: John Wiley & Sons, Ltd.
3. Wold, A. and Dwight, K., *Solid State Chemistry, Synthesis, Structure and Properties of Selected Oxides and Sulphides*. 1993, New York: Chapman & Hall, Inc.
4. Nomura, K., Mizutari, Y., Kawai, H., Nakamura, Y., Yamamoto, O., Solid State Ionics, **132** (2000) p. 235-239.
5. Lee, D., Lee, I., Jeon, Y., Song, R., Solid State Ionics, **176** (2005) p. 1021-1025.
6. Xu, G., Zhang, Y., Liao, C. and Yan, C., Solid State Communication, **121** (2002) p. 45-49.
7. Menchi, A., Scian, A., Materials letters, **59** (2005) p. 2664-2667.
8. Petrova, N. and Todorovsky, D., Materials Research Bulletin, (2005) p. 1-14.
9. Boskovic, S.B., Djurovic, D. R., Zec, S. P., Matovic, B. Z., Zinkevich, M., Aldinger, F., Ceramics International, **34** (2007) p. 2001-2006.
10. Yamamoto, T., Momida, H., Hamada, T., Uda, T., Ohno, T., Thin solid films, **486** (2005) p. 136-140.
11. de Carvalho, E.M.S., Irvine, J.T.S. in *X SOFC*. 2007. Nara, Japan: ECS Trans.
12. Michael, M.S., Fauzi, A., Prabaharan, S.R.S., International Journal of Inorganic Materials, (2) (2000) p. 261-267.
13. Denton, A.R., Ashcroft, N. W., Physical Review A, **43**(6) (1991) p. 3161-3164.
14. Jacob, K.T., Raj, S., Rannesh, L, International Journal of Materials Research, **6** (2007) p. 776-779.
15. Chinn, R.E., *Ceramography, Preparation and Analysis of Ceramic Microstructures*. ASM International. 2002: Materials Park.
16. www.Malvern.co.uk. 2002 [cited 2006 July].

Chapter IV

Electrical Characterisation

4.1. Introduction

Electrochemical Impedance Spectroscopy (EIS) is a powerful method to investigate electrical behaviour of materials and interfaces. It can be used to investigate the fuel cell as a whole, and also to separately study the different processes that take place in the fuel cell in order to determine the influence of each process on the global fuel cell performance [1].

Yttria stabilised zirconia, YSZ, has been intensively studied, and its characteristics, such as high ionic conductivity, low electronic conductivity, good mechanical properties, stability in long term experiments and under reducing and oxidising conditions, made it possible for this material to be used as an electrolyte for solid oxide fuel cells, SOFC [2-5].

Problems with phase stability and the increase of availability of scandia increased the investigation of scandia stabilised zirconia, SSZ, which have higher values for ionic conductivity than YSZ, up to three times. In order to fully stabilise a Sc_2O_3-ZrO_2 system, it is necessary to introduce 8-9 mol % of Sc_2O_3.

SSZ ionic conductivity, at 800 °C, is 0.11-0.12 S/cm [6, 7] and when Sc_2O_3-ZrO_2 is fully stabilised with Y_2O_3, the ionic conductivity, at 800 °C, drops to 0.059 S/cm [4].

Figure 4.1 shows values for conductivity of different materials composed by zirconia, scandia, yttria and ceria, at 600 °C.
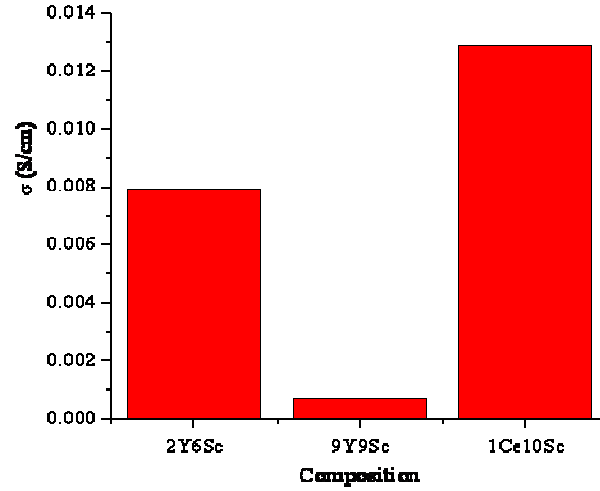
Figure 4.1: Values of conductivity for different composition of zirconia, scandia, yttria and ceria, at 600 °C.

In Figure 4.1, a clear drop in the conductivity occurs when scandia content increases, at 600 °C. For $(Y_2O_3)_2(Sc_2O_3)_6(ZrO_2)_{92}$ (2Y6Sc), the conductivity is 0.0079 S/cm, $(Y_2O_3)_9(Sc_2O_3)_9(ZrO_2)_{82}$ (9Y9Sc) [8] the ionic conductivity is 0.0007 S/cm and $(CeO_2)_1(Sc_2O_3)_{10}(ZrO_2)_{89}$ (1Ce10Sc) [9] the conductivity increased to 0.0129 S/cm, at 600 °C. Although the introduction of Y_2O_3 decreases the ionic conductivity, it will fully stabilise the Sc_2O_3-ZrO_2 system. There is a variation on conductivity when yttria content varies. When the amount of yttria increases conductivity decreases significantly, even when the amount of scandia increases. For a small amount of ceria are introduced conductivity increases significantly [10-12].

Ionic conductivity is strongly dependent on the type and concentration of dopants, as distortions of lattice will occur with the introduction of dopant. When ceria, a large ion, is introduced in the zirconia, it will produce an open structure through which oxygen ions can easily migrate [13]. The introduction of ceria in the system Y_2O_3-Sc_2O_3-ZrO_2, is expected to increase ionic conductivity and decrease the amount of yttria to be introduced in the system.

The acceptor-doped ZrO_2 presents a blocking effect to the ionic transport across the grain boundary. The specific grain boundary conductivity is usually at least two orders

of magnitude lower than that of the bulk. This blocking effect was initially attributed to an intergranular phase of silica, but this idea has been replaced by the idea that the oxygen vacancy depletion in the grain boundary space-charge layer is the cause of the low grain boundary conductivity. The grain boundary blocking effect disappears at intermediate temperature or sufficient dopant concentration [14].

In Ce_2O_3, at low oxygen partial pressures, the valence is changed from 4^+ to 3^+ [15]. When these conditions occur, the vacancies reach a point that they start to order in clusters and can create a wall to ionic conduction [16].

4.2. Experimental

Samples were polished to obtain a smooth surface, on which a platinum paste was applied with a brush, to sinter the platinum the pellets had a thermal treatment at 900 °C for 20 min.

The impedance measurements were performed by two different analysers:

- Solatron 1260 the frequency range swept from 100 MHz to 1Hz, the effective AC voltage amounted to 50 mV.

- Alpha-A, Novocontrol the frequency range swept from 3 MHz to100 mHz and the effective AC voltage amounted to 20 mV.

ZView version 3.0a is used to fit the data from Solatron 1260 and WinFit 3.2 (Novocontrol Technologies) is used to fit data from Alpha-A Novocontrol.

For temperature variation, all pellets were studied in the air and in a range of temperatures from 300 to 900 °C.

The oxygen partial pressure was varied by application of appropriate gas mixtures in the range from 1 to 10^{-24} bar at 700 °C. The composition of the gas mixture was adjusted and maintained constant by using mass flow controllers (Hastings 302). The oxygen

partial pressure was measured by a zirconia-based potentiometric sensor and the temperature was monitored close to the sample by a type-S thermocouple.

4.3. Results and discussion

4.3.1 AC Impedance Measurement as Function of Temperature

To perform these tests, pellets are investigated in air, in a range of temperatures, from 300 to 900 °C. The material used as electrodes is platinum. Several pellets were tested, for each composition. The selected pellets to be presented, in this chapter, are the ones which showed better ionic conductivity.

Table 4.1: Density of the pellets of the system $Ce_xY_{0.2-x}Sc_{0.6}Zr_{3.2}O_{8-\delta}$ ($0 \leq x \leq 0.2$) and the composition $Ce_{0.04}Y_{0.02}Sc_{0.67}Zr_{3.27}O_{7.66}$ and nomenclature, sintered at 1500 °C for 12 hours.

Composition	Theoretical density, g/cm^3	Sample density, g/cm^3	% density	Nomenclature
$Ce_{0.04}Y_{0.02}Sc_{0.67}Zr_{3.27}O_{7.66}$	5.675	5.146	91	initial
$Y_{0.2}Sc_{0.6}Zr_{3.2}O_{7.60}$	5.716	5.126	90	x=0.00
$Ce_{0.04}Y_{0.16}Sc_{0.6}Zr_{3.2}O_{7.62}$	5.769	5.199	91	x=0.04
$Ce_{0.08}Y_{0.12}Sc_{0.6}Zr_{3.2}O_{7.64}$	5.757	5.389	94	x=0.08
$Ce_{0.1}Y_{0.1}Sc_{0.6}Zr_{3.2}O_{7.65}$	5.851	5.191	89	x=0.10
$Ce_{0.12}Y_{0.08}Sc_{0.6}Zr_{3.2}O_{7.66}$	5.807	5.213	90	x=0.12
$Ce_{0.16}Y_{0.04}Sc_{0.6}Zr_{3.2}O_{7.68}$	5.779	5.318	92	x=0.16
$Ce_{0.20}Sc_{0.6}Zr_{3.2}O_{7.70}$	5.798	5.386	93	x=0.20

Table 4.1 shows information about the compositions, density and nomenclature of the pellets, which will be used to perform experiments, in this chapter.

Impedance Spectra

The semi-circle fitting and the equivalent circuit simulation can be found in appendix 1. Values for the resistance of the components, capacitance and respective estimate errors are shown next to the fittings.

$Y_{0.20}Sc_{0.6}Zr_{3.2}O_{7.60}$

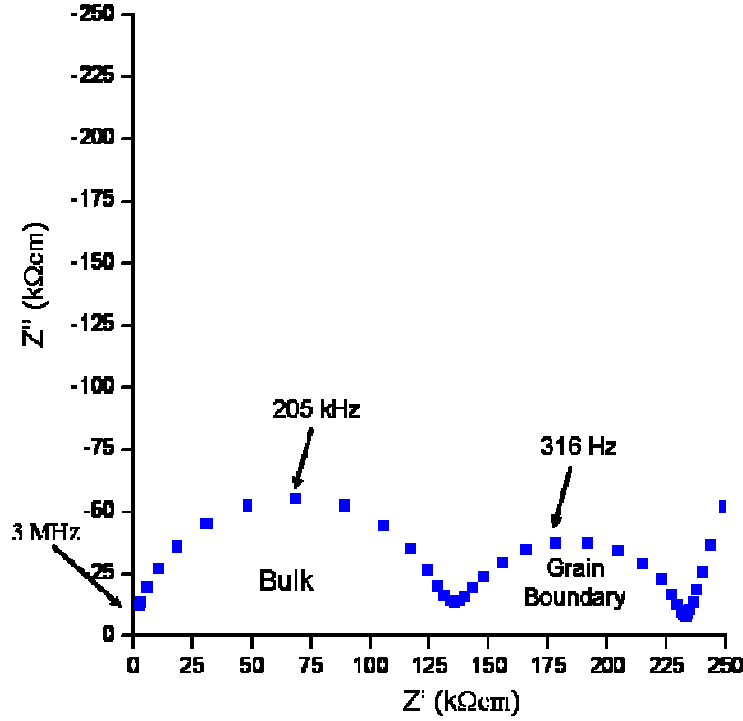Figure 4.2 shows the impedance plot corrected by geometry, recorded at 304 °C, for the composition $Y_{0.20}Sc_{0.6}Zr_{3.2}O_{7.60}$. The different processes are identified in Figure 4.2, Bulk, grain boundary and electrode processes.
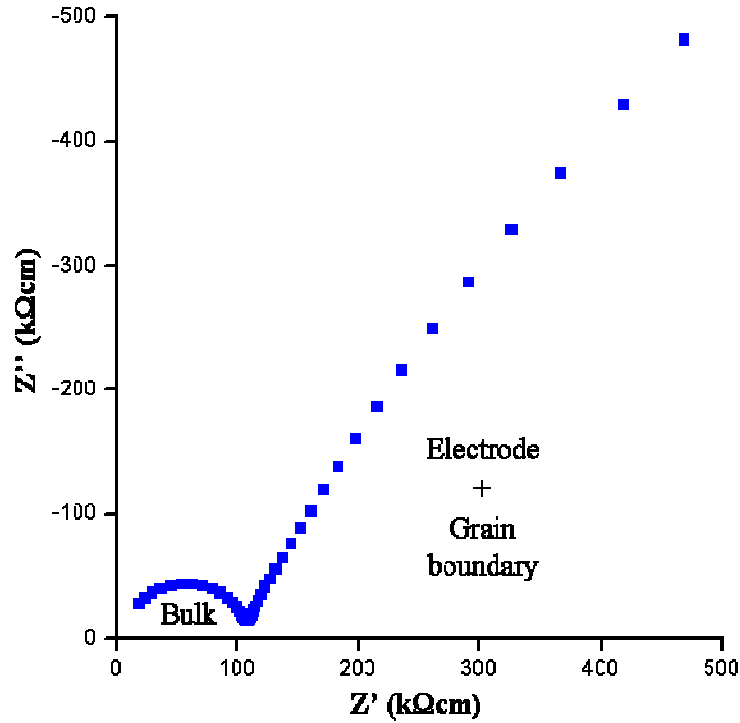
Figure 4.2: Impedance spectra plot corrected by geometry, recorded at 304 °C, for composition $Y_{0.20}Sc_{0.6}Zr_{3.2}O_{7.60}$.

The grain boundary and the electrode curve are difficult to differentiate in the impedance spectra curve, Figure 4.2. Even observing the magnification, Figure 4.3, there is no

possibility of separating grain boundary and electrode process. Fitting curve from Figure 4.2, using Zview programme and the Equivalent Circuit software, version 4.55, it was not possible to fit properly the grain boundary and the electrode processes.
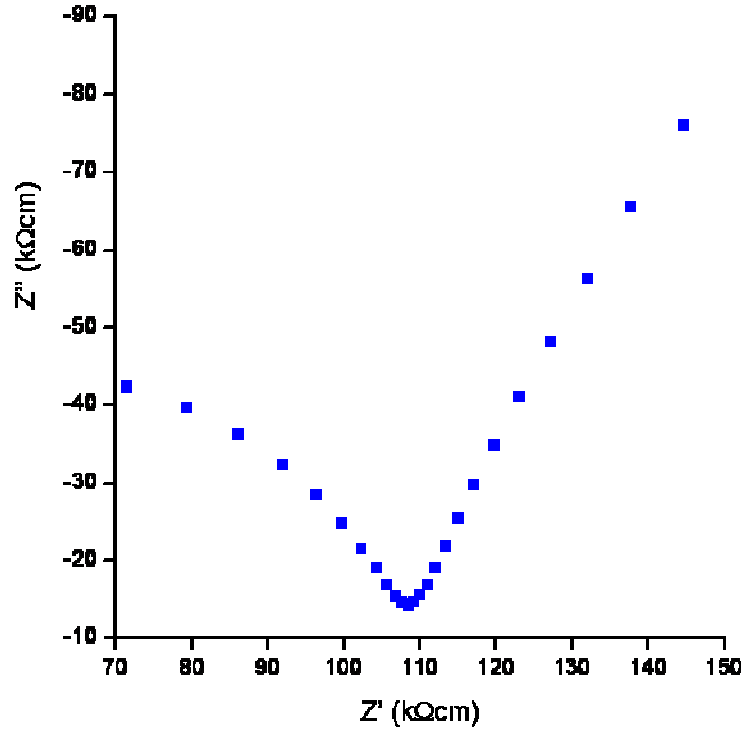
Figure 4.3: Magnification of impedance spectra plot corrected by geometry, recorded at 304 °C, for composition $Y_{0.20}Sc_{0.6}Zr_{3.2}O_{7.60}$.

Table 4.2 shows resistance, resistivity and capacitance, for bulk and grain boundary processes.

Table 4.2: Resistance, resistivity and capacitance, for bulk and grain boundary process, for the composition $Y_{0.20}Sc_{0.6}Zr_{3.2}O_{7.60}$, at 304 °C.

	Resistance, Ω	Resistivity, Ωcm	Capacitance, F/cm
Bulk	$1.51x10^4$	$1.08x10^5$	$5.10x10^{-12}$
Grain Boundary	N/A	N/A	N/A
Total	N/A	N/A	-

$Ce_{0.08}Y_{0.12}Sc_{0.6}Zr_{3.2}O_{7.64}$

Figure 4.4 shows the impedance plot corrected by geometry, recorded at 300 °C, for composition $Ce_{0.08}Y_{0.12}Sc_{0.6}Zr_{3.2}O_{7.64}$. The different processes are indicated.

**Figure 4.4:** Impedance spectra plot corrected by geometry, recorded at 300 °C, for composition $Ce_{0.08}Y_{0.12}Sc_{0.6}Zr_{3.2}O_{7.64}$.

Table 4.3 shows resistance, resistivity and capacitance, for bulk and grain boundary processes, for composition $Ce_{0.08}Y_{0.12}Sc_{0.6}Zr_{3.2}O_{7.64}$.

Table 4.3: Resistance and capacitance, for bulk and grain boundary process, for the composition $Ce_{0.08}Y_{0.12}Sc_{0.6}Zr_{3.2}O_{7.64}$, at 300 °C.

	Resistance, Ω	Resistivity, Ωcm	Capacitance, F/cm
Bulk	$1.39x10^5$	$6.69x10^5$	$2.45x10^{-11}$
Grain Boundary	$1.05x10^5$	$5.05x10^5$	$1.53x10^{-8}$
Total	$2.44x10^5$	$1.17x10^6$	-

$Ce_{0.12}Y_{0.08}Sc_{0.6}Zr_{3.2}O_{7.66}$

Figure 4.5 shows the impedance plot corrected by geometry, recorded at 300 °C, for composition $Ce_{0.12}Y_{0.08}Sc_{0.6}Zr_{3.2}O_{7.66}$. The different processes are indicated.
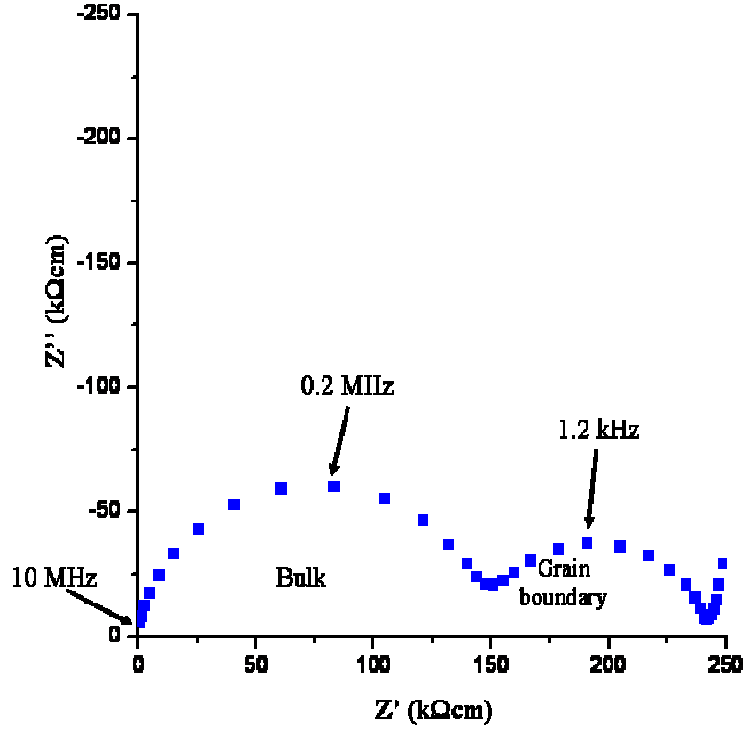
Figure 4.5: Impedance spectra plots corrected by geometry, recorded at 300 °C, for composition $Ce_{0.12}Y_{0.08}Sc_{0.6}Zr_{3.2}O_{7.66}$.

Table 4.4 shows resistance, resistivity and capacitance, for bulk and grain boundary processes, for composition $Ce_{0.12}Y_{0.08}Sc_{0.6}Zr_{3.2}O_{7.66}$.

Table 4.4: Resistance and capacitance, for bulk and grain boundary process, for the composition $Ce_{0.12}Y_{0.08}Sc_{0.6}Zr_{3.2}O_{7.66}$, at 300 °C.

	Resistance, Ω	Resistivity, Ωcm	Capacitance, F/cm
Bulk	4.38×10^{4}	4.11×10^{5}	1.43×10^{-11}
Grain Boundary	2.49×10^{4}	2.34×10^{5}	4.51×10^{-9}
Total	6.87×10^{4}	6.45×10^{5}	-

$Ce_{0.20}Sc_{0.6}Zr_{3.2}O_{7.70}$

Figure 4.6 shows the impedance plot corrected by geometry, recorded at 300 °C, for composition $Ce_{0.20}Sc_{0.6}Zr_{3.2}O_{7.70}$. The different processes are indicated.
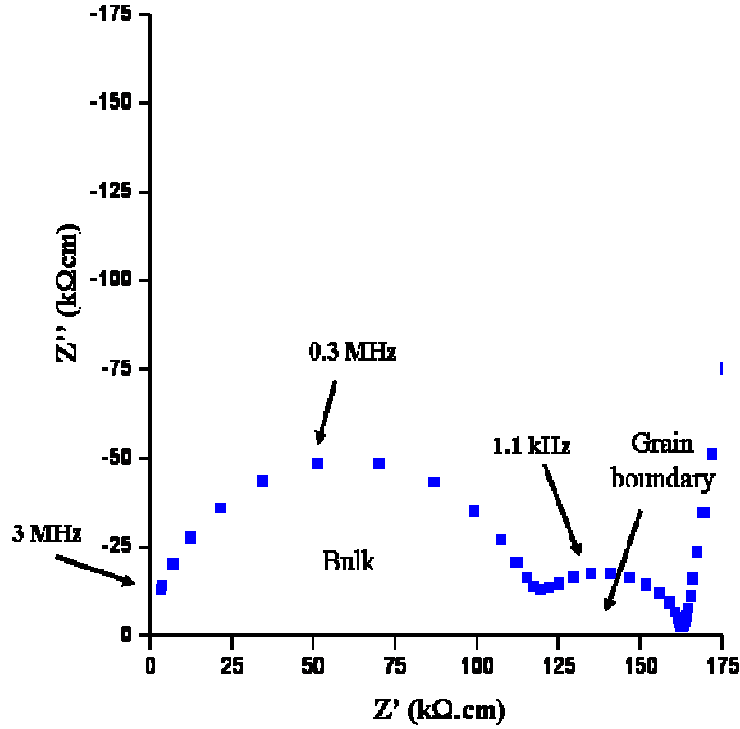
Figure 4.6: Impedance spectra plot corrected by geometry, recorded at 300 °C, for composition $Ce_{0.20}Sc_{0.6}Zr_{3.2}O_{7.70}$.

Table 4.5 shows resistance, resistivity and capacitance, for bulk and grain boundary processes, for composition $Ce_{0.20}Sc_{0.6}Zr_{3.2}O_{7.70}$.

Table 4.5: Resistance and capacitance, for bulk and grain boundary process, for the composition $Ce_{0.20}Sc_{0.6}Zr_{3.2}O_{7.70}$, at 300 °C.

	Resistance, Ω	Resistivity, Ωcm	Capacitance, F/cm
Bulk	$2.84x10^4$	$1.36x10^5$	$1.36x10^{-11}$
Grain Boundary	$1.40x10^4$	$6.66x10^4$	$1.43x10^{-8}$
Total	$4.24x10^4$	$8.02x10^5$	-

All the impedance spectra were recorded at approximately 300 °C; therefore this comparison will be made for low temperature. For the composition $Y_{0.20}Sc_{0.6}Zr_{3.2}O_{7.60}$, in Figure 4.2, composition $Y_{0.20}Sc_{0.6}Zr_{3.2}O_{7.60}$, the bulk response is defined but the grain boundary and electrode response undistinguishable. It was impossible to differentiate when fitting was tried. The impedance spectra, Figure 4.4, composition $Ce_{0.08}Y_{0.12}Sc_{0.6}Zr_{3.2}O_{7.64}$, shows that, at low temperatures, the total conductivity is affected by the response of two different processes, although the bulk is the process which contributes more for the total resistivity. Table 4.3 shows the resistivity values have the same order of magnitude and the values of the capacitance are as expected for each process [17]. For composition $Ce_{0.12}Y_{0.08}Sc_{0.6}Zr_{3.2}O_{7.66}$, Figure 4.5 and Table 4.4, bulk response has a higher contribution, for resistivity, although bulk and grain boundary have the same order of magnitude. Figure 4.6 and Table 4.5, composition $Ce_{0.20}Sc_{0.6}Zr_{3.2}O_{7.70}$, bulk response has a higher contribution, for resistivity than grain boundary response, this difference has an order of magnitude.

For Figure 4.2 the grain boundary and electrode response can not be separated; therefore this composition will not be considered for comparison between compositions. From the observation of Figure 4.4, 4.5 and 4.6, the introduction of ceria promotes a decrease in the grain boundary response, while for the bulk process resistivity increases; the gap between these two values increases with the increase in ceria content. Table 4.3, 4.4 and 4.5 show resistance, resistivity and capacitance values, for bulk, grain boundary processes. The resistivity values, bulk and grain boundary, for composition $Ce_{0.08}Y_{0.12}Sc_{0.6}Zr_{3.2}O_{7.64}$ are similar. When ceria content increases, resistivity values for the bulk process increase; while for the grain boundary process, the resistivity values decrease. The increase in resistivity of the bulk process can be caused by the blocking effect of the large cerium (IV) ions are within the zirconia lattice. The decrease of resistivity in the grain boundary process shows a change in the composition and the structure of the grain boundary, with the increase of ceria, [9]. For composition $Ce_{0.20}Sc_{0.6}Zr_{3.2}O_{7.70}$, which has the highest ceria content, the difference between bulk and grain boundary resistivity is of an order of magnitude. Capacitance values are within the expected values found in literature, [17].
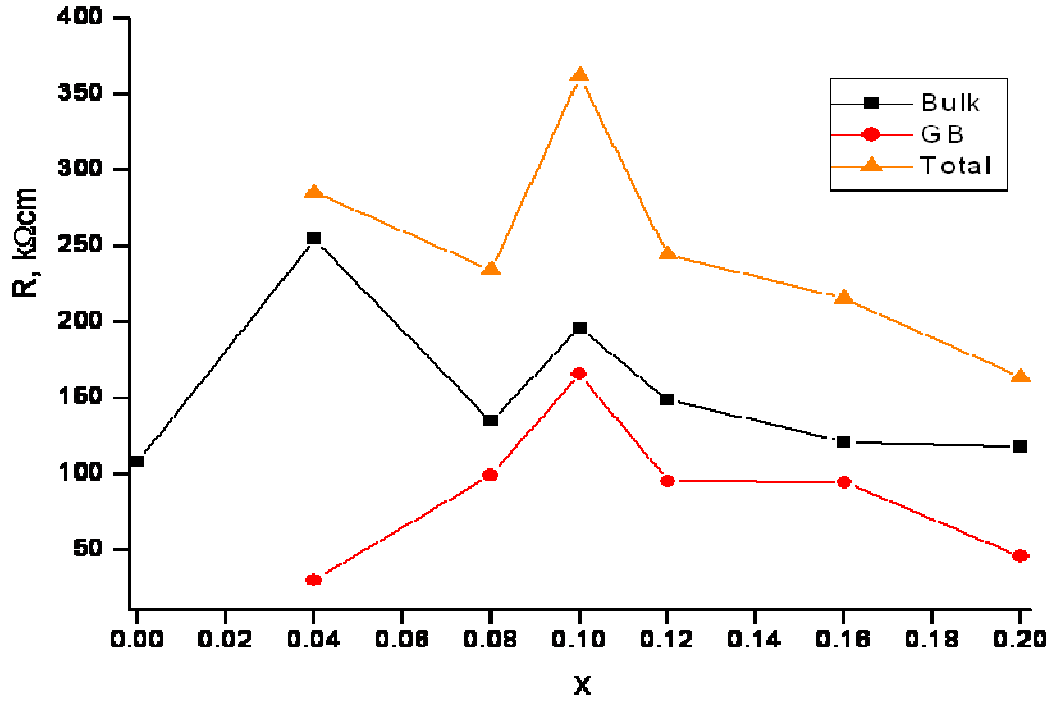
Figure 4.7: Resistance, total, bulk and grain boundary, for all composition, at 300 °C. x equals ceria content.

Figure 4.7 shows the bulk resistivity, the grain boundary resistivity and the total resistivity for all compositions at 300 ºC against x, which is the ceria content for each composition. For composition $Y_{0.20}Sc_{0.6}Zr_{3.2}O_{7.60}$, it was not possible to fit properly the grain boundary component; therefore this value is not represented in Figure 4.7. For composition $Ce_{0.1}Y_{0.1}Sc_{0.6}Zr_{3.2}O_{7.65}$, which has the same amount of ceria and yttria, the total resistivity is the highest and as for bulk and grain boundary components, the values are higher than for the adjacent compositions. If the graphic could be cut in half, it can be observed that the compositions with higher ceria content, higher than 0.1 atoms of ceria, the values for all resistivity components decrease, while for compositions with lower ceria content total resistivity increases. This can indicate that the introduction of ceria promotes conductivity. For compositions $Ce_{0.08}Y_{0.12}Sc_{0.6}Zr_{3.2}O_{7.64}$ and $Ce_{0.16}Y_{0.04}Sc_{0.6}Zr_{3.2}O_{7.68}$, resistivity values for total are similar, the same occurs for the bulk, grain boundary resistivity.

At this temperature, 300 °C, bulk resistivity values are higher than for grain boundary, for all compositions, this indicates that the bulk process is dominant. This difference is more significant for composition $Ce_{0.04}Y_{0.16}Sc_{0.6}Zr_{3.2}O_{7.62}$, where more than 90 % of the total resistivity comes from the bulk resistivity.

Arrhenius plot

Arrhenius plot are plotted to be used in the analyses of the temperature effect on the rates of chemical reactions. At higher temperatures, the probability that two molecules will collide is higher than at lower temperatures. This higher collision rate results in a higher kinetic energy, which has an effect on the activation energy of the reaction. In the Arrhenius plot, if the curve is a straight line, it means that there is only one process thermally activated [18-21]. Arrhenius equation used in the Arrhenius plot for these analyses is as follow,

$$\sigma = Ae^{\frac{-E_a}{kT}} \qquad (4.1)$$

Legend:

$\sigma \rightarrow$ Rate constant, s^{-1}

$A \rightarrow$ Pre-exponential factor: that contains several constants, such as number of collisions, of mobile ions, per second, 2.728 s^{-1}

$E_a \rightarrow$ Activation energy, $eV = J/mol$

$k \rightarrow$ Boltzmann constant, 1.3807 x 10^{-23} JK^{-1}

$T \rightarrow$ Absolute temperature, K

Activation energy, Ea, and pre-exponential factor, A, are the two variable that can be determined by the Arrhenius equation (4.1). The activation energy is the amount of energy required to ensure that a reaction occurs.

The Arrhenius plot is represented with $log\,\sigma T\ vs.\dfrac{1000}{T}$, to solve the equation used (4.1), the logarithm form has to be used, shown in equation (4.2) and (4.3)

$$Log(\sigma) = Log(A) + log\left(e^{\frac{-E_a}{kT}}\right) \qquad (4.2)$$

$$Log(\sigma T) = Log\left(\frac{A}{T}\right) - \frac{E_a}{2.303kT} \qquad (4.3)$$
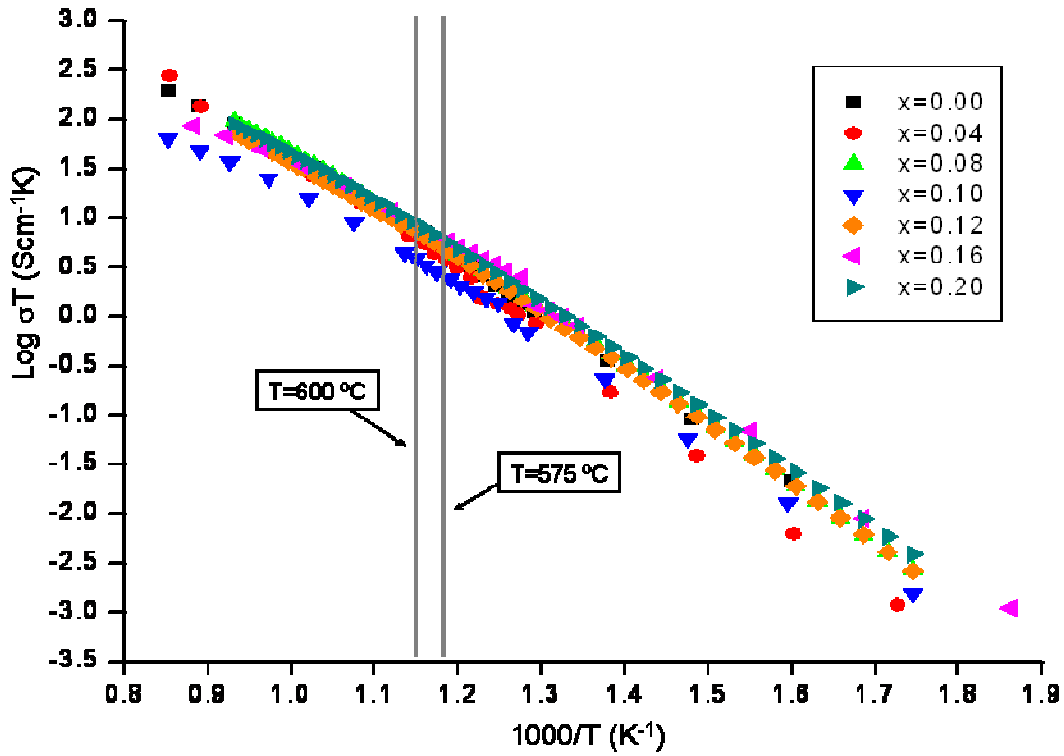
Figure 4.8: Arrhenius plot of total conductivity for the compositions, Table 4.1

The Arrhenius plot, Figure 4.8, shows that all compositions have a similar behaviour; there are two regions in the plot, at high and low temperatures. There is a temperature interval, between 575 and 600 ºC, where all compositions change conductive behaviour.

This change occurs due to the shift from a slower ionic conductive process to a faster ionic conductive process. At low temperature the conductive process is divided in two parts, the first to dissociate oxygen vacancy from a cluster and the second the oxygen vacancy migration process. While at high temperature vacancies are free and the energy necessary is only for the oxygen vacancy migration.

There is no significant difference in conductivity between compositions, although curves with lower ceria content are situated below the ones with higher ceria content. This difference diminishes at high temperatures. The composition $Ce_{0.04}Y_{0.16}Sc_{0.6}Zr_{3.2}O_{7.62}$ has low conductivity at low temperature, but at intermediate and high temperature, conductivity increases to similar values from the other compositions.

Table 4.6 show the values for the ionic conductivity, for compositions of the system $Ce_xY_{0.2-x}Sc_{0.6}Zr_{3.2}O_{8-\delta}$ ($0 \leq x \leq 0.2$), at 600 °C. Compositions which have similar contents of ceria and yttria show lower values for ionic conductivity.

Table 4.6: Values for conductivity at 600 °C

Composition	Conductivity, S/cm
$Y_{0.2}Sc_{0.6}Zr_{3.2}O_{7.60}$	0.010
$Ce_{0.04}Y_{0.16}Sc_{0.6}Zr_{3.2}O_{7.62}$	0.008
$Ce_{0.08}Y_{0.12}Sc_{0.6}Zr_{3.2}O_{7.64}$	0.010
$Ce_{0.1}Y_{0.1}Sc_{0.6}Zr_{3.2}O_{7.65}$	0.006
$Ce_{0.12}Y_{0.08}Sc_{0.6}Zr_{3.2}O_{7.66}$	0.009
$Ce_{0.16}Y_{0.04}Sc_{0.6}Zr_{3.2}O_{7.68}$	0.014
$Ce_{0.20}Sc_{0.6}Zr_{3.2}O_{7.70}$	0.010

The highest conductivity, at 600 °C, belongs to the composition $Ce_{0.16}Y_{0.04}Sc_{0.6}Zr_{3.2}O_{7.68}$. Conductivity values are similar for different compositions in this system, except for the composition $Ce_{0.1}Y_{0.1}Sc_{0.6}Zr_{3.2}O_{7.65}$, which is lower. This composition, which has the same amount of ceria and yttria, shows a poor conductivity when compared to the other compositions. Compositions that have higher ceria content have better conductivity when compared to composition with compositions with lower ceria content.
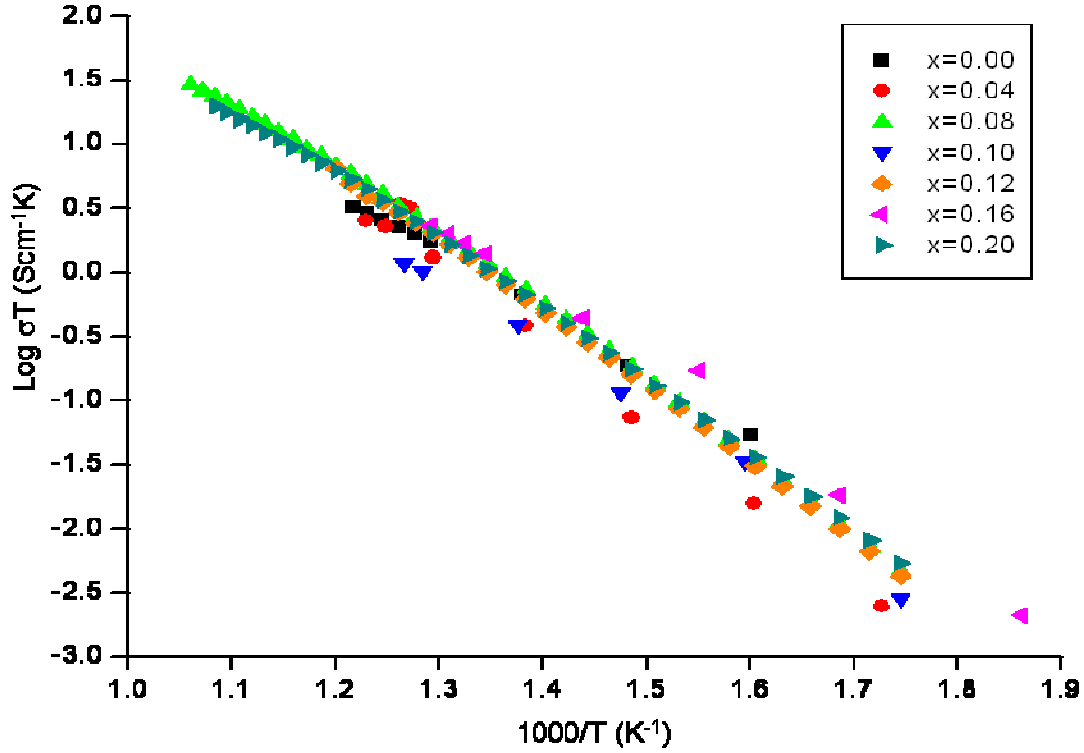
Figure 4.9: Arrhenius plot of conductivity of bulk corrected by density, see Table 4.1

At lower temperatures there is a slight difference in conductivity mainly due to the contribution of the grain boundary, although bulk contribution also shows some dependence upon composition. For temperatures above 700 °C, bulk is the process that dominates total conductivity, but for temperatures below 700 °C, grain boundary determines the electrical transport. This was reported by Lee et al, [22], who states that *"...the small grain size of solid electrolytes is accustomed to decrease the electrical conductivity by increasing low conductive grain boundary area which normally has higher activation energy for the conduction as well. Thus, one can easily expect that the effect of porosity or grain size becomes obvious in low temperature region, where the total conductivity is governed by the electrical conduction through the grain boundary."*

Activation Energy

The ionic conductivity depends on temperature and this dependence is given by the Arrhenius equation (4.1), explain previously in this chapter.

$$\sigma = Ae^{\frac{-E_a}{kT}} \qquad (4.1)$$

The activation energy of any component could be determined by measuring the change in conductivity with temperature. The graph is plotted as $\log \sigma T$ vs. $\dfrac{1000}{T}$ and the slope is given by, $\dfrac{-E_a}{k}$, which should have a linear trend. The slope of the Arrhenius plot allows the activation energy to be calculated from the equation (4.4), the factor one thousand is from the $\dfrac{1000}{T}$:

$$E_a = -\frac{2.303 \times 1.381 \times 10^{-23} \times 1000 \times slope}{1.602 \times 10^{-19}} \ (eV) \qquad (4.4)$$

$$E_a = -0.1984 \times slope \qquad (4.5)$$

The activation energy is directly proportional to the curve slope in the Arrhenius plot, equation (4.5), although the curve slope has a negative signal it is multiplied by a negative coefficient, which leads to a positive activation energy. An example of how the slope is obtained is shown in Figure 4.16.

Doping scandia zirconia with an aliovalent cation will promote the formation of associated defects, such as the formation of vacancy cluster or even the creation of a secondary phase. For zirconia fluorite systems at low temperature, the activation energy is the sum of the oxygen vacancy migration energy and the association energy. This association energy is the minimum energy necessary to dissociate a vacancy dopant from the cluster and has a significant contribution for the total activation energy. At low temperature, the existent pair in YSZ ($Y'_{Zr}V_O^{\cdot\cdot}$) and the existent pair in ScSZ ($Sc'_{Zr}V_O^{\cdot\cdot}$) and

their concentrations will control the ionic properties, namely conductivity, of yttria stabilised zirconia and scandia stabilised zirconia, respectively. At high temperature, vacancies are isolated and migrate freely, therefore the activation energy only accounts the migration enthalpy energy [4].

Table 4.7 shows the activation energy for bulk, grain boundary and total, for all compositions in the system $Ce_xY_{0.2-x}Sc_{0.6}Zr_{3.2}O_{8-\delta}$ ($0 \leq x \leq 0.2$). The activation energy values were obtained by fitting the Arrhenius plot curve, in Figure 4.8, using the curve slope to apply on equation (4.5).

Table 4.7: Activation energy for bulk, grain boundary (GB) and Total

Composition	Ea bulk, eV	Ea GB, eV	Ea Total, eV T<600 °C	Ea Total, eV T>600 °C
$Y_{0.2}Sc_{0.6}Zr_{3.2}O_{7.60}$	0.96	1.22	1.15	0.91
$Ce_{0.04}Y_{0.16}Sc_{0.6}Zr_{3.2}O_{7.62}$	1.25	1.37	1.29	1.07
$Ce_{0.08}Y_{0.12}Sc_{0.6}Zr_{3.2}O_{7.64}$	1.11	1.19	1.16	0.98
$Ce_{0.1}Y_{0.1}Sc_{0.6}Zr_{3.2}O_{7.65}$	1.33	1.22	1.13	0.84
$Ce_{0.12}Y_{0.08}Sc_{0.6}Zr_{3.2}O_{7.66}$	1.15	1.16	1.14	0.93
$Ce_{0.16}Y_{0.04}Sc_{0.6}Zr_{3.2}O_{7.68}$	1.06	1.12	1.11	0.78
$Ce_{0.20}Sc_{0.6}Zr_{3.2}O_{7.70}$	1.10	1.16	1.12	0.92

At lower temperatures, below 600 °C, the activation energy associated with the bulk process is lower than the activation energy associated with the grain boundary process, except for composition $Ce_{0.1}Y_{0.1}Sc_{0.6}Zr_{3.2}O_{7.65}$. In most cases total activation energy, below 600 ºC, has similar values to the grain boundary process; this indicates that at this temperature grain boundary process dominates the activation energy. Politova *et. al.* [4] studied the introduction of yttria in a scandia zirconia matrix and observed an increase of the activation energy when yttria content was increased. In this case, increasing the ceria content and decreasing yttria content will promote slightly total conductivity, Figure 4.8; therefore decreasing the activation energy. This could explain the reason why the activation energy values are similar for all compositions.

As expected, the total activation energy, at high temperatures, above 600 °C, is lower than the total activation energy at temperatures below 600 °C. This is explained with the change of ionic conductive process and less energy necessary to migrate a free oxygen vacancy.

Table 4.8 shows the estimated errors for activation energy for bulk, grain boundary and total. The calculation details are presented in Appendix 2.

Table 4.8: Estimated errors for activation energy for bulk, grain boundary (GB) and Total

Composition	Ea bulk	Ea GB	Ea Total T<600 °C	Ea Total T>600 °C
$Y_{0.2}Sc_{0.6}Zr_{3.2}O_{7.60}$	0.004	0.003	0.003	0.004
$Ce_{0.04}Y_{0.16}Sc_{0.6}Zr_{3.2}O_{7.62}$	0.004	0.014	0.005	0.004
$Ce_{0.08}Y_{0.12}Sc_{0.6}Zr_{3.2}O_{7.64}$	0.002	0.001	0.001	0.002
$Ce_{0.1}Y_{0.1}Sc_{0.6}Zr_{3.2}O_{7.65}$	0.006	0.006	0.002	0.006
$Ce_{0.12}Y_{0.08}Sc_{0.6}Zr_{3.2}O_{7.66}$	0.001	0.001	0.009	0.001
$Ce_{0.16}Y_{0.04}Sc_{0.6}Zr_{3.2}O_{7.68}$	0.008	0.004	0.003	0.006
$Ce_{0.20}Sc_{0.6}Zr_{3.2}O_{7.70}$	0.001	0.001	0.009	0.001

Table 4.8 shows that the errors are not significant for the activation energy components when comparing to the values of the activation energy.

The Arrhenius plot for total conductivity, for the compositions $Ce_{0.04}Y_{0.16}Sc_{0.6}Zr_{3.2}O_{7.62}$ and $Ce_{0.1}Y_{0.1}Sc_{0.6}Zr_{3.2}O_{7.65}$ are shown in Appendix 3 for better observation. Composition $Ce_{0.04}Y_{0.16}Sc_{0.6}Zr_{3.2}O_{7.62}$ has lower values of conductivity for low temperatures, but for temperatures above 600 ºC, conductivity values are similar to the other compositions in the system $Ce_xY_{0.2-x}Sc_{0.6}Zr_{3.2}O_{8-\delta}$ (0≤x≤0.2). Bulk values for conductivity are lower than other compositions; these values are correlated with the activation energy values that are high for temperature below 600 ºC, but at higher temperatures total activation energy drops although remaining higher than total activation energy values for other compositions of the system. The high values for the total activation energy, for composition $Ce_{0.04}Y_{0.16}Sc_{0.6}Zr_{3.2}O_{7.62}$, results from the rapid increase in conductivity for higher temperatures, above 750 ºC, as the activation energy depends on the curve slope, which increases in this temperature region. Figure 4.8 shows that the conductivity still continue to increase for temperatures above 750 ºC, this can indicate that this composition could have a working temperature above 800 ºC, instead of an intermediate temperature, which was one of the purposes of this project.

Composition $Ce_{0.1}Y_{0.1}Sc_{0.6}Zr_{3.2}O_{7.65}$ shows low conductivity, when compared with the other compositions in this system, for both total and bulk, at all temperatures, Figure 4.8

and 4.9. These results correlate with the high values for the activation energy, at low temperatures. At high temperatures, the curve slope slightly decreases, consequently decreasing the value for the activation energy.

Summarising, the Arrhenius plot shown in Figure 4.8 and the activation energy values presented in Table 4.7 are in agreement with Politova *et al.* [4]. There are two different temperature regimes, at low and at high temperatures. At low temperatures, the conductive process is slower, with higher activation energy values, than the conductive process for high temperature, with lower activation energy values. This occurs due to the energy necessary to dissociate an oxygen vacancy from the cluster and to migrate the oxygen vacancy, at low temperatures; whilst for high temperature the energy is only necessary to migrate the oxygen vacancy, as vacancies are free. The variation in conductivity is more significant at low temperatures than at high temperatures, for a same temperature variation; as these processes are thermally activated.

TEM
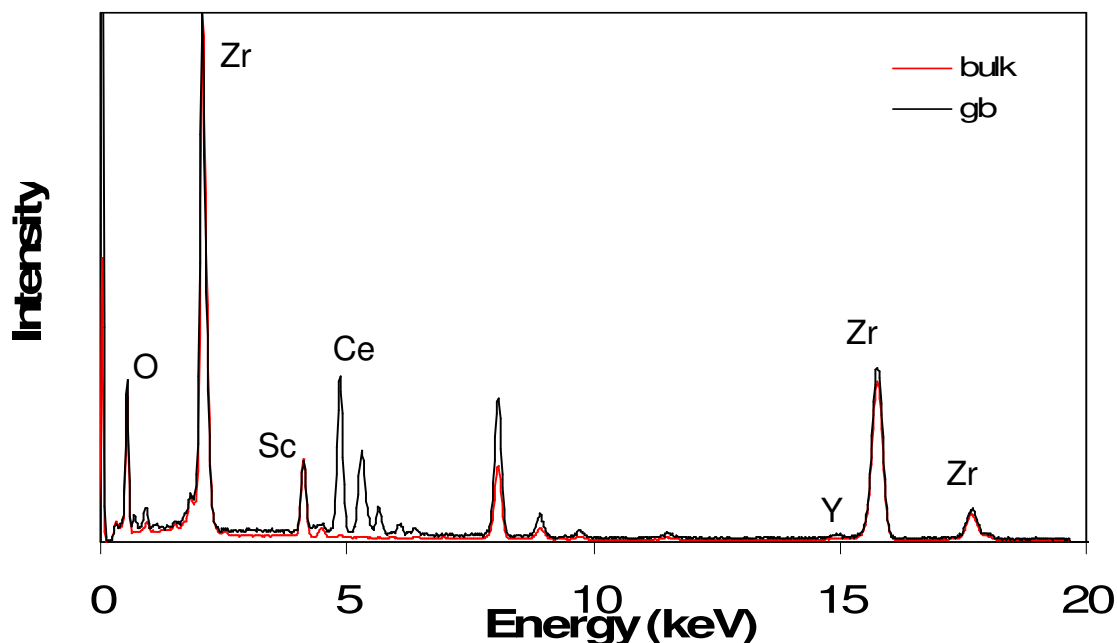
Figure 4.10: EDS from TEM, for different regions of ceramic after ionic conductivity measurements, composition $Ce_{0.08}Y_{0.12}Sc_{0.6}Zr_{3.2}O_{7.64}$. TEM operator Dr. David Miller, University of St. Andrews

The sample used for the TEM observation, has the composition $Ce_{0.08}Y_{0.12}Sc_{0.6}Zr_{3.2}O_{7.64}$. The powders were obtained by the sol-gel and combustion method, after combustion, the powders were calcined at 400 °C, for 3 hours, and then pressed into pellets and sintered at 1500 °C, for 12 hours. The platinum was painted and sintered at 900 °C, for 30 min. The pellet was characterised electrically starting at 300 °C heating up to 900 °C and cooling down back to 300 °C, in intervals of 50 °C. Except in the temperature range from 500 to 600 °C, where the intervals were reduced to 10 °C.

Data from the EDS from TEM, in Figure 4.10, was taken near to the grain boundary, over about 15 nm of from the centre of the grain boundary lines. Figure 4.10 shows that the curve corresponding to the grain boundary has one extra peak, which corresponds to the element cerium, that do not exist on the bulk curve. This can be an indication of the fact that there is cerium segregated into the grain boundaries. The behaviour of cerium can indicate that the matrix of the scandia zirconia does not accommodate the cerium element and segregates it to the grain boundaries. This segregation in the grain boundary can decrease conductivity of the grain boundary and consequently decrease total conductivity.

SEM

Electron microscopy is a powerful and versatile tool to give information on the microstructure of materials, [21, 23].

Calculation for the average grain size, $\overline{G}$:

For this calculation, the equation used is as follows (4.6);

$$L_1 = \left(\frac{\Sigma \dfrac{\Sigma L_L}{A}}{\Sigma N_L} \right) \qquad (4.6)$$

Where,

    L_L → Length of the line for each interception, choose randomly.

    A → Amplification.

$N_L \rightarrow$ Number of grains, which exist inside the lines (L_L).

For the calculation of the grain size average, the relation of Fullman (4.7) has to be used:

$$\overline{G} = 1{,}5 \times L_1 \qquad (4.7)$$

Where,

$\overline{G} \rightarrow$ Average grain size.

The average grain size study was made on three micrographs for the same composition.

The pellets have to be prepared, in order to be examined in the SEM. They are polished and etched before being observed in the SEM. For the etching, the pellets are introduced in the furnace at 1000 °C, the temperature is then increased by 10 °C/min until 1250 °C, where a three-hour dwell is made. After the dwell, the temperature is decreased at the rate of 10 °C/min until it reaches 1000 °C. At this temperature, the pellets are removed from the furnace and left to cool at room temperature. During cutting and polishing the samples, it can damage the samples. Remove some grains or/and pitting are defects introduced during this step.
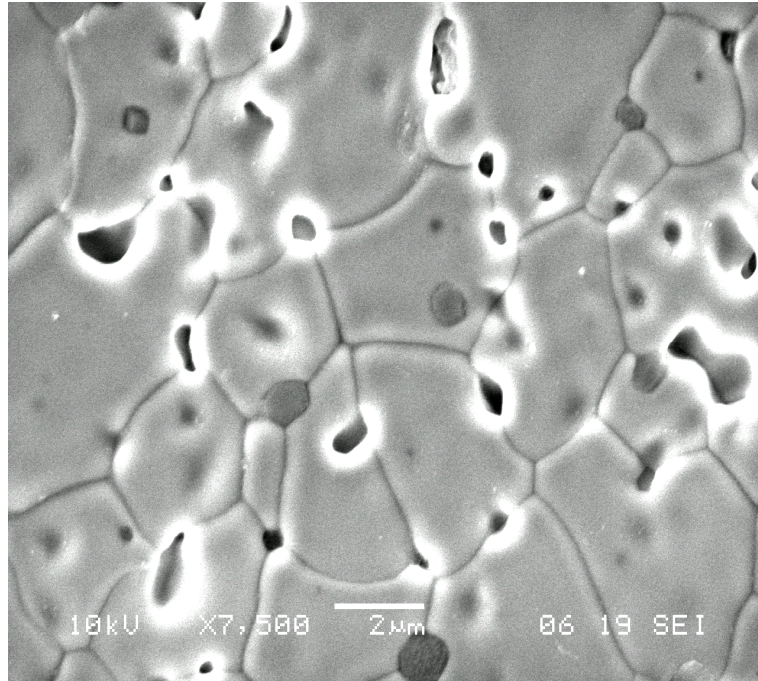
Figure 4.11: Scanning electron micrograph of $Y_{0.2}Sc_{0.6}Zr_{3.2}O_{7.60}$.

The average grain size, for the composition $Y_{0.2}Sc_{0.6}Zr_{3.2}O_{7.60}$, is 4.79 ± 0.8 μm. In this micrograph the existence of smaller grains can be observed, with a darker coloration. There are some irregularities on the surface.
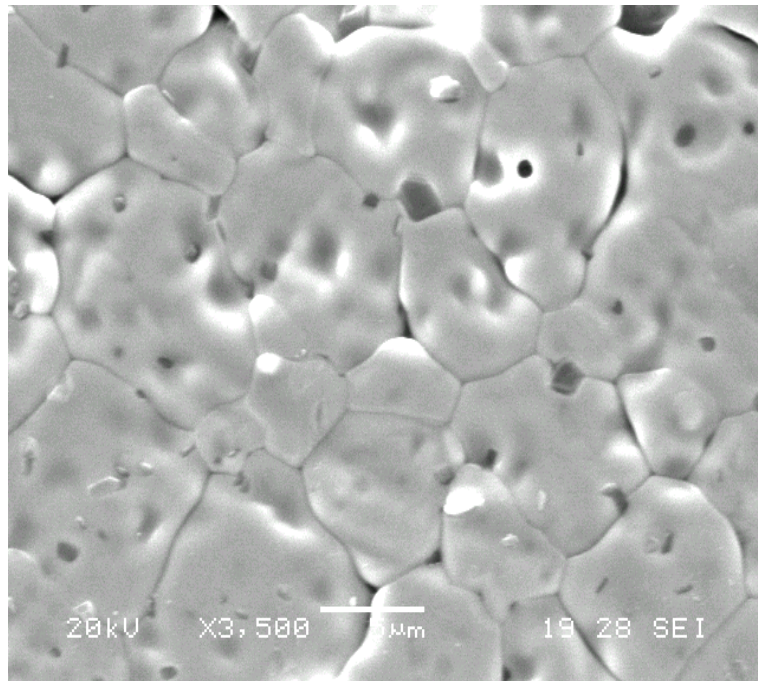
Figure 4.12: Scanning electron micrograph of $Ce_{0.08}Y_{0.12}Sc_{0.6}Zr_{3.2}O_{7.64}$.

In Figure 4.11 and Figure 4.12, surface irregularities and darker colour grains are visible. The average grain size, for the composition $Ce_{0.08}Y_{0.12}Sc_{0.6}Zr_{3.2}O_{7.64}$, is 8.33 ± 1.25 µm, this calculation is for grains with well defined boundaries. With careful inspection, one large grain with some irregularities can be observed, in the top right side of Figure 4.13, these irregularities resemble to not well defined grain boundaries, inside the larger grain.
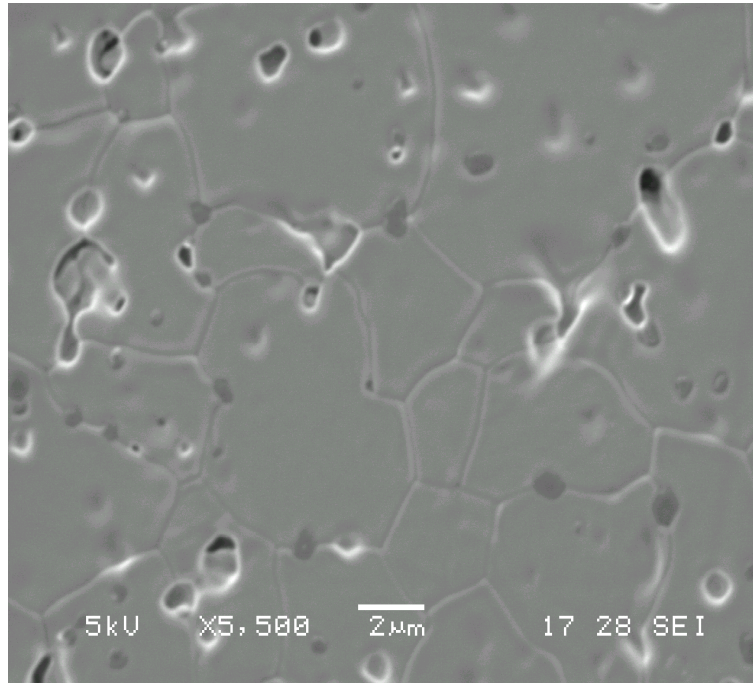
Figure 4.13: Scanning electron micrograph of $Ce_{0.12}Y_{0.08}Sc_{0.6}Zr_{3.2}O_{7.66}$.

The average grain size, for the composition $Ce_{0.12}Y_{0.08}Sc_{0.6}Zr_{3.2}O_{7.66}$, is 6.86 ± 0.8 µm. In all micrographs, large grains, around 5 µm, can be observed, and also smaller "sub-grains", 10-100 nm, inside the larger grains. The aspect of these scanning electron micrographs, Figure 4.11, 4.12 and 4.13, is the same as the micrographs displayed by Badwal, *et al.* [7].

The average grain size, for the composition with no ceria content, is lower than the composition $Ce_{0.08}Y_{0.12}Sc_{0.6}Zr_{3.2}O_{7.64}$ and $Ce_{0.12}Y_{0.08}Sc_{0.6}Zr_{3.2}O_{7.66}$. With the reduction in the average grain size, the average number of grains will also increase, therefore an increase in grain boundary area. This can explain the high resistance at the grain

boundaries [14, 24]. The grains with a darker coloration do not show differences in composition, according to the EDS from SEM, Figure 4.14 and 4.15. These figures are from the same composition $Ce_{0.08}Y_{0.12}Sc_{0.6}Zr_{3.2}O_{7.64}$, but the EDS are directed to different points from the surface of the sample. The EDS analysis is on Table 4.9.
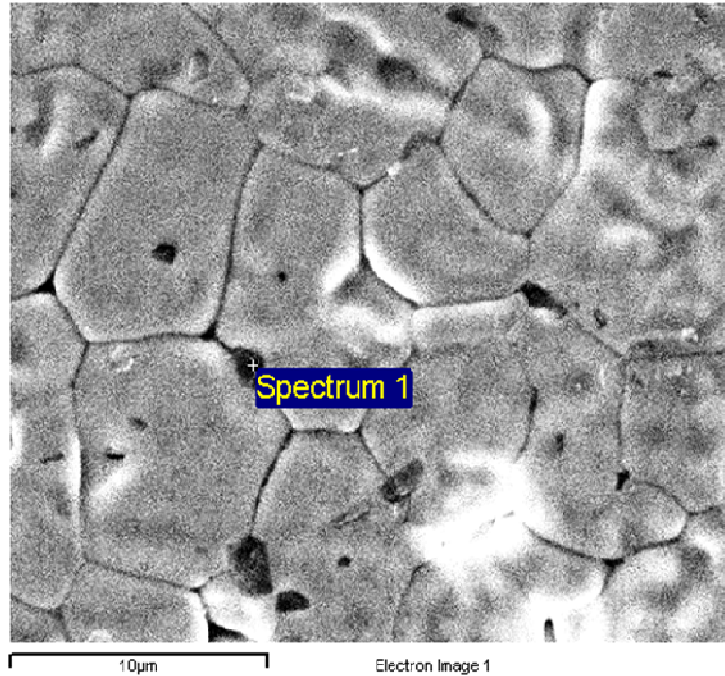
Figure 4.14: Scanning electron micrograph of $Ce_{0.08}Y_{0.12}Sc_{0.6}Zr_{3.2}O_{7.64}$.
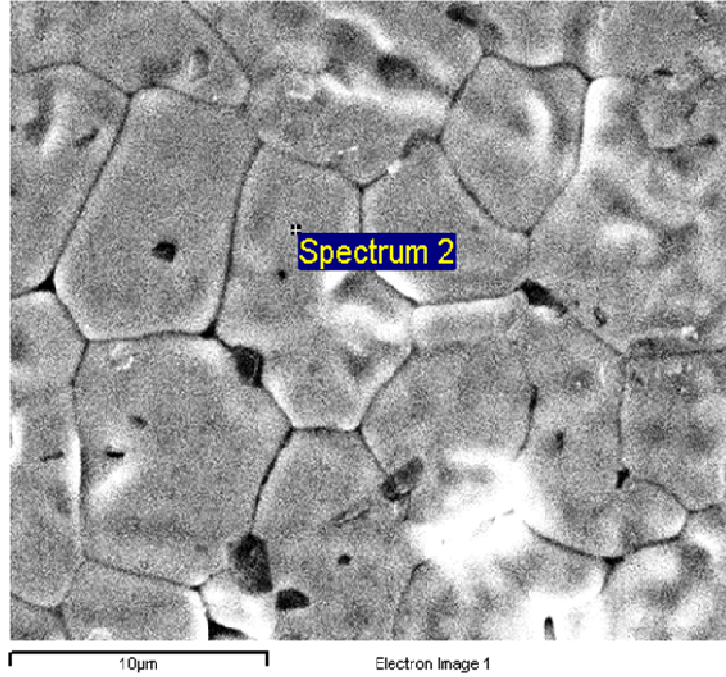
Figure 4.15: Scanning electron micrograph of $Ce_{0.08}Y_{0.12}Sc_{0.6}Zr_{3.2}O_{7.64}$.

Table 4.9 show the EDS analysis of composition $Ce_{0.08}Y_{0.12}Sc_{0.6}Zr_{3.2}O_{7.64}$ in two different points. One with a light coloration and another with a darker coloration; this EDS analysis has the intention to understand if the two points are chemically similar or different, within the detection limits of the equipment.

Table 4.9: EDS for composition $Ce_{0.08}Y_{0.12}Sc_{0.6}Zr_{3.2}O_{7.64}$, in two different points.

	Carbon	Oxygen	Scandium	Yttrium	Zirconium	Cerium
Spectrum 1	24.26	43.35	4.25	0.83	26.57	0.74
Spectrum 2	30.74	37.32	4.22	0.81	26.03	0.88

Note: Results are presented in atomic percent.

The values for the composition elements do not show significant variation. This means that the grains with darker colouration do not have different composition; this can be an effect during the formation of the SEM picture.

4.3.2 Comparison of $Ce_{0.04}Y_{0.02}Sc_{0.67}Zr_{3.27}O_{7.66}$ and $Ce_{0.16}Y_{0.04}Sc_{0.6}Zr_{3.2}O_{7.68}$ Compositions

In this section, the initial composition, $Ce_{0.04}Y_{0.02}Sc_{0.67}Zr_{3.27}O_{7.66}$, which is outside the system investigated in this project, will be compared to the composition with the highest values of conductivity from the system. The initial composition has a low content in ceria and yttria, on the other hand, has a higher content of scandia and zirconia. Table 4.10 shows the pellets density details for the compositions that will be compared.

Table 4.10: Density of pellets for compositions $Ce_{0.04}Y_{0.02}Sc_{0.67}Zr_{3.27}O_{7.66}$ and $Ce_{0.16}Y_{0.04}Sc_{0.6}Zr_{3.2}O_{7.68}$, sintered at 1500 °C for 12 hours.

Composition	Theoretical density (g/cm^3)	Sample density (g/cm^3)	% density	Nomenclature
$Ce_{0.04}Y_{0.02}Sc_{0.67}Zr_{3.27}O_{7.66}$	5.675	5.146	91	Initial
$Ce_{0.16}Y_{0.04}Sc_{0.6}Zr_{3.2}O_{7.68}$	5.779	5.318	92	x=0.16

Figure 4.16 shows the Arrhenius plot of total conductivity for the compositions $Ce_{0.04}Y_{0.02}Sc_{0.67}Zr_{3.27}O_{7.66}$ and $Ce_{0.16}Y_{0.04}Sc_{0.6}Zr_{3.2}O_{7.68}$. Fitted lines are added for each composition and for low and high temperatures regimes. The slope from the fitted lines is used to calculate the activation energy, using equation (4.5).
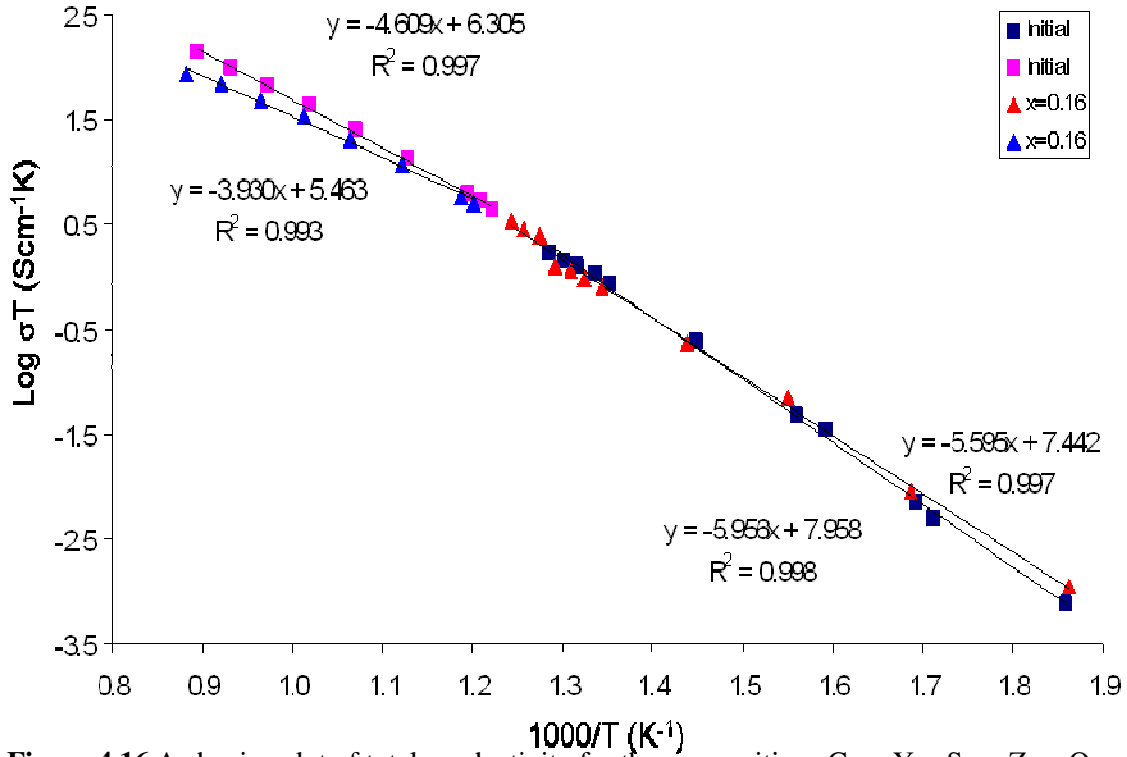
Figure 4.16 Arrhenius plot of total conductivity for the compositions $Ce_{0.04}Y_{0.02}Sc_{0.67}Zr_{3.27}O_{7.66}$ and $Ce_{0.16}Y_{0.04}Sc_{0.6}Zr_{3.2}O_{7.68}$.

As an example how to calculate the activation energy, using the slope, at high temperature for composition $Ce_{0.04}Y_{0.02}Sc_{0.67}Zr_{3.27}O_{7.66}$. Slope = -3.930

$$E_a = -0.1984 \times slope \qquad (4.5)$$

$$E_a = -0.1984 \times (-3.930) = 0.78 \pm 0.006 \ eV$$

The curves in Figure 4.16 have similar behaviour; there are two regions, at low and high temperature. At low temperatures, curves overlap, but at high temperatures, there is a difference between the curves; this difference increases with the increase of temperature. The curve for the composition $Ce_{0.04}Y_{0.02}Sc_{0.67}Zr_{3.27}O_{7.66}$ has slightly higher values for total conductivity, at high temperature. The values for the Arrhenius plot are displayed in Table 4.11.

Table 4.11: Total conductivity, for different temperatures

		Total conductivity, S/cm		
Composition	**Nomenclature**	**350 °C**	**600 °C**	**800 °C**
$Ce_{0.04}Y_{0.02}Sc_{0.67}Zr_{3.27}O_{7.66}$	Initial	5.49×10^{-5}	1.70×10^{-2}	1.02×10^{-1}
$Ce_{0.16}Y_{0.04}Sc_{0.6}Zr_{3.2}O_{7.68}$	x=0.16	7.69×10^{-5}	1.40×10^{-2}	6.50×10^{-2}

Figure 4.17 shows the Arrhenius plot of bulk conductivity for the compositions $Ce_{0.04}Y_{0.02}Sc_{0.67}Zr_{3.27}O_{7.66}$ and $Ce_{0.16}Y_{0.04}Sc_{0.6}Zr_{3.2}O_{7.68}$.
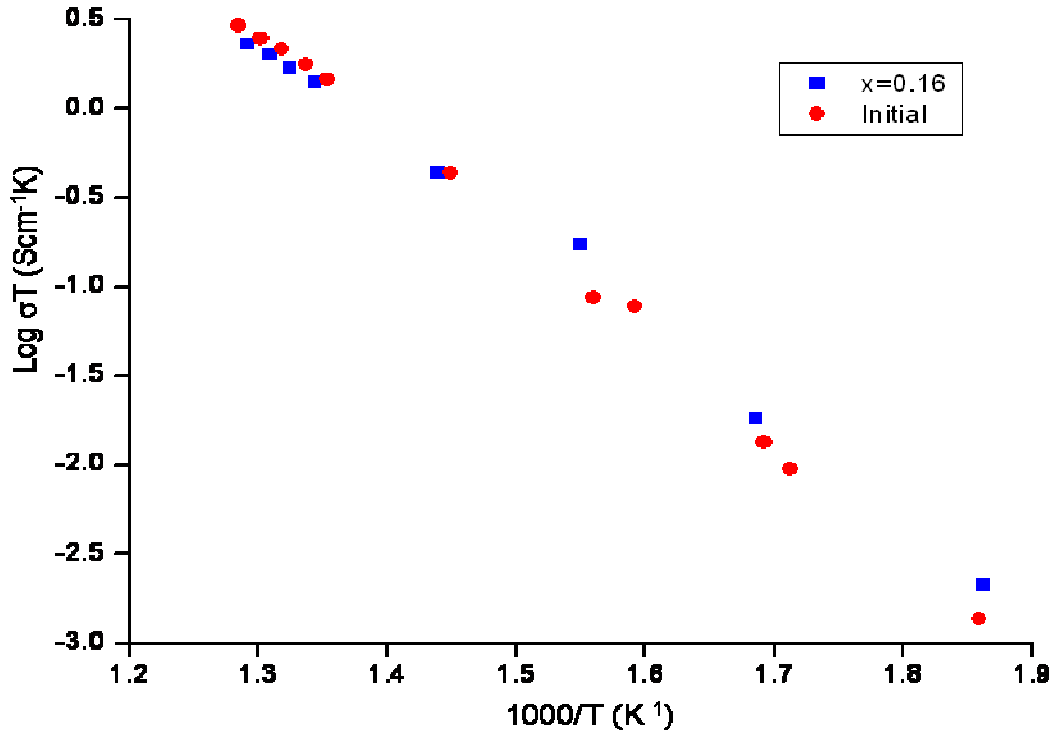
Figure 4.17: Arrhenius plot of bulk conductivity for the compositions $Ce_{0.04}Y_{0.02}Sc_{0.67}Zr_{3.27}O_{7.66}$ and $Ce_{0.16}Y_{0.04}Sc_{0.6}Zr_{3.2}O_{7.68}$.

The initial composition has lower values of bulk conductivity, at lower temperatures between 300 ºC and 450 ºC. For temperature over than 450 ºC, values for bulk conductivity are similar for both compositions. At temperatures over 500 ºC, bulk conductivity values, for the initial composition, are higher than bulk conductivity values for composition $Ce_{0.16}Y_{0.04}Sc_{0.6}Zr_{3.2}O_{7.68}$. This behaviour can occur due to the high

dopant level of $Ce_{0.16}Y_{0.04}Sc_{0.6}Zr_{3.2}O_{7.68}$, which might cause segregation of dopants at the grain boundary and/or formation of vacancy clusters and consequently decrease the conductivity [25].

4.3.3 Comparison of Sol-Gel and Combustion Method and Solid State Synthesis

In this section the electrical properties from samples produced by sol-gel and combustion method and solid state synthesis method will be compared. Table 4.12 show density details of the pellets used for this section and Figure 4.19 shows Arrhenius plot of total conductivity for the composition $Ce_{0.08}Y_{0.12}Sc_{0.6}Zr_{3.2}O_{7.64}$, produced by solid state synthesis and sol-gel and combustion methods.

Table 4.12: Density of the pellets of the $Ce_{0.08}Y_{0.12}Sc_{0.6}Zr_{3.2}O_{7.64}$, for the solid state synthesis and sol-gel and combustion method, sintered at 1500 °C for 12 hours.

Composition	Theoretical density (g/cm³)	Sample density (g/cm³)	% density	Nomenclature
$Ce_{0.08}Y_{0.12}Sc_{0.6}Zr_{3.2}O_{7.64}$	5.814	3.657	63	SSS
$Ce_{0.08}Y_{0.12}Sc_{0.6}Zr_{3.2}O_{7.64}$	5.757	5.359	94	SG-C

The sol-gel and combustion method, as discussed in the chapter III, produced better densified bodies. In this case, there is a difference of 30 % in density.
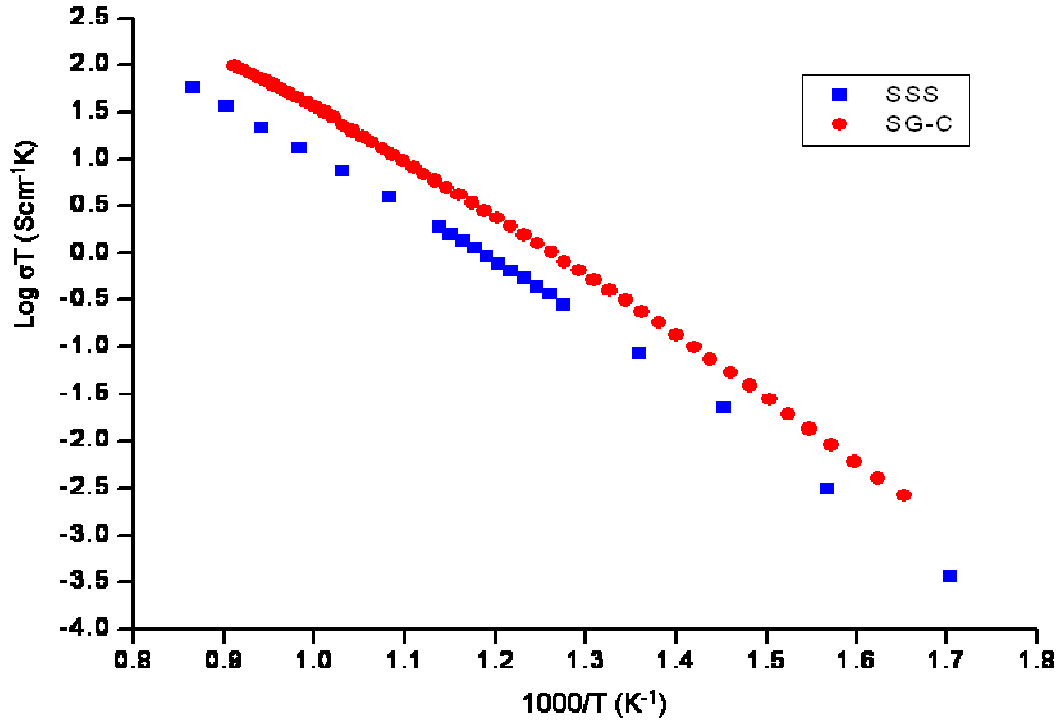
Figure 4.18: Arrhenius plot of total conductivity for the composition $Ce_{0.08}Y_{0.12}Sc_{0.6}Zr_{3.2}O_{7.64}$, produced by solid state synthesis and sol-gel and combustion methods.

In Figure 4.18, curves have the same behaviour; there are two separate regions, one at high temperature and another at low temperature. The sample produced by sol-gel and combustion synthesis is placed above the sample produced by solid state synthesis, for all temperatures. Table 4.13 shows the geometric measurements for pellets with the composition $Ce_{0.08}Y_{0.12}Sc_{0.6}Zr_{3.2}O_{7.64}$, produced by sol-gel and combustion and solid state synthesis.

Table 4.13: Pellet geometric measurements of the $Ce_{0.08}Y_{0.12}Sc_{0.6}Zr_{3.2}O_{7.64}$, for the solid state synthesis and sol-gel and combustion method.

Composition	Thickness, cm	Diameter, cm	Area, cm^2	Nomenclature
$Ce_{0.08}Y_{0.12}Sc_{0.6}Zr_{3.2}O_{7.64}$	0.197	1.298	1.323	SSS
$Ce_{0.08}Y_{0.12}Sc_{0.6}Zr_{3.2}O_{7.64}$	0.145	0.943	0.698	SG-C

There is a significant difference on the geometric factor, as the area for the SSS pellet is almost double than the SG-C pellet. This geometric factor has great impact when conductivity is calculated, as conductivity is inversely proportional to the geometric factor, meaning that the higher is the geometric factor, the lower will be its conductivity. A picture of two pellets can be observed in chapter III, Figure 3.22, there is an obvious geometric difference between them. The aspect of the solid state synthesis pellet is not dense and has high porosity.

Figure 4.19 shows the impedance spectra plot corrected by geometry, for SSS, recorded at 365 °C and SG-C, recorded at 360 °C. This plot was included to be easily observed the difference in resistance for the two pellets.
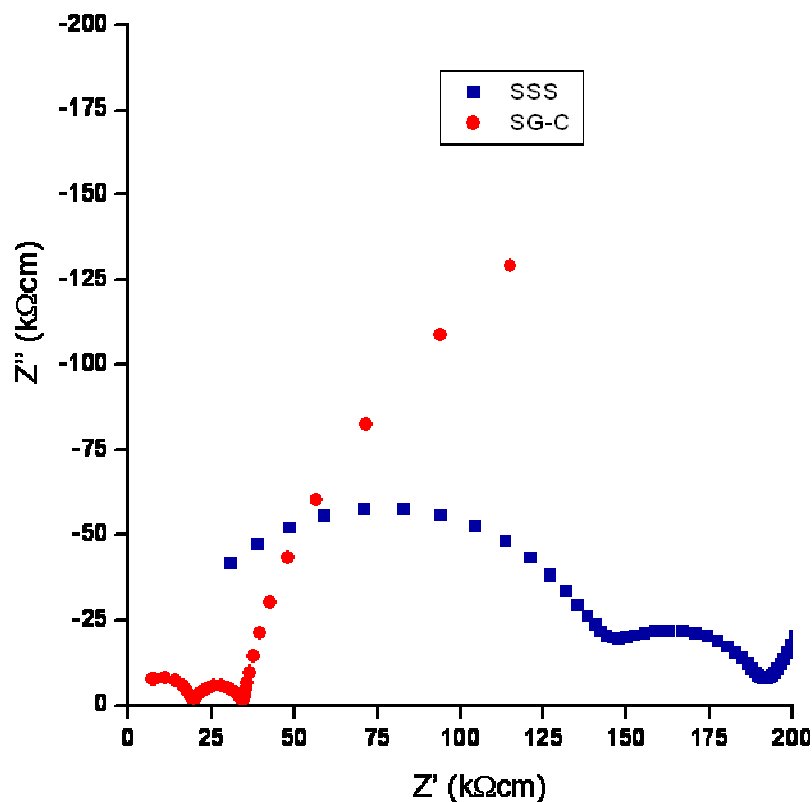
Figure 4.19: Impedance spectra plot corrected by geometry, for SSS, recorded at 365 °C and SG-C, recorded at 360 °C.

Impedance spectra show that the SG-C method has a much lower total resistance than the SSS method. When the processes involved, bulk and grain boundary, are compared, it can be observed that for SG-C, both processes have semi-circles with similar amplitudes, while for the SSS method, the semi-circle for the bulk process has larger amplitude than the one for the grain boundary process. Total conductivity values are presented in Table 4.14, for different temperatures.

Table 4.14: Total conductivity, for the composition $Ce_{0.08}Y_{0.12}Sc_{0.6}Zr_{3.2}O_{7.64}$, for the solid state synthesis and sol-gel and combustion method

Temperature, °C	Conductivity, S/cm	
	SSS	SG-C
350	5.90×10^{-6}	9.34×10^{-6}
500	4.90×10^{-4}	8.44×10^{-4}
800	3.68×10^{-2}	7.29×10^{-2}

Total conductivity values for SG-C are 50% higher than for SSS. This difference in conductivity is suggested to be due to the low density from the SSS pellet and not from the difference in conduction process, which contributes for total conductivity, bulk and grain boundary.
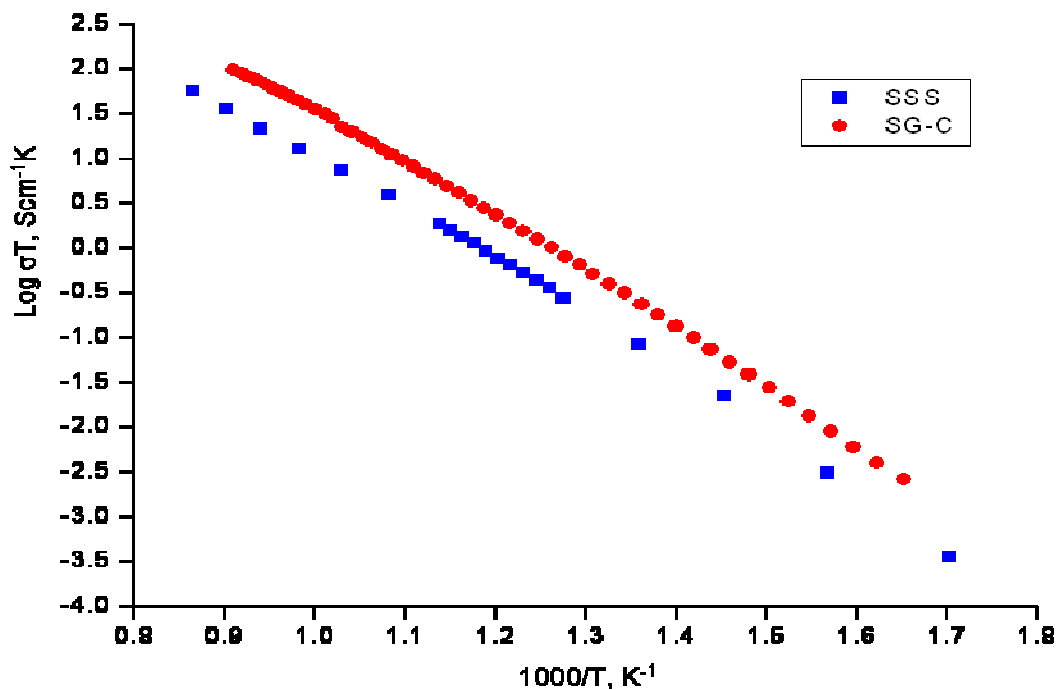
Figure 4.20: Arrhenius plot of bulk conductivity for the composition $Ce_{0.08}Y_{0.12}Sc_{0.6}Zr_{3.2}O_{7.64}$, produced by solid state synthesis and sol-gel and combustion methods.

The Arrhenius plot from Figure 4.20 shows that at lower temperatures, the bulk conductivity for the sample produced by SG-C method is higher than the sample produced by SSS method. At lower temperatures the separation between the curves is narrower and will widen with the increase in temperature.

Ionic conductivity is represented by a flux of ions. This conductivity is made through the solid phase, bulk; when the ion flux encounters a pore, or a pore chain, the ion flux will be interrupted and/or delayed, which will condition the ionic conductivity in the material [26-28]. This can be the explanation for the poor conductivity for the pellet produced by SSS; since samples have the same composition, but powders were produced by two different methods.

4.3.4 AC Impedance Measurement as a Function of Oxygen Partial Pressure

For this section, two compositions were chosen as they show significant differences in the way they behave when subjected to a variation of oxygen partial pressure, more specific samples were subjected to a decrease in oxygen atmosphere. In Table 4.15, the details of the two samples chosen for the experiment are presented, the composition $Y_{0.2}Sc_{0.6}Zr_{3.2}O_{7.60}$ has no ceria content and the composition $Ce_{0.12}Y_{0.08}Sc_{0.6}Zr_{3.2}O_{7.66}$ has a medium level of ceria content, in this system $Ce_xY_{0.2-x}Sc_{0.6}Zr_{3.2}O_{8-\delta}$ ($0 \leq x \leq 0.2$). All the measurements were made at the temperature of 700°C.

Table 4.15: Pellet density for composition $Y_{0.2}Sc_{0.6}Zr_{3.2}O_{7.60}$ and $Ce_{0.12}Y_{0.08}Sc_{0.6}Zr_{3.2}O_{7.66}$ ($0 \leq x \leq 0.2$), sintered at 1500 °C for 12 hours.

Composition	Theoretical density (g/cm³)	Sample density (g/cm³)	% density
$Y_{0.2}Sc_{0.6}Zr_{3.2}O_{7.60}$	5.713	5.213	89
$Ce_{0.12}Y_{0.08}Sc_{0.6}Zr_{3.2}O_{7.66}$	5.807	5.102	90

In Figure 4.21, conductivity of the samples was measured in a range of oxygen partial pressure from 1 to 10^{-24} bars; this corresponds to a reducing regime. The different oxygen partial pressure were achieved by the mixture of three different gases; oxygen, hydrogen and argon.
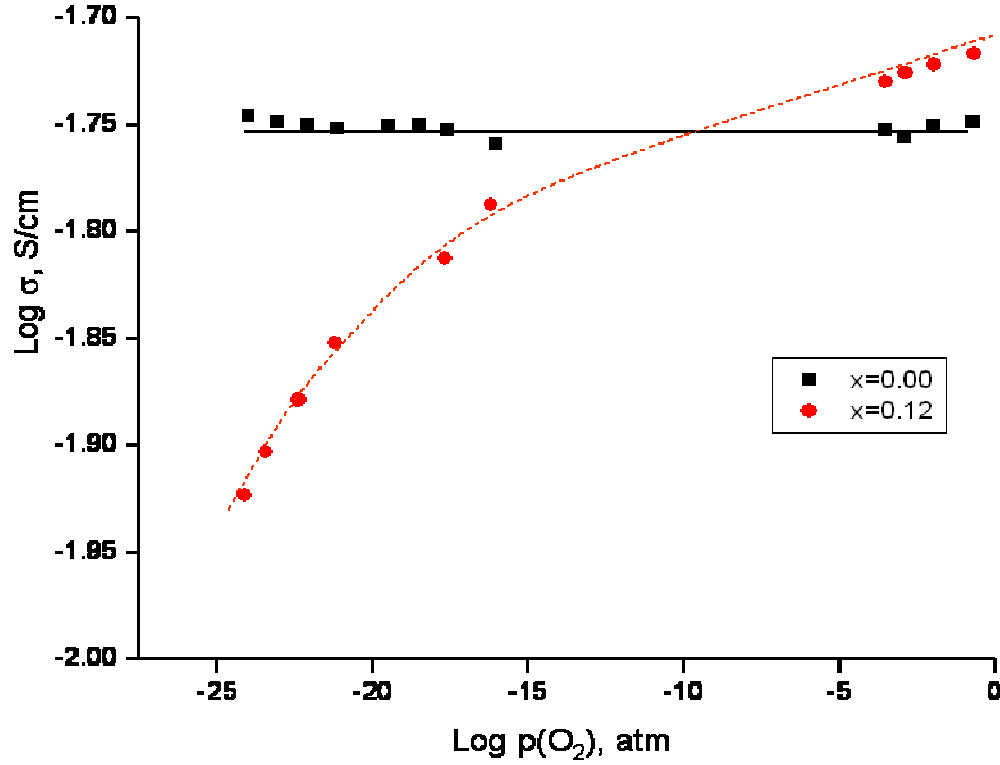
Figure 4.21: Conductivity as a function of oxygen partial pressure, for the compositions
$Y_{0.2}Sc_{0.6}Zr_{3.2}O_{7.60}$ and $Ce_{0.12}Y_{0.08}Sc_{0.6}Zr_{3.2}O_{7.66}$.

Figures 4.22 and 4.23 represent the impedance spectra with different oxygen partial
pressures, for composition $Y_{0.2}Sc_{0.6}Zr_{3.2}O_{7.60}$ and $Ce_{0.12}Y_{0.08}Sc_{0.6}Zr_{3.2}O_{7.66}$, respectively.
The resistance was measured for the following pressures: 0.21 atm, 10^{-4} atm, 10^{-18} atm,
10^{-21} atm, and 10^{-24} atm.
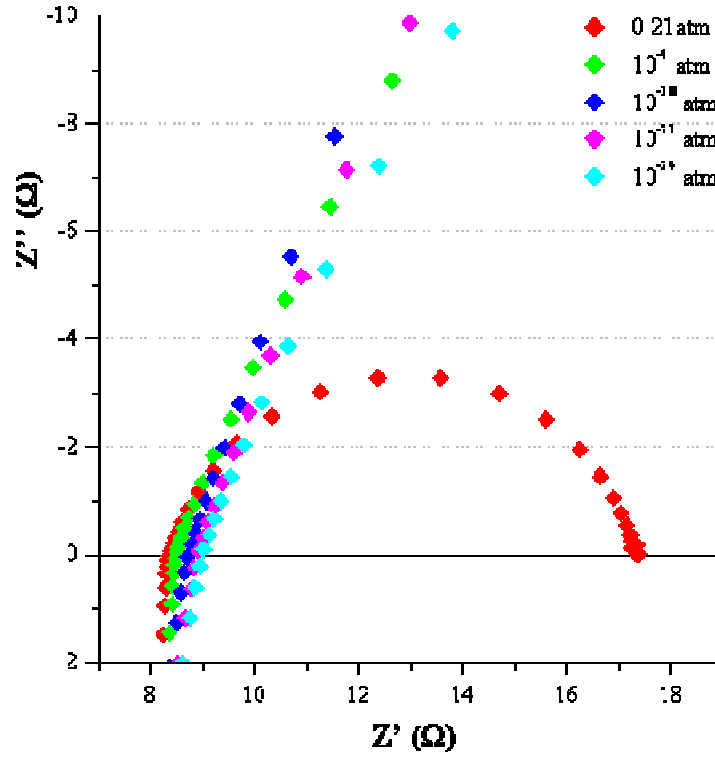
Figure 4.22: Impedance spectra plots, recorded at 700 °C, for composition $Y_{0.2}Sc_{0.6}Zr_{3.2}O_{7.60}$ for different $p(O_2)$.

Table 4.16 shows values of the total resistance, these values were obtained by the data processing from Figure 4.22.

Table 4.16: Values of the resistance for bulk, grain boundary and total, of correspondent $p(O_2)$, for composition $Y_{0.2}Sc_{0.6}Zr_{3.2}O_{7.60}$, at 700 °C

$p(O_2)$, atm	Resistance Total, Ω
0.21	8.39
10^{-4}	8.47
10^{-18}	8.42
10^{-21}	8.43
10^{-24}	8.40

Figure 4.23 shows the Impedance spectra plots, recorded at 700 °C, for composition $Ce_{0.12}Y_{0.08}Sc_{0.6}Zr_{3.2}O_{7.66}$ for different $p(O_2)$.
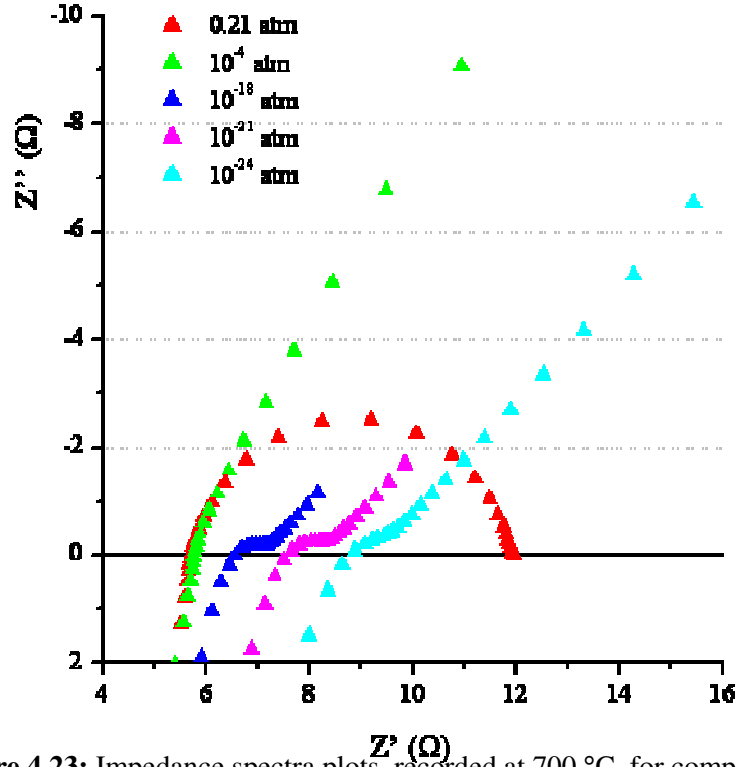
Figure 4.23: Impedance spectra plots, recorded at 700 °C, for composition $Ce_{0.12}Y_{0.08}Sc_{0.6}Zr_{3.2}O_{7.66}$ for different $p(O_2)$.

Table 4.17 shows values of resistance for the different components, these values were obtained by data processing from Figure 4.23.

Table 4.17: Values of the resistance for bulk, grain boundary and total, of correspondent $p(O_2)$, for composition $Ce_{0.12}Y_{0.08}Sc_{0.6}Zr_{3.2}O_{7.66}$, at 700 °C

$p(O_2)$, atm	Resistance bulk, Ω	Resistance GB, Ω	Resistance Total, Ω
0.21	-	-	5.55
10^{-4}	-	-	5.71
10^{-18}	1.14	6.12	7.26
10^{-21}	1.34	6.52	7.86
10^{-24}	1.93	7.44	9.38

By the observation of Figures 4.21, 4.22 and Table 4.16, for the sample with no ceria in its composition, the resistance did not vary significantly while the oxygen partial pressure decreased. There is a significant decrease in electrode/electrolyte interface response from 0.21 atm to 10^{-4} atm, this indicates a change in the electrode/electrolyte

interface behaviour. When the oxygen partial pressure decreases the reaction in the electrode/electrolyte interface is more difficult, due to the decrease of oxygen, in the atmosphere.

By the observation of Figures 4.21, 4.23 and Table 4.17, for the sample with higher ceria content, there is a significant decrease in the conductivity for lower oxygen partial pressures. This sample presents conductivity higher than the sample with no ceria for higher oxygen partial pressure. When oxygen partial pressure decreases this sample presents a significant decrease in conductivity. For the sample with a higher content of ceria, there is an increase in total resistance while oxygen partial pressure decreases; there is also the appearance of a semi-circle for lower oxygen partial pressures. This drop in the conductivity could be a consequence of some clustering of oxygen vacancies and scarcity of oxygen in the atmosphere, causing the ionic conductivity to decrease with increasing vacancy content. Analysing Table 4.17, there are no values for the resistance from the bulk and grain boundary, for oxygen partial pressures above 10^{-18} atm. Resistance for the bulk process increases 69 % from 10^{-18} atm to 10^{-24} atm, whilst for the grain boundary process this increase is only of 22 %. The total resistance increases by 70 % from 0.21 atm to 10^{-4} atm. The sudden increase in the bulk component can be explained by the scarcity of oxygen which will affect the electrode /electrolyte interface response negatively, as there will be no oxygen in the electrode to react with the ions from the electrolyte, therefore conductivity will decrease or even stop. This drop in conductivity could also be a consequence of some clustering of vacancies due to the reduction of ceria; meaning that ionic conductivity decreases with the increasing of vacancies.

Figure 4.24 shows two pictures of TEM of a reduced sample, at 900 °C for 12 hours in 5%H_2/Ar, from the composition $Ce_{0.12}Y_{0.08}Sc_{0.6}Zr_{3.2}O_{7.66}$.
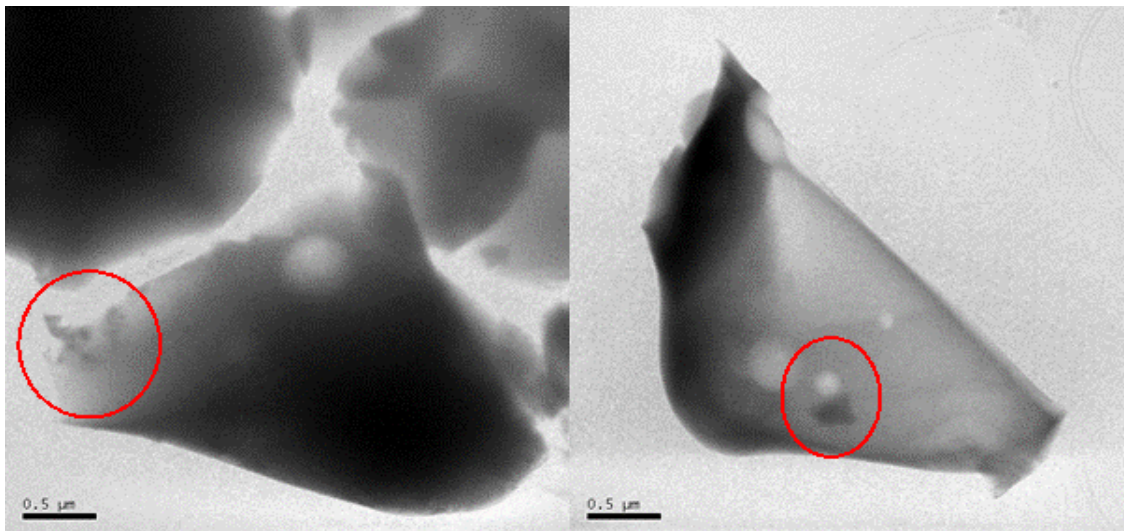
Figure 4.24: TEM picture of a reduced sample, from the composition $Ce_{0.12}Y_{0.08}Sc_{0.6}Zr_{3.2}O_{7.66}$.

Migrating particles to the surface, of the grain, can be observed inside the red circle. These particles could be the segregation of alumina towards the grain boundary.

Figure 4.25 and Figure 4.26 show the variation in conductivity components, bulk and grain boundary, as a function of oxygen partial pressure, at 700 °C, for the compositions $Ce_{0.16}Y_{0.04}Sc_{0.6}Zr_{3.2}O_{7.68}$ and $Ce_{0.20}Sc_{0.6}Zr_{3.2}O_{7.70}$. The measurements used for these Figures were performed by Andreas Egger, University of Leoben. This is the results of the collaboration between the University of St. Andrews and the University of Leoben, where we would supply samples and University of Leoben would perform the measurements.
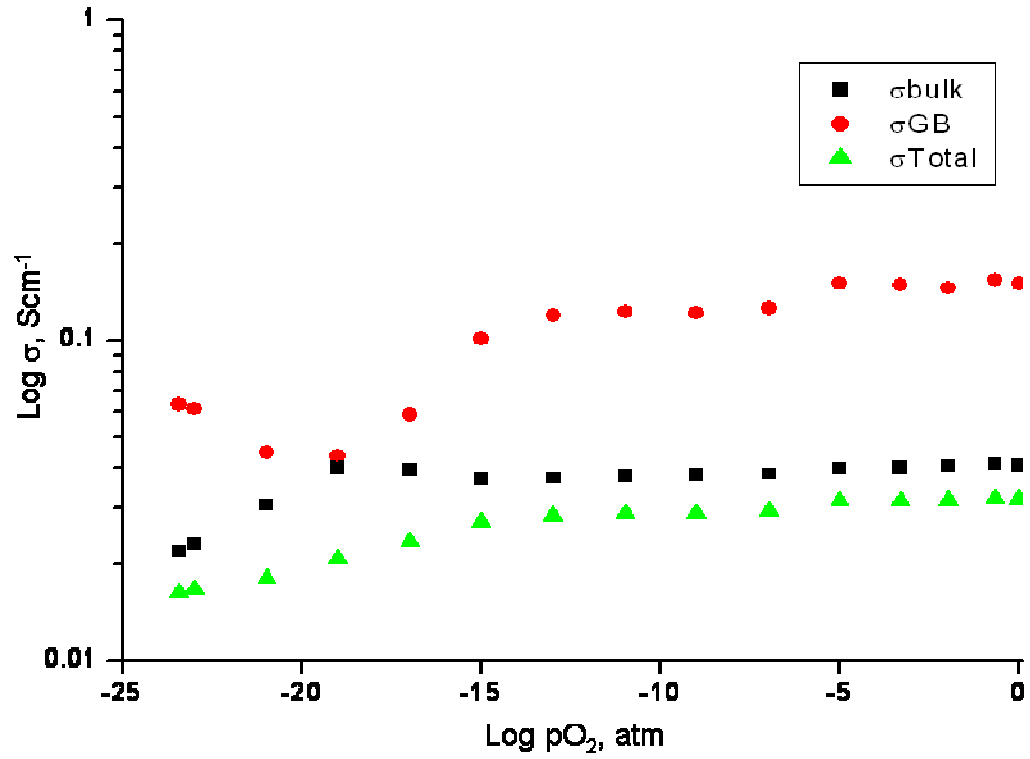
Figure 4.25: Conductivity as function of oxygen partial pressure, for the composition $Ce_{0.16}Y_{0.04}Sc_{0.6}Zr_{3.2}O_{7.68}$. Measurements performed by Andreas Egger, University of Leoben, Austria.
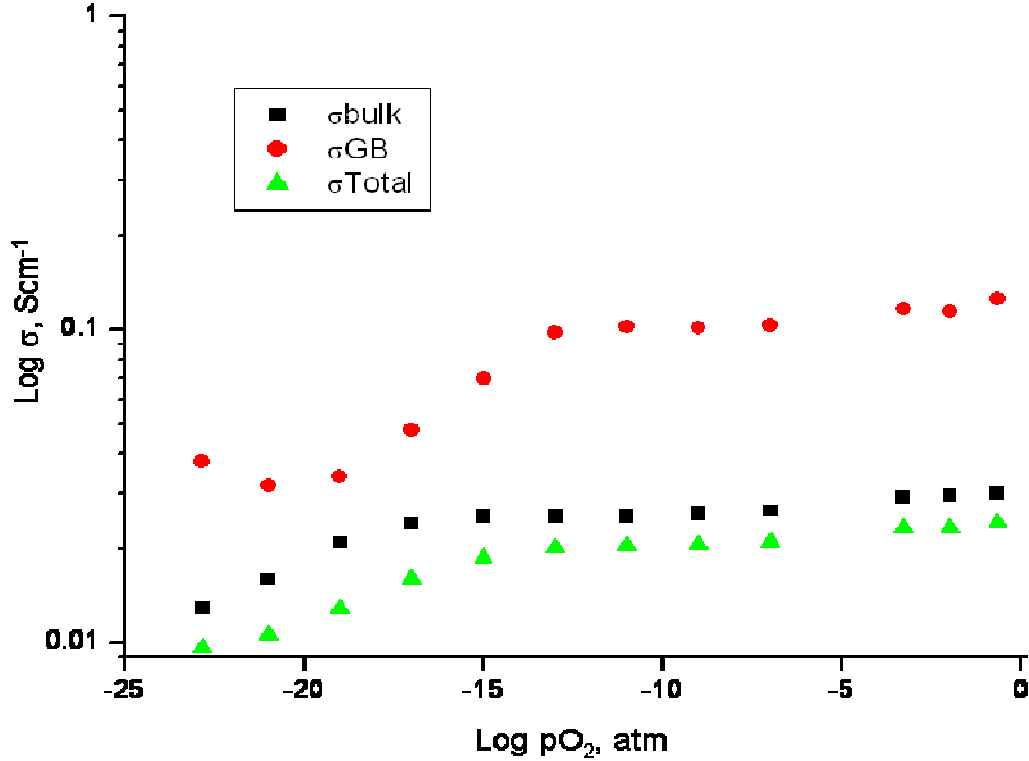
Figure 4.26: Conductivity as function of oxygen partial pressure, for the composition $Ce_{0.20}Sc_{0.6}Zr_{3.2}O_{7.70}$. Measurements performed by Andreas Egger, University of Leoben, Austria.

Figure 4.25 and 4.26 show curves for two different compositions, $Ce_{0.16}Y_{0.04}Sc_{0.6}Zr_{3.2}O_{7.68}$ and $Ce_{0.20}Sc_{0.6}Zr_{3.2}O_{7.70}$. Bulk and grain boundary processes present the same behaviour, at reducing atmosphere, conductivity drops. For the bulk conductivity, this is an indication that the oxygen vacancies order creates an obstacle for ionic conduction, diminishing conductivity. The grain boundary process has a slight increase in conductivity when oxygen partial pressure reaches 10^{-20} atm, this indicates a change in grain boundary which enhance conductivity.

Electronic conductivity

For electronic conductivity to occur, when frequency is 0 Hz, the impedance of the ionic process and the impedance of the charge transfer must be in serial connections, and in parallel connection with the electronic resistance, Figure 4.27.
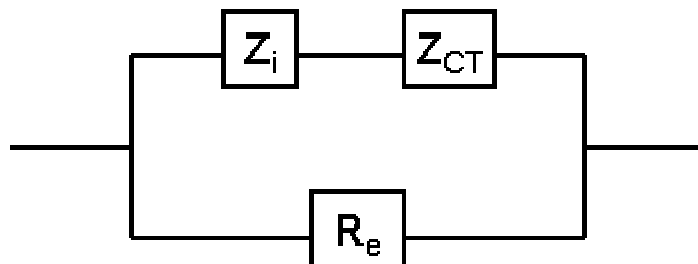
Figure 4.27: Scheme of the circuit, impedance and resistance of ionic and electronic conductivity.

When $f = 0 Hz$, Z must be equal to R_e.

For oxidising atmospheres, the semi-circle corresponding to the electrode process has a value when the frequency is 0 Hz. When in reducing atmospheres, the values for the electrode process will increase greatly. This happens because the lack of oxygen, in the electrode, will limit the conversion between ionic and molecular oxygen, although the ionic conductivity inside the material will not be affected. To determine the electronic conductivity, impedance measures should be performed with blocking electrodes, for example gold.

For all the pellets tested, for this ceria content, there is no evidence of dominant electronic conductivity.
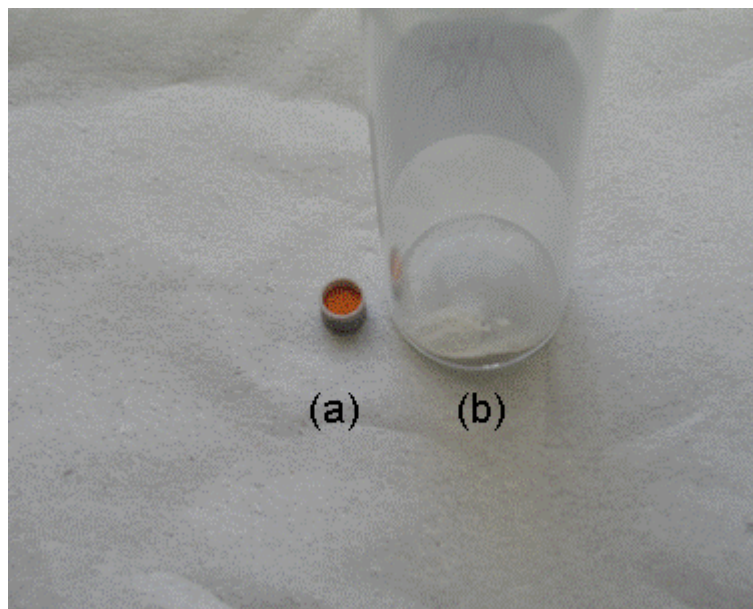
Figure 4.28: Picture of powder from the compositions $Ce_{0.12}Y_{0.08}Sc_{0.6}Zr_{3.2}O_{7.66}$, (a) powders reduced in hydrogen and (b) powder oxidised.

Figure 4.28 shows that the composition reduced in hydrogen has an orange colour, while the powders in the oxidised state are white.

The TGA, Figure 4.29, was performed starting from room temperature up to 900 °C and return to room temperature, in 5%H_2/Ar and after that the gas was switch to air and was run again from room temperature to 900 °C and return to room temperature. This experiment was performed to calculate the amount of oxygen that was removed from the sample, when oxygen partial pressure was removed from the atmosphere. The air run was performed to confirm if the sample would re-absorbed the amount of oxygen, when a change in the atmosphere occurs.
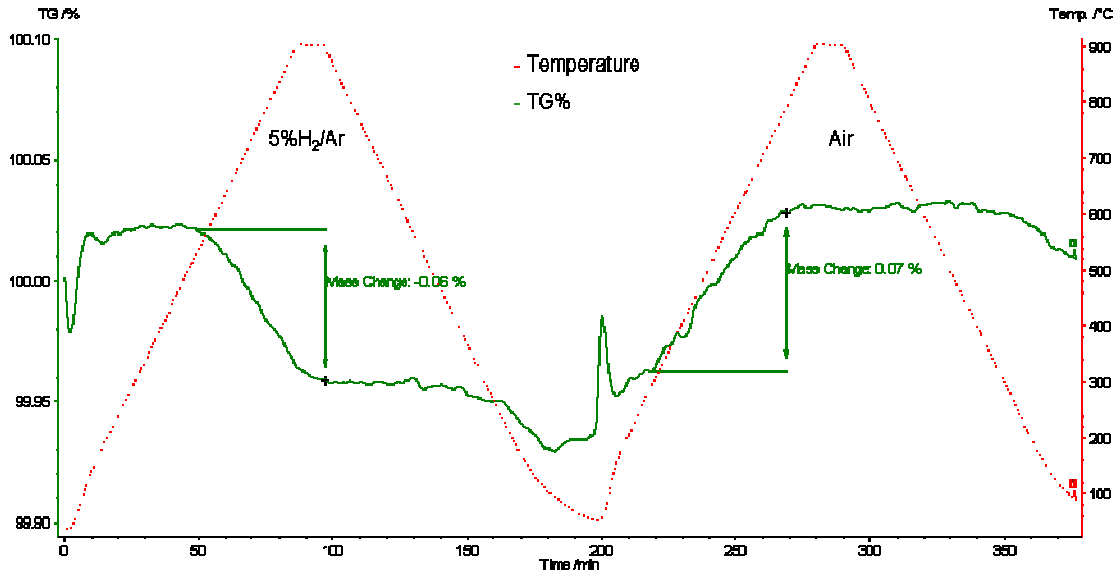
Figure 4.29: TGA, for composition $Ce_{0.08}Y_{0.12}Sc_{0.6}Zr_{3.2}O_{7.64}$, first at $5\%H_2$/Ar and the second in Air.

For the curve of reducing atmospheres, for temperatures between 575 and 900 °C, there is a decrease in mass of 0.06 %, this reaction is reversed in oxidising atmospheres at temperatures between 325 and 600 °C. This change in mass occurs due to the reduction of Ce^{4+} to Ce^{3+}, this way increasing the amount of vacancies in the sample. The extra vacancies will probably order in the matrix, inducing a decrease in conductivity.

$$\frac{\Delta TG * Mr(\ Ce_{0.08}Y_{0.12}Sc_{0.6}Zr_{3.2}O_{7.64}\ ) * 0.01}{16} = 0.02\ oxygen\ atoms$$

In a unit cell there is a loss of 0.02 oxygen atoms, due to the reduction of the cerium, from Ce^{4+} to Ce^{3+}. This means that 0.02 oxygen vacancies are creates when this material is submitted to reducing atmospheres, inducing to the probable clustering of vacancies.

In reducing atmospheres, this material (zirconia based electrolyte) is considered as a n-type semiconductor, and the vacancies (chemical defects) concentration is proportional to $pO_2^{-1/6}$. For intermediate regions the oxide ions are the majority charge carriers, [29].

Figure 1.27 shows the change in defects (electrons, electron holes or ions) concentration with a change in oxygen partial pressure. Figure 4.21 shows the conductivity of the material as a function of oxygen partial pressure. Observing Figure 1.27 and Figure 4.21, one can say that the ionic conductivity on Figure 4.21 decreases with the decrease in the oxygen partial pressure. This can be the result of oxygen deprivation, from the atmosphere, which will condition the reaction at the electro/electrolyte interface. In addition, in these atmosphere conditions, Ce^{4+} will reduce to Ce^{3+}, creating more oxygen vacancies, which will rearrange leading to a blocking affect, thus decreasing the ionic conductivity.

4.4. Summary

AC Impedance Measurement as a Function of Temperature

- All compositions have a similar behaviour; there are two regions in the plot, Figure 4.8, one at high temperatures and another at low temperatures. There is a temperature interval, between 575 and 600 ºC, where all compositions change its conductive behaviour. This change occurs due to the shift from a slower ionic conductive process to a faster ionic conductivity process. At low temperature the conductive process is divided in two parts, the first to dissociate oxygen vacancy from a cluster and the second the oxygen vacancy migration process. While at high temperature vacancies are free and the energy necessary is only for the oxygen vacancy migration.

- When ionic conductivity is compared between all compositions, no significant difference in conductivity is observed, although curves with lower ceria content are located below the curves referring to higher ceria content. These observations are in agreement with Haile [13] and Mogensen [25], who state that the introduction of a large ion will improve conductivity.

- Generally the activation energy for the bulk process is lower than for the grain boundary process. Total activation energy, at high temperatures, above 600 °C, is lower than the total activation energy at temperatures below 600 °C. This is explained with the change of ionic conductive process and less energy necessary to migrate a free oxygen vacancy.

- Ionic conductivity, at 600 °C, for composition $Y_{0.2}Sc_{0.6}Zr_{3.2}O_{7.60}$, has higher values than the ones found in literature, for Y_2O_3-Sc_2O_3-ZrO_2 systems [8, 9]. Ionic conductivity value, for the composition $Ce_{0.04}Y_{0.02}Sc_{0.67}Zr_{3.27}O_{7.66}$ [$(CeO_2)_{1.0}(Y_2O_3)_{0.2}(Sc_2O_3)_{9.2}(ZrO_2)_{89.6}$], $\sigma = 0.017$ S/cm, is higher than for a similar composition $(CeO_2)_1(Sc_2O_3)_{10}(ZrO_2)_{89}$ [9], which has an ionic conductivity of 0.013 S/cm.

- The EDS from TEM, Figure 4.10, shows that the curve corresponding to the grain boundary has two extra peaks, which corresponds to the element cerium

that do not exist on the bulk curve. This can indicate that there is cerium and segregation to the grain boundaries. The behaviour of cerium can indicate that the matrix of the scandia zirconia does not accommodate cerium element and segregates it to the grain boundaries. Figure 4.24 also suggest that aluminium is segregated to the grain boundary.

- In all micrographs, large grains can be observed, which have a size of approximately 5 μm, and also smaller "sub-grains", 10-100 nm, inside the larger grains. Although the sub-grains have a different coloration, the EDS from SEM do not show differences in composition.

Comparison of $Ce_{0.04}Y_{0.02}Sc_{0.67}Zr_{3.27}O_{7.66}$ and $Ce_{0.16}Y_{0.04}Sc_{0.6}Zr_{3.2}O_{7.68}$ compositions

- At low temperatures, curves overlap, but at high temperatures, there is a difference between the curves; this difference increases with the increase of temperature. The curve for the composition $Ce_{0.04}Y_{0.02}Sc_{0.67}Zr_{3.27}O_{7.66}$ has slightly higher values for total conductivity, at high temperature, Figure 4.16.

- Bulk conductivity values at low temperature for initial composition is higher than for the composition $Ce_{0.16}Y_{0.04}Sc_{0.6}Zr_{3.2}O_{7.68}$, this small difference can be caused by segregation of the high level of dopants, in $Ce_{0.16}Y_{0.04}Sc_{0.6}Zr_{3.2}O_{7.68}$, to the grain boundary and/or formation of vacancy clusters and consequently decrease the conductivity [25].

Comparison of sol-gel and combustion method and solid state synthesis method

- The Arrhenius plot, Figure 4.18, shows that ionic conductivity for a pellet produced by SSS is lower than for a pellet produced by SG-C. There are two possible factors which can influence conductivity: (1) the geometric factor; the conductivity is inversely proportional to the geometric factor. (2) Porosity; when the ion flux encounters a pore, or a pore chain, this ion flux is interrupted and/or delayed, which will condition the ionic conductivity in the material [26-28].

AC Impedance Measurement as a Function of Oxygen Partial Pressure

- For the sample with no ceria in its composition, $Y_{0.2}Sc_{0.6}Zr_{3.2}O_{7.60}$, the conductivity does not vary significantly while the oxygen partial pressure

decreases. For the sample with a higher content of ceria, $Ce_{0.12}Y_{0.08}Sc_{0.6}Zr_{3.2}O_{7.66}$, there is a decrease in conductivity while oxygen partial pressure decreases; and there is also the appearance of a semi-circle for lower oxygen partial pressures, Figure 4.23. Two possible explanations for the decrease in conductivity for composition $Ce_{0.12}Y_{0.08}Sc_{0.6}Zr_{3.2}O_{7.66}$ are: (1) when oxygen partial pressure decreases, a reduction of Ce^{4+} to Ce^{3+} occurs, leading to an increase of oxygen vacancies in the sample; these vacancies will rearrange leading to a blocking affect, thus decreasing the ionic conductivity; (2) according to Figure 4.10 and Figure 4.24 a segregation of cerium, yttrium and aluminium to the grain boundary occurs, which will increase resistance at the grain boundary, consequently decreasing conductivity.

- There is a change in the electrode process, when oxygen partial pressure decreases, due to the lack of oxygen, which reduces the conversion rate of oxygen ions on the electrode/electrolyte interface, Figure 4.22 and Figure 4.23. For all the pellets tested with this content of ceria, there is no evidence of dominant electronic conductivity.

References

1. Romero-Castanon, T., Arriaga, L. G., Cano-Castillo, U., Journal of Power Sources, **118** (2003) p. 179-182.
2. Karton, V., Marques, F.M.B. and Atkinson, A., Solid State Ionics, **174** (2004) p. 135-149.
3. http://www.americanelements.com/zr.html. 2005 [cited 2008 November].
4. Politova, T. and Irvine, J.T.S., Solid State Ionics, **168** (2004) p. 153-165.
5. Rey, J.F.Q. and Muccillo, E.N.S., Ceramica, **48**(307) (2002) p. 157-162.
6. Badwal, S.P.S., Solid State Ionics, **76** (1995) p. 67-80.
7. Badwal, S.P.S., Ciacchi, F. T., Rajendram, S. and Drennan, J., Solid State Ionics, **109** (1998) p. 167-186.
8. Yamamura, N., Utsunomiya, N., Mori, T. and Atake, T., Solid State Ionics, **107**(1-2) (1998) p. 185-189.
9. Wang, Z., Cheng, M., Bi, Z., Dong, Y., Zhang, H., Zhang, J., Zhaochi, F. and Li, C., Materials Letters, **59** (2005) p. 2579-2582.
10. Arachi, Y., Sakai, H., Yamamoto, O., Takeda, Y. and Imanishai, N., Solid State Ionics, **121** (1999) p. 133-139.
11. Irvine, J., Politova, T., Zakowsky, N., Kruth, A., Tao, S., Travis, R. and Attia, O. in *Fuel Cell Technologies: State and Perspectives*. 2005: NATO Science series II : Mathematics, physics & chemistry.
12. Badwal, S.P.S., Ciacchi, F. T. and D. Milosevic, Solid State Ionics, **136-137** (2000) p. 91-99.
13. Haile, S.M., Acta Materialia, **51** (2003) p. 5981-6000.
14. Guo, X.a.R.W., Progress in Materials Science, **51** (2006) p. 151-210.
15. Yamamoto, T., Momida, H., Hamada, T., Uda, T., Ohno, T., Thin solid films, **486** (2005) p. 136-140.
16. Kimpton, J., Randle, T.H. and Drennan, J., Solid State Ionics, **149** (2002) p. 89-98.
17. Irvine, J.T.S., Sinclair, D.C., West, Anthony R., Advanced Materials, **2**(3) (1990) p. 132-138.
18. German, R.M., *Sintering Theory and Practice*. 1996, New York: John Wiley & Son.
19. Smith, W.F., *Principles of Materials Science and Engineering*. 3rd ed. 1998, Lisboa: McGraw-Hill.
20. Chang, R., *Quimica*. 5th ed. 1994, Lisboa: McGraw-Hill. 1117.
21. West, A.R., *Basic Solid State Chemistry*. 2nd ed. 1999, Chichester: John Wiley & Sons, Ltd.
22. Lee, D.-S., Kim, W. S., Choi, S. H., Lee, H-W and J-H. Lee, Solid State Ionics, **176** (2005) p. 33-39.
23. Chinn, R.E., *Ceramography, Preparation and Analysis of Ceramic Microstructures*. ASM International. 2002: Materials Park.
24. Setter, N., Waser, R., Acta Materialia, **48** (2000) p. 151-178.
25. Mogensen, M., Lybye, D., Bonanos, N., Hendriksen, P.V. and F.W. Poulsen, Solid State Ionics, **174** (2004) p. 279-286.
26. Rice, R.W., *Porosity of ceramics*. 1998, New York: Marcel Dekker, Inc.

27. Sun, H.T., Cantalini, C. and Pelino, M., Key engineering materials, **115** (1996) p. 167-180.
28. Lux, F., J. Material Science, **28** (1993) p. 285-301.
29. Smart, L., Moore, E., *Solid State Chemistry: An introduction*. 2 ed, ed. Hall, C. 1995, Corwall.

Chapter V

Ageing

5.1. Introduction

This chapter is dedicated to the study of pellets from the system $Ce_xY_{0.2-x}Sc_{0.6}Zr_{3.2}O_{8-\delta}$ ($0 \leq x \leq 0.2$) and the composition $C_{0.04}Y_{0.02}Zr_{3.27}O_{7.66}$, at 600 °C.

The authors, [1-3], state that degradation of conductivity is likely to occur due to a change in the nanostructure of the system. This means that a change in the defect structure and nearest environment of the ions occurs. Zhang *et al.* [4], states that there are four possible microstructural changes, which are responsible for the decrease in conductivity of doped zirconia electrolytes caused by ageing: (1) precipitation of long range ordered phases; (2) formation and precipitation of tetragonal phase in the cubic grains; (3) segregation of dopant-rich layer near grain boundaries and triple points and (4) trapping of oxygen vacancies ($V_O^{\cdot\cdot}$) towards dopant cations with time due to the Coulombic force, short range ordering of oxygen vacancies.

In point (2), the formation and precipitation occur as a result of "growing" of the metastable tetragonal (t or t') or cubic phase in the ZrO_2-Y_2O_3 system and the t'-phase in the ZrO_2-Sc_2O_3 system into low-dopant tetragonal and dopant-rich cubic phases [3, 5-7]. Phase transformation of the zirconia electrolytes can be caused, not only by the type of dopants and dopant concentrations, but also by ageing.

5.2. Experimental

The electrodes used to measure AC impedance, as function of time were made of platinum. The platinum paste was brushed on the base and the top of the pellet surface. After drying the platinum paste, the pellets were sintered at 900 °C, for 30 minutes. The experiment was performed as follow: pellets were introduced in the furnace and heated up to 600 °C, at the rate of 10 $^{\circ}$C/min, and then held at 600 °C. For every measurement,

pellets are removed from the furnace and left in air to cool down. One hour before the measurement, pellets are placed in the jig and inside a furnace at 600 °C. The impedance measurements are performed by means of a frequency response analyzer HP Hewlett-Packard, 4192A LF. The frequency range is 13 MHz-5 Hz and the effective AC voltage amounted to 20 mV. After the end of these experiments, a post-mortem characterisation was performed. Pellets were cut, polished and observed in the SEM.

5.3. Results and discussion

Table 5.1 shows the density of the pellets used in this chapter, from the system $Ce_xY_{0.2-x}Sc_{0.6}Zr_{3.2}O_{8-\delta}$, (0<x<0.2), and for composition $Ce_{0.04}Y_{0.02}Sc_{0.67}Zr_{3.27}O_{7.66}$.

Table 5.1: Density of pellets from the system $Ce_xY_{0.2-x}Sc_{0.6}Zr_{3.2}O_{8-\delta}$ and from composition $Ce_{0.04}Y_{0.02}Sc_{0.67}Zr_{3.27}O_{7.66}$

| Composition	Theoretical density, g/cm^3	Sample density, g/cm^3	% Density	Nomenclature
$Ce_{0.04}Y_{0.02}Sc_{0.67}Zr_{3.27}O_{7.66}$	5.708	5.418	95	Initial
$Y_{0.2}Sc_{0.6}Zr_{3.2}O_{7.60}$	5.699	5.261	92	x=0
$Ce_{0.04}Y_{0.16}Sc_{0.6}Zr_{3.2}O_{7.62}$	5.691	5.334	94	x=0.04
$Ce_{0.08}Y_{0.12}Sc_{0.6}Zr_{3.2}O_{7.64}$	5.725	5.302	93	x=0.08
$Ce_{0.1}Y_{0.1}Sc_{0.6}Zr_{3.2}O_{7.65}$	5.732	5.551	97	x=0.10
$Ce_{0.12}Y_{0.08}Sc_{0.6}Zr_{3.2}O_{7.66}$	5.771	5.339	93	x=0.12
$Ce_{0.16}Y_{0.04}Sc_{0.6}Zr_{3.2}O_{7.68}$	5.779	5.430	94	x=0.16
$Ce_{0.20}Sc_{0.6}Zr_{3.2}O_{7.70}$	5.798	5.326	92	x=0.20

Pellets used in this experiment were sintered at 1500 °C for 12 hours. All densities are above 92%, the highest achieved is for the composition $Ce_{0.1}Y_{0.1}Sc_{0.6}Zr_{3.2}O_{7.65}$, which is 97 %.

5.3.1 AC Impedance measurement as function of time

The following section presents results from AC impedance measurements, for the pellets shown in Table 5.1. During this experiment two pellets for each composition were tested, although in this chapter only the pellets which did not have any problems are presented. These problems are related with stability, irregularity and/or failure of samples between measurements.

Figure 5.1 summarises the changes in the conductivity behaviour against time, for all compositions. The shaded area is to stand out the degradation in conductivity of the pellets.
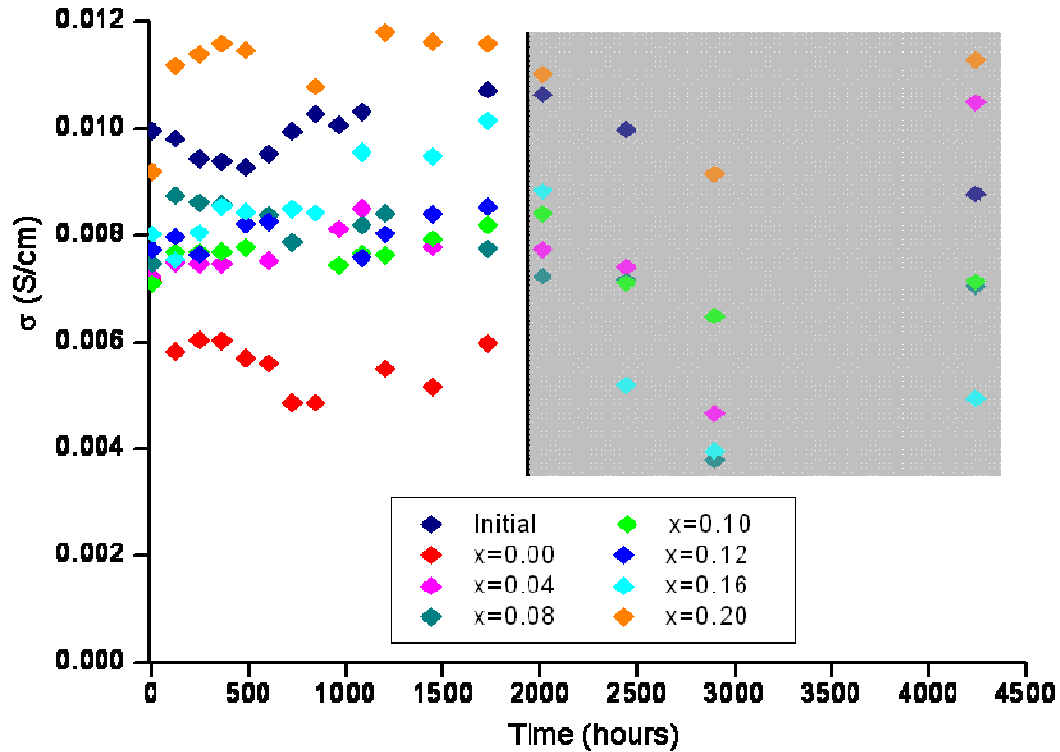
Figure 5.1: Variation of total conductivity as function of time, for compositions of the system $Ce_xY_{0.2-x}Sc_{0.6}Zr_{3.2}O_{8-\delta}$ (0<x<0.2) and the composition $Ce_{0.04}Y_{0.02}Sc_{0.67}Zr_{3.27}O_{7.66}$, at 600 °C

For the first 1800 hours of the experiment, there is no significant variation of conductivity, although some oscillation can be observed. The stability of the conductivity is in agreement with results from Haering *et al* [5, 7]. After 1800 hours, shaded area in Figure 5.1, all compositions decrease their conductivity, until time equal 2896 hours. During this experiment a power failure occurred at approximately 3500 hours and last for 36 hours, therefore the last measurement at 4240 hours was excluded from discussion, as the conductivity values increased instead of the expected decrease.

Composition $Ce_{0.20}Sc_{0.6}Zr_{3.2}O_{7.70}$ (in orange) has the highest conductivity and also has the highest amount of ceria, on the other hand, the composition with no ceria content (in red) has the lowest conductivity values. There are no measurements for the pellets from the composition with no ceria, after 1729 hours, because they were damaged.

The values for total conductivity, for the first measurement, time equals 0 hours, are lower than for the second measurement, after 480 hours, except for compositions $Y_{0.2}Sc_{0.6}Zr_{3.2}O_{7.60}$ and $Ce_{0.16}Y_{0.04}Sc_{0.6}Zr_{3.2}O_{7.68}$, Figure 5.1. One possible explanation is that the first measurement could have been performed at a slightly lower temperature than for the remaining part of the experiment.

Table 5.2 shows the values for conductivity of the first measurement, time equals 0 hours. Measurement for time equals 480 hours is included, to have stable temperature conditions, for comparison. The fourth column presents values for conductivity from the temperature variation experiment in chapter IV.

Table 5.2: Conductivity of the first measurement for the ageing experiment and conductivity of other samples for the same composition

Composition	Conductivity after 0 hours, S/cm	Conductivity after 480 hours, S/cm	Conductivity from chapter 4, S/cm
$Ce_{0.04}Y_{0.02}Sc_{0.67}Zr_{3.27}O_{7.66}$	0.0100	0.0093	0.016
$Y_{0.2}Sc_{0.6}Zr_{3.2}O_{7.60}$	0.0071	0.0057	0.010
$Ce_{0.04}Y_{0.16}Sc_{0.6}Zr_{3.2}O_{7.62}$	0.0072	0.0075	0.008
$Ce_{0.08}Y_{0.12}Sc_{0.6}Zr_{3.2}O_{7.64}$	0.0075	0.0085	0.010
$Ce_{0.1}Y_{0.1}Sc_{0.6}Zr_{3.2}O_{7.65}$	0.0071	0.0078	0.006
$Ce_{0.12}Y_{0.08}Sc_{0.6}Zr_{3.2}O_{7.66}$	0.0077	0.0082	0.009
$Ce_{0.16}Y_{0.04}Sc_{0.6}Zr_{3.2}O_{7.68}$	0.0080	0.0084	0.014
$Ce_{0.20}Sc_{0.6}Zr_{3.2}O_{7.70}$	0.0092	0.0115	0.010

For all compositions there is a slight increase in conductivity after 480 hours when compared with conductivity values for 0 hours, except for compositions $Y_{0.2}Sc_{0.6}Zr_{3.2}O_{7.60}$. This can reinforce the idea of the first measurement, for the ageing experiment, being performed at temperatures slightly below 600 °C and the difference in conductivity, in some compositions, can also be due to the better ionic conductivity of the samples.

Conductivity values from the fourth column are the best obtained in the temperature variation experiment, from chapter IV, for each composition of the system $Ce_xY_{0.2-x}Sc_{0.6}Zr_{3.2}O_{8-\delta}$ (0<x<0.2) and the composition $Ce_{0.04}Y_{0.02}Sc_{0.67}Zr_{3.27}O_{7.66}$. When samples of the ageing experiment are compared with the samples from chapter IV, there are some differences: for compositions $Ce_{0.04}Y_{0.16}Sc_{0.6}Zr_{3.2}O_{7.62}$, $Ce_{0.12}Y_{0.08}Sc_{0.6}Zr_{3.2}O_{7.66}$ and $Ce_{0.20}Sc_{0.6}Zr_{3.2}O_{7.70}$, the difference in conductivity is less than 20 %; for compositions $Ce_{0.04}Y_{0.02}Sc_{0.67}Zr_{3.27}O_{7.66}$, $Y_{0.2}Sc_{0.6}Zr_{3.2}O_{7.60}$, $Ce_{0.08}Y_{0.12}Sc_{0.6}Zr_{3.2}O_{7.64}$, and $Ce_{0.16}Y_{0.04}Sc_{0.6}Zr_{3.2}O_{7.68}$, the difference varies from 30 to 75 %. In the case of the composition $Ce_{0.1}Y_{0.1}Sc_{0.6}Zr_{3.2}O_{7.65}$ conductivity value of the ageing sample is higher than the sample from chapter IV. Although these ageing samples present lower conductivity when compared with the samples from chapter IV, the samples with higher ceria content have higher conductivity than samples with lower ceria content.

AC Impedance Spectra of $Ce_{0.04}Y_{0.16}Sc_{0.6}Zr_{3.2}O_{7.62}$

The results are presented and commented, firstly analysing the composition behaviour through time, and then comparing the behaviour of the different compositions.
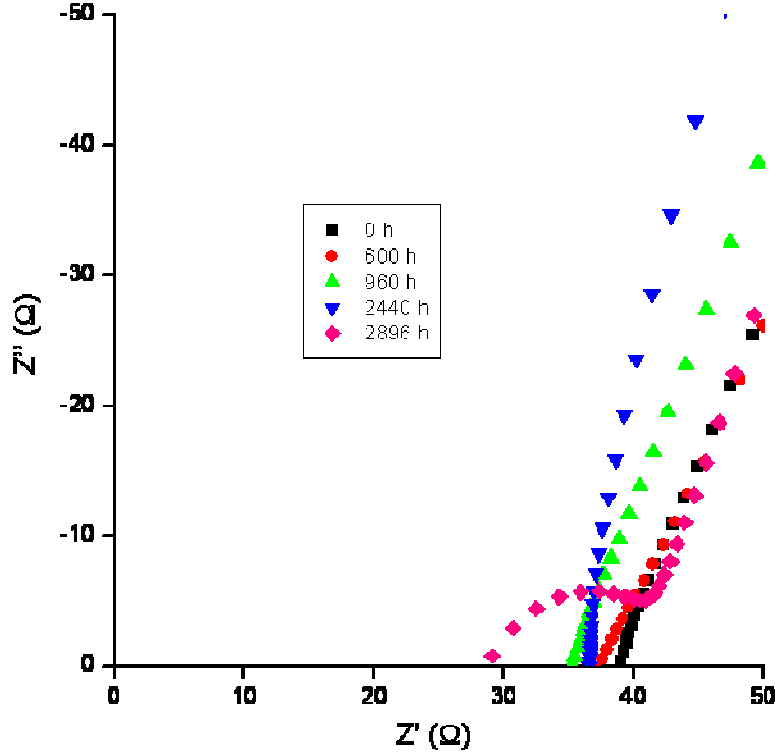
Figure 5.2: Impedance spectra plot from the composition $Ce_{0.04}Y_{0.16}Sc_{0.6}Zr_{3.2}O_{7.62}$, at 600 °C.

Figure 5.2 shows the AC impedance spectra for composition $Ce_{0.04}Y_{0.16}Sc_{0.6}Zr_{3.2}O_{7.62}$ and Table 5.3 shows the values for resistance and capacitance.

Table 5.3: Bulk resistance, grain boundary resistance and total resistance and capacitance correspondent to the semi-circle.

Time, hours	Resistance bulk, Ω	Resistance GB, Ω	Resistance Total, Ω	Capacitance, F/cm
0	-	-	38.88	-
600	-	-	37.41	-
960	-	-	34.96	-
2440	-	-	36.62	-
2896	40.49	16.52	57.01	1.31×10^{-8}

Observing Figure 5.2 and Table 5.3, one can say that the resistance decreases, from the beginning of the experiment to 960 hours. From 960 hours until 2440 hours, the resistance increases; when the measurement is performed at 2896 hours there is an increase in resistance and in addition there is the appearance of a semi-circle, which provides values for the bulk and grain boundary resistance, shown in Table 5.3.

AC Impedance Spectra of $Ce_{0.08}Y_{0.12}Sc_{0.6}Zr_{3.2}O_{7.64}$

Figure 5.3 shows the impedance spectra for composition $Ce_{0.08}Y_{0.12}Sc_{0.6}Zr_{3.2}O_{7.64}$ and Figure 5.4 shows a magnification of the area of interest. Table 5.4 show values for bulk resistance, grain boundary resistance and total resistance and the capacitance correspondent to the second semi-circle.
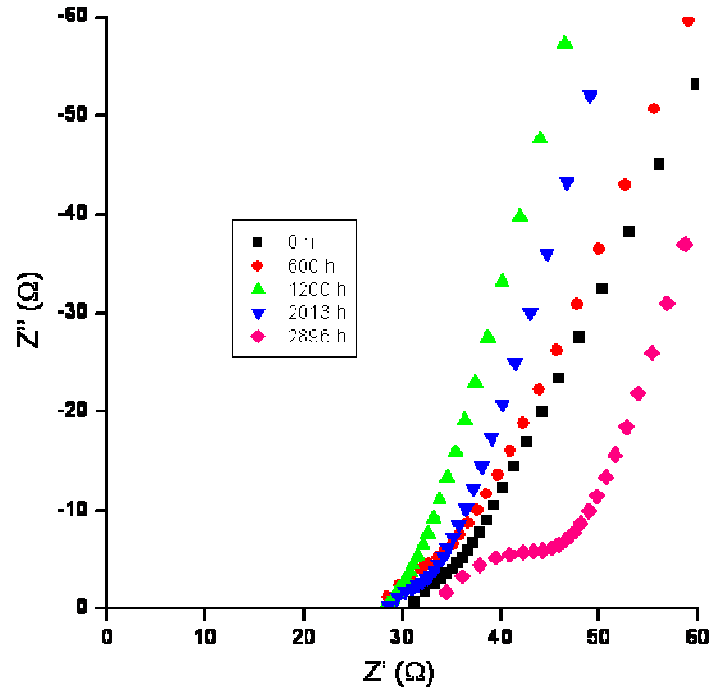
Figure 5.3: Impedance spectra plot from the composition $Ce_{0.08}Y_{0.12}Sc_{0.6}Zr_{3.2}O_{7.64}$, at 600 °C.
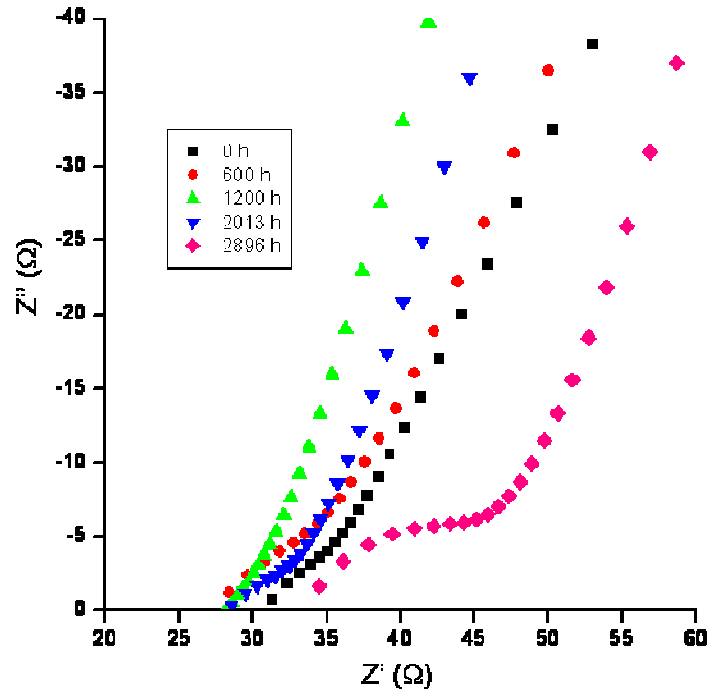
Figure 5.4: Magnification of the impedance spectra plot from the composition
$Ce_{0.08}Y_{0.12}Sc_{0.6}Zr_{3.2}O_{7.64}$, at 600 °C.

Table 5.4: Bulk resistance, grain boundary resistance and total resistance and capacitance
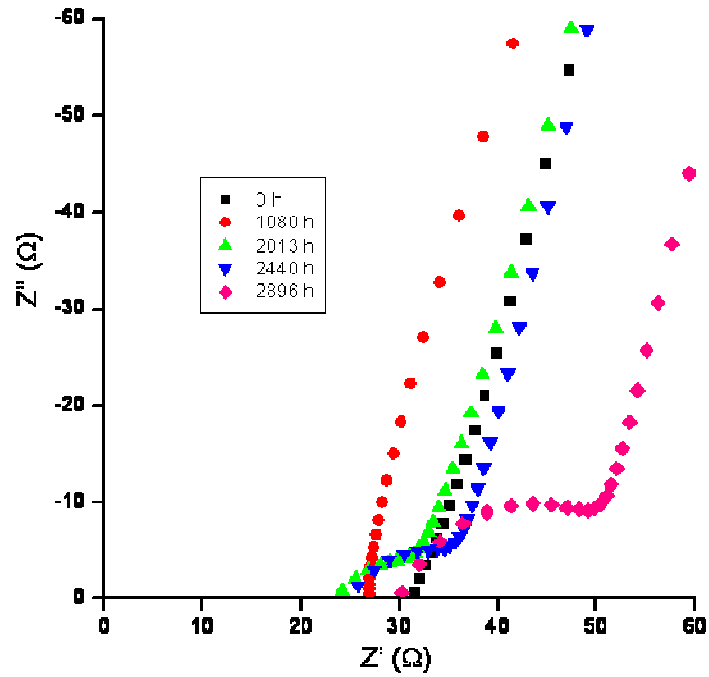correspondent to the semi-circle.

Time, hours	Resistance bulk, Ω	Resistance GB, Ω	Resistance Total, Ω	Capacitance, F/cm
0	-	-	30.72	-
600	-	-	27.79	-
1200	-	-	27.68	-
2013	-	-	29.48	-
2896	33.01	22.25	55.26	1.48×10^{-8}

Observing Figure 5.3 and Table 5.4, one can say that the total resistance decreases from
the beginning of the experiment until 1200 hours. From 1200 hours until 2013 hours
resistance increases. Measurement performed after 2896 of working hours has a sudden
increase in resistance. This can indicate that after 2013 hours a change in microstructure
and/or a change in the grain boundary occur. A semi-circle appears and capacitance
value related to this semi-circle have an order of magnitude 10^{-8} F/cm. This is a well

sintered sample; therefore the semi-circle could correspond to a grain boundary component and/or the result of the blocking effect from the electrode component.

AC Impedance Spectra of $Ce_{0.16}Y_{0.04}Sc_{0.6}Zr_{3.2}O_{7.68}$

Figure 5.5 shows the impedance spectra for composition $Ce_{0.16}Y_{0.04}Sc_{0.6}Zr_{3.2}O_{7.68}$, at 600 °C. Table 5.5 show values for bulk resistance, grain boundary resistance and total resistance and the capacitance correspondent to the second semi-circle.

Figure 5.5: Impedance spectra plot from the composition $Ce_{0.16}Y_{0.04}Sc_{0.6}Zr_{3.2}O_{7.68}$, at 600 °C.

Table 5.5: Bulk resistance, grain boundary resistance and total resistance and capacitance correspondent to the semi-circle.

Time, hours	Resistance bulk, Ω	Resistance GB, Ω	Resistance Total, Ω	Capacitance, F/cm
0	-	-	31.59	-
1080	-	-	27.09	-
2013	22.88	20.11	42.99	4.73×10^{-8}
2440	24.29	20.50	44.79	2.01×10^{-8}
2896	30.25	28.05	58.30	9.12×10^{-9}

Composition $Ce_{0.16}Y_{0.04}Sc_{0.6}Zr_{3.2}O_{7.68}$ has higher conductivity values than compositions with lower ceria content in the system, but after approximately 1800 hours of this experiment conductivity has a rapid decrease, Figure 5.1.

For the first 1080 hours of the experiment, there is only one semi-circle, corresponding to the electrode process, no other processes were registered. After 2013 hours, there is the appearance of a second semi-circle, which becomes more defined with the increase of time. After the appearance of this second semi-circle, total resistance rapidly increases. Capacitance values have the order of magnitude 10^{-8} F/cm and with time this value decreases. As this sample is well sintered; therefore the semi-circle could correspond to a grain boundary component [8, 9].

Values for total, bulk and grain boundary resistance are presented in Table 5.5. Bulk and grain boundary resistance increase significantly after 2440 hours. This can indicate degradation of the grain boundary and/or a change in the microstructure of the grain boundary, after 2013 hours, leading to an ageing and an increase in resistance.

AC Impedance Spectra of Ce$_{0.20}$Sc$_{0.6}$Zr$_{3.2}$O$_{7.70}$

Figure 5.6 shows the impedance spectra for composition Ce$_{0.20}$Sc$_{0.6}$Zr$_{3.2}$O$_{7.70}$, at 600 °C. Table 5.6 show values for total resistance.
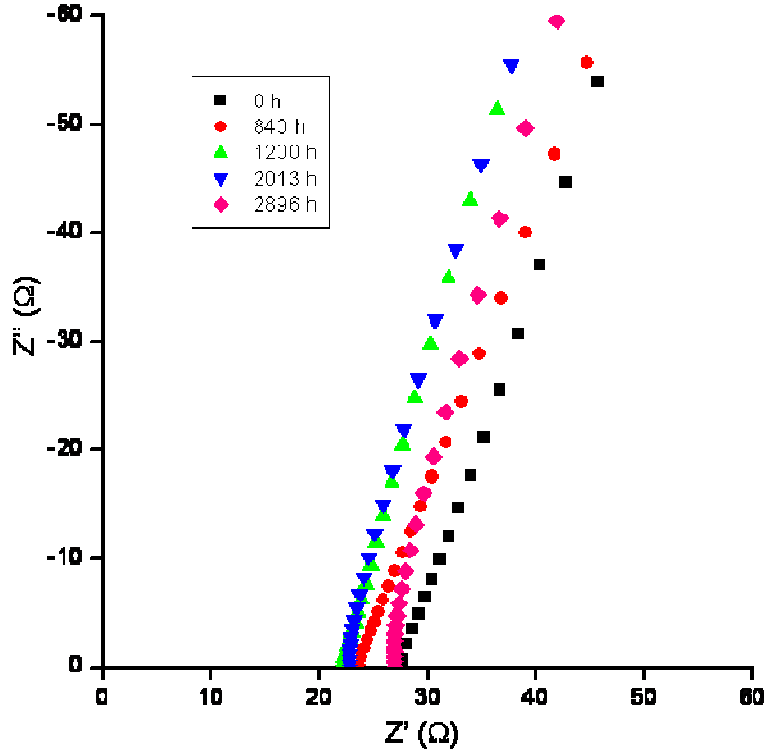
Figure 5.6: Impedance spectra plot from the composition Ce$_{0.20}$Sc$_{0.6}$Zr$_{3.2}$O$_{7.70}$, at 600 °C.

Table 5.6: Total Resistance for different times.

Time, hours	Total Resistance, Ω
0	27.59
840	23.91
1200	22.10
2013	22.81
2896	27.01

There is a decrease in the total resistance from 0 hours to 2013 hours, as curves are located in the left side of the curve for 0 hours. The measurement at 2896 hours shows

that total resistance has increased since the measurement at 2013 hours. After 2013 hours, resistance increases indicating ageing of the sample.

Comparison between compositions

There is a pattern which occurs for all compositions analysed, until 1800 hours, conductivity is fairly stable; after 1800 hours, conductivity decreases until the end of the experiment, indicating ageing. This is in agreement with Haering *et al.* [5]and Nomura *et al.* [10], who state that compositions with scandia content lower than 11 mol%, present degradation in conductivity in first 500 hours but when scandia content is higher than 11 mol% no degradation is observed in first 500 hours. The total dopant content is 11 mol% from all compositions in the system.

Compositions $Ce_{0.04}Y_{0.16}Sc_{0.6}Zr_{3.2}O_{7.62}$ and $Ce_{0.08}Y_{0.12}Sc_{0.6}Zr_{3.2}O_{7.64}$ have similar behaviour throughout this experiment; initially resistance slightly decreases until 1800 hours but after this time resistance starts to increase. When a measurement is taken at 2896 hours a semi-circle appears and it is possible to obtain values for bulk and grain boundary resistance. Composition $Ce_{0.16}Y_{0.04}Sc_{0.6}Zr_{3.2}O_{7.68}$ has a slight decrease of resistance until 1800 hours, after this time resistance starts to increase. From 2013 hours until 2440 hours resistance increases slowly, but after this time 2896 hours bulk and grain boundary resistance increase significantly. *"This is most likely that an ordering process and the formation of microdomains in the low temperature range during long annealing is responsible for conductivity degradation in cubic phase samples"*, as stated by Politova *et al.* [11].

For composition $Ce_{0.20}Sc_{0.6}Zr_{3.2}O_{7.70}$, there is a clear increase in resistance, after 2013 hours, indicating ageing.

The effect which most contributes for the conductivity is the defect association, their concentration and their transformation. As these defects play a major role for the electrical conductivity, it will influence the conductivity degradation too. One way to promote conductivity is to increase the oxygen vacancy number, by doping zirconia with a trivalent oxide. However if the dopant concentration is high, it creates a high level of

vacancies, which will rearrange, hindering conductivity. In addition the increase of vacancies will create an electrostatic interaction between the oxygen vacancies and the dopant cations. This leads to an ordering of the cations during annealing causing the formation of anions microdomains, therefore causing conductivity degradation [5, 7, 10, 11].
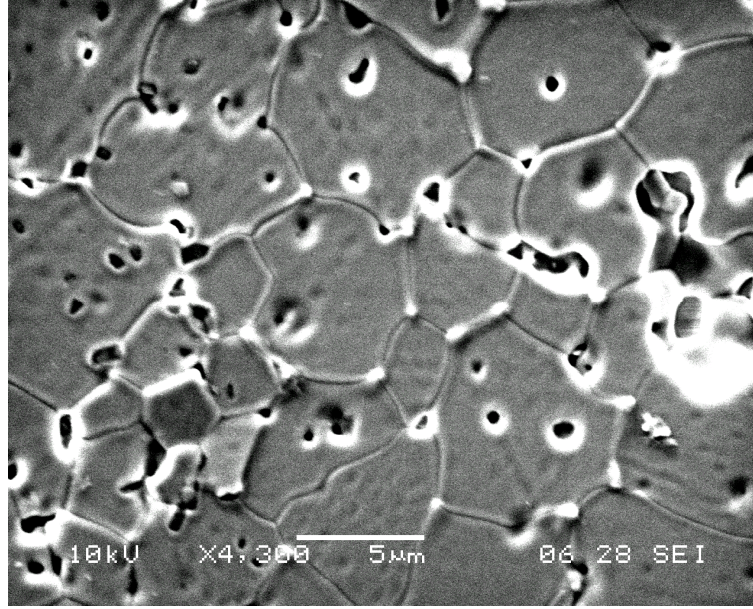
Scanning Electron Micrographics, SEM

After the experiment, the pellets were prepared to be observed in the scanning electron microscope. The details about the procedure to prepare the pellets are in section 4.3.1 SEM, in chapter IV.

Figures 5.7 and 5.9 are micrographs from samples after AC impedance measurements and etching; they are shown for comparison with Figures 5.8 and Figure 5.10, respectively. The samples used for micrographs in Figure 5.8 and Figure 5.10 are the ones used for the ageing experiment. The information regarding Figure 5.7 and Figure 5.9 is presented in chapter IV.
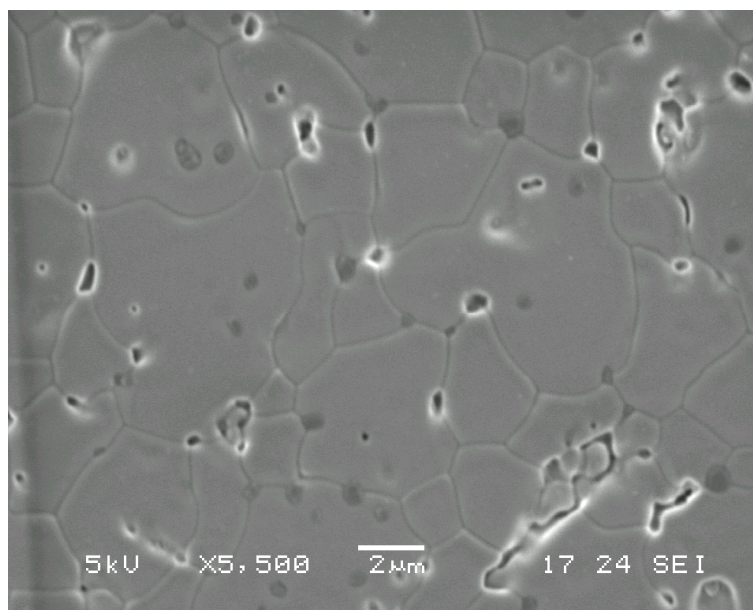
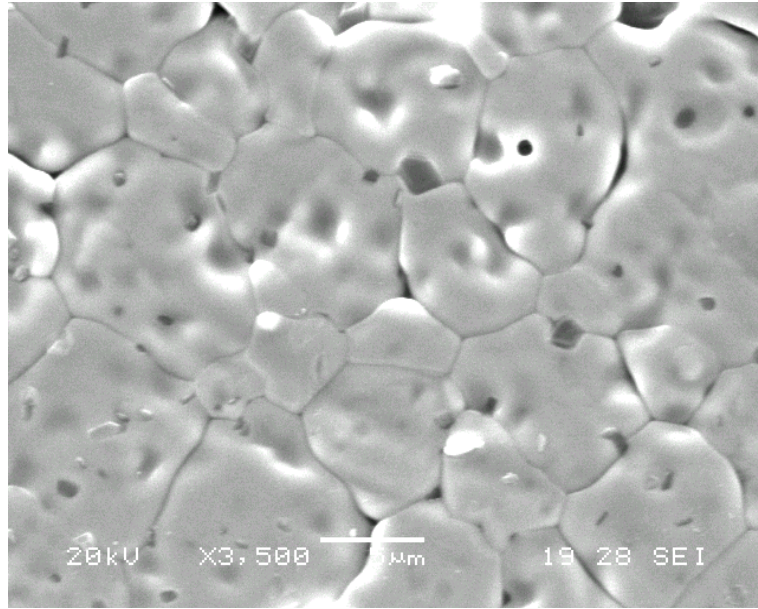**Figure 5.7:** Scanning electron micrograph of $Ce_{0.04}Y_{0.08}Sc_{0.6}Zr_{3.2}O_{7.60}$, not aged

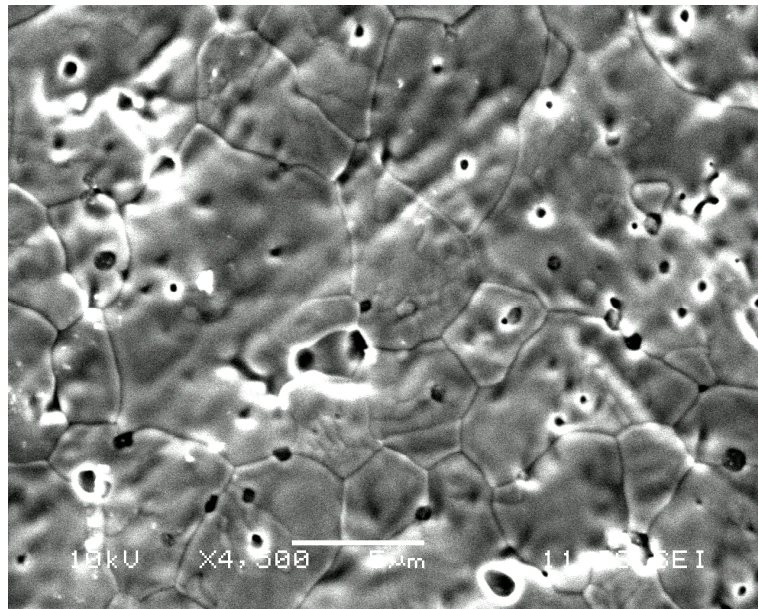**Figure 5.8:** Scanning electron micrograph of $Ce_{0.04}Y_{0.08}Sc_{0.6}Zr_{3.2}O_{7.60}$, after ageing.

In Figure 5.8, micrograph shows an average grain size of $\bar{G} = 7.13 \pm 1.25$ μm, the grain boundaries are well defined and the hill and valley microstructure can be observed. In the sample with no ageing, Figure 5.7, most pores are located in the grain boundary; while in sample after ageing, pores are observed within the grain, bulk. In the bottom left of Figure 5.8, a region with some damage can be observed.

When Figure 5.7 and Figure 5.8 are compared, the first observation is that grains with darker colouration do not appear in the sample after ageing. The surface in Figure 5.8 has surface irregularities on the surface that are not shown on Figure 5.7.
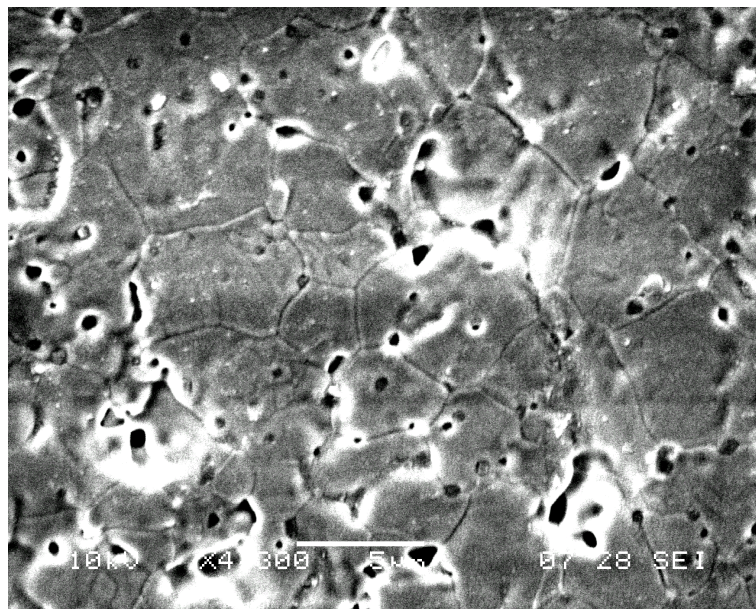
Figure 5.9: Scanning electron micrograph of $Ce_{0.08}Y_{0.12}Sc_{0.6}Zr_{3.2}O_{7.64}$, not aged

Figure 5.10: Scanning electron micrograph of $Ce_{0.08}Y_{0.12}Sc_{0.6}Zr_{3.2}O_{7.64}$, after ageing.

Figure 5.10 shows an average grain size of $\bar{G} = 7.68 \pm 1.25$ μm. The grain boundaries are well defined but it looks that there are smaller grains inside larger ones. It has the appearance that grains start to be divided inside the larger grains. This could be the

indication of microstructure ageing, therefore increasing the grain boundary resistance. The hill and valley microstructure is also visible [12]. Comparing Figure 5.9 and Figure 5.10, the sample aged shows degradation.

Figure 5.11: Scanning electron micrographic of $Ce_{0.16}Y_{0.04}Sc_{0.6}Zr_{3.2}O_{7.68}$, after ageing

Figure 5.11 shows significant damage on the surface, the hill and valley microstructure is more visible [12]. There are pores inside grains and it appears that smaller grains are inside larger grains this way is not accurate to estimate grain size. Cracks and fissures can be observed, showing microstructure deterioration of the sample.
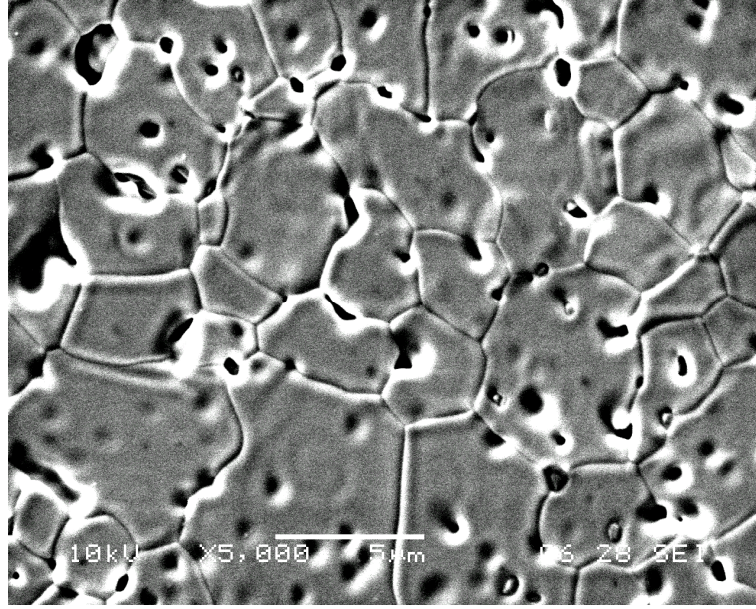
Figure 5.12: Scanning electron micrographic of $Ce_{0.2}Sc_{0.6}Zr_{3.2}O_{7.70}$, after ageing

Figure 5.12 shows an average grain size of $\bar{G} = 6.07 \pm 1.25$ µm. The hill and valley microstructure is visible [12], there are some irregularities on the surface and smaller grains are positioned inside the larger grains.

When comparing micrographs with aged and not aged samples, the first observation is that grains with darker colouration do not appear on the aged samples. Visually, in aged samples, the surface seems to be irregular and damaged; in the microstructure there are cracks and fissures. In some cases, as for compositions $Ce_{0.08}Y_{0.12}Sc_{0.6}Zr_{3.2}O_{7.64}$ and $Ce_{0.16}Y_{0.04}Sc_{0.6}Zr_{3.2}O_{7.68}$, shown in Figure 5.10 and Figure 5.11, respectively, damage is clearly visible. Smaller grains, with not well defined grain boundary, can be observed inside larger grains with well defined grain boundaries. On the other hand, for compositions $Ce_{0.04}Y_{0.08}Sc_{0.6}Zr_{3.2}O_{7.60}$ and $Ce_{0.2}Sc_{0.6}Zr_{3.2}O_{7.70}$, Figure 5.8 and Figure 5.12, respectively, some damage on the surface can be observed, but not as extensive as in Figure 5.10 and Figure 5.11.

Composition $Ce_{0.16}Y_{0.04}Sc_{0.6}Zr_{3.2}O_{7.68}$, Figure 5.11, displays significant surface damage, which correlates with the appearance of a semi-circle for time equals 2013 hours and from this time grain boundary resistance increases until the end of the experiment, Figure 5.5 and Table 5.5.

Impedance spectra for composition $Ce_{0.2}Sc_{0.6}Zr_{3.2}O_{7.70}$, Figure 5.6, do not show any semi-circle during all experiment, which correlates with a less damaged surface, Figure 5.12.

5.4. Summary

- For the first 1800 hours, all compositions present fairly stable conductivity values. After this time conductivity decreases; in some cases, compositions $Ce_{0.04}Y_{0.08}Sc_{0.6}Zr_{3.2}O_{7.60}$ and $Ce_{0.20}Sc_{0.6}Zr_{3.2}O_{7.70}$, this decreases is rapid.

- Composition $Ce_{0.16}Y_{0.04}Sc_{0.6}Zr_{3.2}O_{7.68}$, Figure 5.5, shows the appearance of a semi-circle, with capacitance values with an order of magnitude 10^{-8} F/cm. From this semi-circle, values for bulk and grain boundary resistance can be obtained; these resistance values increase with time. This a well sintered sample; therefore the semi-circle could correspond to a grain boundary component and/or the result of the blocking effect from the electrode component. The SEM, Figure 5.12, shows that this sample has cracks and fissures on the surface, indicating microstructure deterioration.

- When micrographs from samples after AC impedance and samples after the ageing are compared, the first observation is that grains with darker colouration do not appear in the samples after ageing. The surface of samples after ageing has irregularities that are not present on the surface of samples after AC impedance. For all micrographs of samples after ageing, the grain boundaries are well defined and an increase of pores inside grains can be observed, in some cases the surface is damaged showing cracks and fissures. For all compositions, the hill and valley microstructure is visible [12].

- For all composition there is an ageing due to rearrangement involving the defects introduced by dopants. These defects will order during long annealing, originating conductivity degradation.

References

1. Murakami, Y., Nagano, I., and H. Yamamoto, Journal Material Science Letters, **16** (1997) p. 1686-1688.
2. Badwal, S.P.S., Solid State Ionics, **52** (1992) p. 23-32.
3. Ciacchi, F.T. and Badwal, S.P.S., Journal European Ceramic Society, **7** (1991) p. 197-206.
4. Zhang, T.S., Ma, J., Kong, L.B., Chan, S. H. and J. A. Kilner, Solid State Ionics, **170** (2004) p. 209-217.
5. Haering, C., Roosen, A., Schichl, H. and M. Schnoeller, Solid State Ionics, **176** (2005) p. 261-268.
6. Ciacchi, F.T., Badwal, S.P.S. and Drennan, J., Journal European Ceramic Society, **7**(3) (1991) p. 185-195.
7. Haering, C., Roosen, A. and H. Schichl, Solid State Ionics, **176** (2005) p. 253-259.
8. Irvine, J.T.S., Sinclair, D.C., West, Anthony R., Advanced Materials, **2**(3) (1990) p. 132-138.
9. MacDonald, J.R., *Impedance Spectroscopy, emphasizing solid materials and systems*. 1987, New York: John Wiley & Son.
10. Nomura, K., Mizutari, Y., Kawai, H., Nakamura, Y., Yamamoto, O., Solid State Ionics, **132** (2000) p. 235-239.
11. Politova, T. and Irvine, J.T.S., Solid State Ionics, **168** (2004) p. 153-165.
12. Schmidt, M.S., Hansen, K. V., Norrman, K., Mogensen, M., Solid State Ionics, (179) (2008) p. 1436-1441.

Chapter VI

Conclusions

6.1 Conclusions

A combined sol-gel and combustion method was used to produce nano-particle for the system $Ce_xY_{0.2-x}Sc_{0.6}Zr_{3.2}O_{8-\delta}$ ($0 \leq x \leq 0.2$) and $Ce_{0.04}Y_{0.02}Sc_{0.67}Zr_{3.27}O_{7.66}$. All compositions show presence of a single phase, with a cubic fluorite-type structure. Lattice parameter increases, according the Vegard's law, from 5.1040(1) to 5.115(1) Å, in the system $Ce_xY_{0.2-x}Sc_{0.6}Zr_{3.2}O_{8-\delta}$ ($0 \leq x \leq 0.2$).

ICP results show that the sol-gel and combustion method produces homogeneous materials, regarding its composition. There is a reasonable amount of aluminium which might be introduced as a scandia impurity and/or during the combustion stage when aluminium foil is used to cover the beaker. The amount of silicon is negligible.

The sol-gel and combustion method produces nano-particles, although some hard agglomerates (shells) can be formed during the combustion stage, which is violent. SEM pictures also reveal a wide range of grain sizes and the formation of grains with non spherical shape. To breakdown the hard agglomerates, strong mechanical processes are introduced. Using the planetary ball mill, the density increases from 82 %, without any mechanical treatment, to 95 %.

Electrical behaviour

Conductive behaviour can be explained in terms of defect association, their concentration and their transformation.

All compositions have a similar behaviour. In the Arrhenius plot there are two regions, one at high temperatures and another at low temperatures. There is a temperature interval, between 575 and 600 ºC, where all compositions change its conductive behaviour. This change occurs due to the shift from a slower ionic conductive process to a faster ionic conductivity process. At low temperature the conductive process is divided

in two parts, the first to dissociate oxygen vacancy from a cluster and the second the oxygen vacancy migration process. While at high temperature vacancies are free and the energy necessary is only for the oxygen vacancy migration.

When samples with no ceria content are subjected to a decrease in oxygen partial pressure, no significant variation in conductivity is observed. For samples with medium ceria content, $Ce_{0.12}Y_{0.08}Sc_{0.6}Zr_{3.2}O_{7.66}$, are subject to a decrease in oxygen partial pressure, conductivity decreases. This phenomenon can be explained by the reduction of Ce^{4+} to Ce^{3+}, increasing the number of oxygen vacancies leading to an ordering of oxygen vacancies and/or the segregation of aluminium to the grain boundary, decreasing conductivity.

The ageing experiments, at 600 °C, show stability during the first 1800 hours and a decrease in conductivity after 1800 hours, indicating ageing. This ageing can occur by the creation of an electrostatic interaction between the oxygen vacancies and the dopant cations. This leads to an ordering of the cations, and quite possibly migration, during annealing causing the formation of anions microdomain regions, therefore causing conductivity degradation.

6.2 Further Work

There are two different areas where some aspects could be further explored. The first part is about the powder production and the second part, to relate microstructure and conductive process.

Powder production by the sol-gel and combustion method can be improved, in order to avoid the hard agglomerates formation; the amount of fuel, glycine, should be reduced to a level where the combustion would take place but less violently. On the other hand, even without changing the powder production method, stronger mechanical separation processes and chemical dispersants can be experimented in order to reduce those hard agglomerates. For example, an ultra-sonic bath can be used to separate particles.

In the second part, using TEM to understand what changes in microstructure that oxygen partial pressure, temperature and time will cause in the material.

6.3 Publications

- W. Preis, J. Waldhäusl, A. Egger, W. Sitte, E. De Carvalho, J.T.S. Irvine, "*Electrical Properties of bulk and grain boundaries of Scandia-Stabilized Zirconia Co-Doped With Yttria and Ceria*", ECS Trans, October 2009, vol.25, N.2, pages 1635-1642.

- Adjiman, C., Atkinson, A., Azad, A., Baker, R., Brandon, N., Brett, D., Clague, R., Carvalho, E., Corre, G., Choy, K-L., Irvine, J. Marquis, A., Miller, D., Offer, G., Pointon, K., Pyke, S., Slecuk, A., Scott, K. and Shearing, P. "*A Review of Progress in the UK Supergen Fuel Cell Programme*", ECS Trans, October 2009, Vol. 25, N. 2, pages 35-42.

- E. de Carvalho, W. Preis, W. Sitte and J.T.S.Irvine, "*Investigation of Conductivity of $(Ce_xY_{0.2-x}Sc_{0.6})Zr_{3.2}O_{8-\delta}$ system and its Dependence upon Oxygen Partial Pressure*", Solid State Ionics (2009) under review.

- E. de Carvalho and J.T.S. Irvine, "*High Sinterability Doped Scandia Zirconia Powders*", ECS Trans, June 2007, vol.7 N.1, pages. 2223-2231.
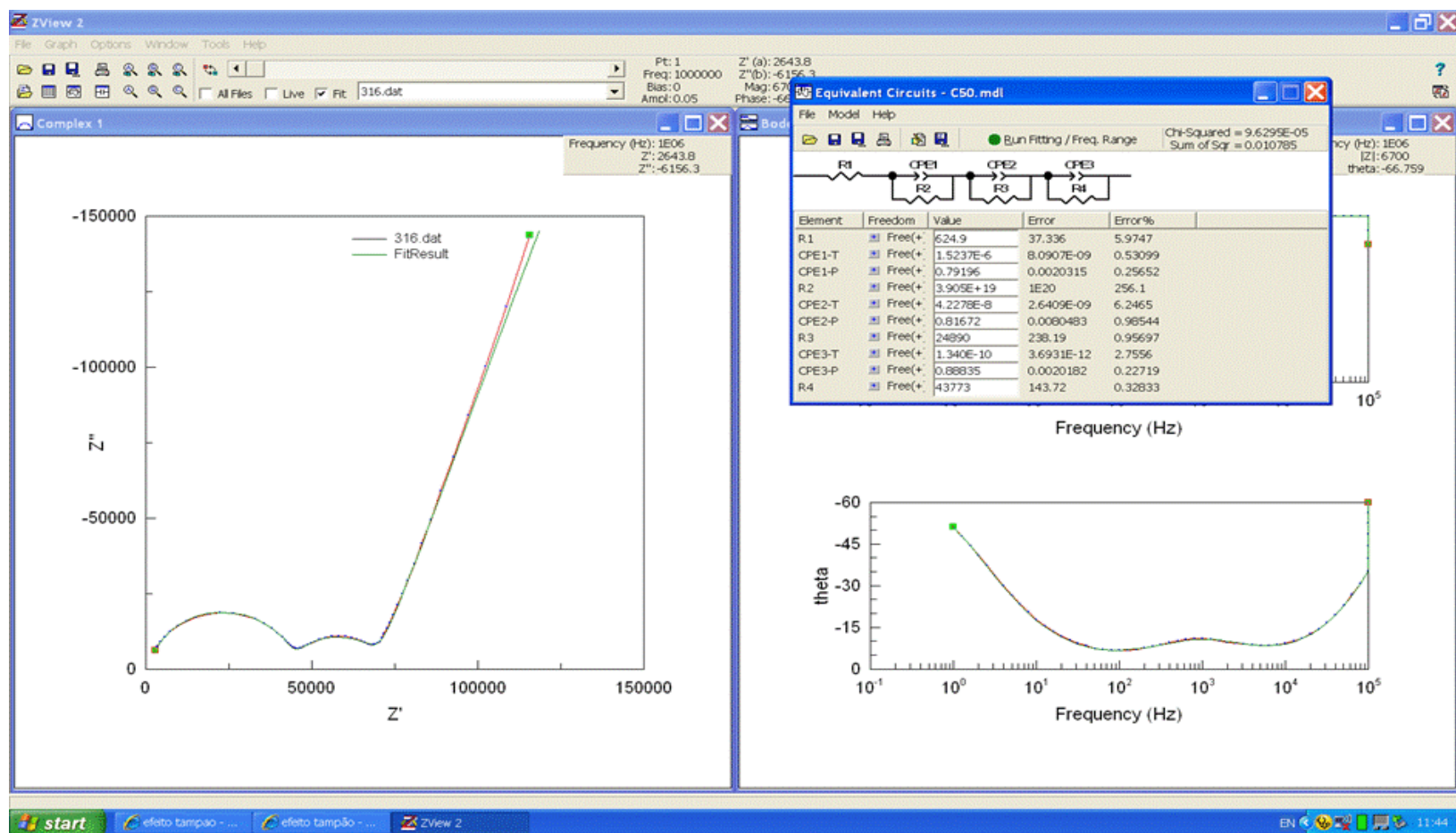
Appendix 1
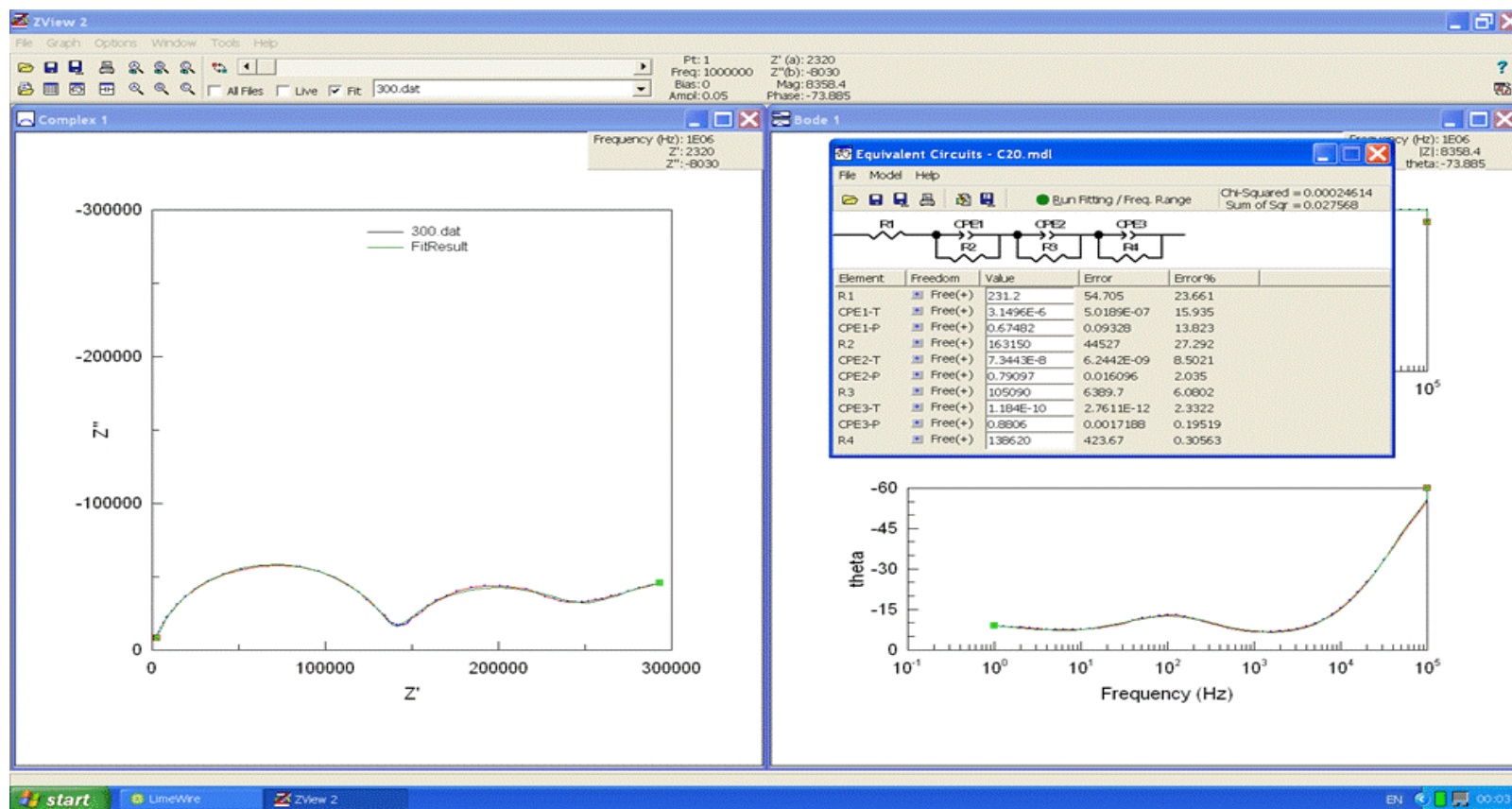
Figure 1: Fitting of the impedance spectra plot corrected by geometry, recorded at 300 °C, for composition $Ce_{0.08}Y_{0.12}Sc_{0.6}Zr_{3.2}O_{7.64}$.
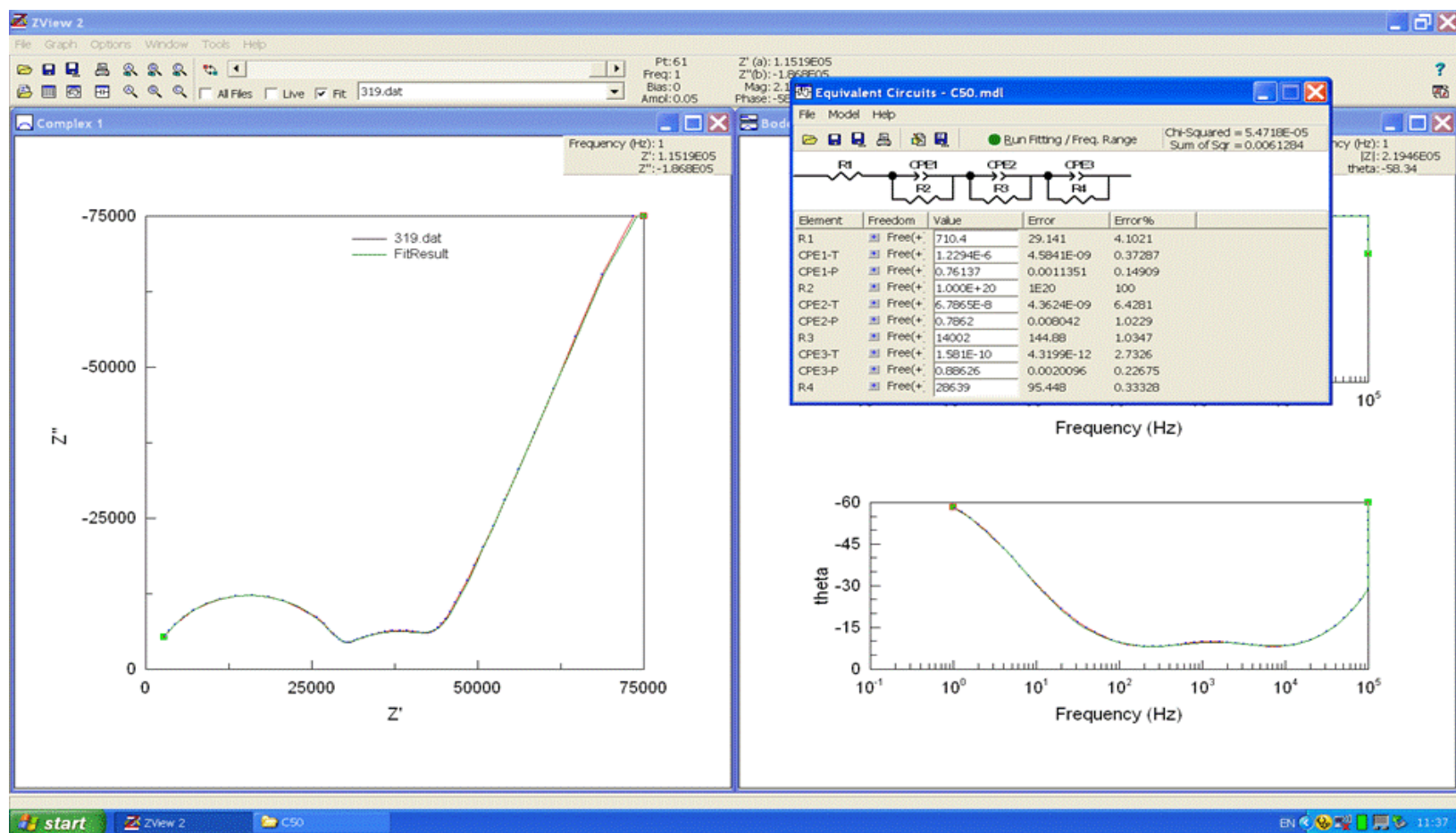
Appendix

Figure 2: Fitting of the impedance spectra plot corrected by geometry, recorded at 300 °C, for composition $Ce_{0.12}Y_{0.08}Sc_{0.6}Zr_{3.2}O_{7.66}$.

Figure 3: Fitting of the impedance spectra plot corrected by geometry, recorded at 300 °C, for composition $Ce_{0.20}Sc_{0.6}Zr_{3.2}O_{7.70}$.

Appendix 2

To estimate the errors of Table 4.8, from chapter IV. The linearization of the Arrhenius plot curve provides the values for the slope, with which the values for the activation energy are obtained. The estimate I used the method of minimal squared deviation.

If the linear correlation coefficient is known, the standard deviation for the linear trend slope can be obtained from:

$$\Delta m = |m| \sqrt{\frac{\frac{1}{r^2} - 1}{n - 2}} \qquad (1)$$

The correlation coefficient r measures the degree of correlation correspondent to the equation that is obtained from the linearization of the curve. The closer r value is to 1, better will be the fitted line between the original curve and the linear trend.

Example:

Figure 4 shows the Arrhenius plot of conductivity of bulk corrected by density, for composition $Y_{0.2}Sc_{0.6}Zr_{3.2}O_{7.60}$, as an example, how to estimate the error of the activation energy.
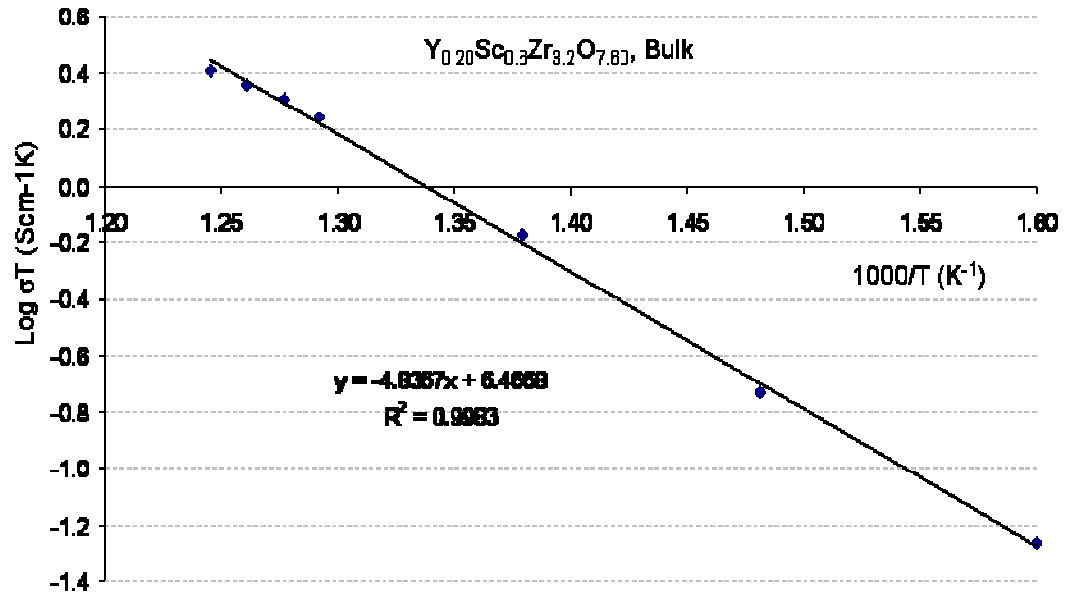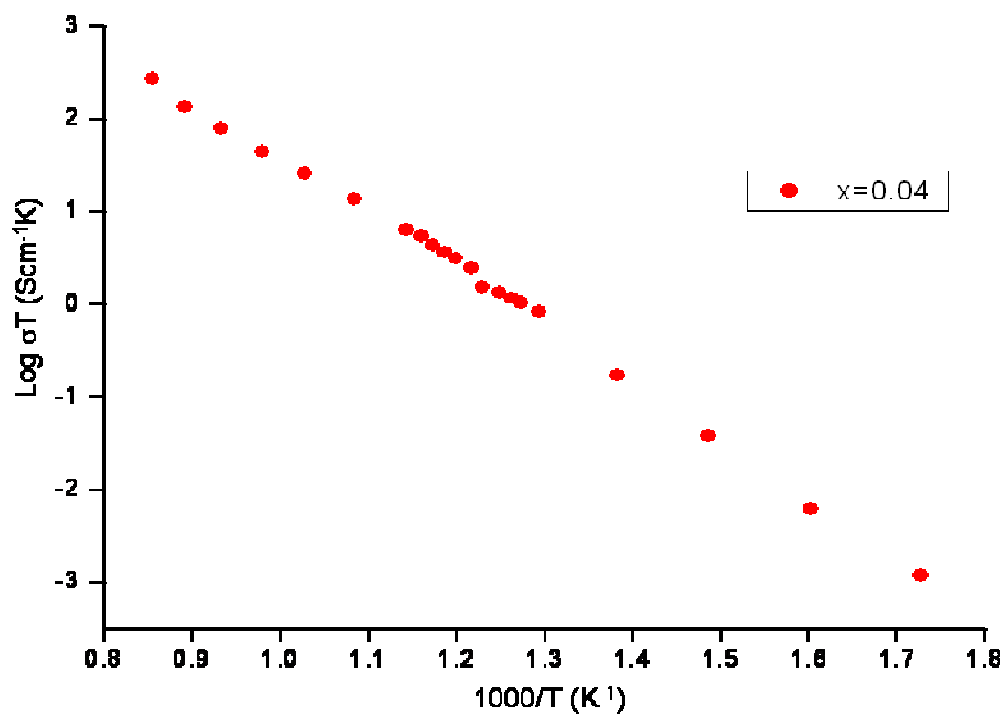
Figure 4: Arrhenius plot of conductivity of bulk corrected by density, at low temperature, for composition $Y_{0.2}Sc_{0.6}Zr_{3.2}O_{7.60}$.

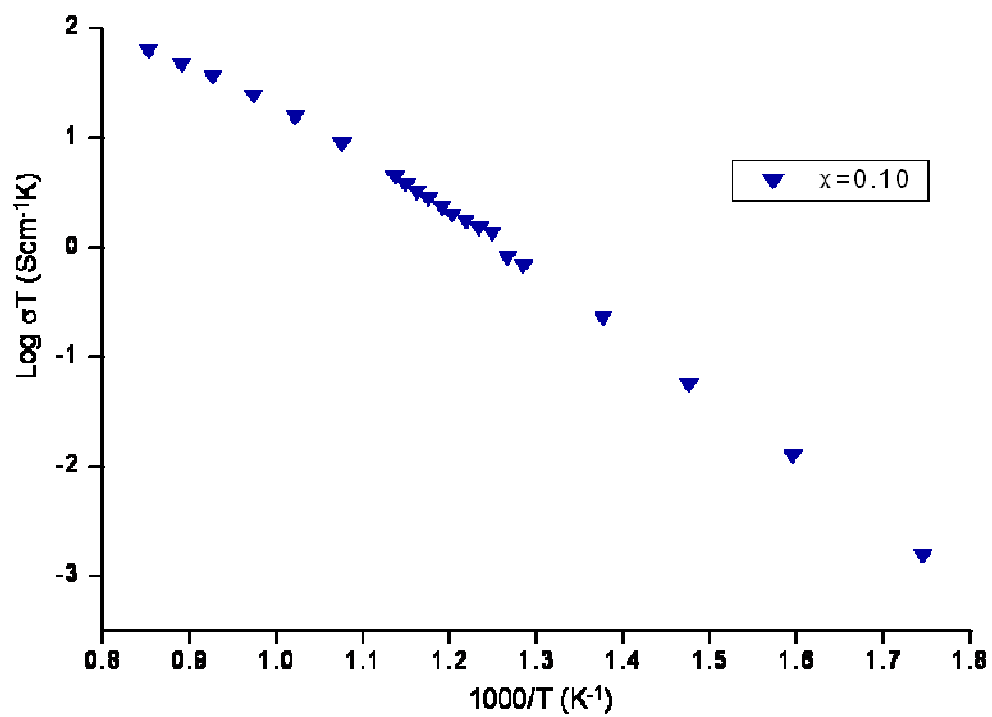Replacing the values obtained in Figure 4 in equation (1),

$$\Delta m = |0.9596| \sqrt{\frac{\frac{1}{0.9983^2} - 1}{7 - 2}}$$

$$\Delta m = 0.004$$

Appendix 3

Figure 5: Arrhenius plot of total conductivity for composition $Ce_{0.04}Y_{0.16}Sc_{0.6}Zr_{3.2}O_{7.62}$.

Figure 6: Arrhenius plot of total conductivity for composition $Ce_{0.1}Y_{0.1}Sc_{0.6}Zr_{3.2}O_{7.65}$